



## THESE DE DOCTORAT

Présentée à

l'Université de Lille

Ecole Doctorale Sciences pour L'Ingénieur Lille Nord-de France

Chimie des matériaux

par Kilaparathi Sravan Kumar

### **Carbon-based electrocatalysts for CO<sub>2</sub> reduction, PET hydrolysate, and water splitting towards value-added products.**

Catalyseurs électrochimiques à base de carbone pour la réduction du CO<sub>2</sub>, l'hydrolyse du PET et la séparation de l'eau en vue de produits à valeur ajoutée.

Soutenue le 14 decembre 2023 devant le jury composé de:

Rapporteur	Dr. François Ozanam	Laboratoire de Physique de la Matière Condensée, Ecole Polytechnique
Rapporteur	Dr. Corinne Lagrost	Institut des Sciences Chimiques de Rennes
Examineur	Prof. Henri Happy	IEMN, Université de Lille, France
Examineur	Assoc Prof. Hong Li	Nanyang Technological University, Singapore
Co-directrice de thèse	Prof. Sabine Szunerits,	IEMN, Université de Lille, France
Directeur de thèse	Dr. Rabah Boukherroub	IEMN, CNRS



## Abstract

This study tackles the major global challenges such as CO<sub>2</sub> emissions, energy crisis and PET plastic waste mismanagement, which not only pollutes the environment but also contributes to CO<sub>2</sub> emissions during incineration. The innovative approach presented in this thesis offers a dual solution, addressing both PET waste and CO<sub>2</sub> emissions simultaneously.

Two remarkable systems have been explored in this thesis. The first utilized Bismuth oxide carbonate (BOC) functionalized reduced graphene oxide (rGO) for cathodic CO<sub>2</sub> electroreduction (CO<sub>2</sub>RR), while CuCoO on rGO was employed for anodic PET hydrolysate oxidation. Impressively, the anodic CuCoO@rGO catalyst displayed exceptional electro-activity, achieving an outstanding Faradaic efficiency (FE) of 85.7% at 1.5V vs. RHE. Simultaneously, the cathodic BOC@rGO catalyst demonstrated an impressive FE of 97.4% at -0.8 V vs. RHE, facilitating the production of formate from CO<sub>2</sub>RR. When integrated into an electrolyzer setup, this approach resulted in formic acid production at a low cell voltage of 1.9 V and a remarkable formate FE of 151.8% at 10 mA cm<sup>-2</sup>.

Another system employed a 3D activated carbon felt (aCF) electrode as substrate and Bismuth has been deposited electrochemically on the CF (Bi@aCF) which acts as the cathode CO<sub>2</sub>RR and nickel cobalt phosphate-deposited carbon felt (NiCoPO<sub>x</sub>@CF) for the anodic PET hydrolysate oxidation process. This setup achieved a high FE of 94% during CO<sub>2</sub>RR at -0.8 V vs. RHE, producing formate, and a FE of 95% for anodic PET hydrolysate oxidation to formate at a low potential of 1.5 V vs. RHE. Remarkably, the two-electrode electrolyzer attained an extraordinary FE of 157% to produce formate at a cell voltage of 1.8 V. This breakthrough represents a novel

pathway for upcycling PET waste, reducing CO<sub>2</sub> emissions, and promoting environmental sustainability.

Additionally, our experiments also delved into water electrolysis, where a novel strategy involving Ru embedded in a carbon nitride matrix was proposed. This approach, utilizing a covalent organic framework 2D CIN-1 structure with coordinated Ru<sup>+2</sup>, resulted in Ru oxide nanoparticles with low-valence Ru sites arranged in nanowires between layers of graphitic carbon nitride after pyrolysis. This material exhibited significantly lower overpotentials for both hydrogen evolution reaction (HER) and oxygen evolution reaction (OER) compared to benchmark Pt and RuO<sub>2</sub> catalysts, demonstrating remarkable catalytic stability. This discovery holds tremendous promise for advancing the field of water splitting and contributing to the development of sustainable energy solutions.

**Keywords:** Electrocatalysis, Carbon dioxide, Electrochemical reduction, Polyethylene terephthalate - Oxidation, Hydrolysis, Graphene oxide, Copper catalysts, Cobalt catalysts, Ruthenium catalysts, Formates.

## Résumé

Cette étude aborde les principaux défis mondiaux tels que les émissions de CO<sub>2</sub>, la crise énergétique et la mauvaise gestion des déchets plastiques PET, qui non seulement polluent l'environnement mais contribuent également aux émissions de CO<sub>2</sub> lors de l'incinération. L'approche innovante présentée dans cette thèse offre une double solution, abordant simultanément les déchets PET et les émissions de CO<sub>2</sub>.

Deux systèmes remarquables ont été explorés dans cette thèse. Le premier utilisait du carbonate d'oxyde de bismuth (BOC) fonctionnalisé de l'oxyde de graphène réduit (rGO) pour l'électroréduction cathodique du CO<sub>2</sub> (CO<sub>2</sub>RR), tandis que CuCoO sur rGO était utilisé pour l'oxydation anodique de l'hydrolysate de PET. De manière impressionnante, le catalyseur anodique CuCoO@rGO a affiché une électroactivité exceptionnelle, atteignant un rendement faradique (FE) exceptionnel de 85,7 % à 1,5 V par rapport à RHE. Simultanément, le catalyseur cathodique BOC@rGO a démontré un FE impressionnant de 97,4 % à -0,8 V par rapport au RHE, facilitant la production de formiate à partir de CO<sub>2</sub>RR. Lorsqu'elle est intégrée dans une configuration d'électrolyseur, cette approche a abouti à une production d'acide formique à une faible tension de cellule de 1,9 V et à un FE formiate remarquable de 151,8 % à 10 mA cm<sup>-2</sup>.

Un autre système utilisait une électrode 3D en feutre de charbon actif (aCF) comme substrat et du bismuth a été déposé électrochimiquement sur le CF (Bi@aCF) qui agit comme la cathode CO<sub>2</sub>RR et un feutre de carbone déposé au phosphate de nickel-cobalt (NiCoPO<sub>x</sub>@CF) pour l'anode. Procédé d'oxydation de l'hydrolysate de PET. Cette configuration a atteint un FE élevé de 94 % pendant CO<sub>2</sub>RR à -0,8 V par rapport au RHE, produisant du formiate, et un FE de 95 % pour

l'oxydation anodique de l'hydrolysat de PET pour former un formiate à un faible potentiel de 1,5 V par rapport au RHE. Remarquablement, l'électrolyseur à deux électrodes a atteint un FE extraordinaire de 157 % pour produire du formiate à une tension de cellule de 1,8 V. Cette percée représente une nouvelle voie pour valoriser les déchets de PET, réduire les émissions de CO<sub>2</sub> et promouvoir la durabilité environnementale.

De plus, nos expériences ont également porté sur l'électrolyse de l'eau, où une nouvelle stratégie impliquant du Ru intégré dans une matrice de nitrure de carbone a été proposée. Cette approche, utilisant une structure organique covalente 2D CIN-1 avec Ru + 2 coordonné, a abouti à des nanoparticules d'oxyde de Ru avec des sites Ru de faible valence disposés en nanofils entre des couches de nitrure de carbone graphitique après pyrolyse. Ce matériau présentait des surpotentiels significativement inférieurs pour la réaction de dégagement d'hydrogène (HER) et la réaction de dégagement d'oxygène (OER) par rapport aux catalyseurs de référence au Pt et au RuO<sub>2</sub>, démontrant une stabilité catalytique remarquable. Cette découverte est extrêmement prometteuse pour faire progresser le domaine du fractionnement de l'eau et contribuer au développement de solutions énergétiques durables.

**Mots-clés:** Électrocatalyse, Dioxyde de carbone, Réduction électrochimique, Polyéthylène téréphtalate – Oxydation, Hydrolyse, Oxyde de graphène, Catalyseurs au cuivre, Catalyseurs au cobalt, Catalyseurs au ruthenium, Formiates.

## ACKNOWLEDGMENTS

To begin, I'd like to express my heartfelt gratitude to Dr. Rabah Boukherroub and Prof. Sabine Szunerits for warmly welcoming me into their research team. I am profoundly thankful for their unwavering guidance, support, enthusiasm, and kindness. Their approach to the world of science and research served as a tremendous source of inspiration for me. I extend my deepest appreciation for steering me in the right direction and aiding me in gaining invaluable research experience, encompassing scientific thinking, laboratory techniques, and the art of writing publications.

I'd also like to extend my gratitude to the members of the evaluation committee, Dr. François ozanam, Dr. Corinne lagrost, Prof. Henri Happy, and Prof. Hong Li for their dedicated efforts in assessing my Ph.D. work. Your precious time and insightful opinions regarding my research are genuinely appreciated. I would like to take a moment to extend my sincere thanks to all of my wonderful colleagues for their unwavering support, engaging discussions, and willingness to share their expertise. Working alongside Alex for three years in the same laboratory has been an absolute pleasure, and I am immensely grateful for the generous help and invaluable advice I've received from you.

I am deeply grateful to Mr. Anupam Prasoon for his unwavering support and guidance throughout my PhD studies. I have had the privilege of knowing him since my undergraduate years, and he has consistently stood by my side in every situation imaginable. His invaluable support, both academically and personally, has been a cornerstone of my success during this challenging academic journey. Ines de Hoon holds a special place in my heart, and I cannot express my gratitude enough for her constant presence by my side throughout this incredible journey. Our interactions were always filled with joy, and the time we spent together was truly memorable.

These moments and the memories we created will remain cherished in my heart for the rest of my life. I would like to thank and show my gratitude to Michele Iodato, a remarkable individual who has brought laughter, extroverted energy, and an incredible friendliness into my life. His extroverted nature has a way of bringing people together, creating a warm and welcoming atmosphere wherever he goes. I am truly fortunate to have Michele as a part of my life, and I am deeply appreciative of the laughter and friendship he has generously shared.

Nonetheless, I would like to express my heartfelt gratitude to all the incredible individuals who have been a part of the NanoBioInterfaces group, both past and present. Your contributions have been invaluable, and I want to extend special thanks to Nasrin Shokouhfar, Teresa Rodriguez, Yuanyuan Miao, Zhiran Yu (Zohan), Yi zhang, Zhaohui zhang, Tomasz Swebocki, Elizaveta Sviridova, Emerson giovanelli, Léa Rosselle, Shakila behzadifar, Anna Voronova, and Vlad Mishyn. Working alongside each of you has been a privilege, and our shared experiences in Lille will forever hold a special place in my heart. I also would like to thank Mr. Jash Mehta, Vikas Madhur, Shubham Semwal who were there with me from day one of my PhD journey.

I'd like to extend my sincere appreciation to Smita, whose unwavering support has been a constant source of strength during my lowest moments. Having you in my life is a true blessing, and I am profoundly grateful for the love, companionship, and unwavering support you provide. Lastly, but certainly not least, I want to extend my heartfelt gratitude to my parents, extended family members, and friends for their unwavering support throughout these years. I am deeply thankful for each and every one of you.

# Contents

Chapter 1.....	11
General Introduction.....	11
1.1 Global Challenges: Climate, Plastic, Energy .....	11
1.2 Carbon Capture and Storage Technologies.....	18
1.3 Utilization of carbon dioxide .....	25
1.4 Electrochemical CO <sub>2</sub> reduction .....	26
1.5 Coupling anodic reactions with CO <sub>2</sub> RR .....	38
1.6. Water splitting .....	44
1.6 Objectives and outline of the thesis .....	48
References .....	50
Chapter 2.....	70
Covalent Organic Framework Derived Synthesis of Ru Embedded in Carbon Nitride for Hydrogen and Oxygen Evolution Reactions .....	70
Abstract.....	72
2.1. Introduction .....	73
2.2. Experimental .....	75
2.3 Results and Discussion .....	78
2.4. Conclusion.....	91
References .....	93
Chapter 3.....	104
Simultaneous Upcycling of PET Plastic Waste and CO <sub>2</sub> Reduction through Co-electrolysis: A Novel Approach for Integrating CO <sub>2</sub> Reduction and PET Hydrolysate Oxidation .....	104
Abstract.....	105
3.1 Introduction .....	106
3.2 Experimental section .....	108
3.3 Results and discussion .....	112
3.4 Conclusion.....	134
References .....	135
Chapter 4.....	139
Pulse Electrodeposition of Bismuth on Activated Carbon Felt for Efficient Electrocatalytic CO <sub>2</sub> Reduction and NiCoPO <sub>x</sub> for Effective Anodic PET Degradation to Formate .....	139

Abstract.....	140
4.1 Introduction .....	141
4.2 Materials and methods .....	144
4.3. Results and discussion .....	147
4.4. Conclusion.....	163
References .....	164
Chapter 5.....	171
Conclusions and future perspectives .....	171
Appendix .....	174
Experimental methods and Characterization .....	174
Publications.....	177

# Chapter 1

## General Introduction

### 1.1 Global Challenges: Climate, Plastic, Energy

In an increasingly interconnected world, the emergence of salient issues about pollution and plastic waste has garnered pronounced attention in recent times. Undoubtedly, carbon dioxide (CO<sub>2</sub>) emissions emerge as a pervasive variable across these monumental challenges. Global CO<sub>2</sub> emissions have consistently risen since the pre-industrial era, culminating in a total of 36.8 gigatons (Gt) in 2022 [1]. This followed Covid-19 pandemic-induced fluctuations, with 2021 showing a 6% rebound [2]. Emissions from energy combustion increased by 423 million metric tons, while industrial process emissions fell by 102 million metric tons [1]. Before the onset of the Industrial Revolution, CO<sub>2</sub> concentrations remained relatively stable at approximately 280 parts per million (ppm) for nearly thousands of years of human civilization [3]. However, since then, human activities have contributed to releasing an estimated 1.5 trillion tons of CO<sub>2</sub> emissions (figure 1). A significant portion of these emissions will have enduring atmospheric warming effects for thousands of years [4].

Presently, CO<sub>2</sub> levels have reached a state comparable to the conditions during the Pliocene Climatic Optimum, which occurred around 4.1 to 4.5 million years ago. During this period, CO<sub>2</sub> concentrations were approximately 400 ppm or higher. It is important to note that sea levels during the Pliocene Climatic Optimum were considerably elevated, ranging between 5 to 25 meters higher than the current levels. Such elevated sea levels had the potential to submerge numerous modern cities across the world [5].

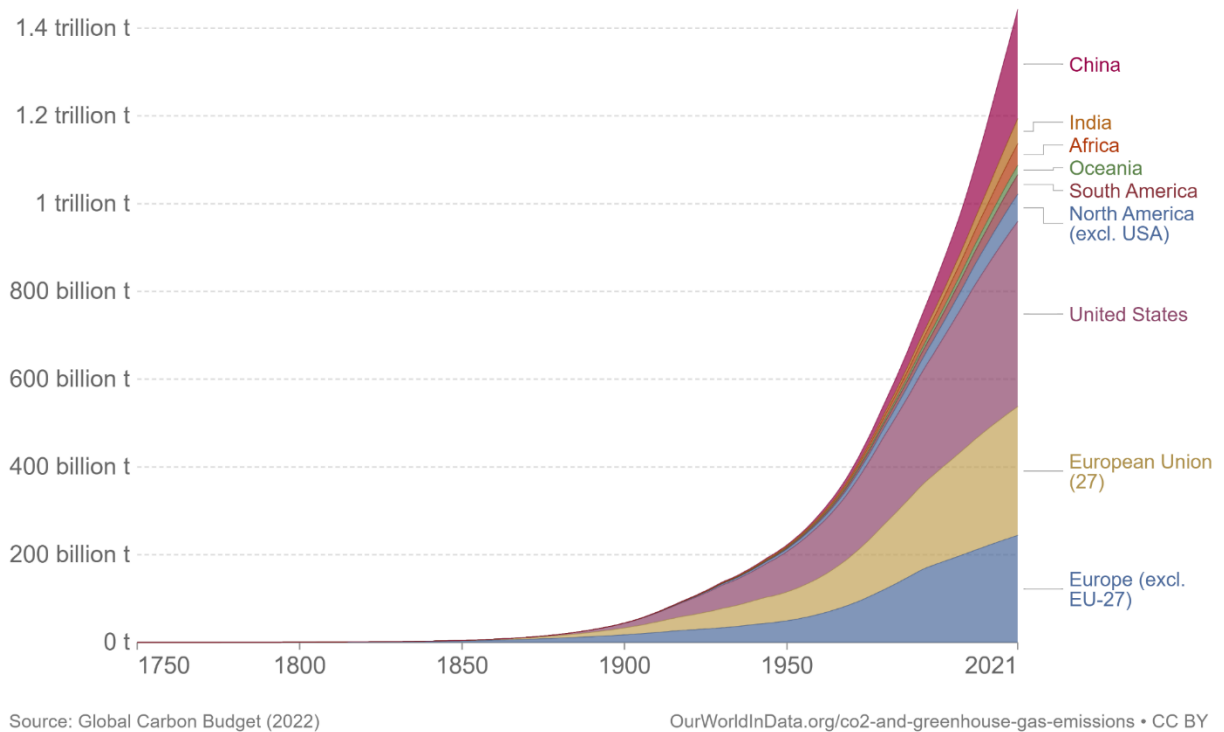


**Figure 1.** *Cumulative CO<sub>2</sub> emissions by different regions in the world [figure from [6]].*

In addition, plastic waste presents another significant challenge, contributing to global CO<sub>2</sub> emissions and the detriment of the environment and society. Recent investigations have revealed that plastic alone accounts for nearly 3.4% of the overall global greenhouse gas emissions—a staggering proportion, surpassing the carbon emissions attributed to the aviation industry [7]. This stark reality establishes plastic as a substantial catalyst for the progression of global warming. Global plastics production was estimated at 390.7 million metric tons in 2021, marking an annual increase of 4% [8]. However, persisting along the current trajectory in plastic production and waste management paints a sobering picture—an accumulative 12,000 million metric tons of plastic waste could potentially find its way into landfills or the natural environment by 2050 (figure 2) [9], [10].

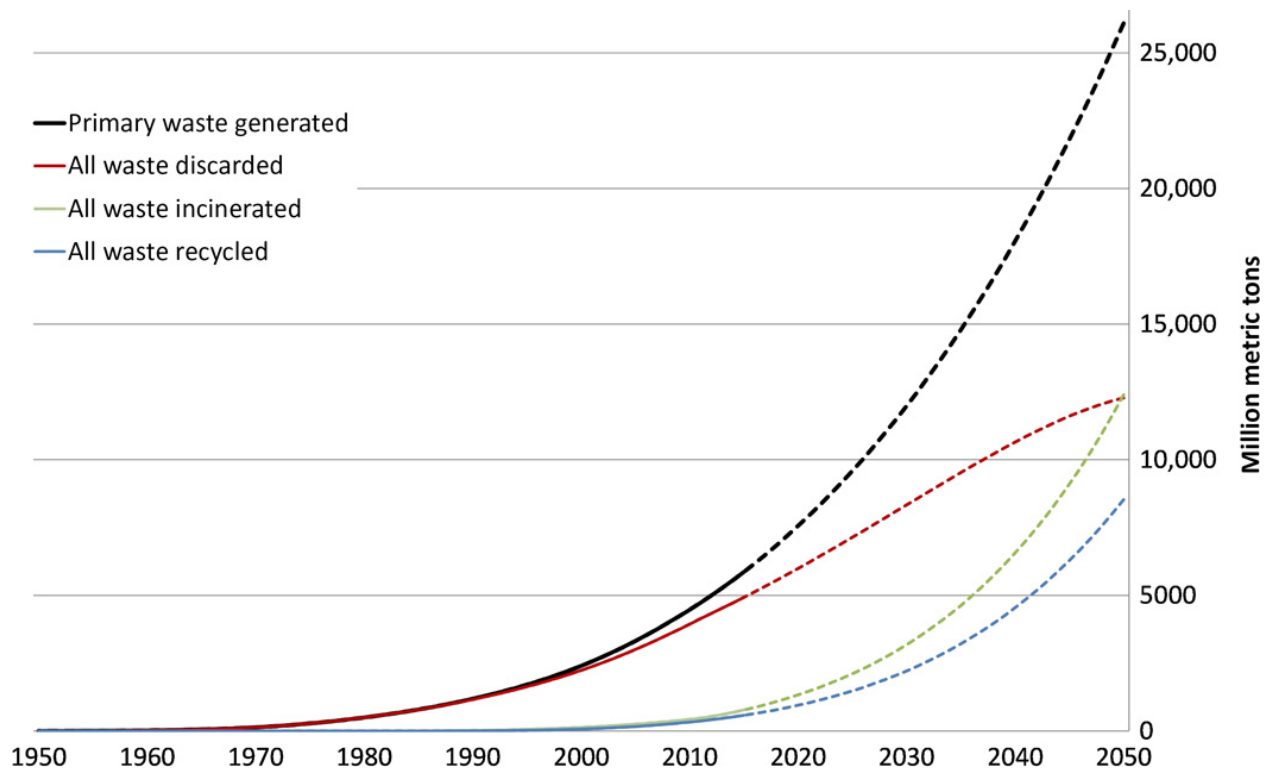


**Figure 2.** Cumulative production and management of plastic waste (measured in million metric tons). The solid lines represent past records spanning from 1950 to 2015, while the dashed lines depict extrapolations of these historical patterns until 2050 [Figure adapted from [10]].

In 2015 alone, plastics production contributed to the release of 1.78 Gt of CO<sub>2</sub>-equivalent emissions. Furthermore, it has been revealed that as of 2021, 90% of the world's plastics is made from chemicals sourced from fossil fuels. Projections highlight a concerning trajectory, with this figure anticipated to surge to an alarming 6.5 Gt CO<sub>2</sub>-eq by 2050 [11]. Nonetheless, when synergistically employed, the implementation of renewable energy solutions, coupled with recycling initiatives and demand-centric management strategies, holds the capacity to maintain 2050 emissions at a level akin to that of 2015. Moreover, substituting fossil fuel feedstock with renewable alternatives such as hydrogen (H<sub>2</sub>), a clean and versatile energy carrier, presents an avenue for additional emission reduction, ultimately culminating in an absolute decrease from

prevailing emission levels. Currently, numerous industries rely on gray hydrogen as a fuel source, a hydrogen variant derived from fossil fuels. However, this approach raises concerns, due to its environmental impact and contribution to carbon emissions. Hence, there is an imperative to develop solutions that effectively can address these issues without inadvertently creating new challenges. These solutions should be environmentally friendly and ensure the avoidance of unintended negative consequences.

### **1.1.2 Global policies: Climate, Plastic, Energy**

**(a) CO<sub>2</sub> emissions:** The notable rise in global population and energy demand has led to a substantial upsurge in carbon dioxide (CO<sub>2</sub>) emissions over the past two decades. Various strategies have been enacted in recent years to achieve net zero carbon emissions by 2050. Scientific research unequivocally demonstrates that to prevent the most severe consequences of climate change and safeguard a habitable earth, it is imperative to curtail the global temperature increase to a maximum of 1.5°C above levels before the industrial era [12].

The initial global accord mandating a decrease in greenhouse gas (GHG) emissions comes from the Kyoto Protocol, associated with the United Nations Framework Convention on Climate Change. It was sanctioned in 1997 and became effective from 2005. The first commitment phase of the protocol necessitated developed nations to curtail their emissions of GHGs by an average of 5% compared to 1990 levels within the 5-year period of 2008-2012. The precise reduction targets depended on the country's political and economic conditions. In the subsequent commitment period (2013-2020), they have called for a minimum 18% reduction in GHG emissions from 1990 levels [13]. To put the second commitment period of the Kyoto Protocol into operation, the consent of two-thirds of the participating countries (144 nations) was necessary. However, as of October 1, 2015, only 49 countries had endorsed the second commitment period. Since not all countries

ratified the Kyoto Protocol and significant emitters like the United States refrained from participation, establishing new international accords has become imperative [14].

Later, the 2015 Paris Agreement has been established during the Climate Change Conference (COP) 21, which limits the 1.5°C threshold, necessitates a 45% reduction in emissions by 2030, ultimately reaching a state of equilibrium where emissions released and removed from the atmosphere are balanced by 2050 by oceans and forests. The planet's temperature has already elevated by approximately 1.1°C compared to the late 1800s, and emissions are still increasing [15].

The Glasgow Climate Pact was recently enacted during COP26, marking a significant achievement. This pact involves pledges to transition away from coal-based energy, cease and undo deforestation, lower methane emissions, and expedite the transition to electric vehicles. Additionally, the pact attains worldwide commitments towards achieving nearly net-zero emissions. Notably, around 153 countries have presented their targets for the year 2030. A notable milestone is the consensus of 190 nations to reduce coal-based energy gradually, acknowledged as a significant driver of climate change [16].

The European Union (EU) has instituted various policies, with the 20-20-20 policy standing out as particularly impactful. This strategy aims to achieve three significant goals by the year 2020: first, a 20% reduction in GHG's compared to the levels of 1990; second, a 20% enhancement in energy efficiency across the EU; and third, the attainment of 20% renewable energy consumption in the EU's total energy usage [17].

**(b) Plastic waste:** Policies that reduce demand for plastics promote product longevity through repair and reuse, and improve waste management and recyclability systems are practical

approaches to reduce plastic escape into the environment. The United States introduced the "Marine Plastic Pollution Research and Control Act" in 1987 as one of the first policy steps in plastic waste control. This legislation prohibits the discharge of plastics into the seawater and waste disposal from merchant ships, cruise ships, military boats, or other means [18].

In June 2018, during the G7 Summit, significant progress was undergone in adopting the Ocean Plastics Charter by countries like Canada, the United Kingdom, and the European Union. This charter lays out actions to tackle pollution and recognizes the urgent need for measures to address the severe impact of marine debris on our oceans, coastal regions, and ecosystems [19].

Several governments have taken measures to prohibit the sale of lightweight bags, implement charges for them, or establish levies on stores selling them [20]. Leading the way, the government of Bangladesh implemented a comprehensive ban on lightweight plastic bags in 2002. From 2010 to 2019, we witnessed a three-fold increase in public policies aiming to eliminate plastic carryout bags gradually [21]. Up to 2022, 99 countries have introduced such bans, with varying degrees of enforcement, while 32 countries opt for a fee per bag. Certain regions at the sub-national level have also enacted bans and charges [22]. In 2013, the European Commission proposed decreasing the usage of lightweight plastic carrier bags. According to this proposal, member states within the EU were given the flexibility to determine the most suitable strategies for discouraging the utilization of plastic bags [23]. Subsequently, on April 29, 2015, the European Parliament approved Directive 2015/720 to achieve a 50% and 80% decline in plastic bags by 2017 and 2018, respectively [24], [25].

**(c) Energy:** One of the early energy policies initiated by governments to support renewable energy emerged in response to the 1970s oil crisis, characterized by petroleum shortages, air pollution, and acid rain [26]. Detailed analyses were conducted to explore the potential of

hydrogen generated from fossil fuels in addressing energy needs. However, by the 1990s, concerns about climate change resulting from CO<sub>2</sub> emissions reshaped the concept of a hydrogen economy, shifting the focus from fossil fuels to renewable energy sources [26].

In 1993, Japan implemented the International Clean Energy Network Using Hydrogen Conversion (WE-NET) to trade hydrogen from renewable energy sources. This initiative was rooted in integrating the Sunshine and Moonlight projects that began in the early 1970s, aimed at advancing new energy technologies and energy-saving measures [27].

In 2001, the European Union initiated a project called CUTE (Clean Urban Transport for Europe). Under this project, the EU allocated 18.5 million euros to nine European cities: Amsterdam, Madrid, Hamburg, Barcelona, Luxembourg, Stuttgart, Porto, Stockholm, and London. The project's objective was to support the implementation of fuel cell and hydrogen-powered public transport systems in these cities, thereby promoting clean and sustainable urban transportation solutions [28].

In 2003, the United States established the International Partnership for Hydrogen and Fuel Cells in the Economy (IPHE), an international collaboration involving 20 countries. The primary objective of this partnership is to advance the development and deployment of hydrogen and fuel cell technologies. IPHE also serves as a platform for discussions on critical topics, such as policies, safety measures, and regulations related to hydrogen and fuel cells [29]. In 2023, the United Kingdom launched a program to support Bioenergy with Carbon Capture and Storage (BECCS) technologies. This initiative received substantial funding of 26 million pounds. The program aims to facilitate hydrogen production from biogenic feedstocks, while incorporating carbon capture techniques [30].

### **1.1.3 Solutions: Climate, Plastic waste and Energy**

Governments have implemented numerous comprehensive solutions globally to confront these three challenges. However, the commonly embraced approaches generally focus on reducing plastic consumption and waste, decreasing energy consumption, and reshaping our outlook on resources and waste management. Nevertheless, these broad strategies can only provide temporary relief. Instead, we must invest significantly in scientific research to develop solutions that can effectively address all three global issues. A careful analysis of these challenges reveals the common and paramount issue of CO<sub>2</sub> emissions. Effectively addressing CO<sub>2</sub> emissions has the potential to alleviate many of the difficulties associated with all three of these issues.

CO<sub>2</sub> utilization emerges as a highly effective and economically viable option for mitigating and curbing CO<sub>2</sub> emissions. This reduction of CO<sub>2</sub> can be achieved via two distinct strategies: firstly, the carbon capture and storage (CCS) approach, and secondly, the harnessing of CO<sub>2</sub> as a chemical feedstock, commonly referred to as Carbon Capture and Utilization (CCU) [31]. The coordination of these two strategies is crucial, given the requisite need for pure CO<sub>2</sub> streams as a chemical feedstock. In essence, CCS technologies focus on capturing and subsequently sequestering substantial volumes of CO<sub>2</sub>, while the chemical utilization of CO<sub>2</sub> is oriented towards producing value-added products [31]. It is important to note that both strategies are still in the early stages of development. Nevertheless, the prospects for achieving improved outcomes appear promising through rigorous research endeavors and the introduction of novel materials.

## **1.2 Carbon Capture and Storage Technologies**

In 1977, Cesare Marchetti introduced the concept of CCS (Carbon Capture and Storage), proposing capturing CO<sub>2</sub> emissions from key fuel conversion sources like coal power plants [32]. The

captured CO<sub>2</sub> would then be injected into appropriate deep-sea locations using natural thermohaline circulations. The IEA has asserted that this technology can potentially reduce global CO<sub>2</sub> emissions by 17% by 2050. Therefore, CCS should be an integral part of the policy in every country worldwide to mitigate the severe effects of global warming [33]. In technical terms, CCS involves the capture of CO<sub>2</sub> emissions from coal power plants, industrial complexes, and natural gas wells. This captured CO<sub>2</sub> is later transported via pipelines to a suitable geological site for long-term storage (figure 3) [33].

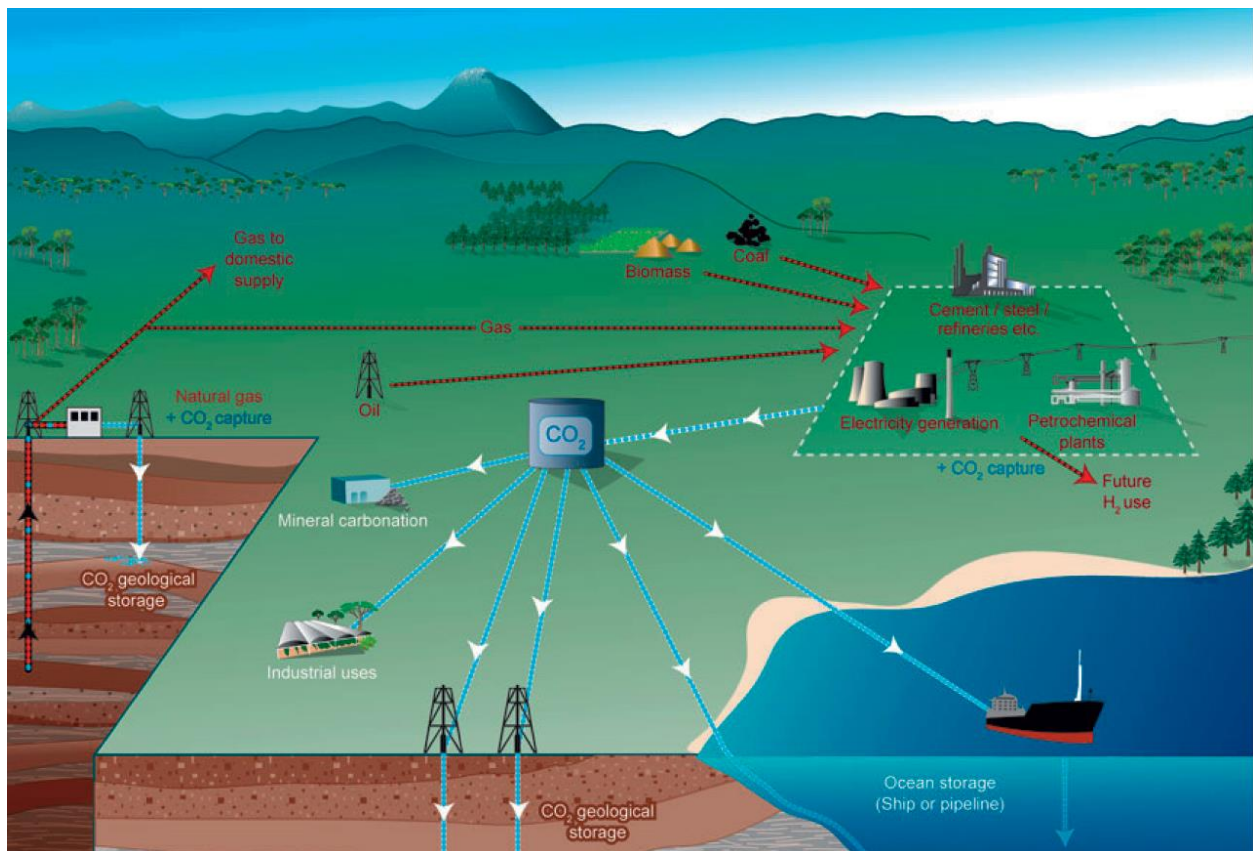
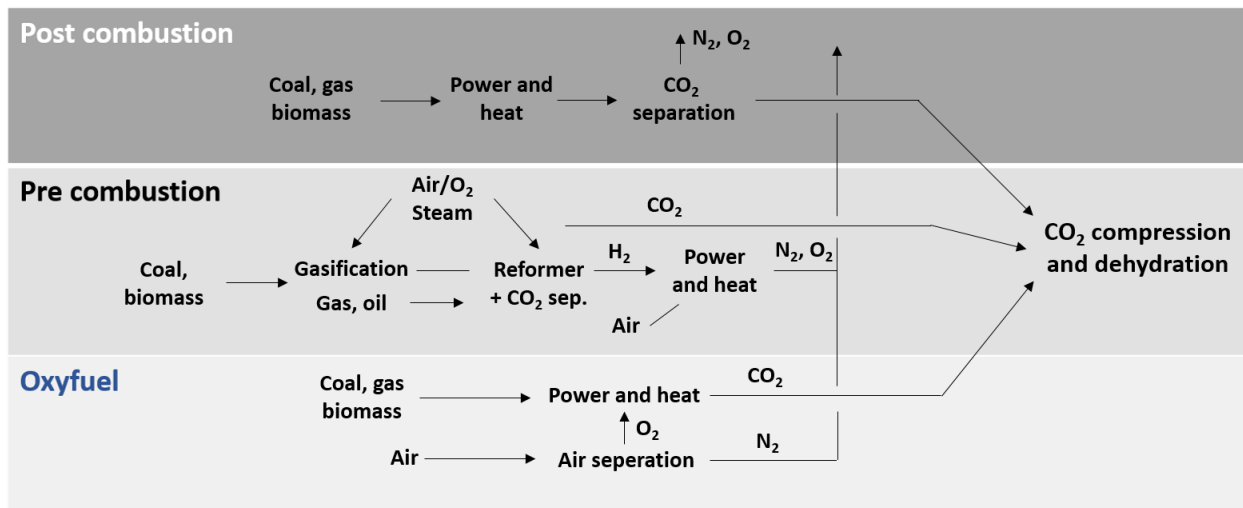


**Figure 3.** Illustrative diagram of potential CCS systems, which depicts the sources where CCS could be applicable and outlines various choices for transporting and storing CO<sub>2</sub> [figure adapted from [33]].

However, this practice encompasses numerous parameters, processes, and phenomena requiring meticulous measurement, recording, and monitoring. It is essential to guarantee that the injected CO<sub>2</sub> remains securely contained for thousands of years, preventing any potential seepage back to the surface.

### 1.2.1 Carbon Capture Technologies

Capturing CO<sub>2</sub> emissions from mobile sources is significantly more challenging and less economically feasible than big stationary sources, such as industries and power plants [31]. There are three primary strategies for capturing CO<sub>2</sub> emissions from the combustion of fossil fuels and biomass, each with distinct characteristics (scheme 1):



**Scheme 1.** Schematic illustrating processes and systems for the capture of CO<sub>2</sub> (adapted from [34]).

#### a. Post-combustion (captured after the combustion process):

In post-combustion capture, combustion occurs within the combustion chamber, in which a mixture of fuel and air generates heat and produces flue gases. One way to capture CO<sub>2</sub> is the

introduction of organic solvents into the exhaust gas stream after combustion, such as aqueous piperazine. The solvent absorbs the CO<sub>2</sub> subsequently, the CO<sub>2</sub>-loaded solvent is regenerated through heating. The rejuvenated solvent can then be reused in a cyclic fashion for CO<sub>2</sub> capture. This method is primarily employed to extract CO<sub>2</sub> from the flue gas emissions of power plants and industrial facilities [35], [36]. However, post-combustion CO<sub>2</sub> capture can also be carried out using adsorbents, membranes, and hybrid materials.

**b. Pre-combustion (separated prior to combustion process)**

A pre-combustion capture system is carried out by a reaction between the primary fuel and either oxygen, air, or steam to generate synthetic gas, primarily composed of H<sub>2</sub>, CO<sub>2</sub>, CO, and minor CH<sub>4</sub>. The synthetic gas mixture is then subjected to a water gas shift reaction (WGS) with steam, leading to the production of hydrogen (H<sub>2</sub>) and carbon dioxide (CO<sub>2</sub>) [34]. Subsequently, CO<sub>2</sub> is easily separated from the mixture and captured, yielding a fuel rich in H<sub>2</sub>, which can be utilized in various applications, such as gas turbines, engines, fuel cells, boilers, or furnaces [37]. Integrated Gasification Combined Cycle (IGCC) plants, which use syngas as a fuel, can implement a pre-combustion capture system for CO<sub>2</sub> reduction.

**c. Oxy-fuel combustion (combustion with high O<sub>2</sub> content).**

In this approach, instead of using atmospheric air (composed of N<sub>2</sub> and O<sub>2</sub>), pure oxygen (O<sub>2</sub>) is employed to initiate combustion within the combustion chamber. The fuel and pure oxygen mixture is then ignited in the combustion chamber, generating heat energy while releasing by-products like water vapor and concentrated CO<sub>2</sub> gas. The water vapor is subsequently removed through a series of compression, cooling, and condensation processes. This method is relatively

costly and requires more energy than other capture methods. However, it enables the efficient removal of CO<sub>2</sub> gas, typically with a concentration exceeding 95%, from the exhaust gases [38].

### **1.2.2 Transport of captured CO<sub>2</sub>**

CO<sub>2</sub> that has been captured can be transported through two primary methods: under high pressure as a liquid or above 73.7 bar (at a critical temperature of 31°C) in the supercritical phase. It is important to note that reaching and maintaining such high pressures for CO<sub>2</sub> transport necessitates an additional energy input. Nonetheless, this mode of transportation can evolve into a significant infrastructure component in its own right. When it comes to large-scale CO<sub>2</sub> transportation, two predominant modes are considered: pipelines and shipping (figure 3). The estimated costs for onshore pipeline transport typically range from 1 to 3 euros per ton for a 250-kilometer distance, while offshore transport falls within the 2 to 4 euro per ton range for the same distance. However, opting for shipping requires the development of complex infrastructure. Another viable option involves the use of trucks or trains equipped with cooled pressure tanks. However, this approach comes at a higher cost, exceeding 25 euros per ton for a 250-kilometer journey. It is essential to recognize that such transportation methods, owing to their expense, limited capacity, and environmental considerations, are most practical as temporary solutions rather than long-term strategies for large-scale CO<sub>2</sub> transport [34].

### **1.2.3 Storage of captured CO<sub>2</sub>**

Storing carbon dioxide (CO<sub>2</sub>) is a critical step in any carbon capture and sequestration (CCS) project. CO<sub>2</sub> can be stored underground for extended periods. Still, it is essential to thoroughly assess and characterize the storage sites to prevent potential risks associated with leakage during and after storage [39], [40]. When CO<sub>2</sub> is dissolved in water, it becomes denser than water and is

retained through a process called solubility trapping. However, its solubility is influenced by factors such as brine salinity, temperature, and pressure, with studies indicating variations in its solubility under different conditions [39]. Depending on the reservoir's temperature and pressure, CO<sub>2</sub> can exist in four distinct phases: gas, liquid, supercritical, and solid (hydrate), as shown in Figure 4. Supercritical conditions, characterized by temperatures exceeding 31.1°C and pressures exceeding 7.3 MPa, are commonly preferred for CO<sub>2</sub> storage due to their ability to accommodate a significant volume of CO<sub>2</sub>. These characteristics of CO<sub>2</sub>, along with other factors, play a crucial role in selecting suitable storage sites in CCS technology, as emphasized by various studies. Geological formation options, such as depleted hydrocarbon reservoirs, saline aquifers, and basalts are some examples of potential sites for CO<sub>2</sub> storage [39], [41].

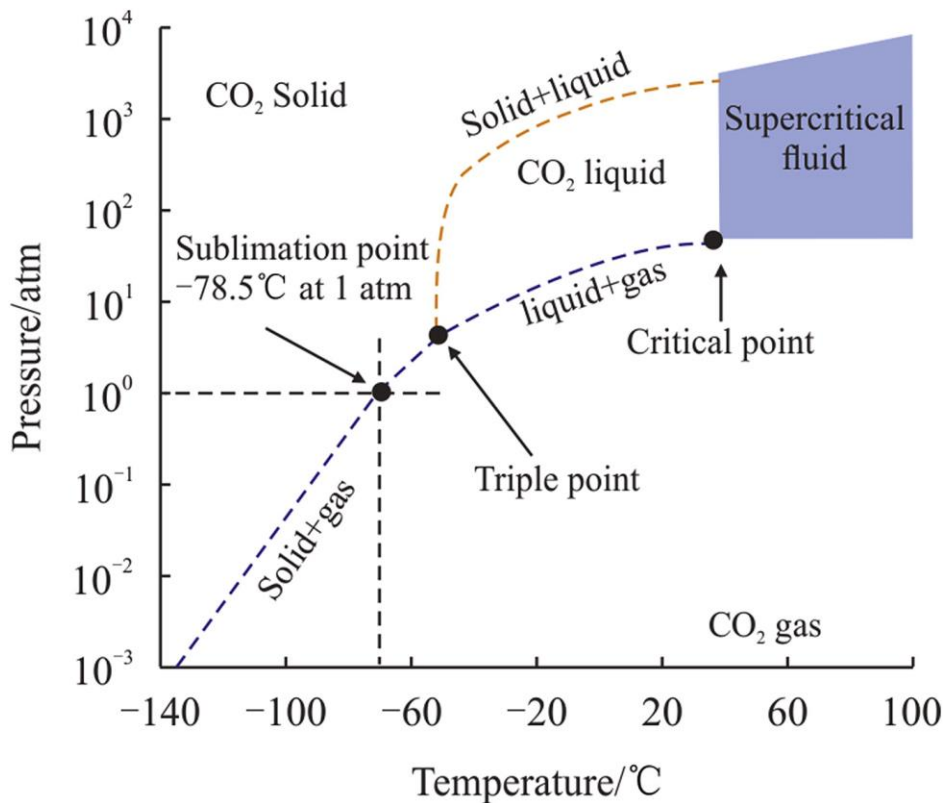


**Figure 4.** Phase diagram depicting temperature and pressure variations, highlighting the supercritical fluid region of CO<sub>2</sub> [adapted from [42]].

Nevertheless, the primary concern revolves around the expenses and energy demands, with a notable portion, approximately 75%, of the overall costs allocated to the capture and compression processes. Storing the captured CO<sub>2</sub> typically represents a cost-intensive stage that does not inherently generate profits. However, there are instances where CO<sub>2</sub> storage can serve a value-enhancing purpose, especially in oil and natural gas extraction. In these cases, CO<sub>2</sub> injection is employed to boost the production yields of oil and natural gas fields [43]. This approach is already in use in Norway, where substantial quantities of separated CO<sub>2</sub> are reintroduced into depleted gas reservoirs.

### **1.2.3 Drawbacks of CCS technologies**

While CCS technologies hold promise in mitigating CO<sub>2</sub> emissions, they yield only a few advantages. CCS is solely aimed at preventing CO<sub>2</sub> release into the atmosphere. Power plants using fossil fuels and CCS will produce less electricity for the same fuel input, resulting in increased capital and operational expenses. Concerns about the safety of storing large volumes of CO<sub>2</sub> in a single location arise due to the potential for leaks, which could lead to environmental contamination if not appropriately managed. Natural disasters like earthquakes or human-induced incidents, such as war-related damage to underground storage reservoirs, may exacerbate the risk of leaks.

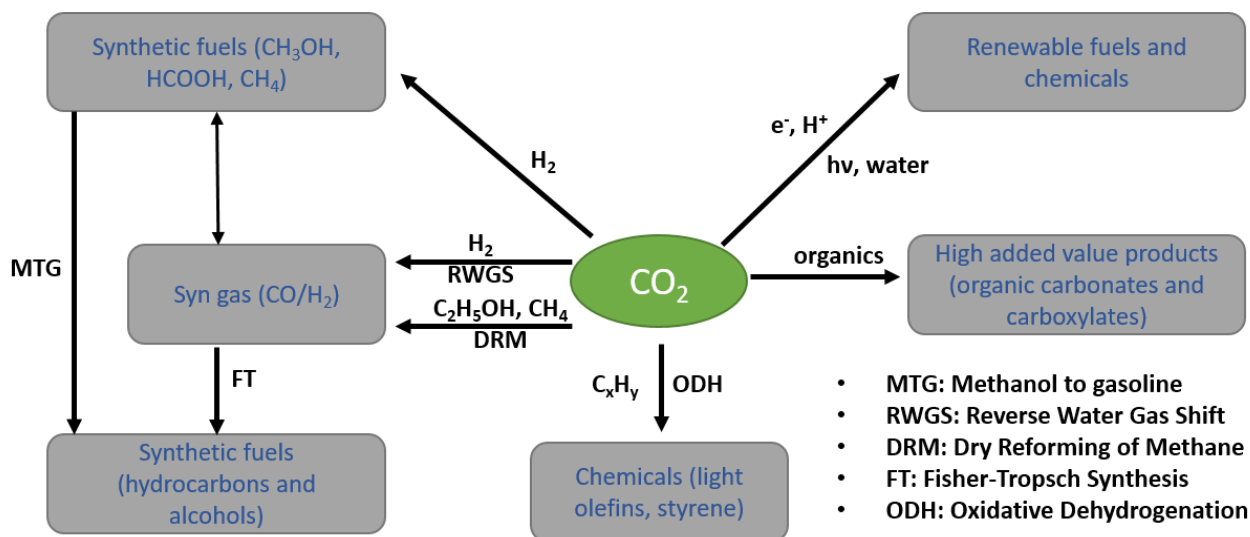
In such circumstances, utilizing CO<sub>2</sub> as a chemical feedstock represents a more environmentally friendly and cost-effective alternative, which will be explored further in the next section in detail.

### 1.3 Utilization of carbon dioxide

Over the past few decades, the perception of CO<sub>2</sub> has undergone a significant transformation across scientific, societal, and industrial realms. CO<sub>2</sub> is no longer viewed solely as a detrimental pollutant; it is recognized as a valuable chemical compound and a crucial carbon source. The technologies employed for capturing and separating CO<sub>2</sub>, whether already in use or in the development process, can yield exceptionally pure CO<sub>2</sub> streams that can be utilized in the manufacturing of chemicals and fuels. Implementing CO<sub>2</sub> as a chemical feedstock offers several distinct advantages:

- It could be used as an intriguing raw material for chemical industries with minimal costs.
- Rather than storing carbon dioxide passively through CCS, CO<sub>2</sub> is actively recycled. This approach also reduces the expenses associated with transporting CO<sub>2</sub>.
- Engaging in producing new chemicals opens up opportunities for companies to expand their market presence.
- CCU presents the chance to manufacture organic chemicals in a more environmentally friendly manner. It is particularly noteworthy, because many traditional organic synthesis methods generate pollutants, whereas CO<sub>2</sub> serves as a "green" alternative to toxic compounds like phosgene in the production of polycarbonates.

Carbon-based chemical products have already been synthesized by harnessing CO<sub>2</sub> as a raw material. These products include carbon monoxide (CO), methane (CH<sub>4</sub>), ethane (C<sub>2</sub>H<sub>6</sub>), and ethanol (C<sub>2</sub>H<sub>5</sub>OH), as well as longer carbon chain products achieved through the Fisher-Tropsch reaction [44]–[47]. However, the primary objective in this process is initiating the reduction of CO<sub>2</sub> due to its remarkable stability, which necessitates a substantial input of energy.



**Scheme 2.** Catalytic pathways for the conversion of carbon dioxide ( $\text{CO}_2$ ) into fuels and chemical compounds [adapted from [48]].

It can be achieved through various methods, including biological processes, reforming techniques, photochemical reactions, and electrochemical processes [49], [50]. Among these approaches, electrochemical conversion into hydrocarbons or carbon monoxide is particularly appealing due to its mild reaction conditions, control over external factors, such as electrolytes, applied voltage, and can reach high current densities (high product yield).

## 1.4 Electrochemical $\text{CO}_2$ reduction

Extensive research is currently underway to address the challenge of transforming  $\text{CO}_2$  from a pollutant into a valuable resource. In this context, electrochemistry offers a distinct advantage, because it can harness electricity from renewable sources rather than relying on fossil fuels [51]. The electrochemical approach for reducing  $\text{CO}_2$  has the potential to establish a synthetic carbon cycle seamlessly and can convert  $\text{CO}_2$  into valuable chemicals, thereby enhancing energy efficiency and economic viability. However, to create an operational setup for the  $\text{CO}_2$  reduction

reaction (CO<sub>2</sub>RR), it is essential to evaluate the thermodynamic and kinetic aspects of this process. To facilitate reduction, CO<sub>2</sub> must undergo a transformation from its linear shape to a bent configuration, leading to formation of intermediate radical anion CO<sub>2</sub><sup>•-</sup> [52]. In the upcoming sections, we will delve deeper into the intricacies of this mechanism. The inert nature of CO<sub>2</sub> molecules poses a challenging task in achieving the selective production of desired products. One of the primary hurdles lies in the competition with the hydrogen evolution reaction (HER), as it operates at a comparable standard reduction potential to the CO<sub>2</sub>RR [52]. Nevertheless, a thorough exploration of the underlying mechanisms can guide us in designing and developing of cutting-edge electrocatalysts that have the capability to selectively generate specific chemical products. Furthermore, a range of C<sub>2</sub>-, C<sub>3</sub>-based chemical products can be formed as a result of multiple proton and electron transfer reactions during the CO<sub>2</sub>RR, as illustrated in table 1. Therefore, it is of paramount importance to explore the catalyst surface properties that promote these intricate processes involving multiple proton and electron couplings [53]–[55]. During the late 1900s, Hori *et al.* conducted a pioneering study on metallic electrocatalysts suitable for facilitating the CO<sub>2</sub>RR. They classified these metal electrocatalysts into four distinct groups based on their ability to selectively produce specific products [56], [57].

**Table 1.** Theoretical equilibrium potentials of CO<sub>2</sub>RR and Hori et al. classification of metallic electrocatalysts for subsequent products. [56], [57].

	Major product half-cell reactions	Equilibrium Potential (V vs. RHE)	Metal electrocatalysts
<b>Group 1</b>	$2\text{H}_2\text{O} + 2\text{e}^- \rightarrow 2\text{H}_2 + 2\text{OH}^-$	0.0	Pt, Ti, Fe, Ni
<b>Group 2</b>	$\text{CO}_2 + \text{H}_2\text{O} + 2\text{e}^- \rightarrow \text{CO} + 2\text{OH}^-$	-0.10	Ag, Au, Zn
<b>Group 3</b>	$\text{CO}_2 + \text{H}_2\text{O} + 2\text{e}^- \rightarrow \text{HCOO}^- + \text{OH}^-$	-0.03	Pb, Hg, In, Sn, Bi, Pd
	$\text{CO}_2 + 5\text{H}_2\text{O} + 6\text{e}^- \rightarrow \text{CH}_3\text{OH} + 6\text{OH}^-$	0.03	Cu
<b>Group 4</b>	$\text{CO}_2 + 6\text{H}_2\text{O} + 8\text{e}^- \rightarrow \text{CH}_4 + 8\text{OH}^-$	0.18	Cu
	$2\text{CO}_2 + 8\text{H}_2\text{O} + 12\text{e}^- \rightarrow \text{C}_2\text{H}_4 + 12\text{OH}^-$	0.08	Cu

We can note here that copper has exceptional tendency to convert CO<sub>2</sub> into products with more than two electrons involved, owing to its property of having a negative adsorption energy for \*CO (carbon monoxide adsorbed on the catalyst surface) and a positive adsorption energy for \*H (hydrogen adsorbed on the catalyst surface).

In order to make the CO<sub>2</sub> reduction process economically viable and feasible in practical terms, several key objectives must be met such as the production of any given product should be selective, with a Faraday efficiency exceeding 90%, economically profitable and the resulting products should be readily separable [58]. While C2, C3 products have been primary areas of interest, they face challenges, such as low selectivity and the requirement for significant energy input [59].

With these objectives in mind, the production of formate/formic acid holds greater value compared to other CO<sub>2</sub>RR products. Formic acid, being a stable and non-toxic liquid, boasts significant market potential across various applications, including hydrogen carrier systems and formic acid fuel cells. Formic acid exhibits a remarkable hydrogen storage capacity, reaching up to 4.35% of its weight [59]. Under standard pressure and temperature conditions, the hydrogen gas storage capacity of formic acid is an astonishing 580 times higher than that of an equivalent volume of hydrogen gas [60]. Group 3 transition metals (table 1) tend to produce formate as major product during the CO<sub>2</sub>RR process [61]–[66]. However, the majority of these metals encounter challenges related to low Faradaic efficiency (FE) and low partial current density, due to the presence of the competing HER [67]. Recent progress in the field has unveiled that the use of electrodes with large surface areas, particularly Cu, Bi, Sn, metal doped on carbon materials, can enhance both high FE and prolonged operational lifespans (Table 2) [68], [69].

**Table 2.** Summary of CO<sub>2</sub>RR of some reported electrocatalysts.

<i>Catalyst</i>	<i>Electrolyte</i>	<i>Potential applied (V)</i>	<i>FE (%)</i>	<i>References</i>
<i>Ultrathin Bi nanosheets</i>	0.5M NaHCO <sub>3</sub>	-1V vs. RHE	90	[63]
<i>Bi dendrite</i>	0.5M KHCO <sub>3</sub>	-0.74V vs. SCE	89	[66]
<i>Size tunable nano Bi</i>	0.5M KHCO <sub>3</sub>	-1.6V vs. SCE	98.4	[70]
<i>Mesoporous SnO<sub>2</sub></i>	0.5M NaHCO <sub>3</sub>	-0.9V vs. RHE	83	[71]
<i>Sulfide-derived Cu</i>	0.1M KHCO <sub>3</sub>	-0.8V vs. RHE	60	[72]
<i>Cu-doped Bi NPs</i>	0.5M KHCO <sub>3</sub>	-1.2V vs. RHE	90	[73]
<i>Bi/rGO</i>	0.1M KHCO <sub>3</sub>	-0.8V vs. RHE	98	[74]
<i>Bi/Bi<sub>2</sub>O<sub>2</sub>CO<sub>3</sub> nanosheets</i>	0.5M NaHCO <sub>3</sub>	-0.7V vs. RHE	85	[75]

In this thesis, we will delve into a comprehensive discussion of these systems to provide a deeper understanding.

## 1.4.1 Fundamentals of CO<sub>2</sub>RR

### 1.4.1.1. Parameters to assess CO<sub>2</sub>RR

The effectiveness of CO<sub>2</sub>RR can be quantified by various fundamental parameters, including the onset potential, Faradaic efficiency (FE), energy efficiency (EE), current density, and Tafel slope [76]. Typically, most studies have assessed the performance of different materials using an H-type cell consisting of anodic and cathodic chamber separated by an ion exchange membrane with an electrolyte (KHCO<sub>3</sub> or NaHCO<sub>3</sub>) of various concentrations (figure 5).

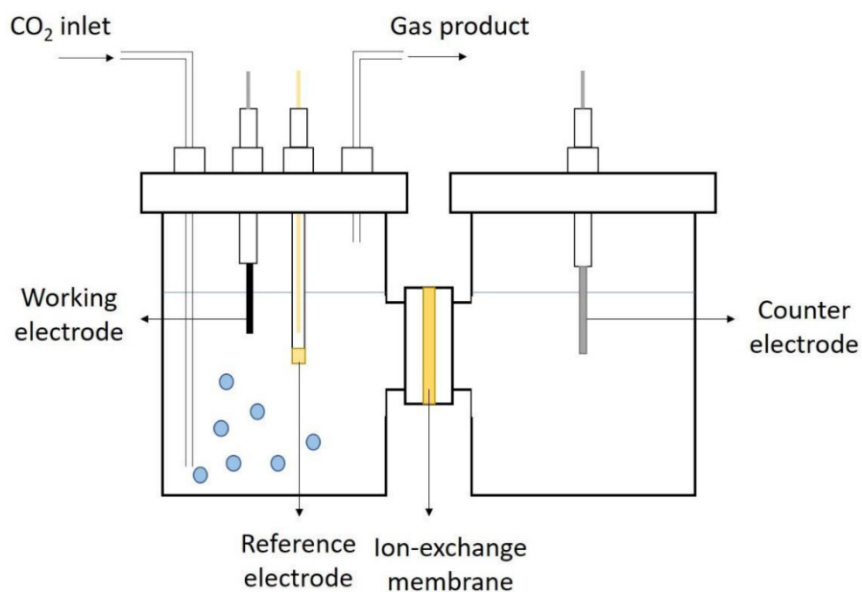


**Figure 5.** *H-cell type electrochemical setup used during CO<sub>2</sub>RR [80].*

This setup involves the oxygen evolution reaction (OER) occurring at the anode side. Nevertheless, in some cases, alternative anodic reactions have been explored as replacements for OER to

decrease cell voltage and yield more valuable products than oxygen [77]–[79]. We will discuss in detail this topic in subsequent sections of this introduction.

- (a) **Onset potential:** It represents the voltage applied to the electrocatalyst with respect to any reference electrode at which the desired product starts forming. The onset potential is consistently lower than the standard reduction potentials due to the presence of a kinetic energy barrier. The difference between the onset potential and the standard reduction potential is referred to as the onset overpotential.
- (b) **Faradaic efficiency:** Faradaic efficiency (FE) is the percentage of the total supplied charge utilized to generate the desired product and is closely linked to product selectivity, determined by the following equation:

$$FE = \frac{naF}{Q}$$

where  $a$  represents the number of transferred electrons,  $n$  denotes the quantity of the specific product in moles,  $F$  is the Faraday's constant equal to  $96,485 \text{ C mol}^{-1}$ ,  $Q$  is the amount of charge consumed during reduction in Coulombs (C) [81].

- (c) **Current density ( $J$ ):** It is defined as the current measured per unit geometric area of the working electrode. It also reflects the rate at which reduction reactions occur and suggests the potential for industrial applications. To determine the current density for specific products, the overall current density is multiplied by the corresponding Faradaic Efficiency (FE) [82].

$$J_{specific} = J_{geo} \times FE_{specific}$$

(d) **Energy efficiency (EE):** Energetic efficiency (EE) is a parameter that indicates how effectively overall energy is used to produce the desired product.

$$EE = \frac{E_0 \times FE}{E_0 + \eta}$$

$E_0$  represents the equilibrium potential across the cell and  $\eta$  is the overpotential [83].

(e) **Tafel slope:** The Tafel slope is the steepness of a plot that relates overpotential (a measure of the excess voltage required for a reaction to occur) to the logarithm of the partial current density. This value serves as an indicator of the reaction pathway and the step that limits the overall reaction rate. Generally, a smaller Tafel slope suggests a more efficient catalytic performance.

In the context of CO<sub>2</sub>RR, a Tafel slope of 118 mV dec<sup>-1</sup> indicates that the rate-determining step (RDS) for CO<sub>2</sub> reduction is the generation of an intermediate through the initial one-electron transfer step. Conversely, a slope of 59 mV dec<sup>-1</sup> indicates faster electron transfer to CO<sub>2</sub> prior to RDS [82].

#### 1.4.1.2 Electrochemical reactors

The widespread application of CO<sub>2</sub>RR faces significant challenges, primarily stemming from competing reactions, like the HER, and undesirable side reactions. Additionally, low reactant concentrations at the vicinity of the catalyst's surface pose a substantial hurdle. This issue becomes even more problematic at higher current density levels, because the CO<sub>2</sub> concentration at the electrode depletes rapidly due to the fast consumption of CO<sub>2</sub> in the electrochemical reactions [84]. Unfavorable local pH conditions exacerbate the problem, thereby restricting the maximum achievable current density in CO<sub>2</sub>RR. Numerous electrochemical flow reactors or cells have been

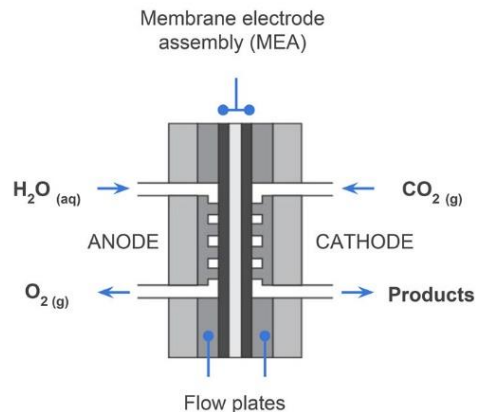
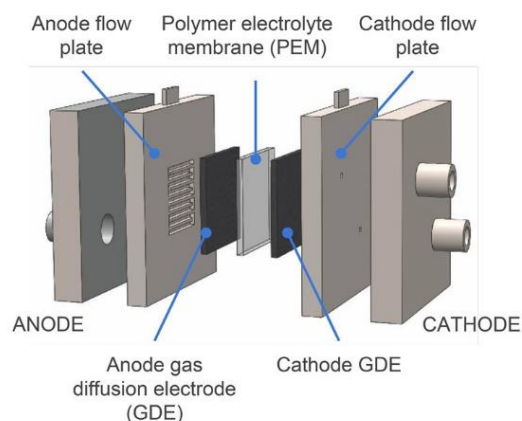
utilized as of now, including aqueous electrolytic cells with membranes [85], solid oxide electrolysis cells [86], and microfluidic electrolytic cells [87].

- (a) **H-Cell:** In a typical H-type electrolyzer, the CO<sub>2</sub>RR takes place at the cathode in a carbonate-based electrolyte saturated with CO<sub>2</sub> (figure 5). Depending on practical requirements, the electrolytes used in the cathode and anode compartments can be the same or different and the membrane that separates them can be adjusted accordingly. Various analytical techniques, such as gas chromatography, nuclear magnetic resonance spectrometry, and liquid chromatography-mass spectrometry, can be used to detect the resulting products.

Despite the widespread use of H-type electrolyzers for studying CO<sub>2</sub>RR, there are limitations to consider. One issue is the relatively long distance between the working electrode and the counter electrode, which can hinder the system due to limited dissolved CO<sub>2</sub> and challenges related to mass transportation. As a result, these factors often lead to low electrolysis current densities, typically less than 100 mA cm<sup>-2</sup>, significantly restricting their practical applications [88].

- (b) **Flow cell reactors:** Recently researchers have started employing flow reactors to increase the current density during CO<sub>2</sub>RR. These reactors can be broadly categorized into two types: membrane-based flow cells and microfluidic flow cells, depending on their architectural design [89]. In a typical flow cell, a continuous supply of CO<sub>2</sub> to the cathode is achieved through either external circulation of CO<sub>2</sub>-dissolved electrolyte or direct introduction of CO<sub>2</sub> gas using a gas diffusion electrode (GDE) [90].

### A) Membrane Reactor



### B) Microfluidic Reactor

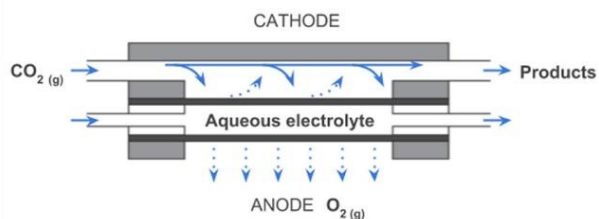
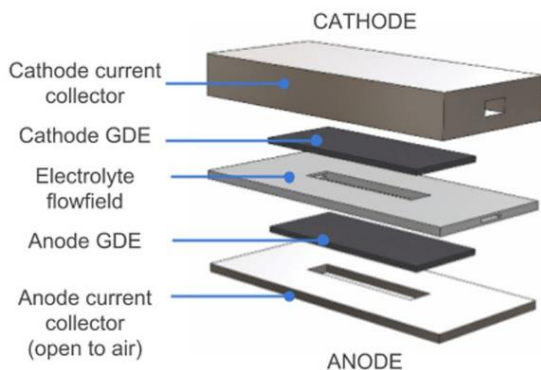


**Figure 6 (a).** Schematic of general membrane-based electrode assembly and its cross section view. **(b)** Schematic of microfluidic flow cell and its cross-section view (Adapted from [89]).

A membrane-based electrolytic flow cell (figure 6a) with a laminar structure reduces the cell volume and shortens the gap between the cathode and anode, thereby greatly alleviating mass transport limitations. Moreover, this setup offers a substantial number of catalytic sites that are accessible to the electrolyte, resulting in a high concentration of liquid products within the electrolyte. This, in turn, enhances the sensitivity for the detection and quantification of the products [90].

The microfluidic flow cell (figure 6b) operates by utilizing an extremely narrow channel that separates the anode from the cathode, with the liquid electrolyte flowing between them. This setup eliminates the need for a membrane to separate the anode and cathode. Within this reactor, both the GDEs are separated apart by a Nafion-117 membrane. Electrolytes are then introduced at a constant rate for continuous flow, which offers real-time sample collection and product analysis. Additionally, this configuration enables the assessment of individual electrode performance and the monitoring of the polarization of both electrodes using an external reference electrode [91].

Nevertheless, when employing a direct CO<sub>2</sub> flow system within the reactors, it becomes necessary to employ a gas diffusion electrode as the working electrode. The gas diffusion electrode is designed in a manner that prevents the passage of liquid products through the CO<sub>2</sub> gas channel, while the gas diffusion layer, located on the opposite side of the electrode and possessing hydrophobic properties, facilitates the interaction of gases with the electrolyte. In this thesis, we have employed aqueous-based H-type electrolytic cells.

#### **1.4.2 Progress in CO<sub>2</sub>RR electrocatalysts to formate**

As previously discussed in our earlier sections, formate is regarded as a more practical and valuable product in the context of CO<sub>2</sub>RR. However, the generation of formate requires large overpotentials even though the theoretical electrochemical potential is -0.250 V *vs.* RHE for formic acid at pH 7. This substantial overpotential needed is primarily due to the barrier associated with the initial electron transfer required to form the CO<sub>2</sub> radical intermediate, which is inadequately stabilized by the electrode surface [51], [92]. Also, unfortunately, this high overpotential falls within a potential range where the HER can also compete with CO<sub>2</sub> conversion, presenting a significant challenge in CO<sub>2</sub>RR. The mechanism governing the conversion of CO<sub>2</sub> to formate or formic acid

is not yet fully elucidated. However, it has been reported that this mechanism involves three primary steps: (1) the adsorption of the reactant onto the working electrode's surface, (2) electron and proton transfer processes, and (3) the subsequent desorption of the resulting products from the working electrode [67].

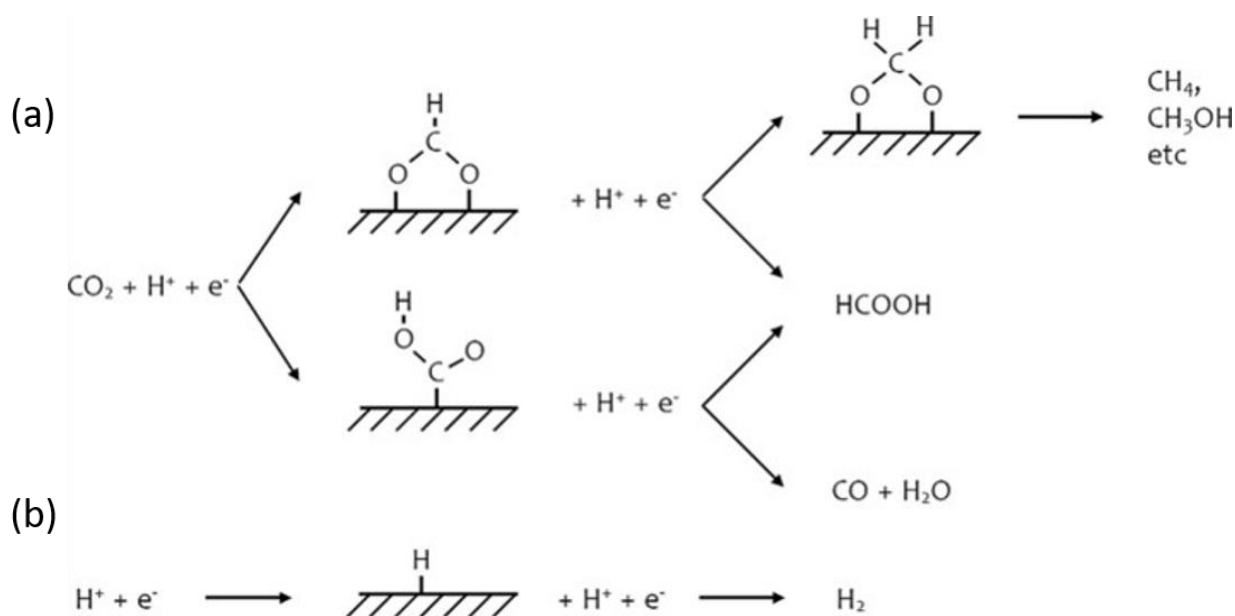


**Figure 7 (a).** Reaction mechanism for the CO<sub>2</sub>RR into various products, and **(b)** simultaneous competing hydrogen evolution reaction [adapted from [67]].

Various metallic electrocatalysts such as Bi, Sn, In, etc, have been developed in these recent years for reducing the overpotential.

**(a) Bismuth (Bi):** Due to its cost-effectiveness and low toxicity, Bi has garnered significant attention as a promising candidate for catalyzing the CO<sub>2</sub>RR. A range of nanostructured catalysts based on bismuth, including bismuth metal [93], bismuth sub-carbonate (Bi<sub>2</sub>O<sub>2</sub>CO<sub>3</sub>) [94], [95], bismuth oxide [96], [97], and bismuth oxyhalide [98] have been engineered to enhance the efficiency of CO<sub>2</sub>RR. To date, most nanoparticle catalysts based on bismuth have demonstrated a high level of selectivity (exceeding 90%) in producing

formate. However, they still face challenges related to low catalytic activity and limited stability. Therefore, it is imperative to engineer more efficient catalysts containing more active coordinated sites and favorable crystal facets. Furthermore, the efficient deposition of metallic nanoparticles onto carbon nanostructures is highly advantageous due to the substantial surface area they provide. This approach also helps to prevent the aggregation of nanoparticles, thus preserving a greater number of active sites for catalytic processes [99]. Zhang et al. achieved the production of formate through the utilization of bismuth nanoparticles immobilized within nitrogen-doped porous carbon (Bi@NPC). The catalytic measurements were performed in 0.1 M KHCO<sub>3</sub> solution and exhibited a high formate FE of 92% and substantial formate current density of 14.4 mA.cm<sup>-2</sup> at a relatively low potential of -1.5 V (V vs. SCE), which was superior to control bismuth nanoparticles (Bi-NP) [100]. In 2020, Jiang and co-authors reported a hybrid composite of bismuth and reduced graphene oxide (Bi-rGO) that was synthesized through a straightforward co-reduction process. The hybrid catalyst exhibited an improved performance with respect to pure Bi in catalyzing the reduction of CO<sub>2</sub> to HCOOH. The highest FE for formate production with the Bi-rGO hybrid reached an impressive 98% at a relatively low potential of -0.85 V (V vs. RHE), which outperformed the pure Bi counterpart (59.8% at -0.85 V) [101]. In this thesis, we will discuss more about Bi electrocatalysts in detail.

**(b) Tin (Sn):** Sn is classified within the post-transition-metal category and presents a compelling prospect as an electrocatalyst, due to its notable selectivity in catalyzing the conversion of CO<sub>2</sub> into formate. Furthermore, Sn possesses the advantage of being abundant on Earth and non-toxic, akin to bismuth (Bi). In recent years, numerous catalysts utilizing Sn have been developed. For example, Zhao et al. employed an electrochemical

deposition method to create a Sn-based catalyst on a copper (Cu) film. This film featured a sequence of deposited Sn catalysts, yielding an optimal current density of  $15 \text{ mA}\cdot\text{cm}^{-2}$  with an associated faradaic efficiency (FE) of approximately 91% [102]. Meanwhile, mesoporous  $\text{SnO}_2$  nanosheets coated onto carbon cloth exhibited a notably high partial geometric current density of  $45 \text{ mA}\cdot\text{cm}^{-2}$ , with a FE of around 87% for the formation of formate [103]. On the other hand, binary or multi-component metallic catalysts, characterized by unique nanoscale structures, such as alloys, core-shell arrangements, and interconnected monometallic nanoparticles, offer significant advantages in facilitating the  $\text{CO}_2\text{RR}$ .

## 1.5 Coupling anodic reactions with $\text{CO}_2\text{RR}$

A significant challenge in  $\text{CO}_2\text{RR}$  we face today is the high overpotential required for product generation, with a significant portion of this challenge occurring due to the oxygen evolution reaction (OER) in the anodic compartment. A high standard equilibrium potential of 1.23 V versus RHE is necessary to facilitate the oxidation of water, leading to a loss of 90% of the overall energy input during the reaction [104]. Moreover, the sluggish kinetics associated with the four-electron transfer process further exacerbate the overpotential issue. Additionally, the presence of oxygen radical species has the potential to degrade the membranes utilized within the electrolyzer, consequently reducing the electrolyzer's operational lifespan [105]. Simultaneously, the relatively modest market value of oxygen and the considerable expense associated with OER catalysts such as iridium would result in low profitability. In light of these constraints, there has been a recent proposal and exploration of an alternative strategy. This approach involves linking the  $\text{CO}_2\text{RR}$  with value-added anodic processes in lieu of OER [106]. Through this approach, it becomes possible to either generate identical products on both the cathode and anode, or produce different

products as required, all while requiring a reduced cell voltage for product formation. Numerous proof-of-concept investigations have been carried out to date, exploring the integration of various value-added anodic electrosynthesis processes with CO<sub>2</sub>RR. These processes encompass alcohol oxidation, halide oxidation and biomass oxidation reactions, and the oxidation of ethylene glycol *via* PET hydrolysis; however, only a few reactions would generate formate [107], [108].

(a) **Methanol oxidation reaction (MOR):** The methanol oxidation reaction (MOR) aimed at producing formate represents the most straightforward and extensively studied alcohol oxidation reaction when paired with CO<sub>2</sub>RR. Recently, Zhang and colleagues devised a two-electrode electrolysis setup employing aligned indium sulfide nanorods (InS NRs) as the cathode in 0.5 M KHCO<sub>3</sub> solution, while utilizing (oxy)hydroxide-coated nickel phosphide nanoparticles (np-Ni<sub>3</sub>P) as the anode in a 1 M KOH solution, either with or without the addition of 0.5 M methanol. In this system, the principal products arising from the anodic MOR and the cathodic CO<sub>2</sub>RR are formate molecules. Remarkably, the system exhibited a lower cell voltage requirement of 2.286 V to attain a current density of 50 mA cm<sup>-2</sup>, as compared to the conventional CO<sub>2</sub>RR||OER system, which necessitated a higher voltage of 2.543 V [109]. Similarly, there have been multiple other studies showcasing the coupling of MOR with CO<sub>2</sub>RR for the efficient production of formate. Nonetheless, within this configuration, only formate is generated in a liquid state, making it considerably easier to separate and eliminating the issue of CO<sub>2</sub> crossover from the cathode. In conventional setups, as much as 70% of the input CO<sub>2</sub> crosses the cell and mixes with the oxygen produced at the anode. The process of recovering CO<sub>2</sub> from this mixed stream imposes a substantial energy penalty [110].

- (b) **Glycerol oxidation reaction (GOR):** Glycerol is a significant precursor that is typically produced in large quantities within the biodiesel and soap manufacturing sectors. Nevertheless, glycerol can be oxidized in anodic compartment to synthesize various compounds, including glyceraldehyde, glyceric acid, and formate [111]. Recently, Verma and colleagues unveiled a groundbreaking discovery where the electrocatalytic oxidation of glycerol led to a remarkable 53% reduction in electrical energy consumption. This reduction was achieved by combining the CO<sub>2</sub>RR with GOR to produce formate and lactate as end products [104]. Subsequently, Pei *et al.* successfully established a two-electrode system for GOR-assisted CO<sub>2</sub>RR. They used an anode composed of surface-sulfurized nickel-cobalt hydroxide nanoneedles supported on a nickel foam (Ni<sub>0.33</sub>Co<sub>0.67</sub>(OH)<sub>2</sub>@HOS/NF) and a cathode coated with bismuth oxyiodide (BiOI). This system achieved the simultaneous generation of formate from the anodic GOR and CO<sub>2</sub>RR at the cathode, with impressive faradaic efficiencies of 90% and 92%, respectively. These results were obtained at a cell voltage of 1.9 V and a current density of 22.4 mA cm<sup>-2</sup> [112].
- (c) **PET hydrolysate oxidation:** As outlined in our preceding sections, a significant surge in global plastic waste has been observed, necessitating substantial energy consumption for recycling. However, an intriguing alternative involves the production of formate through the electrochemical oxidation of ethylene glycol, a monomer generated during the alkaline hydrolysis of polyethylene terephthalate (PET) [113]. Recently, Wang and co-authors reported a process involving the electrochemical reforming of PET hydrolysate coupled with CO<sub>2</sub>RR. They employed a NiCo<sub>2</sub>O<sub>4</sub> nanowire anode and a SnO<sub>2</sub> nanosheet cathode to construct a two-electrode electrolyzer. This configuration enabled the simultaneous generation of formate, achieving an overall formate FE of 155% at a cell voltage of 1.9 V.

Nonetheless, numerous investigations have explored the conversion of PET hydrolysate into formate at the anode and hydrogen at the cathode. However, the integration of this process with CO<sub>2</sub>RR has been significantly constrained. This thesis aims to delve deeper into this subject, conducting further research to expand our understanding of this novel approach [79].

**Table 3.** Summary of anodic reactions of some reported electrocatalysts.

<i>Catalyst</i>	<i>Organic molecule</i>	<i>Electrolyte</i>	<i>Potential</i>	<i>Current density</i>	<i>reference</i>
<i>NiCoFe-LDHs</i>	HMF	1M KOH	1.43	10	[114]
<i>NiCo-LDH/NF</i>	CH <sub>3</sub> OH	1M KOH	1.33	10	[115]
<i>Co-Ni<sub>3</sub>N/CC</i>	Ethylene glycol	1M KOH	1.18	10	[116]
<i>Ni-Mo-N/CC</i>	Glycerol	1M KOH	1.30	10	[117]
<i>CoxP@NiCo-LDH</i>	CH <sub>3</sub> OH	1M KOH	1.24	10	[118]
<i>CoNi<sub>0.25</sub>P</i>	Ethylene glycol	1M KOH	1.8	500	[119]

However, there are various approaches to address the issue of plastic waste, which are classified into landfilling, mechanical, chemical, functional recycling and incineration, as illustrated in Figure 8 [120], [121]. Alternatively, from a chemical standpoint, these methods can be categorized based on the extent of carbon bond cleavage (C–X/C–C) of the polymer chain, which is directly linked to factors such as CO<sub>2</sub> emissions, microplastic pollution, and consumption of energy

resources. During landfilling, the cleavage of C–X/C–C bonds proceeds at an extremely slow rate, resulting in the polymer waste persisting on the planet without any structural change and practical utilization (Figure 8a). However, incineration offers the potential for energy recovery (figure 8e), but it is essential to account for the energy requirements during the entire process, which includes complete degradation of C–X/C–C bonds in polymer chains (80–140 kcal mol<sup>-1</sup> for C–C/C–C bonds) [122]. Previous studies have shown that polymer waste recycling conserves 2–3 times more energy than incinerating plastic waste. Nevertheless, incineration releases GHGs and harmful substances, which are not environmentally friendly. In mechanical recycling, transforming polymer waste into poor quality polymer products through mechanical processes like melting, grinding, re-granulating, and compounding takes place (Figure 8b) [123], [124]. Alternatively, mechanically recycled polymer waste can also be combined with other materials, such as sand and wood to create new building materials [121].

Moreover, this method requires the raw plastic waste to be in extremely pure form and uniform. As a result, there is almost zero CO<sub>2</sub> emissions (or releases in a very negligible amount) due to the minimal cleavage of C–X/C–C bonds, which is environmentally friendly. Nonetheless, the quality of the polymer deteriorates during thermal processing, which leads to less number of polymer chains. Nevertheless, this approach does not address the challenges of recycling polymer mixtures and thermosetting plastics [125], [126].

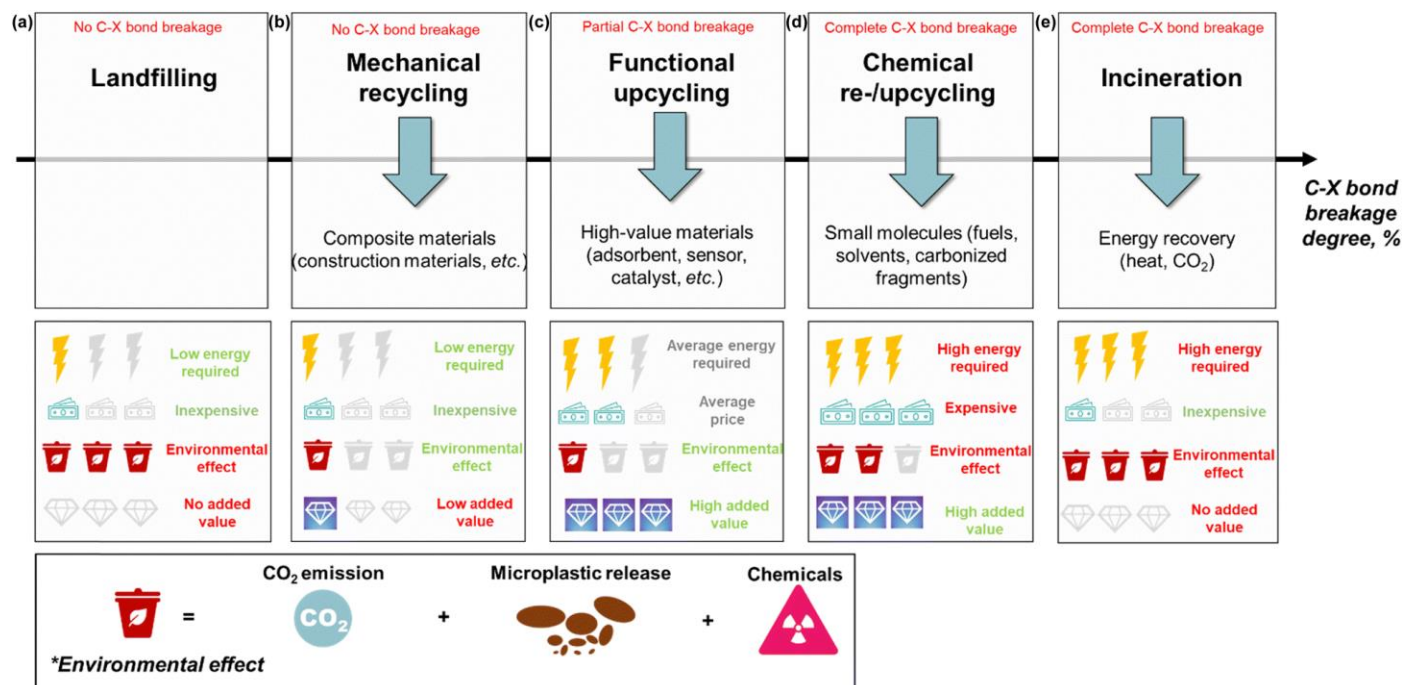


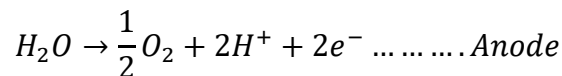
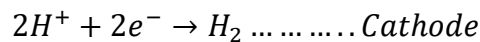
**Figure 8.** Different strategies for plastic management. (a) landfilling; (b) mechanical recycling; (c) functional upcycling; (d) chemical re-/upcycling; and (e) incineration (adapted from [121]).

During chemical treatment, it involves the partial breaking of C–X/C–C bonds, specifically the depolymerization into monomers or the generation of new small molecules (Figure 8d) [127]. Although depolymerization followed by repolymerization yields polymer products of higher quality compared to mechanical recycled polymers, achieving complete cleavage of C–X/C–C bonds demands more energy, or the use of high price catalysts. Despite the monomers of high value added and new small molecules, the energy and feedstock costs associated with chemical recycling raise concerns about its financial efficiency [127]. Therefore, in this thesis, our focus will be on the electroreforming of PET plastic waste to generate value-added products, such as formate, using innovative and highly efficient electrocatalysts.

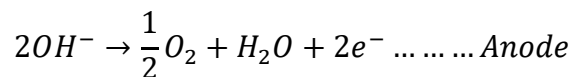
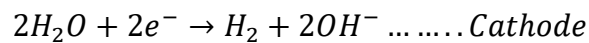
## 1.6. Water splitting

As we explored in our earlier discussions, there exists a connection between CO<sub>2</sub> emissions and plastic waste with the ongoing global energy crisis. This connection arises from the fact that fossil fuels are a primary source of both CO<sub>2</sub> emissions and the carbon-based fuels used in plastic production. Consequently, the solution lies in finding environmentally friendly alternatives to carbon-based fuels, and in this context, hydrogen generated through water electrolysis emerges as a promising substitute. Nonetheless, the widespread production of hydrogen faces a significant obstacle, because it demands a substantial thermodynamic potential of 1.23 V to split water effectively into hydrogen and oxygen (108). The process of water electrolysis occurs within a designated electrolyte, resulting in the generation of hydrogen at the cathode and oxygen at the anode. The specific manner in which the water splitting process unfolds varies depending on the type of electrolyte employed, as detailed below [128]:

If the electrolyte is acidic,



If the electrolyte is neutral or alkaline medium,



Nonetheless, researchers are currently engaged in extensive investigations aimed at developing a catalyst with bifunctional capabilities. Such a catalyst would have the ability to generate both hydrogen at the cathode and oxygen at the anode [129], [130]. First-row transition metal compounds, specifically those based on Co, Ni, and Fe, combined with heterostructures, have been the subject of extensive research as they exhibit high electrocatalytic activity, are abundantly available on Earth, and are cost-effective. Jiang *et al.* conducted an experiment in which they synthesized a cobalt phosphorus-derived (Co–P) film using the potentiodynamic electrodeposition method for catalyzing overall water splitting [131]. In their study, the Co–P films demonstrated an exceptional catalytic performance for both the hydrogen evolution reaction (HER) and the oxygen evolution reaction (OER) in a 1M KOH solution. Achieving a current density of  $10 \text{ mA cm}^{-2}$  required overpotentials of merely -94 mV for HER and 345 mV for OER, relative to the reversible hydrogen electrode (RHE). Furthermore, the corresponding Tafel slopes were as low as 42 and 47  $\text{mV dec}^{-1}$ , respectively. Notably, when used as both the anode and cathode catalysts in an electrolyzer, the Co–P films exhibited superior activity and stability even when compared to the integrated Pt and  $\text{IrO}_2$  catalyst combination.

Qiao and colleagues developed 3D porous electrodes made of Ni combined with nickel phosphide ( $\text{Ni}_8\text{P}_3$ ) or nickel sulfide ( $\text{Ni}_9\text{S}_8$ ) through a process involving the phosphorization or sulfurization on Ni foam treated by acid. The resulting materials could be directly utilized as stand-alone bifunctional electrodes for carrying out full electrochemical water splitting in alkaline environments. They implemented an advanced water electrolyzer using Ni/ $\text{Ni}_8\text{P}_3$  as both the anode and cathode in a 1M KOH solution. Remarkably, this setup required only a cell voltage of 1.61 V to achieve a water splitting current density of  $10 \text{ mA cm}^{-2}$ . The exceptional performance in overall water splitting was attributed to the self-supporting 3D structure, strong physical contact between

components, rapid charge transport, and the electronic effects induced by the specific structure [132].

However, even when the activity meets the requirements for practical applications, non-precious metal-based materials often fall short in terms of durability and cannot match the performance of platinum (Pt) electrocatalysts. Among the numerous metal-based catalysts assessed for HER catalysis, ruthenium (Ru), a member of the platinum group metals, has received extensive examination due to its cost-effectiveness (4% of Pt cost), high efficiency in HER, and stability. In essence, the efficiency of the HER process is closely associated with the strength of the metal-hydrogen (M–H) bonds present on the catalyst's surface and the overpotential needed for hydrogen reduction [133], [134].

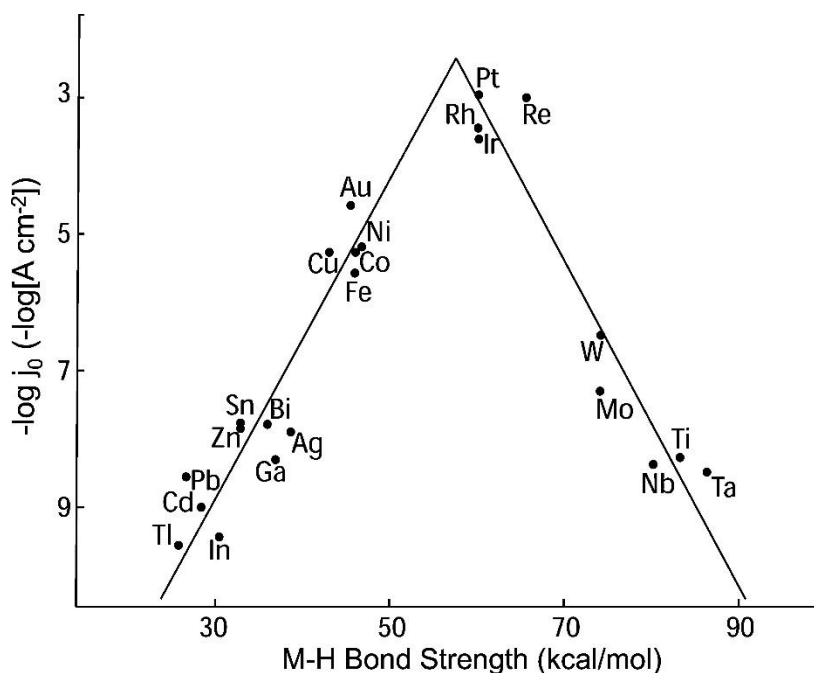


**Figure 9.** Volcano plot by Trasatti for pure metals in acidic solution [adapted from 115].

The Gibbs free energy ( $\Delta G$ ) of the Ru–H bond closely aligns with that of the optimal Pt–H bond located at the center of the volcano plot for HER (figure 9). Nonetheless, there is a tendency for

Ru nanoparticles to agglomerate together, which reduces the available active sites for catalysis [135]. Several studies have addressed this concern. Mahmood *et al.*, for instance, have synthesized a Ru-based catalyst designed for HER that can function effectively in both acidic and alkaline environments. This catalyst consists of Ru nanoparticles evenly dispersed within a nitrogen-rich two-dimensional porous carbon structure, denoted as Ru@C<sub>2</sub>N. The Ru@C<sub>2</sub>N electrocatalyst demonstrates impressive turnover frequencies at a low overpotential of 25 mV (0.67 H<sub>2</sub> s<sup>-1</sup> in a 0.5 M H<sub>2</sub>SO<sub>4</sub> solution and 0.75 H<sub>2</sub> s<sup>-1</sup> in a 1.0 M KOH solution) and minimal overpotentials at a current density of 10 mA cm<sup>-2</sup> (13.5 mV in a 0.5 M H<sub>2</sub>SO<sub>4</sub> solution and 17.0 mV in a 1.0 M KOH solution). Furthermore, it exhibits excellent stability in both acidic and alkaline conditions. These performance characteristics are comparable to, and, in some cases, even surpass those of the platinum-based Pt/C catalyst for HER [136].

Kweon and colleagues have demonstrated the effectiveness of an electrocatalyst consisting of Ru nanoparticles firmly anchored onto multiwalled carbon nanotubes (Ru@MWCNT) for catalyzing the HER, showcasing exceptional activity and durability. This catalyst achieved remarkably low overpotentials of 13 and 17 mV at a current density of 10 mA cm<sup>-2</sup> in 0.5 M H<sub>2</sub>SO<sub>4</sub> and 1.0 M KOH solutions, respectively, outperforming the commercial Pt/C catalyst. In practical water-splitting system construction and analysis, Ru@MWCNT generated 15.4% more hydrogen per unit of power consumption compared to commercial Pt/C, and its Faradaic efficiency stands at 92.28%, surpassing Pt/C, which achieved 85.97% [135].

In this thesis, we will delve further into various systems involving ruthenium nanoparticles to investigate their potential for facilitating the overall process of water splitting.

## 1.6 Objectives and outline of the thesis

The primary goal of this thesis is to develop highly efficient, durable, and environmentally friendly electrocatalysts capable of catalyzing thermodynamically unfavorable reactions, including water splitting and CO<sub>2</sub> reduction. The thesis is structured into four chapters, each focusing on different materials, their characterization, and measurements. More comprehensive details will be presented in each respective chapter.

**Chapter 1** provides an overview of global challenges related to environmental issues and the solutions implemented to address these concerns. It also outlines the motivation behind this thesis, highlighting the importance of CO<sub>2</sub> electrocatalytic reduction. Additionally, it discusses the integration of CO<sub>2</sub> reduction with other organic reactions, such as PET hydrolysate oxidation, aimed at enhancing product yields and later, we briefly discussed the electrocatalytic water splitting.

In **Chapter 2**, in collaboration with Dr. Vitaly Ordonsky's team, we prepared a novel electrocatalyst comprising Ru/RuO<sub>2</sub> nanowires embedded in a carbon nitride matrix. This material was synthesized using a two-dimensional imine-based covalent organic framework (COF) that incorporated a Ru<sup>II</sup>-2-diphenylphosphinobenzaldehyde complex. Through pyrolysis at 500 °C under a N<sub>2</sub> atmosphere, we successfully produced highly dispersed RuO<sub>2</sub> nanoparticles containing low-valence Ru sites within the layers of carbon nitride. This electrocatalyst demonstrated exceptional performance, with a remarkably low overpotential of 53 mV at -10 mA cm<sup>-2</sup> for the hydrogen evolution reaction (HER) and 280 mV at 10 mA cm<sup>-2</sup> for the oxygen evolution reaction (OER) in a 1M KOH electrolyte. Furthermore, in a two-electrode electrolyzer setup, it exhibited

an overpotential of only 286 mV at 10 mA cm<sup>-2</sup> in a 1M KOH solution, surpassing the performance of many other reported electrocatalysts.

In **Chapter 3** of our study, we have introduced an innovative methodology that integrates the CO<sub>2</sub>RR with the PET hydrolysate oxidation reaction to concurrently generate formate on both the anode and cathode. In this context, we have synthesized two catalysts: Bismuth oxide carbonate (BOC) functionalized reduced graphene oxide (rGO) for the cathodic CO<sub>2</sub>RR and CuCoO on rGO for the anodic PET hydrolysate oxidation. The anodic CuCoO@rGO catalyst demonstrated substantial electro-activity and an impressive FE of 85.7% at 1.5V vs. RHE, while the cathodic BOC@rGO catalyst achieved an FE of 97.4% at -0.8 V vs. RHE, enabling efficient formate production through CO<sub>2</sub>RR. The application of this approach in a 2-electrode electrolyzer resulted in the production of formate with a low cell voltage of 1.9 V at 10 mA cm<sup>-2</sup> and formate FE of 151.8%. This innovative method offers a unique avenue for upcycling PET waste, reducing CO<sub>2</sub> emissions, and promoting environmental sustainability.

In Chapter 4 of our study, we have utilized carbon felt (CF) as a substrate due to its favorable characteristics, such as a high surface area and cost-effectiveness. To enhance its hydrophilicity, we employed an electrochemical oxidation process at 2.5V vs. RHE in a 1M KOH solution for 30 minutes. This method effectively created a hydrophilic surface rich in oxygen content on the CF surface. Following substrate activation, we proceeded to deposit bismuth (Bi) onto the activated carbon felt (aCF) using a pulse electrodeposition (PD) technique, with a 5-second OFF period and a 2-second ON period in a bismuth salt electrolyte bath. This Bi-based electrocatalyst, employed for CO<sub>2</sub> reduction reactions (CO<sub>2</sub>RR), exhibited an impressive Faradaic efficiency (FE) of 94% with an overpotential of 0.71V in 0.5M KHCO<sub>3</sub>. Simultaneously, we utilized a straightforward electrodeposition method to deposit nickel-cobalt-phosphate oxide (NiCoPO<sub>x</sub>) onto aCF,

employing a mixture of cobalt and nickel in a phosphate electrolyte bath. This NiCoPOx deposition aimed to facilitate the oxidation of anodic PET hydrolysates. The electrocatalyst successfully converted ethylene glycol present in the PET hydrolysate solution into formate at a low potential of 1.5V vs. RHE with an impressive FE of 95%. Furthermore, we constructed a two-electrolyzer setup utilizing these electrocatalysts. In this configuration, we achieved a formate FE of 157% at a low cell voltage of 1.8V, showcasing the efficiency and efficacy of our developed system.

## References

- [1] “IEA (2023), CO2 Emissions in 2022, IEA, Paris.” <https://www.iea.org/reports/co2-emissions-in-2022>
- [2] S. J. Davis *et al.*, “Emissions rebound from the COVID-19 pandemic,” *Nat. Clim. Chang.*, vol. 12, no. 5, pp. 412–414, 2022, doi: 10.1038/s41558-022-01332-6.
- [3] “NOAA Global Monitoring Laboratory, Scripps Institute of Oceanography at the University of California San Diego.” <https://gml.noaa.gov/>
- [4] P. Friedlingstein *et al.*, “Global Carbon Budget 2022,” *Earth Syst. Sci. Data*, vol. 14, no. 11, pp. 4811–4900, 2022, doi: 10.5194/essd-14-4811-2022.
- [5] O. A. Dumitru *et al.*, “Constraints on global mean sea level during Pliocene warmth,” *Nature*, vol. 574, no. 7777, pp. 233–236, 2019, doi: 10.1038/s41586-019-1543-2.
- [6] H. Ritchie, M. Roser, and P. Rosado, “CO<sub>2</sub> and greenhouse gas emissions,” *Our world data*, 2020.
- [7] OECD, “Greenhouse gas emissions from primary plastics,” 2022, doi: <https://doi.org/https://doi.org/10.1787/1ac580ff-en>.

- [8] OECD, “Plastics use by region - projections,” 2022, doi:  
<https://doi.org/https://doi.org/10.1787/913b14f3-en>.
- [9] OECD, “Plastic waste by end-of-life fate and region - projections,” 2022, doi:  
<https://doi.org/https://doi.org/10.1787/e4e8c086-en>.
- [10] R. Geyer, J. R. Jambeck, and K. L. Law, “Production, use, and fate of all plastics ever made,” *Sci. Adv.*, vol. 3, no. 7, p. e1700782, 2017, doi: 10.1126/sciadv.1700782.
- [11] OECD, *Global Plastics Outlook*. 2022. doi:  
<https://doi.org/https://doi.org/10.1787/aa1edf33-en>.
- [12] Intergovernmental Panel on Climate Change (IPCC), Ed., “Framing and Context,” in *Global Warming of 1.5°C: IPCC Special Report on Impacts of Global Warming of 1.5°C above Pre-industrial Levels in Context of Strengthening Response to Climate Change, Sustainable Development, and Efforts to Eradicate Poverty*, Cambridge: Cambridge University Press, 2022, pp. 49–92. doi: DOI: 10.1017/9781009157940.003.
- [13] “United Nations Framework Convention on Climate Change, Kyoto Protocol.”  
[http://unfccc.int/kyoto\\_protocol/items/2830.php](http://unfccc.int/kyoto_protocol/items/2830.php) (accessed Sep. 02, 2023).
- [14] “(IEA) International Energy Agency, Key Trends in CO2 emissions, Excerpt from: CO2 emissions from fuel combustion Paris, France, 2015.”
- [15] “United Nations Conference on Climate Change (COP21).”  
<https://www.un.org/sustainabledevelopment/cop21/> (accessed Aug. 28, 2023).
- [16] “United Nations Conference on Climate Change (COP26).”  
<https://www.un.org/en/climatechange/cop26> (accessed Sep. 03, 2023).

- [17] “COM(2014) 15 final, Communication From The Commission To The European Parliament, The Council, The European Economic and Social Committee and The Committee of the Regions, A policy framework for climate and energy in the period from 2020 to 2030,, Europea.” <https://eur-lex.europa.eu/legal-content/EN/ALL/?uri=COM:2014:15:FIN> (accessed Sep. 03, 2023).
- [18] R. A. Mosbacher, “Report of the Secretary of Commerce to the Congress of the United States on the effects of plastic debris on the marine environment pursuant to section 2203 of Public Law 100-220, the Marine Plastic Pollution Research and Control Act of 1987,” 1989.
- [19] “G7 summit 2018 ocean plastics charter.” <https://plasticactioncentre.ca/directory/ocean-plastics-charter/#:~:text=The Charter outlines concrete actions,%2C coastal communities%2C and ecosystems.> (accessed Sep. 05, 2023).
- [20] D. Xanthos and T. R. Walker, “International policies to reduce plastic marine pollution from single-use plastics (plastic bags and microbeads): A review,” *Mar. Pollut. Bull.*, vol. 118, no. 1–2, pp. 17–26, May 2017, doi: 10.1016/j.marpolbul.2017.02.048.
- [21] BBC News, “Onyanga-Omara, Jane (14 September 2013). ‘Plastic bag backlash gains momentum,’” BBC News. [Online]. Available: <https://www.bbc.com/news/uk-24090603>
- [22] T. D. Nielsen, K. Holmberg, and J. Stripple, “Need a bag? A review of public policies on plastic carrier bags - Where, how and to what effect?,” *Waste Manag.*, vol. 87, pp. 428–440, Mar. 2019, doi: 10.1016/j.wasman.2019.02.025.
- [23] European Commission, “Environment: Commission proposes to reduce the use of plastic bags.” [https://ec.europa.eu/commission/presscorner/detail/en/IP\\_13\\_1017](https://ec.europa.eu/commission/presscorner/detail/en/IP_13_1017) (accessed Sep.

- 06, 2023).
- [24] Cécile Barbière, “EU to halve plastic bag use by 2019.” [Online]. Available: <https://www.euractiv.com/section/sustainable-dev/news/eu-to-halve-plastic-bag-use-by-2019/>
- [25] “Directive 2015/720 of 29 April 2015 of the European Parliament and of the Council amending Directive 94/62/EC as regards reducing the consumption of lightweight plastic carrier bags.” <https://eur-lex.europa.eu/legal-content/EN/TXT/?uri=CELEX:32015L0720> (accessed Sep. 06, 2023).
- [26] “IEA (2019), The Future of Hydrogen, IEA, Paris <https://www.iea.org/reports/the-future-of-hydrogen>, License: CC BY 4.0”, [Online]. Available: <https://www.iea.org/reports/the-future-of-hydrogen>
- [27] C. Mitsugi, A. Harumi, and F. Kenzo, “WE-NET: Japanese hydrogen program,” *Int. J. Hydrogen Energy*, vol. 23, no. 3, pp. 159–165, 1998, doi: [https://doi.org/10.1016/S0360-3199\(97\)00042-6](https://doi.org/10.1016/S0360-3199(97)00042-6).
- [28] M. Saxe, A. Folkesson, and P. Alvfors, “Energy system analysis of the fuel cell buses operated in the project: Clean Urban Transport for Europe,” *Energy*, vol. 33, no. 5, pp. 689–711, 2008, doi: <https://doi.org/10.1016/j.energy.2008.01.001>.
- [29] “International Partnership for the Hydrogen Economy.” <https://www.iphe.net/> (accessed Sep. 06, 2023).
- [30] M. A. Quader and S. Ahmed, “Chapter Four - Bioenergy With Carbon Capture and Storage (BECCS): Future Prospects of Carbon-Negative Technologies,” in *Clean Energy*

- for Sustainable Development*, M. G. Rasul, A. kalam Azad, and S. C. Sharma, Eds., Academic Press, 2017, pp. 91–140. doi: <https://doi.org/10.1016/B978-0-12-805423-9.00004-1>.
- [31] A. J. Hunt, E. H. K. Sin, R. Marriott, and J. H. Clark, “Generation, Capture, and Utilization of Industrial Carbon Dioxide,” *ChemSusChem*, vol. 3, no. 3, pp. 306–322, 2010, doi: <https://doi.org/10.1002/cssc.200900169>.
- [32] C. Marchetti, “On geoengineering and the CO<sub>2</sub> problem,” *Clim. Change*, vol. 1, no. 1, pp. 59–68, 1977, doi: [10.1007/BF00162777](https://doi.org/10.1007/BF00162777).
- [33] B. Metz, O. Davidson, H. C. De Coninck, M. Loos, and L. Meyer, *IPCC special report on carbon dioxide capture and storage*. Cambridge: Cambridge University Press, 2005.
- [34] I. In, B. Metz, O. Davidson, H. C. Coninck, M. Loos, and L. A. Meyer, “Special Report on Carbon Dioxide Capture and Storage,” Metz, B., Davidson, O., Coninck, HC, Loos, M., Meyer, LA, Eds, 2005.
- [35] M. Wang, A. Lawal, P. Stephenson, J. Sidders, and C. Ramshaw, “Post-combustion CO<sub>2</sub> capture with chemical absorption: A state-of-the-art review,” *Chem. Eng. Res. Des.*, vol. 89, no. 9, pp. 1609–1624, 2011, doi: <https://doi.org/10.1016/j.cherd.2010.11.005>.
- [36] Y. Wang, L. Zhao, A. Otto, M. Robinius, and D. Stolten, “A Review of Post-combustion CO<sub>2</sub> Capture Technologies from Coal-fired Power Plants,” *Energy Procedia*, vol. 114, pp. 650–665, 2017, doi: <https://doi.org/10.1016/j.egypro.2017.03.1209>.
- [37] M. N. Anwar *et al.*, “CO<sub>2</sub> capture and storage: A way forward for sustainable environment,” *J. Environ. Manage.*, vol. 226, pp. 131–144, 2018, doi:

<https://doi.org/10.1016/j.jenvman.2018.08.009>.

- [38] B. J. P. Buhre, L. K. Elliott, C. D. Sheng, R. P. Gupta, and T. F. Wall, “Oxy-fuel combustion technology for coal-fired power generation,” *Prog. Energy Combust. Sci.*, vol. 31, no. 4, pp. 283–307, 2005, doi: <https://doi.org/10.1016/j.pecs.2005.07.001>.
- [39] T. Ajayi, J. S. Gomes, and A. Bera, “A review of CO<sub>2</sub> storage in geological formations emphasizing modeling, monitoring and capacity estimation approaches,” *Pet. Sci.*, vol. 16, no. 5, pp. 1028–1063, 2019, doi: 10.1007/s12182-019-0340-8.
- [40] S. Bachu, “CO<sub>2</sub> storage in geological media: Role, means, status and barriers to deployment,” *Prog. Energy Combust. Sci.*, vol. 34, no. 2, pp. 254–273, 2008, doi: <https://doi.org/10.1016/j.pecs.2007.10.001>.
- [41] C. Cao, H. Liu, Z. Hou, F. Mehmood, J. Liao, and W. Feng, “A Review of CO<sub>2</sub> Storage in View of Safety and Cost-Effectiveness,” *Energies*, vol. 13, no. 3, 2020, doi: 10.3390/en13030600.
- [42] A. Raza, R. Gholami, R. Rezaee, V. Rasouli, and M. Rabiei, “Significant aspects of carbon capture and storage – A review,” *Petroleum*, vol. 5, no. 4, pp. 335–340, 2019, doi: <https://doi.org/10.1016/j.petlm.2018.12.007>.
- [43] K. Sumida *et al.*, “Carbon Dioxide Capture in Metal–Organic Frameworks,” *Chem. Rev.*, vol. 112, no. 2, pp. 724–781, Feb. 2012, doi: 10.1021/cr2003272.
- [44] G. A. Olah, A. Goeppert, and G. K. S. Prakash, “Chemical Recycling of Carbon Dioxide to Methanol and Dimethyl Ether: From Greenhouse Gas to Renewable, Environmentally Carbon Neutral Fuels and Synthetic Hydrocarbons,” *J. Org. Chem.*, vol. 74, no. 2, pp.

- 487–498, Jan. 2009, doi: 10.1021/jo801260f.
- [45] Z. Zhan, W. Kobsiriphat, J. R. Wilson, M. Pillai, I. Kim, and S. A. Barnett, “Syngas Production By Coelectrolysis of CO<sub>2</sub>/H<sub>2</sub>O: The Basis for a Renewable Energy Cycle,” *Energy & Fuels*, vol. 23, no. 6, pp. 3089–3096, Jun. 2009, doi: 10.1021/ef900111f.
- [46] W. Li, H. Wang, Y. Shi, and N. Cai, “Performance and methane production characteristics of H<sub>2</sub>O–CO<sub>2</sub> co-electrolysis in solid oxide electrolysis cells,” *Int. J. Hydrogen Energy*, vol. 38, no. 25, pp. 11104–11109, 2013, doi: <https://doi.org/10.1016/j.ijhydene.2013.01.008>.
- [47] O. O. James, A. M. Mesubi, T. C. Ako, and S. Maity, “Increasing carbon utilization in Fischer–Tropsch synthesis using H<sub>2</sub>-deficient or CO<sub>2</sub>-rich syngas feeds,” *Fuel Process. Technol.*, vol. 91, no. 2, pp. 136–144, 2010, doi: <https://doi.org/10.1016/j.fuproc.2009.09.017>.
- [48] N. Homs, J. Toyir, and P. R. de la Piscina, “Chapter 1 - Catalytic Processes for Activation of CO<sub>2</sub>,” S. L. B. T.-N. and F. D. in C. Suib, Ed., Amsterdam: Elsevier, 2013, pp. 1–26. doi: <https://doi.org/10.1016/B978-0-444-53882-6.00001-2>.
- [49] C. Stewart and M.-A. Hessami, “A study of methods of carbon dioxide capture and sequestration—the sustainability of a photosynthetic bioreactor approach,” *Energy Convers. Manag.*, vol. 46, no. 3, pp. 403–420, 2005, doi: <https://doi.org/10.1016/j.enconman.2004.03.009>.
- [50] M. Mikkelsen, M. Jørgensen, and F. C. Krebs, “The teraton challenge. A review of fixation and transformation of carbon dioxide,” *Energy Environ. Sci.*, vol. 3, no. 1, pp. 43–81, 2010, doi: 10.1039/B912904A.

- [51] Y. Chen and M. W. Kanan, “Tin Oxide Dependence of the CO<sub>2</sub> Reduction Efficiency on Tin Electrodes and Enhanced Activity for Tin/Tin Oxide Thin-Film Catalysts,” *J. Am. Chem. Soc.*, vol. 134, no. 4, pp. 1986–1989, Feb. 2012, doi: 10.1021/ja2108799.
- [52] J. Schneider, H. Jia, J. T. Muckerman, and E. Fujita, “Thermodynamics and kinetics of CO<sub>2</sub>{,} CO{,} and H<sup>+</sup> binding to the metal centre of CO<sub>2</sub>reductioncatalysts,” *Chem. Soc. Rev.*, vol. 41, no. 6, pp. 2036–2051, 2012, doi: 10.1039/C1CS15278E.
- [53] Z. Sun, T. Ma, H. Tao, Q. Fan, and B. Han, “Fundamentals and Challenges of Electrochemical CO<sub>2</sub> Reduction Using Two-Dimensional Materials,” *Chem*, vol. 3, no. 4, pp. 560–587, 2017, doi: <https://doi.org/10.1016/j.chempr.2017.09.009>.
- [54] Z. Wang, F. Wang, Y. Peng, and Y. Han, “Direct observation of liquid nucleus growth in homogeneous melting of colloidal crystals,” *Nat. Commun.*, vol. 6, no. 1, p. 6942, 2015, doi: 10.1038/ncomms7942.
- [55] Y. Matsubara, “Unified Benchmarking of Electrocatalysts in Noninnocent Second Coordination Spheres for CO<sub>2</sub> Reduction,” *ACS Energy Lett.*, vol. 4, no. 8, pp. 1999–2004, Aug. 2019, doi: 10.1021/acsenergylett.9b01180.
- [56] Y. Hori, “Electrochemical CO<sub>2</sub> Reduction on Metal Electrodes BT - Modern Aspects of Electrochemistry,” C. G. Vayenas, R. E. White, and M. E. Gamboa-Aldeco, Eds., New York, NY: Springer New York, 2008, pp. 89–189. doi: 10.1007/978-0-387-49489-0\_3.
- [57] Y. Hori, H. Wakebe, T. Tsukamoto, and O. Koga, “Electrocatalytic process of CO selectivity in electrochemical reduction of CO<sub>2</sub> at metal electrodes in aqueous media,” *Electrochim. Acta*, vol. 39, no. 11, pp. 1833–1839, 1994, doi: [https://doi.org/10.1016/0013-4686\(94\)85172-7](https://doi.org/10.1016/0013-4686(94)85172-7).

- [58] M. Ma, K. Djanashvili, and W. A. Smith, “Controllable Hydrocarbon Formation from the Electrochemical Reduction of CO<sub>2</sub> over Cu Nanowire Arrays,” *Angew. Chemie Int. Ed.*, vol. 55, no. 23, pp. 6680–6684, 2016, doi: <https://doi.org/10.1002/anie.201601282>.
- [59] X. Lu, D. Y. C. Leung, H. Wang, M. K. H. Leung, and J. Xuan, “Electrochemical Reduction of Carbon Dioxide to Formic Acid,” *ChemElectroChem*, vol. 1, no. 5, pp. 836–849, 2014, doi: <https://doi.org/10.1002/celec.201300206>.
- [60] C. Fellay, N. Yan, P. J. Dyson, and G. Laurenczy, “Selective Formic Acid Decomposition for High-Pressure Hydrogen Generation: A Mechanistic Study,” *Chem. – A Eur. J.*, vol. 15, no. 15, pp. 3752–3760, 2009, doi: <https://doi.org/10.1002/chem.200801824>.
- [61] Z. B. Hoffman, T. S. Gray, K. B. Moraveck, T. B. Gunnoe, and G. Zangari, “Electrochemical Reduction of Carbon Dioxide to Syngas and Formate at Dendritic Copper–Indium Electrocatalysts,” *ACS Catal.*, vol. 7, no. 8, pp. 5381–5390, Aug. 2017, doi: [10.1021/acscatal.7b01161](https://doi.org/10.1021/acscatal.7b01161).
- [62] S. Kim *et al.*, “Shape-controlled bismuth nanoflakes as highly selective catalysts for electrochemical carbon dioxide reduction to formate,” *Nano Energy*, vol. 39, pp. 44–52, 2017, doi: <https://doi.org/10.1016/j.nanoen.2017.05.065>.
- [63] P. Su, W. Xu, Y. Qiu, T. Zhang, X. Li, and H. Zhang, “Ultrathin Bismuth Nanosheets as a Highly Efficient CO<sub>2</sub> Reduction Electrocatalyst,” *ChemSusChem*, vol. 11, no. 5, pp. 848–853, 2018, doi: <https://doi.org/10.1002/cssc.201702229>.
- [64] X. Zheng *et al.*, “Sulfur-Modulated Tin Sites Enable Highly Selective Electrochemical Reduction of CO<sub>2</sub> to Formate,” *Joule*, vol. 1, no. 4, pp. 794–805, 2017, doi: <https://doi.org/10.1016/j.joule.2017.09.014>.

- [65] F. Lei *et al.*, “Metallic tin quantum sheets confined in graphene toward high-efficiency carbon dioxide electroreduction,” *Nat. Commun.*, vol. 7, no. 1, p. 12697, 2016, doi: 10.1038/ncomms12697.
- [66] J. H. Koh *et al.*, “Facile CO<sub>2</sub> Electro-Reduction to Formate via Oxygen Bidentate Intermediate Stabilized by High-Index Planes of Bi Dendrite Catalyst,” *ACS Catal.*, vol. 7, no. 8, pp. 5071–5077, Aug. 2017, doi: 10.1021/acscatal.7b00707.
- [67] J. S. Yoo, R. Christensen, T. Vegge, J. K. Nørskov, and F. Studt, “Theoretical Insight into the Trends that Guide the Electrochemical Reduction of Carbon Dioxide to Formic Acid,” *ChemSusChem*, vol. 9, no. 4, pp. 358–363, 2016, doi: <https://doi.org/10.1002/cssc.201501197>.
- [68] N. Yang, S. R. Waldvogel, and X. Jiang, “Electrochemistry of Carbon Dioxide on Carbon Electrodes,” *ACS Appl. Mater. Interfaces*, vol. 8, no. 42, pp. 28357–28371, Oct. 2016, doi: 10.1021/acsami.5b09825.
- [69] P. K. Jiwanti, S. Sultana, W. P. Wicaksono, and Y. Einaga, “Metal modified carbon-based electrode for CO<sub>2</sub> electrochemical reduction: A review,” *J. Electroanal. Chem.*, vol. 898, p. 115634, 2021, doi: <https://doi.org/10.1016/j.jelechem.2021.115634>.
- [70] Y. Xiong *et al.*, “Rapid synthesis of amorphous bimetallic copper-bismuth electrocatalysts for efficient electrochemical CO<sub>2</sub> reduction to formate in a wide potential window,” *J. CO<sub>2</sub> Util.*, vol. 51, p. 101621, 2021, doi: <https://doi.org/10.1016/j.jcou.2021.101621>.
- [71] N. Han *et al.*, “Self-templated synthesis of hierarchical mesoporous SnO<sub>2</sub> nanosheets for selective CO<sub>2</sub> reduction,” *J. Mater. Chem. A*, vol. 7, no. 3, pp. 1267–1272, 2019, doi: 10.1039/C8TA10959A.

- [72] K. R. Phillips, Y. Katayama, J. Hwang, and Y. Shao-Horn, “Sulfide-Derived Copper for Electrochemical Conversion of CO<sub>2</sub> to Formic Acid,” *J. Phys. Chem. Lett.*, vol. 9, no. 15, pp. 4407–4412, Aug. 2018, doi: 10.1021/acs.jpcclett.8b01601.
- [73] M. Y. Zu, L. Zhang, C. Wang, L. R. Zheng, and H. G. Yang, “Copper-modulated bismuth nanocrystals alter the formate formation pathway to achieve highly selective CO<sub>2</sub> electroreduction,” *J. Mater. Chem. A*, vol. 6, no. 35, pp. 16804–16809, 2018, doi: 10.1039/C8TA05355C.
- [74] Y.-X. Duan, K.-H. Liu, Q. Zhang, J.-M. Yan, and Q. Jiang, “Efficient CO<sub>2</sub> Reduction to HCOOH with High Selectivity and Energy Efficiency over Bi/rGO Catalyst,” *Small Methods*, vol. 4, no. 5, p. 1900846, May 2020, doi: <https://doi.org/10.1002/smt.201900846>.
- [75] Y. Zhang, X. Zhang, Y. Ling, F. Li, A. M. Bond, and J. Zhang, “Controllable Synthesis of Few-Layer Bismuth Subcarbonate by Electrochemical Exfoliation for Enhanced CO<sub>2</sub> Reduction Performance,” *Angew. Chemie Int. Ed.*, vol. 57, no. 40, pp. 13283–13287, Oct. 2018, doi: <https://doi.org/10.1002/anie.201807466>.
- [76] H.-R. “Molly” Jhong, S. Ma, and P. J. A. Kenis, “Electrochemical conversion of CO<sub>2</sub> to useful chemicals: current status, remaining challenges, and future opportunities,” *Curr. Opin. Chem. Eng.*, vol. 2, no. 2, pp. 191–199, 2013, doi: <https://doi.org/10.1016/j.coche.2013.03.005>.
- [77] Y. Pan *et al.*, “Renewable formate from sunlight, biomass and carbon dioxide in a photoelectrochemical cell,” *Nat. Commun.*, vol. 14, no. 1, p. 1013, 2023, doi: 10.1038/s41467-023-36726-3.

- [78] X. Wei, Y. Li, L. Chen, and J. Shi, “Formic Acid Electro-Synthesis by Concurrent Cathodic CO<sub>2</sub> Reduction and Anodic CH<sub>3</sub>OH Oxidation,” *Angew. Chemie Int. Ed.*, vol. 60, no. 6, pp. 3148–3155, 2021, doi: <https://doi.org/10.1002/anie.202012066>.
- [79] J. Wang *et al.*, “Electrocatalytic Valorization of Poly(ethylene terephthalate) Plastic and CO<sub>2</sub> for Simultaneous Production of Formic Acid,” *ACS Catal.*, vol. 12, no. 11, pp. 6722–6728, Jun. 2022, doi: [10.1021/acscatal.2c01128](https://doi.org/10.1021/acscatal.2c01128).
- [80] R. Lin, J. Guo, X. Li, P. Patel, and A. Seifitokaldani, “Electrochemical Reactors for CO<sub>2</sub> Conversion,” *Catalysts*, vol. 10, no. 5, 2020, doi: [10.3390/catal10050473](https://doi.org/10.3390/catal10050473).
- [81] A. Del Castillo, M. Alvarez-Guerra, J. Solla-Gullón, A. Sáez, V. Montiel, and A. Irabien, “Electrocatalytic reduction of CO<sub>2</sub> to formate using particulate Sn electrodes: Effect of metal loading and particle size,” *Appl. Energy*, vol. 157, pp. 165–173, 2015, doi: <https://doi.org/10.1016/j.apenergy.2015.08.012>.
- [82] L. Zhang, Z.-J. Zhao, and J. Gong, “Nanostructured Materials for Heterogeneous Electrocatalytic CO<sub>2</sub> Reduction and their Related Reaction Mechanisms,” *Angew. Chemie Int. Ed.*, vol. 56, no. 38, pp. 11326–11353, 2017, doi: <https://doi.org/10.1002/anie.201612214>.
- [83] P. De Luna, C. Hahn, D. Higgins, S. A. Jaffer, T. F. Jaramillo, and E. H. Sargent, “What would it take for renewably powered electrosynthesis to displace petrochemical processes?,” *Science (80-. )*, vol. 364, no. 6438, p. eaav3506, Apr. 2019, doi: [10.1126/science.aav3506](https://doi.org/10.1126/science.aav3506).
- [84] T. Burdyny *et al.*, “Nanomorphology-Enhanced Gas-Evolution Intensifies CO<sub>2</sub> Reduction Electrochemistry,” *ACS Sustain. Chem. Eng.*, vol. 5, no. 5, pp. 4031–4040, May 2017,

doi: 10.1021/acssuschemeng.7b00023.

- [85] T. Yamamoto, D. A. Tryk, A. Fujishima, and H. Ohata, "Production of syngas plus oxygen from CO<sub>2</sub> in a gas-diffusion electrode-based electrolytic cell," *Electrochim. Acta*, vol. 47, no. 20, pp. 3327–3334, 2002, doi: [https://doi.org/10.1016/S0013-4686\(02\)00253-0](https://doi.org/10.1016/S0013-4686(02)00253-0).
- [86] S. Uhm and Y. D. Kim, "Electrochemical conversion of carbon dioxide in a solid oxide electrolysis cell," *Curr. Appl. Phys.*, vol. 14, no. 5, pp. 672–679, 2014, doi: <https://doi.org/10.1016/j.cap.2014.02.013>.
- [87] B. A. Rosen *et al.*, "Ionic Liquid-Mediated Selective Conversion of CO<sub>2</sub> to CO at Low Overpotentials," *Science (80-. )*, vol. 334, no. 6056, pp. 643–644, 2011, doi: [10.1126/science.1209786](https://doi.org/10.1126/science.1209786).
- [88] X. Sun *et al.*, "Molybdenum–Bismuth Bimetallic Chalcogenide Nanosheets for Highly Efficient Electrocatalytic Reduction of Carbon Dioxide to Methanol," *Angew. Chemie Int. Ed.*, vol. 55, no. 23, pp. 6771–6775, 2016, doi: <https://doi.org/10.1002/anie.201603034>.
- [89] D. M. Weekes, D. A. Salvatore, A. Reyes, A. Huang, and C. P. Berlinguette, "Electrolytic CO<sub>2</sub> Reduction in a Flow Cell," *Acc. Chem. Res.*, vol. 51, no. 4, pp. 910–918, Apr. 2018, doi: [10.1021/acs.accounts.8b00010](https://doi.org/10.1021/acs.accounts.8b00010).
- [90] K. P. Kuhl, E. R. Cave, D. N. Abram, and T. F. Jaramillo, "New insights into the electrochemical reduction of carbon dioxide on metallic copper surfaces," *Energy Environ. Sci.*, vol. 5, no. 5, pp. 7050–7059, 2012, doi: [10.1039/C2EE21234J](https://doi.org/10.1039/C2EE21234J).
- [91] A. S. Hollinger, R. J. Maloney, R. S. Jayashree, D. Natarajan, L. J. Markoski, and P. J. A.

- Kenis, “Nanoporous separator and low fuel concentration to minimize crossover in direct methanol laminar flow fuel cells,” *J. Power Sources*, vol. 195, no. 11, pp. 3523–3528, 2010, doi: <https://doi.org/10.1016/j.jpowsour.2009.12.063>.
- [92] S. Liu *et al.*, “Efficient CO<sub>2</sub> Electroreduction with a Monolayer Bi<sub>2</sub>WO<sub>6</sub> through a Metallic Intermediate Surface State,” *ACS Catal.*, vol. 11, no. 20, pp. 12476–12484, Oct. 2021, doi: [10.1021/acscatal.1c02495](https://doi.org/10.1021/acscatal.1c02495).
- [93] F. Yang *et al.*, “Bismuthene for highly efficient carbon dioxide electroreduction reaction,” *Nat. Commun.*, vol. 11, no. 1, p. 1088, 2020, doi: [10.1038/s41467-020-14914-9](https://doi.org/10.1038/s41467-020-14914-9).
- [94] L. Lin *et al.*, “A Nanocomposite of Bismuth Clusters and Bi<sub>2</sub>O<sub>2</sub>CO<sub>3</sub> Sheets for Highly Efficient Electrocatalytic Reduction of CO<sub>2</sub> to Formate,” *Angew. Chemie Int. Ed.*, vol. 62, no. 3, p. e202214959, 2023, doi: <https://doi.org/10.1002/anie.202214959>.
- [95] D. Yao, C. Tang, A. Vasileff, X. Zhi, Y. Jiao, and S.-Z. Qiao, “The Controllable Reconstruction of Bi-MOFs for Electrochemical CO<sub>2</sub> Reduction through Electrolyte and Potential Mediation,” *Angew. Chemie Int. Ed.*, vol. 60, no. 33, pp. 18178–18184, 2021, doi: <https://doi.org/10.1002/anie.202104747>.
- [96] M. Zhang *et al.*, “Engineering a conductive network of atomically thin bismuthene with rich defects enables CO<sub>2</sub> reduction to formate with industry-compatible current densities and stability,” *Energy Environ. Sci.*, vol. 14, no. 9, pp. 4998–5008, 2021, doi: [10.1039/D1EE01495A](https://doi.org/10.1039/D1EE01495A).
- [97] S. Liu, X. F. Lu, J. Xiao, X. Wang, and X. W. (David) Lou, “Bi<sub>2</sub>O<sub>3</sub> Nanosheets Grown on Multi-Channel Carbon Matrix to Catalyze Efficient CO<sub>2</sub> Electroreduction to HCOOH,” *Angew. Chemie Int. Ed.*, vol. 58, no. 39, pp. 13828–13833, 2019, doi: <https://doi.org/10.1002/anie.201908000>.

<https://doi.org/10.1002/anie.201907674>.

- [98] J. Zhu *et al.*, “Bilayer nanosheets of unusual stoichiometric bismuth oxychloride for potassium ion storage and CO<sub>2</sub> reduction,” *Nano Energy*, vol. 75, p. 104939, 2020, doi: <https://doi.org/10.1016/j.nanoen.2020.104939>.
- [99] S. Liu *et al.*, “Rational design of carbon-based metal-free catalysts for electrochemical carbon dioxide reduction: A review,” *J. Energy Chem.*, vol. 36, pp. 95–105, 2019, doi: <https://doi.org/10.1016/j.jechem.2019.06.013>.
- [100] D. Zhang *et al.*, “High efficiency and selectivity from synergy: Bi nanoparticles embedded in nitrogen doped porous carbon for electrochemical reduction of CO<sub>2</sub> to formate,” *Electrochim. Acta*, vol. 334, p. 135563, 2020, doi: <https://doi.org/10.1016/j.electacta.2019.135563>.
- [101] X. Jiang, Q. Wang, X. Xiao, J. Chen, Y. Shen, and M. Wang, “Interfacial engineering of bismuth with reduced graphene oxide hybrid for improving CO<sub>2</sub> electroreduction performance,” *Electrochim. Acta*, vol. 357, p. 136840, 2020, doi: <https://doi.org/10.1016/j.electacta.2020.136840>.
- [102] C. Zhao and J. Wang, “Electrochemical reduction of CO<sub>2</sub> to formate in aqueous solution using electro-deposited Sn catalysts,” *Chem. Eng. J.*, vol. 293, pp. 161–170, 2016, doi: <https://doi.org/10.1016/j.cej.2016.02.084>.
- [103] F. Li, L. Chen, G. P. Knowles, D. R. MacFarlane, and J. Zhang, “Hierarchical Mesoporous SnO<sub>2</sub> Nanosheets on Carbon Cloth: A Robust and Flexible Electrocatalyst for CO<sub>2</sub> Reduction with High Efficiency and Selectivity,” *Angew. Chemie Int. Ed.*, vol. 56, no. 2, pp. 505–509, 2017, doi: <https://doi.org/10.1002/anie.201608279>.

- [104] S. Verma, S. Lu, and P. J. A. Kenis, “Co-electrolysis of CO<sub>2</sub> and glycerol as a pathway to carbon chemicals with improved technoeconomics due to low electricity consumption,” *Nat. Energy*, vol. 4, no. 6, pp. 466–474, 2019, doi: 10.1038/s41560-019-0374-6.
- [105] D. A. Salvatore *et al.*, “Designing anion exchange membranes for CO<sub>2</sub> electrolyzers,” *Nat. Energy*, vol. 6, no. 4, pp. 339–348, 2021, doi: 10.1038/s41560-020-00761-x.
- [106] J. Jack, W. Zhu, J. L. Avalos, J. Gong, and Z. J. Ren, “Anode co-valorization for scalable and sustainable electrolysis,” *Green Chem.*, vol. 23, no. 20, pp. 7917–7936, 2021, doi: 10.1039/D1GC02094C.
- [107] J. Na *et al.*, “General technoeconomic analysis for electrochemical coproduction coupling carbon dioxide reduction with organic oxidation,” *Nat. Commun.*, vol. 10, no. 1, p. 5193, 2019, doi: 10.1038/s41467-019-12744-y.
- [108] Z. Xu, C. Peng, and G. Zheng, “Coupling Value-Added Anodic Reactions with Electrocatalytic CO<sub>2</sub> Reduction,” *Chem. – A Eur. J.*, vol. 29, no. 11, p. e202203147, 2023, doi: <https://doi.org/10.1002/chem.202203147>.
- [109] Y. Zhang *et al.*, “Aligned InS Nanorods for Efficient Electrocatalytic Carbon Dioxide Reduction,” *ACS Appl. Mater. Interfaces*, vol. 14, no. 22, pp. 25257–25266, Jun. 2022, doi: 10.1021/acsami.2c01152.
- [110] K. Xie, A. Ozden, R. K. Miao, Y. Li, D. Sinton, and E. H. Sargent, “Eliminating the need for anodic gas separation in CO<sub>2</sub> electroreduction systems via liquid-to-liquid anodic upgrading,” *Nat. Commun.*, vol. 13, no. 1, p. 3070, 2022, doi: 10.1038/s41467-022-30677-x.

- [111] A. M. Verma, L. Laverdure, M. M. Melander, and K. Honkala, “Mechanistic Origins of the pH Dependency in Au-Catalyzed Glycerol Electro-oxidation: Insight from First-Principles Calculations,” *ACS Catal.*, vol. 12, no. 1, pp. 662–675, Jan. 2022, doi: 10.1021/acscatal.1c03788.
- [112] Y. Pei, Z. Pi, H. Zhong, J. Cheng, and F. Jin, “Glycerol oxidation-assisted electrochemical CO<sub>2</sub> reduction for the dual production of formate,” *J. Mater. Chem. A*, vol. 10, no. 3, pp. 1309–1319, 2022, doi: 10.1039/D1TA07119J.
- [113] H. Zhou *et al.*, “Electrocatalytic upcycling of polyethylene terephthalate to commodity chemicals and H<sub>2</sub> fuel,” *Nat. Commun.*, vol. 12, no. 1, p. 4679, 2021, doi: 10.1038/s41467-021-25048-x.
- [114] M. Zhang, Y. Liu, B. Liu, Z. Chen, H. Xu, and K. Yan, “Trimetallic NiCoFe-Layered Double Hydroxides Nanosheets Efficient for Oxygen Evolution and Highly Selective Oxidation of Biomass-Derived 5-Hydroxymethylfurfural,” *ACS Catal.*, vol. 10, no. 9, pp. 5179–5189, May 2020, doi: 10.1021/acscatal.0c00007.
- [115] M. Li *et al.*, “Value-Added Formate Production from Selective Methanol Oxidation as Anodic Reaction to Enhance Electrochemical Hydrogen Cogeneration,” *ChemSusChem*, vol. 13, no. 5, pp. 914–921, Mar. 2020, doi: <https://doi.org/10.1002/cssc.201902921>.
- [116] X. Liu *et al.*, “Upcycling PET in parallel with energy-saving H<sub>2</sub> production via bifunctional nickel-cobalt nitride nanosheets,” *Nano Res.*, vol. 16, no. 4, pp. 4625–4633, 2023, doi: 10.1007/s12274-022-5085-9.
- [117] Y. Li, X. Wei, L. Chen, J. Shi, and M. He, “Nickel-molybdenum nitride nanoplate electrocatalysts for concurrent electrolytic hydrogen and formate productions,” *Nat.*

- Commun.*, vol. 10, no. 1, p. 5335, 2019, doi: 10.1038/s41467-019-13375-z.
- [118] M. Li *et al.*, “CoxP@NiCo-LDH heteronanosheet arrays as efficient bifunctional electrocatalysts for co-generation of value-added formate and hydrogen with less-energy consumption,” *J. Energy Chem.*, vol. 50, pp. 314–323, 2020, doi: <https://doi.org/10.1016/j.jechem.2020.03.050>.
- [119] H. Zhou *et al.*, “Electrocatalytic upcycling of polyethylene terephthalate to commodity chemicals and H<sub>2</sub> fuel,” *Nat. Commun. 2021 121*, vol. 12, no. 1, pp. 1–9, Aug. 2021, doi: 10.1038/s41467-021-25048-x.
- [120] M. Okan, H. M. Aydin, and M. Barsbay, “Current approaches to waste polymer utilization and minimization: a review,” *J. Chem. Technol. & Biotechnol.*, vol. 94, no. 1, pp. 8–21, 2019, doi: <https://doi.org/10.1002/jctb.5778>.
- [121] O. Guselnikova *et al.*, “‘Functional upcycling’ of polymer waste towards the design of new materials,” *Chem. Soc. Rev.*, vol. 52, no. 14, pp. 4755–4832, 2023, doi: 10.1039/D2CS00689H.
- [122] B. deBaskerville Darwent, *Bond dissociation energies in simple molecules*. US Government Printing Office Washington, DC, 1970.
- [123] J. Cui and E. Forssberg, “Mechanical recycling of waste electric and electronic equipment: a review,” *J. Hazard. Mater.*, vol. 99, no. 3, pp. 243–263, 2003, doi: [https://doi.org/10.1016/S0304-3894\(03\)00061-X](https://doi.org/10.1016/S0304-3894(03)00061-X).
- [124] K. Ragaert, L. Delva, and K. Van Geem, “Mechanical and chemical recycling of solid plastic waste,” *Waste Manag.*, vol. 69, pp. 24–58, 2017, doi:

<https://doi.org/10.1016/j.wasman.2017.07.044>.

- [125] I. Vollmer *et al.*, “Beyond Mechanical Recycling: Giving New Life to Plastic Waste,” *Angew. Chemie Int. Ed.*, vol. 59, no. 36, pp. 15402–15423, 2020, doi: <https://doi.org/10.1002/anie.201915651>.
- [126] J.-P. Lange, “Managing Plastic Waste—Sorting, Recycling, Disposal, and Product Redesign,” *ACS Sustain. Chem. Eng.*, vol. 9, no. 47, pp. 15722–15738, Nov. 2021, doi: [10.1021/acssuschemeng.1c05013](https://doi.org/10.1021/acssuschemeng.1c05013).
- [127] C. Jehanno *et al.*, “Critical advances and future opportunities in upcycling commodity polymers,” *Nature*, vol. 603, no. 7903, pp. 803–814, 2022, doi: [10.1038/s41586-021-04350-0](https://doi.org/10.1038/s41586-021-04350-0).
- [128] A. Lasia, “Hydrogen evolution reaction,” *Handb. fuel cells*, vol. 2, pp. 416–440, 2010.
- [129] J. Luo *et al.*, “Water photolysis at 12.3% efficiency via perovskite photovoltaics and Earth-abundant catalysts,” *Science (80-. )*, vol. 345, no. 6204, pp. 1593–1596, 2014, doi: [10.1126/science.1258307](https://doi.org/10.1126/science.1258307).
- [130] H. Wang *et al.*, “Bifunctional non-noble metal oxide nanoparticle electrocatalysts through lithium-induced conversion for overall water splitting,” *Nat. Commun.*, vol. 6, no. 1, p. 7261, 2015, doi: [10.1038/ncomms8261](https://doi.org/10.1038/ncomms8261).
- [131] N. Jiang, B. You, M. Sheng, and Y. Sun, “Electrodeposited Cobalt-Phosphorous-Derived Films as Competent Bifunctional Catalysts for Overall Water Splitting,” *Angew. Chemie Int. Ed.*, vol. 54, no. 21, pp. 6251–6254, 2015, doi: <https://doi.org/10.1002/anie.201501616>.

- [132] G.-F. Chen *et al.*, “Efficient and Stable Bifunctional Electrocatalysts Ni/NixMy (M = P, S) for Overall Water Splitting,” *Adv. Funct. Mater.*, vol. 26, no. 19, pp. 3314–3323, 2016, doi: <https://doi.org/10.1002/adfm.201505626>.
- [133] T. R. Cook, D. K. Dogutan, S. Y. Reece, Y. Surendranath, T. S. Teets, and D. G. Nocera, “Solar Energy Supply and Storage for the Legacy and Nonlegacy Worlds,” *Chem. Rev.*, vol. 110, no. 11, pp. 6474–6502, Nov. 2010, doi: [10.1021/cr100246c](https://doi.org/10.1021/cr100246c).
- [134] S. Trasatti, “Work function, electronegativity, and electrochemical behaviour of metals: III. Electrolytic hydrogen evolution in acid solutions,” *J. Electroanal. Chem. Interfacial Electrochem.*, vol. 39, no. 1, pp. 163–184, 1972, doi: [https://doi.org/10.1016/S0022-0728\(72\)80485-6](https://doi.org/10.1016/S0022-0728(72)80485-6).
- [135] D. H. Kweon *et al.*, “Ruthenium anchored on carbon nanotube electrocatalyst for hydrogen production with enhanced Faradaic efficiency,” *Nat. Commun.*, vol. 11, no. 1, p. 1278, 2020, doi: [10.1038/s41467-020-15069-3](https://doi.org/10.1038/s41467-020-15069-3).
- [136] J. Mahmood *et al.*, “An efficient and pH-universal ruthenium-based catalyst for the hydrogen evolution reaction,” *Nat. Nanotechnol.*, vol. 12, no. 5, pp. 441–446, 2017, doi: [10.1038/nnano.2016.304](https://doi.org/10.1038/nnano.2016.304).

# Chapter 2

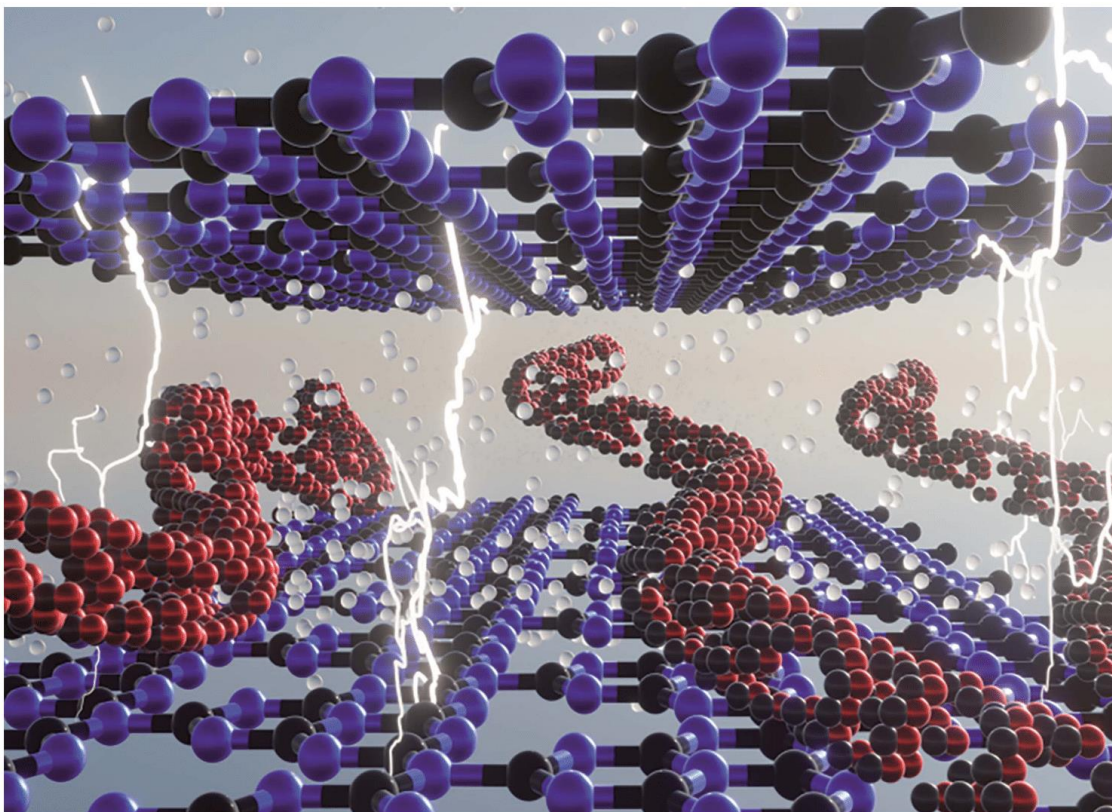
## Covalent Organic Framework Derived Synthesis of Ru Embedded in Carbon Nitride for Hydrogen and Oxygen Evolution Reactions

This chapter represents a collaborative effort with Dr. Vitaly Ordmosky's group from UCCS, Lille, who were responsible for synthesizing and characterizing the materials used in our study. The electrochemical analyses, however, were carried out by myself. Furthermore, I am pleased to note that this work has been published in RSC Journal of Materials Chemistry A with equal first authorship, and the publication details are as follows:

Tianyu Gao<sup>1#</sup>, Kilaparthi Sravan Kumar<sup>2#</sup>, Zhen Yan<sup>3</sup>, Maya Marinova<sup>4</sup>, Martine Trentesaux<sup>1</sup>, Mohammed A. Amin<sup>5</sup>, Sabine Szunerits<sup>2</sup>, Yong Zhou<sup>1</sup>, Vlad Martin-Diaconescu<sup>6</sup>, Sebastien Paul<sup>1\*</sup>, Rabah Boukherroub<sup>2\*</sup>, and Vitaly Ordmosky<sup>1\*</sup>

Reference: *J. Mater. Chem. A*, 2023,**11**, 19338-19348

DOI: <https://doi.org/10.1039/D3TA01362F>



Showcasing research from Unité de Catalyse et Chimie du Solide (UCCS) and Institut d'électronique de microélectronique et de nanotechnologie (IEMN), Université de Lille, Lille, France.

Covalent organic framework derived synthesis of Ru embedded in carbon nitride for hydrogen and oxygen evolution reactions

We present an innovative approach for the synthesis of highly dispersed low-valence Ru oxide nanoparticles in the form of nanowires between carbon nitride layers using pyrolysis of 2D CIN-1 covalent organic framework (COF) material with embedded Ru(II) complexes. The resulting electrocatalyst demonstrates exceptional efficiency in water electrolysis with lower overpotentials for both hydrogen and oxygen production in comparison with Pt and RuO<sub>2</sub> reference catalysts, respectively.

As featured in:



See S. Paul, R. Boukherroub, V. Ordonsky *et al.*, *J. Mater. Chem. A*, 2023, 11, 19338.

## Abstract

The hydrogen and oxygen evolution reactions (HER and OER) are two steps in electrochemical water splitting for conversion of electric power to chemical energy. The main challenge remains the development of efficient, stable and cheap electrocatalysts able to perform both reactions under alkaline conditions. Single atom Ru stabilized by nitrogen-doped carbon and RuO<sub>2</sub> are currently the materials of choice for HER and OER reactions, respectively. Here, we propose a strategy for preparation of Ru embedded in a carbon nitride matrix for efficient HER and OER reactions in KOH solution. It is based on the preparation of a covalent organic framework 2D CIN-1 structure with coordinated Ru<sup>II</sup>, producing Ru oxide nanoparticles with low valence Ru sites arranged in the form of nanowires between layers of graphitic carbon nitride after pyrolysis. The material demonstrates smaller overpotentials for HER and OER in comparison with benchmark Pt and RuO<sub>2</sub> catalysts, and high catalytic stability.

## 2.1. Introduction

Hydrogen (H<sub>2</sub>) is considered as a promising and preferred alternative to fossil fuels due to its high energy density of 120 kJ/g and eco-friendly emission. Electrocatalytic water splitting, an effective and environmentally-friendly technology for H<sub>2</sub> production, has attracted great attention over the last years [1-4] and is based on cathodic hydrogen evolution reaction (HER) and anodic oxygen evolution reaction (OER) [5]. Noble metal-based catalysts, especially Pt-based catalysts, are at the forefront in boosting the sluggish OER and HER kinetics and remain the benchmark materials for both reactions due to their favorable kinetics for HER and OER [6]. However, the high cost of Pt metal limits its consideration for commercial and large use applications for water splitting.

Over the last few decades, a large number of alternative electrocatalysts have been proposed, including non-noble metal and metal-free-based catalysts [7-11]. Ruthenium is one of the best Pt analogs as it possesses a similar metal hydride (M-H) bond strength of 65 kcal/mol,[12, 13] is available and five times cheaper than Pt. Various scientific reports revealed that the HER performance of Ru is comparable to or even better than that of Pt, in both neutral and alkaline media. Recently, Baek *et al.* synthesized Ru nanoparticles (~2 nm) uniformly dispersed on graphene nanoplatelets (Ru@GnP), and underlined the outstanding HER performance in both acidic and alkaline electrolytes with small overpotentials of 13 mV in 0.5M H<sub>2</sub>SO<sub>4</sub> and 22 mV in 1M KOH at a current density of 10 mA cm<sup>-2</sup>[14]. Feng *et al.* reported the electrochemical performance of ruthenium/N-doped carbon (Ru/CN), prepared by electrochemical polymerization of aniline on graphite foam (GF) and dipping the obtained aniline/GF in Ru salt, followed by subsequent pyrolysis of the Ru<sup>3+</sup>/aniline complex at 900 °C. The resulting material has shown excellent electrocatalytic HER activity with an overpotential of 21 mV (10 mA cm<sup>-2</sup>) in 1M KOH

[15]. Qiu *et al.* synthesized Ru-based electrocatalysts with abundant Ru active sites using bimetallic MOFs (CuRu-MOF) through pyrolysis and etching of Cu. The as-prepared ultrafine Ru nanoparticles anchored onto hierarchically porous carbon (Ru-HPC) exhibited outstanding HER activity with a low Tafel slope value of  $33.9 \text{ mV dec}^{-1}$ , even lower than commercial 20% Pt/C ( $41 \text{ mV dec}^{-1}$ ) [16].

Although the recent publications proposed the use of transition metals for OER [17], the rutile phase of ruthenium oxide ( $\text{RuO}_2$ ) still serves as a benchmark material for OER in both acidic and alkaline media [18, 19]. The OER activities have been studied for different particle sizes, different crystal structures, different degrees of hydration and electronic states [20-22].  $\text{RuO}_2$  is limited by its low anodic stability under acidic conditions, especially at high overpotentials as well as by its reduced energy density ( $\approx 400 \text{ Wh kg}^{-1}$ , theoretically), and related low mass activity [22].

Considering that Ru could be used for both HER and OER reactions, it would be highly desirable to develop a Ru-based electrocatalyst for efficient water splitting. Ru@ $\text{RuO}_2$  core-shell nanorods, synthesized by oxidation of Ru nanorods, demonstrated indeed high efficiency for both OER and HER reactions reaching overpotentials of 320 and 137 mV, respectively, at the current density of  $10 \text{ mA cm}^{-2}$  [23]. A possible strategy to improve the electrocatalytic performance would be through the design of catalysts containing highly dispersed Ru stabilized by nitrogen-doped carbon to provide both HER and OER properties of Ru at the same time. Ru-N bonding provides several important advantages in comparison with other materials related to favorable electronic structure of ruthenium, the synergistic effects between Ru and N-doped carbon in reducing water dissociation energy, improved adsorption properties of intermediate reactants and high stability of the Ru species avoiding metal sintering [24, 25].

Recently, solid-state pyrolysis of porous organic networks such as MOF was widely applied for the facile preparation of metal nanostructures incorporated in porous carbon materials [26-30]. Covalent organic frameworks (COFs) are a new type of microporous materials which are constructed by the covalent linkage of organic building blocks [31, 32]. Because of ordered pores, carbon-rich layers and diverse heteroatoms, COFs are promising precursors for the synthesis of carbon-based materials. Surprisingly, they have not been yet used for the preparation of carbon nitrides.

In this work, we synthesized a 2D imine-based COF with an incorporated Ru<sup>II</sup>-2-diphenylphosphinobenzaldehyde complex. The pyrolysis of this material at 500 °C under N<sub>2</sub> atmosphere produced highly dispersed RuO<sub>2</sub> nanoparticles containing low valence Ru sites between the layers of carbon nitride. The material provided a high activity for HER and OER in 1M KOH.

## 2.2. Experimental

### 2.2.1. Materials and reagents

RuCl<sub>3</sub>·H<sub>2</sub>O, 2-(diphenylphosphino)benzaldehyde (DBP), melamine, 1,3,5-triformylbenzene, 1,4-diaminobenzene, 1,4-dioxane and acetic acid were purchased from Sigma-Aldrich. Piparazinedicarbaldehyde, *N,N*-dimethylformamide (DMF), dry ethanol, acetone, dichloromethane (CH<sub>2</sub>Cl<sub>2</sub>) and tetrahydrofuran (THF) were procured from Alfa Aesar. Dimethyl sulfoxide (DMSO) was obtained from Acros Organics.

### 2.2.2. Synthesis of materials

**Ru-DBP:** The tube of Radleys Carousel Reactor was charged with RuCl<sub>3</sub>·xH<sub>2</sub>O (0.03 g), 2-(diphenylphosphino)benzaldehyde (DBP) (0.03 g) and dimethyl sulfoxide (DMSO, 12 mL). Then,

the tube was degassed with dry N<sub>2</sub> and refluxed at 180 °C for 72 h. After that, the precipitated black product was isolated by filtration and washed with dry ethanol, acetone, THF and dichloromethane sequentially. Finally, the product was dried at 100 °C for 48 h to obtain the desired powder Ru-DBP complex.

**Ru@CIN-1:** The tube of Radleys Carousel Reactor was charged with RuCl<sub>3</sub>·xH<sub>2</sub>O (0.03 g), 2-(diphenylphosphino)benzaldehyde (0.03 g), piparazinedicarbaldehyde (0.17 g), melamine (0.100 g) and DMSO (12 mL) according to the procedure of CIN-1 material synthesis [33]. The tube was degassed with dry N<sub>2</sub> and refluxed at 180 °C for 72 h in the inert atmosphere. After cooling to room temperature, the precipitated product was isolated by filtration and washed with dry ethanol, acetone, THF and dichloromethane sequentially. Finally, the product was dried at 100 °C for 48 h to obtain the desired powder **Ru@CIN-1**. Pure **CIN-1** was synthesized by the same method without the addition of RuCl<sub>3</sub>·xH<sub>2</sub>O and 2-(diphenylphosphino)benzaldehyde.

Ru@CIN-1 and pure CIN-1 were calcinated under N<sub>2</sub> atmosphere at 500 °C for 2 h to yield **Ru@g-CN<sub>x</sub>** and **g-CN<sub>x</sub>**, respectively.

### 2.2.3. Electrochemical methods

The electrocatalytic measurements were performed using a ModuLab-MTS electrochemical test station (Solartron, France) with a conventional three-electrode configuration consisting of a 3 mm diameter glassy carbon (GC) electrode coated with Ru@g-CN<sub>x</sub>, Saturated Calomel Electrode (SCE), Hg|Hg<sub>2</sub>Cl<sub>2</sub>, and Pt coil as the working, reference and counter electrodes, respectively. Before starting the experiments, an aqueous electrolyte solution (1M KOH) was degassed using nitrogen for at least 30 min. Further, linear sweep voltammetry (LSV) was performed at a scan rate of 5 mV s<sup>-1</sup> to record the polarization curves.

In order to determine the electrocatalytically-active surface area (ECSA), double-layer capacitance ( $C_{dl}$ ) was calculated by performing cyclic voltammetry (CV) at different scan rates in the non-Faradaic potential range (0.11 to 0.24V vs. RHE) of the material.  $C_{dl}$  ( $\mu\text{F cm}^{-2}$ ) value is determined from the slope of the current density ( $\text{mA cm}^{-2}$ ) as a function of the scan rate ( $\text{mV s}^{-1}$ ) plot. Electrochemical impedance spectroscopy (EIS) was performed at an AC amplitude of 10 mV in a frequency range from 1 kHz to 0.1 Hz at -0.03V vs. RHE. The long-term stability experiments were conducted using the chronopotentiometric technique at a constant current density of -10 mA  $\text{cm}^{-2}$ . The reference electrode (SHE) was calibrated to the reversible hydrogen electrode (RHE) according to the Nernst equation:

$$E (\text{RHE}) = E (\text{Hg/Hg}_2\text{Cl}_2) + (0.242 + 0.059 * \text{pH})$$

The pH of the electrolyte solution (1M KOH) was experimentally determined using mettler toledo pH meter and found to be 13.6 (average of three sets). Hence, we have used this value for calibration during all electrocatalytic experiments. All the electrochemical analyses were plotted without  $iR$  correction.

In order to prepare the catalyst-modified GC working electrode, 3 mg of the desired catalyst was dispersed in 1 mL of water by ultrasonication for 30 min and then 10  $\mu\text{L}$  of the catalyst suspension was drop-casted onto the GC electrode and dried at 60 °C overnight. Hence, the mass loading on the electrode surface was 0.042  $\text{mg.cm}^{-2}$ . Further, all the results were repeated at least three times to confirm the reproducibility of the material. The turnover frequency (TOF,  $\text{s}^{-1}$ ) measurements were carried out using the formula  $Q = \frac{I}{xnF}$ , where  $I$  is the current (A),  $x$  is a number of electrons transferred during HER (2) and OER (4),  $F$  is the faraday constant (96485C) and  $n$  is the number of active sites calculated by cyclic voltammograms [34].

## 2.3 Results and Discussion

### 2.3.1. COF derived synthesis of Ru@g-CN<sub>x</sub>

A covalent organic framework CIN-1 was synthesized by condensation of piparazinedicarbaldehyde with melamine (**Figure 1**). The CHNO analysis revealed the absence of oxygen in CIN-1 with a composition close to the theoretical values (C, 50.5 %; N, 44.2 %; H, 5.3 %) for condensation of an aldehyde with melamine (**Table 1**). The incorporation of 0.4 wt.% of Ru was achieved by the addition of 2-(diphenylphosphino)benzaldehyde as a ligand coordinating with RuCl<sub>3</sub> during the crystallization of CIN-1, keeping the composition similar to that of CIN-1.

The pyrolysis of the prepared COF materials by treatment of CIN-1 and Ru@CIN-1 at 500 °C under N<sub>2</sub> flow was used to prepare graphitic materials. The chemical analysis of g-CN<sub>x</sub> and Ru@g-CN<sub>x</sub> revealed a decrease in the hydrogen content and an increase in the contribution of carbon in comparison with nitrogen (**Table 1**), which could be assigned to the partial deamination of the material. The increase in the oxygen content could be ascribed to partial oxidation of the material during contact with air after pyrolysis. The content of Ru in Ru@g-CN<sub>x</sub> increased to 0.9 wt.% during pyrolysis due to a decrease in the contribution of C, H and N in the material. X-ray diffraction (XRD) analysis of pure CIN-1 (**Figure 2a**) showed only one broad peak at 20° corresponding to the (001) reflection related to interplanar stacking [35]. As reported in the literature, microporous polymers based on Schiff base chemistry are usually amorphous [36]. It is interesting to note that Ru@CIN-1 displayed additionally a sharp peak at 11.9° ascribed to the (100) inplanar structural packing of the CIN-1. The increased crystallinity could be assigned to the incorporation of the Ru-DBP complex into the CIN-1 structure which increases the size of the network layer [37]. The XRD patterns of g-CN<sub>x</sub> and Ru@g-CN<sub>x</sub>, after pyrolysis (**Figure 2a**), exhibited a distinct shift of the diffraction peak to 26.3° in comparison with the parent materials;

this peak is typical of the (002) diffraction plane for interlayer stacking in graphitic carbon nitrides with the distance between layers of about 0.34 nm, according to Bragg equation [38].

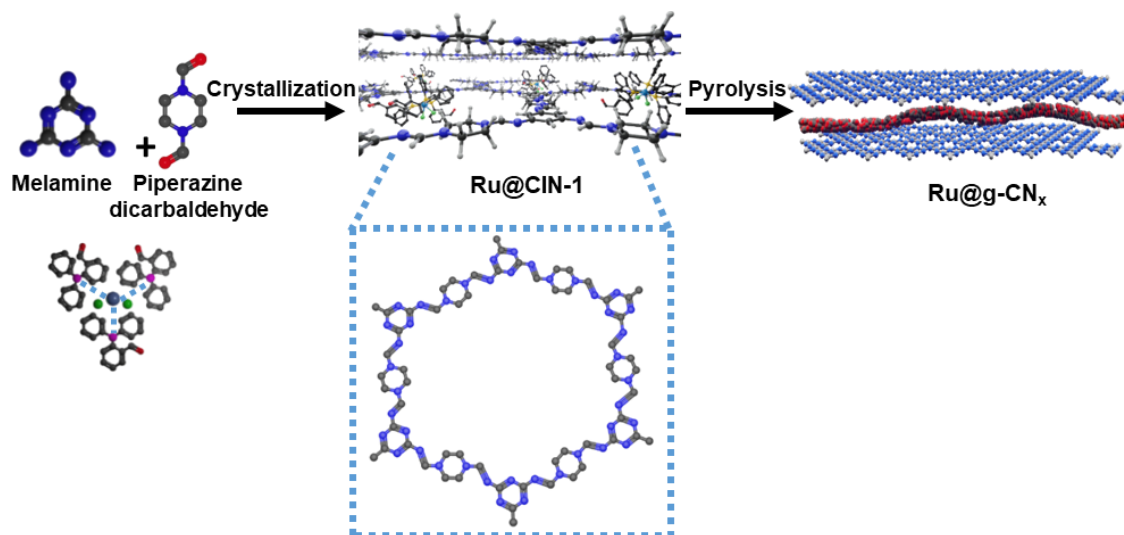


**Figure 1.** Schematic illustration of the synthesis of Ru carbon nitride catalyst.

As shown in **Figure 2b**, the FTIR spectra of pure CIN-1 and Ru@CIN-1 depicted distinct peaks of triazine ring vibrations at 1540, 1490 and 1340  $\text{cm}^{-1}$  [33, 39]. The FTIR spectrum of Ru-DBP complex comprised peaks at 1967  $\text{cm}^{-1}$  assigned to coordinated C=O stretching vibration, and 1630 and 1400  $\text{cm}^{-1}$  due to carbon-carbon stretching vibrations of the aromatic rings [40]. The disappearance of C=O group vibrations and the appearance of benzene aromatic ring vibrations during the crystallization of Ru@CIN-1 indicated the successful incorporation of Ru-DBP complex into the CIN-1 structure. FTIR spectra of g-CN<sub>x</sub> and Ru@g-CN<sub>x</sub> (**Figure 2b**) revealed the appearance of bands at 1677 and 1579  $\text{cm}^{-1}$ , and a group of peaks in the range of 1250-1500  $\text{cm}^{-1}$  ascribed respectively to C=N and aromatic C-N stretching vibrations [41, 42].

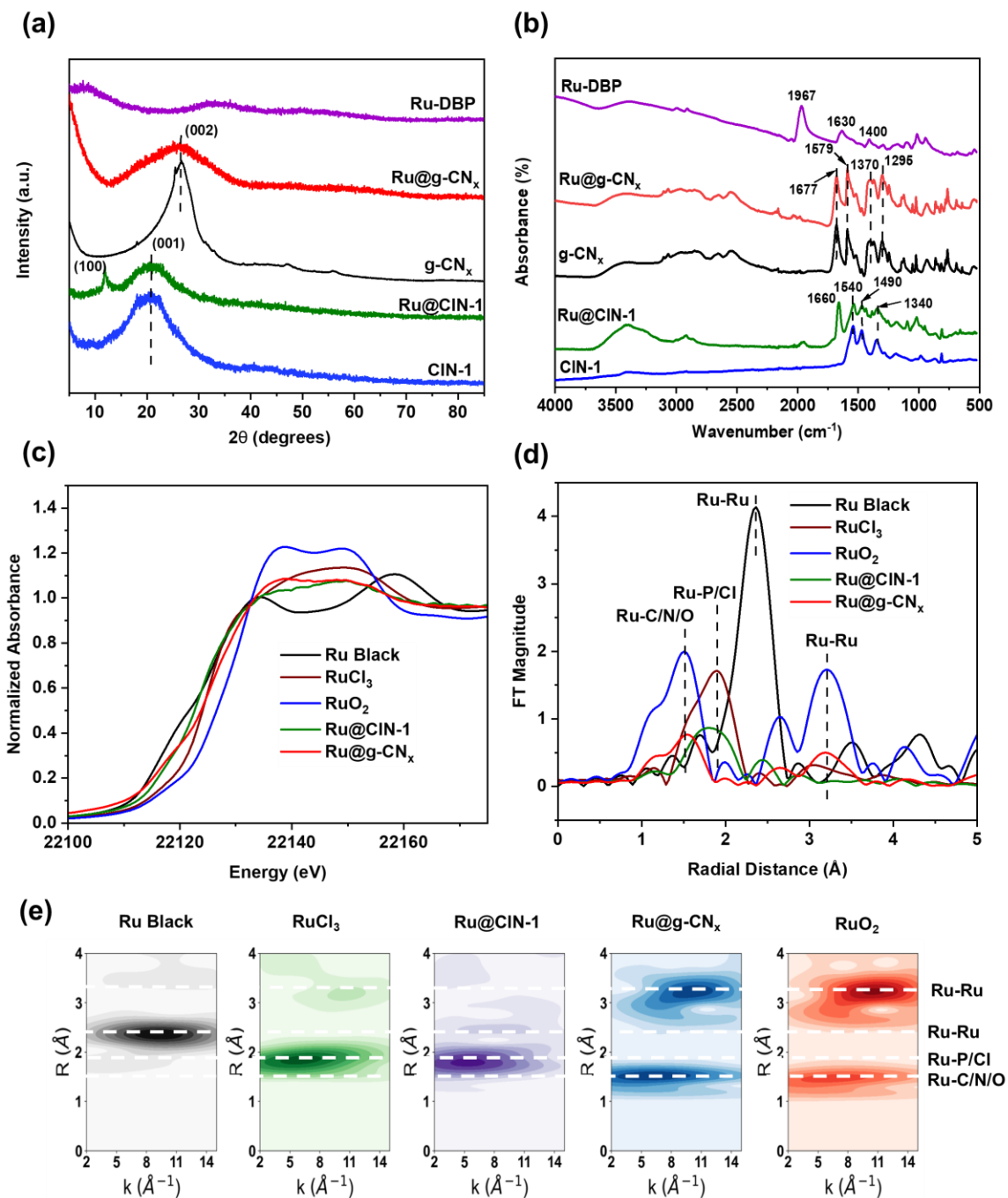


**Figure 2.** (a) XRD, (b) FTIR, (c) Ru K-edge XANES spectra, (d) Fourier transformed  $\chi(k)$ -functions of the EXAFS spectra and (e) Cauchy WT-EXAFS of Ru-DBP, Ru@CIN-1, CIN-1, Ru, RuO<sub>2</sub>, g-CN<sub>x</sub> and Ru@g-CN<sub>x</sub>.

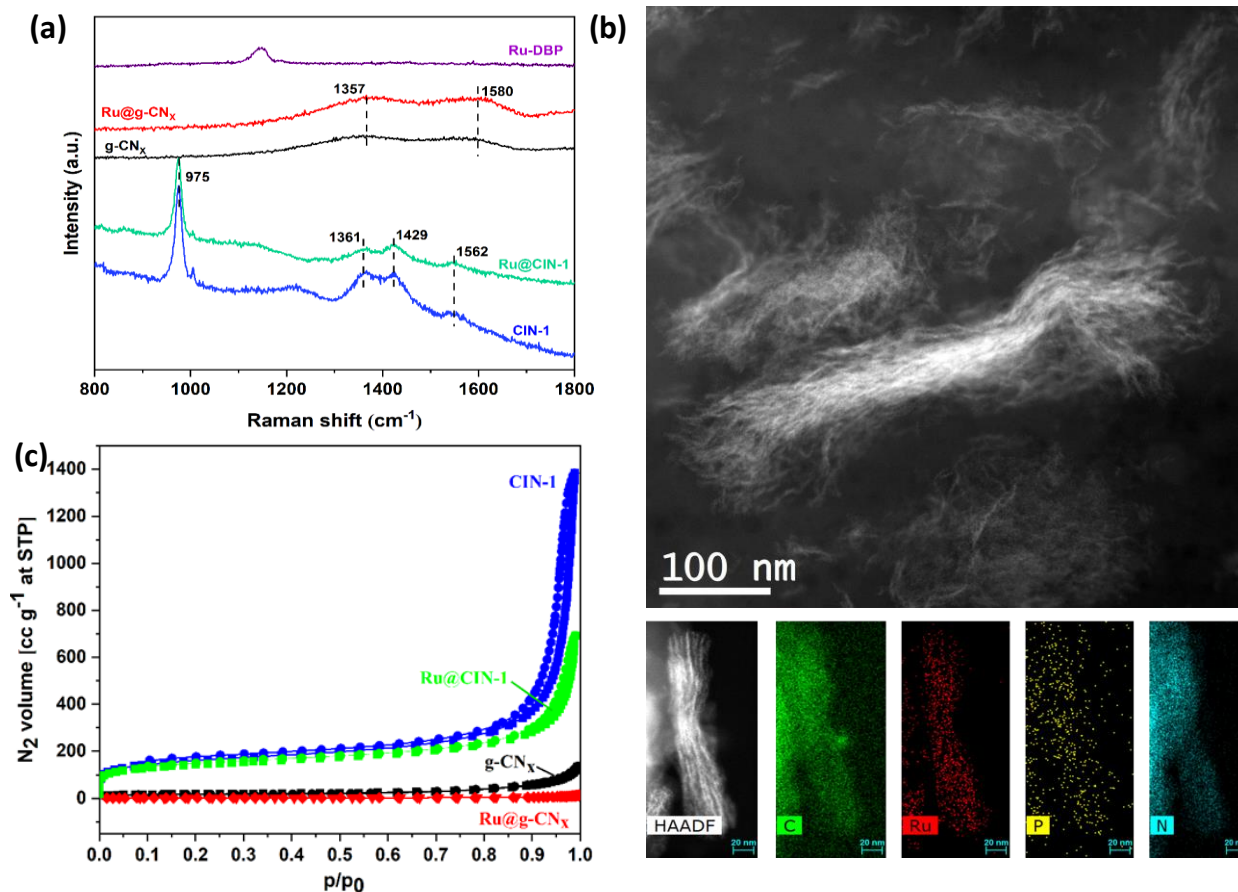


**Figure 3.** (a) Raman spectra of Ru-DBP, Ru@CIN-1, CIN-1, Ru@g-CN<sub>x</sub> and g-CN<sub>x</sub>. (b) TEM images of Ru@g-CN<sub>x</sub> with EDX mapping of C, N, P and Ru elements. (c) N<sub>2</sub> adsorption-desorption isotherms of Ru@CIN-1, CIN-1, Ru@g-CN<sub>x</sub> and g-CN<sub>x</sub>.

Raman spectra of pure CIN-1 and Ru@CIN-1 (**Figure 3a**) confirmed FTIR results by the presence of characteristic features of the triazine ring (975 cm<sup>-1</sup>), piperazine ring (1361 & 1429 cm<sup>-1</sup>) and imine (C=N) stretching vibrations (1562 cm<sup>-1</sup>) [39]. This differs from the Raman plots of g-CN<sub>x</sub> and Ru@g-CN<sub>x</sub> which comprised the characteristics D- and G-bands at around 1357 and 1580 cm<sup>-1</sup> related to the lattice defects caused by graphite edges with sp<sup>3</sup> bonds of carbon and graphitic phase containing sp<sup>2</sup> bonds of carbon, respectively [29, 43, 44].

**Table 1.** Physical characteristics of CIN-1, g-CN<sub>x</sub>, Ru@CIN-1 and Ru@g-CN<sub>x</sub>.

Materials	Composition (wt.%)						S <sub>BET</sub> (m <sup>2</sup> g <sup>-1</sup> )	Pore volume (cm <sup>3</sup> g <sup>-1</sup> )
	C	O	N	H	P	Ru		
CIN-1	47.0	–	48.7	4.3	–	–	419.5	0.26
Ru@CIN-1	47.0	0.1	47.5	4.3	0.1	0.4	400.2	0.20
g-CN <sub>x</sub>	53.0	10.7	33.9	2.4	–	–	61.8	0.21
Ru@g-CN <sub>x</sub>	39.7	10.9	33.9	2.5	1.2	0.9	23.9	0.18

Transmission electron microscopy (TEM) images demonstrated that pyrolysis resulted in the arrangement of Ru nanoparticles in the form of nanowires between the layers of graphitic carbon nitride for Ru@g-CN<sub>x</sub> in comparison with the generation of large carbon nitride particles for g-CN<sub>x</sub> material (**Figure 3b**). These Ru nanowires extend to the size of 500 nm and consist of Ru nanoparticles localized between carbon nitride layers, according to the proposed structure of the initial material. Elemental mapping demonstrated that Ru, N, P and C are present together in the material and pyrolysis does not affect the distribution of elements.

The CIN-1 and Ru@CIN-1 materials exhibited a type II N<sub>2</sub> adsorption isotherm with sharp uptake below 0.05 P/P<sub>0</sub>, indicating the presence of micropores between the layers and a second uptake at higher relative pressure originating from the textural pores generated by COF nanoparticles (**Figure 3c**). The Brunauer-Emmett-Teller (BET) surface area values of CIN-1 and Ru@CIN-1 are 419 and 400 m<sup>2</sup> g<sup>-1</sup>, respectively, which match well the literature [45] (**Table 1**). Pyrolysis induced a significant decrease of N<sub>2</sub> adsorption in comparison with the parent materials reaching 62 and 23 m<sup>2</sup>/g for g-CN<sub>x</sub> and Ru@g-CN<sub>x</sub>, respectively, which are usual values for carbon nitride materials [46, 47] (**Figure 3c**).

The electronic state of Ru was studied by X-ray absorption spectroscopy (XAS) analysis (**Figures 2c-e**). The Ru@CIN-1 X-ray absorption near edge structure (XANES) and Extended X-ray absorption fine structure (EXAFS) spectra featured a similar profile to that of RuCl<sub>3</sub> although

the Ru centers are effectively more reduced in Ru@CIN-1 compared to RuCl<sub>3</sub>. The pyrolysis produced Ru@g-CN<sub>x</sub> possessing a spectrum with a shape reminiscent of that of RuO<sub>2</sub>, with significantly lower intensity and a broader white line. Similarly, Fourier Transform (FT) EXAFS of the Ru@g-CN<sub>x</sub> sample showed patterns, consistent with the presence of RuO<sub>2</sub>, of lower intensity, equivalent to ~30% RuO<sub>2</sub> character. Furthermore, the intensity ratios of the first coordination shell attributable to Ru-C/N/O at ~1.97 Å in the sample relative to the longer scattering shells in the 3 to 6 Å range of 1.2:1 relative to the 1:1 found in the RuO<sub>2</sub> reference inferred the presence of single Ru centers most probably stabilized by N of carbon nitride (**Figure 2**). Together with the low coordination number, and rising edge energies indicating an average Ru oxidation of +0.5 for Ru@g-CN<sub>x</sub>, the data are consistent with low valence Ru centers, [48] having a low coordination number together with a RuO<sub>2</sub> lattice having O vacancies. XPS Ru 3d analysis confirms the presence of Ru<sup>2+</sup> in Ru@CIN-1 and Ru-DBP with peaks at 281.4 and 280.9 eV, respectively (**Figure 6c**). Ru@g-CN<sub>x</sub> has two doublets with BE Ru 3d<sub>5/2</sub> 280.7 and 282.4 eV, which can be assigned to RuO<sub>2</sub> and Ru(OH)<sub>3</sub>, respectively.

To conclude, the characterization results demonstrated Ru incorporation in the presence of triphenylphosphine ligand in the structure of CIN-1 material. Pyrolysis of COF-based materials led to the generation of graphitic carbon nitride materials with RuO<sub>2</sub> nanowires containing Ru in a low valence state.

### 2.3.2. Electrochemical properties

The performance of the Ru@g-CN<sub>x</sub> coated on GC electrode for HER in potassium hydroxide (1M KOH) solution was investigated by performing LSV polarizations at a scan rate of 5 mV s<sup>-1</sup>. The overpotential *versus* the reversible hydrogen electrode (RHE) at 10 mA cm<sup>-2</sup>, the anticipated current density for a 12.3% efficient solar water-splitting device, was used to assess

the HER performance. **Figures 4a** revealed that Ru@g-CN<sub>x</sub> had superior electrocatalytic activity by requiring only 53.2 mV for driving a current density of 10 mA cm<sup>-2</sup>, which is far better than those of RuO<sub>2</sub>, g-CN<sub>x</sub>, Ru@CIN-1 and CIN-1.

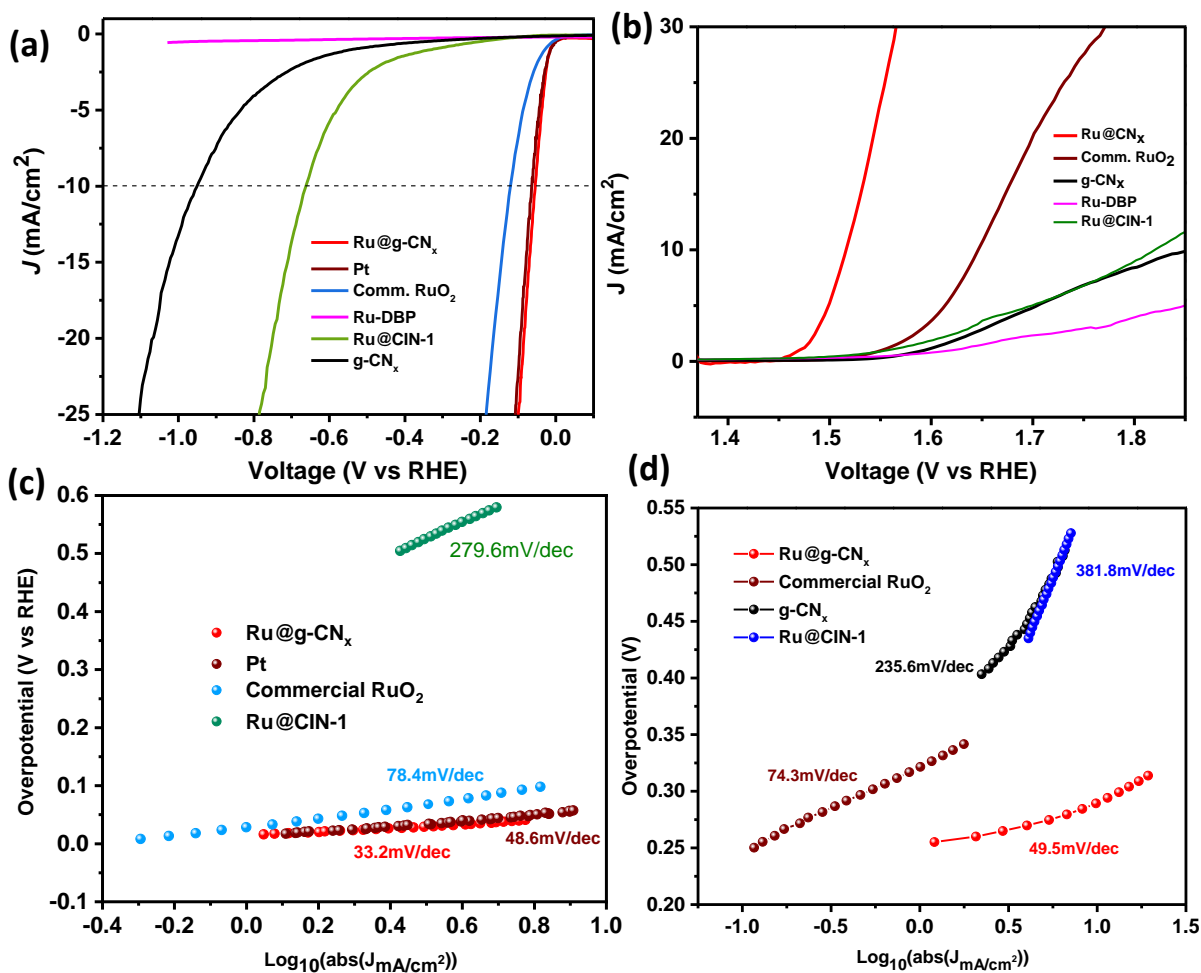


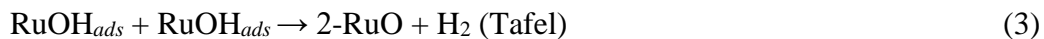
**Figure 4.** (a) HER polarization curves of Pt, Ru@g-CN<sub>x</sub>, commercial RuO<sub>2</sub>, Ru@CIN-1, Ru-DBP and g-CN<sub>x</sub> acquired at a scan rate of 5 mV s<sup>-1</sup> in 1M KOH solution. (b) OER polarization curves of commercial RuO<sub>2</sub>, Ru@g-CN<sub>x</sub>, Ru@CIN-1 and g-CN<sub>x</sub> (c) Tafel plots and slope values of RuO<sub>2</sub>, Pt, Ru@g-CN<sub>x</sub>, Ru@CIN-1 and g-CN<sub>x</sub> derived from cathodic polarization LSV plots of (a). (d) Tafel plots and slope values of Ru@g-CN<sub>x</sub>, RuO<sub>2</sub>, Ru@CIN-1 and g-CN<sub>x</sub> derived from anodic polarization LSV plots of (b).

**Table 2.** Comparison table of Ru based electrocatalysts for HER in 1M KOH

Catalyst	Overpotential (At 10mA cm <sup>-2</sup> )	Tafel slope (mV dec <sup>-1</sup> )	Stability	References
<b>Ru@C<sub>2</sub>N</b>	17	38	Not given	50
<b>RuP<sub>x</sub>@NPC</b>	74	70	10 h	51
<b>Ru<sub>2</sub>P@PNC/CC-900</b>	50	66	10 h	52
<b>RuP<sub>2</sub>@NPC</b>	52	69	10 h	53
<b>Ni<sub>1.5</sub>Co<sub>1.4</sub>P@Ru</b>	52	50	6 h	54
<b>Ru/C</b>	24	33	Not given	55
<b>ah-RuO<sub>2</sub>@C</b>	63	62	100h	56
<b>NiCoP@rGO</b>	59	50	18 h at 250 mV static potential	57
<b>RuCo alloy</b>	28	31	Not given	58
<b>Ru-doped CuO/MoS<sub>2</sub></b>	198	113	15 h	59
<b>4H/fcc Ru NTs</b>	23	29.4	Not given	60
<b>RuND/C</b>	43.4	49	2.5 h at -0.05 V	61
<b>Pd@RuNRs</b>	30	30	12 h at -0,031 V	62
<b>Cu<sub>2-x</sub>S@Ru NPs</b>	82	48	12 h at -0.05 V	63
<b>Ru<sub>2</sub>Ni<sub>2</sub>SNs</b>	40	23.4	Not given	64
<b>Ru@g-CN<sub>x</sub></b>	<b>53.2</b>	<b>33.2</b>	<b>45 h at -10 mA cm<sup>-2</sup></b>	<b>This work</b>

This interface also displayed better catalytic activity than the benchmarked Pt electrode exhibiting an overpotential of 63.7 mV at 10 mA cm<sup>-2</sup> and comparable to the performance of the most efficient materials reported in the literature [49] (**Table 2**).

The Tafel slope analysis gave us profound insight into the kinetic analysis of HER derived from the LSV plots usually with lower Tafel slopes attributed to faster kinetics. **Figure 4c** illustrates the Tafel slope of the Ru@g-CN<sub>x</sub> electrode, which is close to 30 mV dec<sup>-1</sup>, indicating a faster HER rate and Tafel-Volmer mechanism (1, 3) with electrochemical H<sub>2</sub> desorption as the rate-determining step in the HER process. The Tafel slopes values of Ru@CIN-1 (279.6 mV dec<sup>-1</sup>) and RuO<sub>2</sub> (78.4 mV dec<sup>-1</sup>) were also determined from the LSV curves, which are significantly higher than Ru@g-CN<sub>x</sub>, suggesting that the HER proceeds via a primary discharge step.



Furthermore, the oxygen evolution performance of Ru@g-CN<sub>x</sub> was assessed in 1.0 M KOH aqueous solution in a three-electrode system. It could be seen from the LSV curves of Ru@g-CN<sub>x</sub>, RuO<sub>2</sub>, Ru@CIN-1 and g-CN<sub>x</sub> that the oxygen evolution takes place at a much lower overpotential of 280 mV for Ru@g-CN<sub>x</sub> at a benchmark current density of 10 mA cm<sup>-2</sup>, as shown in **Figure 4**.

**Table 3.** Comparison table of Ru based electrocatalysts for OER in 1M KOH

Catalyst	Overpotential (At 10mA cm <sup>-2</sup> )	Tafel slope (mV dec <sup>-1</sup> )	Stability	References
0.27-RuO <sub>2</sub> @C	250	68	100 h	56
Ru <sub>2</sub> Ni <sub>2</sub> SNs/C	310	75	Not given	64
Ru-doped CuO/MoS <sub>2</sub>	201	229	20 h	59
NiCoP/rGO	270	65.7	18 h at 50mA cm <sup>-2</sup>	57
RuO <sub>2</sub> /N-C	280	56	18h at 1.5 V	66
NiFeRu-LDH	225	32.4	10 h at 10 mA cm <sup>-2</sup>	67
Ni <sub>1.25</sub> Ru <sub>0.75</sub> P	340	Not given	20 h at 1.57 mA cm <sup>-2</sup>	68
RuIrO <sub>x</sub>	250	50	Not given	69
<b>Ru@g-CN<sub>x</sub></b>	<b>280</b>	<b>49.5</b>	<b>45 h at 10 mA cm<sup>-2</sup></b>	<b>This work</b>

The Tafel slope value of Ru@g-CN<sub>x</sub> is around 49.5 mV dec<sup>-1</sup>, lower than that of commercial RuO<sub>2</sub> (74.3 mV dec<sup>-1</sup>), Ru@CIN-1 (381.8mV dec<sup>-1</sup>) and g-CN<sub>x</sub> (235.6 mV dec<sup>-1</sup>), which states that the kinetics of Ru@g-CN<sub>x</sub> for water oxidation reaction follows the Volmer–Heyrovsky reaction pathway (**Figure 4**). The Ru@g-CN<sub>x</sub> catalyst features a performance comparable to that of the most efficient materials for OER [65] (**Table 3**).

The result was further supported by the Nyquist plots, showing that Ru@g-CN<sub>x</sub> has enhanced electron transfer ability compared to Ru@CIN-1 and g-CN<sub>x</sub>, as shown in **Figure 5**. The three samples exhibited comparable solution resistance (R<sub>s</sub>) values, as shown in EIS Nyquist graphs, but different charge transfer resistance (R<sub>ct</sub>) values. The sequence of HER activity is well supported

by the fact that Ru@g-CN<sub>x</sub> owns the smallest R<sub>ct</sub> of 45.8 Ω and Ru@CIN-1 and g-CN<sub>x</sub> displayed the largest R<sub>ct</sub> values. The smallest charge transfer implies fast electron transfer to the interface during the HER or OER, which, in turn, guarantees better catalytic activity.

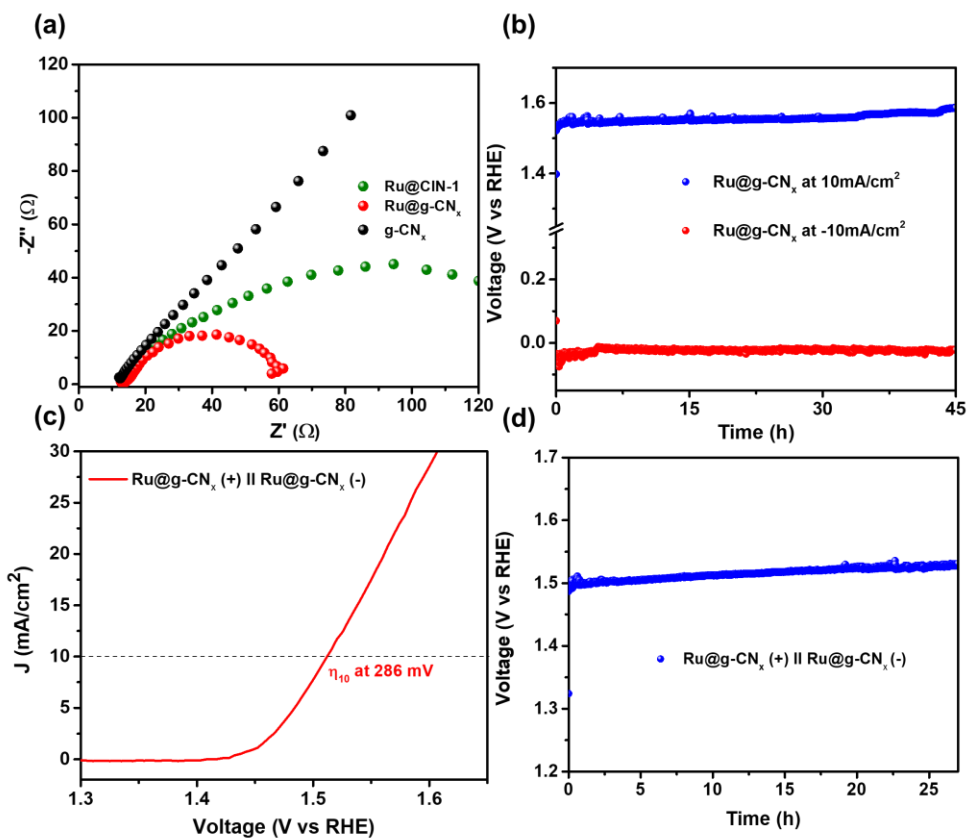


**Figure 5.** (a) Nyquist plots of various materials recorded in the range of 1 KHz to 0.1Hz at a constant potential of 30 mV vs. RHE at 10 mV amplitude. (b) Chronopotentiometric plots of Ru@g-CN<sub>x</sub> at a current density of 10 mA cm<sup>-2</sup> and -10 mA cm<sup>-2</sup> for OER and HER, respectively in 1M KOH. (c) LSV plot of overall water splitting in 1M KOH using Ru@g-CN<sub>x</sub> as both anode and cathode. (d) Chronoamperometric measurements of overall water splitting in 1M KOH aqueous solution at a constant current density of 10 mA cm<sup>-2</sup> using Ru@g-CN<sub>x</sub> as both anode and cathode.

LSV measurements of the catalysts were subsequently carried out in the presence of blocking ligands like thiocyanate ion (SCN<sup>-</sup>) to identify the HER-active centers of the Ru@g-CN<sub>x</sub>.

According to **Figure 6a** the Ru@g-CN<sub>x</sub> electrocatalyst's LSV curve revealed a sharp cathodic shift when SCN<sup>-</sup> is present, indicating that Ru particles serve as the active sites.

For the practical application of any catalyst, stability is one of the key factors being judged. The long-term stability of the Ru@g-CN<sub>x</sub> catalyst was probed by potential–time plots in an alkaline environment. The chronopotentiometric plots of the Ru@g-CN<sub>x</sub> catalyst performed in 1.0 M KOH aqueous solution at current densities of -10 mA cm<sup>-2</sup> and 10 mA cm<sup>-2</sup> for HER and OER, respectively, are depicted in **Figure 5**. After constant current density for 45 h, a limited decline (about 3%) of the catalyst performance for OER was registered, while no obvious decrease in performance was observed during the HER stability test. This robustness indicates that the catalyst is by far one of the best catalysts reported for water splitting. The analysis of hydrogen and oxygen production showed that Ru@g-CN<sub>x</sub> achieved a Faradaic efficiency (FE) of almost 100% for actual water splitting, i.e. (99.78 and 99.73% for the HER and OER, respectively) (**Figure 6b**). It is interesting to note that Ru according to XPS analysis is still in the form of mixture of RuO<sub>2</sub> and Ru(OH)<sub>3</sub> after OER reaction, however, it is partially reduced to metallic Ru after HER reaction (**Figure 6c**). The change of the oxidation state to adapt for the target reaction explains high efficiency in both HER and OER reactions. A variety of 2D or 1D metal nanostructured hydroxides/oxides of transition metals have been used as well for both HER and OER [70, 71].

In order to understand the enhancement of electrocatalytic activity during HER and OER for Ru@g-CN<sub>x</sub> compared to Ru@CIN-1 and g-CN<sub>x</sub>, the electrochemical active surface areas (ECSAs) were determined from the electrical double-layer capacitance ( $C_{dl}$ ). Cyclic voltammograms were measured in a non-Faradaic potential region between 0.1 to 0.25 V vs. RHE at different scan rates. Theoretically, it is acknowledged that the ECSA is proportional to its  $C_{dl}$  value for electrocatalysts of similar composition.

The  $C_{dl}$  values of Ru@g-CN<sub>x</sub> (9.1 mF cm<sup>-2</sup>), g-CN<sub>x</sub> (0.25 mF cm<sup>-2</sup>), CIN-1 (0.75 mF cm<sup>-2</sup>) were calculated from the slope of the straight line of the current density vs. scan rate curves in **Figure 6d**. Hence, the ECSA experiments revealed that the Ru@g-CN<sub>x</sub> catalyst had the highest number of active sites caused by the lattice defects. This explains the catalytic behavior of the catalyst. The ECSA-normalized LSV curves for both HER and OER were plotted to understand the intrinsic catalytic activity of the samples. In **Figure 6e, 6f** we see that in both HER and OER, Ru@g-CN<sub>x</sub> has higher catalytic activity than the precursor compounds. Due to the robust catalytic activity of the Ru@g-CN<sub>x</sub>, we were motivated to perform the overall water splitting in a 2-electrode system at 10 mA cm<sup>-2</sup> for 26 h, as shown in **Figure 5**. The LSV plot of the system recorded an overpotential of just 286 mV vs. RHE at a scan rate of 5 mV s<sup>-1</sup>.

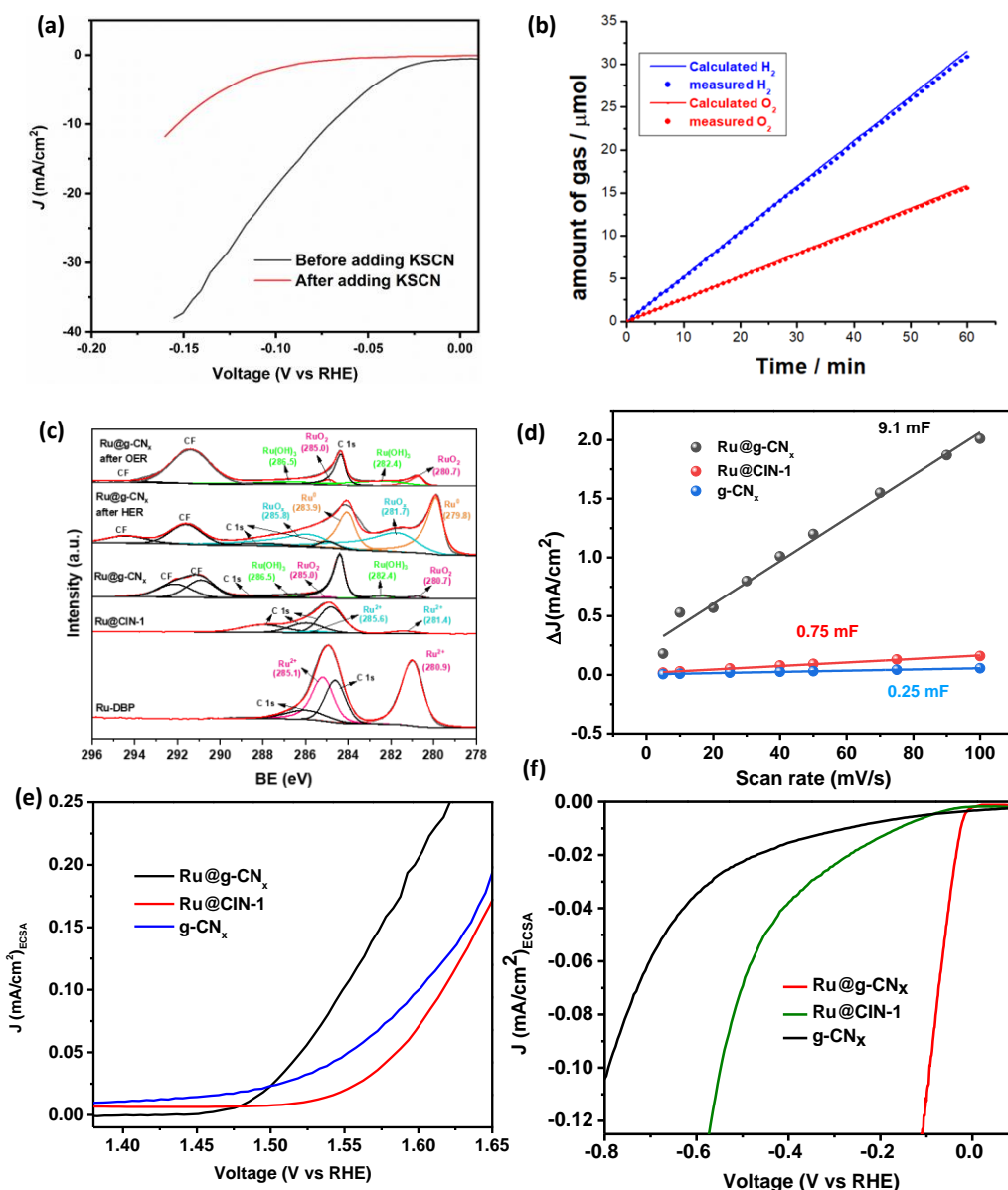


**Figure 6.** (a) LSV cathodic polarization curves of Ru@g-CN<sub>x</sub> in 1M KOH electrolyte solution before and after adding KSCN. (b) Faradaic efficiency measurements for both HER and OER by the best performing catalyst (Ru@g-CN<sub>x</sub>) in 1 M KOH. The electrode was held at -1.0 V vs. RHE (for the HER) and +1.0 V vs. RHE (for the OER) for 1 h in 1.0 M KOH solutions at 25 °C. (c) XPS 3d Ru spectra of Ru-DBP, Ru@CIN-1, Ru@g-CN<sub>x</sub> before and after HER and OER reaction (d) Variation of the double layer charging (e,f) ECSA-normalized LSV curves of HER polarization curves and OER polarization curves.

The chronopotentiometric plot showed that the catalyst had a good performance at a constant supply of  $10 \text{ mA cm}^{-2}$  in 1M KOH electrolyte solution with limited degradation of 1.35% after 26 h. The electrolyzer only required a cell voltage of 1.51 V to generate a current density of  $10 \text{ mA cm}^{-2}$ , which is quite outstanding and comparable to the newly announced state-of-the-art materials for total water splitting (**Table 4**).

**Table 4.** Comparison table of some excellent electrocatalysts for overall water splitting in 1M KOH

Catalyst	Electrolyte	Cell voltage (At $10 \text{ mA cm}^{-2}$ )	References
RuCu NSs	1 M KOH	1.49V	72
NC-CNT/CoP	1M KOH	1.63 V	73
Mo-Co <sub>9</sub> S <sub>8</sub> @C	1M KOH	1.56V	74
Ru-NiFe-P	1M KOH	1.47V	75
Co <sub>9</sub> S <sub>8</sub> -NSC@Mo <sub>2</sub> C	1M KOH	1.61	76
Pt-CoS <sub>2</sub> /CC	1M KOH	1.55	77
RuTe <sub>2</sub> -400	1M KOH	1.57 V	78
Ru-NiCoP/NF	1M KOH	1.515 V	79
<b>Ru@g-CN<sub>x</sub></b>	1M KOH	1.51V	<b>This work</b>

## 2.4. Conclusion

In summary, we demonstrated the synthesis of a novel functional Ru electrocatalyst embedded in graphite carbon nitride prepared by pyrolysis of a covalent organic framework incorporated Ru complex. It resulted in the generation of Ru oxide nanowires with a low valence state of Ru between the layers of graphitic carbon nitride after pyrolysis. The resulting material exhibited a very low overpotential of just 53.2 mV to achieve a current density of  $10 \text{ mA cm}^{-2}$  and a Tafel slope of  $33.2 \text{ mV dec}^{-1}$  for HER in an alkaline medium (1M KOH). In addition, the catalyst performed very well during OER with an overpotential of only 280 mV at  $10 \text{ mA cm}^{-2}$  and a low

Tafel slope of  $49.5 \text{ mV dec}^{-1}$ , exceeding the performance of commercially available  $\text{RuO}_2$ . The improved catalytic activity was attributed to the generation of a large number of active sites, as witnessed by electrochemical active surface area and charge transfer resistance results from EIS results. Further, chronopotentiometry measurements concluded that the catalyst is highly stable in a corrosion-free environment for at least 45 h producing both hydrogen and oxygen. Furthermore, the robustness of the developed electrocatalyst was demonstrated in full water splitting configuration with a slight degradation of 1.35% for at least 26 h for delivering a current density of  $10 \text{ mA cm}^{-2}$ .

## References

- [1] H. Ishaq, I. Dincer, and C. Crawford, "A review on hydrogen production and utilization: Challenges and opportunities," *International Journal of Hydrogen Energy*, vol. 47, no. 62, pp. 26238-26264, 2022/07/22/ 2022.
- [2] P. J. Megía, A. J. Vizcaíno, J. A. Calles, and A. Carrero, "Hydrogen Production Technologies: From Fossil Fuels toward Renewable Sources. A Mini Review," *Energy & Fuels*, vol. 35, no. 20, pp. 16403-16415, 2021/10/21 2021.
- [3] L. Schlapbach and A. Züttel, "Hydrogen-storage materials for mobile applications," *Nature*, vol. 414, no. 6861, pp. 353-358, 2001/11/01 2001.
- [4] J. A. Turner, "Sustainable Hydrogen Production," *Science*, vol. 305, no. 5686, pp. 972-974, 2004/08/13 2004.
- [5] W. Zhou *et al.*, "Recent developments of carbon-based electrocatalysts for hydrogen evolution reaction," *Nano Energy*, vol. 28, pp. 29-43, 2016/10/01/ 2016.
- [6] M. Carmo, D. L. Fritz, J. Mergel, and D. Stolten, "A comprehensive review on PEM water electrolysis," *International Journal of Hydrogen Energy*, vol. 38, no. 12, pp. 4901-4934, 2013/04/22/ 2013.
- [7] S. H. Ahn *et al.*, "Electrodeposited Ni dendrites with high activity and durability for hydrogen evolution reaction in alkaline water electrolysis," *Journal of Materials Chemistry*, 10.1039/C2JM31439H vol. 22, no. 30, pp. 15153-15159, 2012.
- [8] X. Wen, X. Yang, M. Li, L. Bai, and J. Guan, "Co/CoOx nanoparticles inlaid onto nitrogen-doped carbon-graphene as a trifunctional electrocatalyst," *Electrochimica Acta*, vol. 296, 11/01 2018.

- [9] A. Phuruangrat, D. J. Ham, S. J. Hong, S. Thongtem, and J. S. Lee, "Synthesis of hexagonal WO<sub>3</sub> nanowires by microwave-assisted hydrothermal method and their electrocatalytic activities for hydrogen evolution reaction," *Journal of Materials Chemistry*, 10.1039/B918783A vol. 20, no. 9, pp. 1683-1690, 2010.
- [10] R. Subbaraman *et al.*, "Trends in activity for the water electrolyser reactions on 3d M(Ni,Co,Fe,Mn) hydr(oxy)oxide catalysts," *Nature Materials*, vol. 11, no. 6, pp. 550-557, 2012/06/01 2012.
- [11] W.-J. Jiang *et al.*, "Crystallinity-Modulated Electrocatalytic Activity of a Nickel(II) Borate Thin Layer on Ni<sub>3</sub>B for Efficient Water Oxidation," *Angewandte Chemie International Edition*, <https://doi.org/10.1002/anie.201703183> vol. 56, no. 23, pp. 6572-6577, 2017/06/01 2017.
- [12] S. Cherevko *et al.*, "Oxygen and hydrogen evolution reactions on Ru, RuO<sub>2</sub>, Ir, and IrO<sub>2</sub> thin film electrodes in acidic and alkaline electrolytes: A comparative study on activity and stability," *Catalysis Today*, vol. 262, pp. 170-180, 2016/03/15/ 2016.
- [13] B. Sarkar, D. Das, and K. K. Nanda, "pH-dependent hydrogen evolution using spatially confined ruthenium on hollow N-doped carbon nanocages as a Mott–Schottky catalyst," *Journal of Materials Chemistry A*, 10.1039/D1TA02375F vol. 9, no. 24, pp. 13958-13966, 2021.
- [14] F. Li, G.-F. Han, H.-J. Noh, I. Ahmad, I.-Y. Jeon, and J.-B. Baek, "Mechanochemically Assisted Synthesis of a Ru Catalyst for Hydrogen Evolution with Performance Superior to Pt in Both Acidic and Alkaline Media," *Advanced Materials*, <https://doi.org/10.1002/adma.201803676> vol. 30, no. 44, p. 1803676, 2018/11/01 2018.
- [15] J. Zhang *et al.*, "Ruthenium/nitrogen-doped carbon as an electrocatalyst for efficient hydrogen evolution in alkaline solution," *Journal of Materials Chemistry A*, 10.1039/C7TA08764K vol. 5, no. 48, pp. 25314-25318, 2017.

- [16] T. Qiu *et al.*, "Highly exposed ruthenium-based electrocatalysts from bimetallic metal-organic frameworks for overall water splitting," *Nano Energy*, vol. 58, pp. 1-10, 2019/04/01/ 2019.
- [17] Y. Wang, L. Zhao, J. Ma, and J. Zhang, "Confined interface transformation of metal-organic frameworks for highly efficient oxygen evolution reactions," *Energy & Environmental Science*, 10.1039/D2EE01073A vol. 15, no. 9, pp. 3830-3841, 2022.
- [18] H. Sun and W. Jung, "Recent advances in doped ruthenium oxides as high-efficiency electrocatalysts for the oxygen evolution reaction," *Journal of Materials Chemistry A*, 10.1039/D1TA03452A vol. 9, no. 28, pp. 15506-15521, 2021.
- [19] J. Song *et al.*, "A review on fundamentals for designing oxygen evolution electrocatalysts," *Chemical Society Reviews*, 10.1039/C9CS00607A vol. 49, no. 7, pp. 2196-2214, 2020.
- [20] E. Tsuji, A. Imanishi, K.-i. Fukui, and Y. Nakato, "Electrocatalytic activity of amorphous RuO<sub>2</sub> electrode for oxygen evolution in an aqueous solution," *Electrochimica Acta*, vol. 56, no. 5, pp. 2009-2016, 2011/02/01/ 2011.
- [21] K. Biswas and C. N. Rao, "Synthesis and characterization of nanocrystals of the oxide metals, RuO<sub>2</sub>, IrO<sub>2</sub>, and ReO<sub>3</sub>," (in eng), *J Nanosci Nanotechnol*, vol. 7, no. 6, pp. 1969-74, Jun 2007.
- [22] Y. Qin *et al.*, "RuO<sub>2</sub> electronic structure and lattice strain dual engineering for enhanced acidic oxygen evolution reaction performance," *Nature Communications*, vol. 13, no. 1, p. 3784, 2022/07/01 2022.
- [23] R. Jiang, D. T. Tran, J. Li, and D. Chu, "Ru@RuO<sub>2</sub> Core-Shell Nanorods: A Highly Active and Stable Bifunctional Catalyst for Oxygen Evolution and Hydrogen Evolution Reactions," *ENERGY & ENVIRONMENTAL MATERIALS*, vol. 2, no. 3, pp. 201-208, 2019.

- [24] J. Wang *et al.*, "Robust Ru-N metal-support interaction to promote self-powered H<sub>2</sub> production assisted by hydrazine oxidation," *Nano Energy*, vol. 100, p. 107467, 2022/09/01/ 2022.
- [25] X. Gao *et al.*, "Ru/RuO<sub>2</sub> Nanoparticle Composites with N-Doped Reduced Graphene Oxide as Electrocatalysts for Hydrogen and Oxygen Evolution," *ACS Applied Nano Materials*, vol. 3, no. 12, pp. 12269-12277, 2020/12/24 2020.
- [26] G. Kim, J. Yang, N. Nakashima, and T. Shiraki, "Highly Microporous Nitrogen-doped Carbon Synthesized from Azine-linked Covalent Organic Framework and its Supercapacitor Function," *Chemistry*, vol. 23, no. 69, pp. 17504-17510, Dec 11 2017.
- [27] L. Chen, L. Zhang, Z. Chen, H. Liu, R. Luque, and Y. Li, "A covalent organic framework-based route to the in situ encapsulation of metal nanoparticles in N-rich hollow carbon spheres," *Chem Sci*, vol. 7, no. 9, pp. 6015-6020, Sep 1 2016.
- [28] Q. Xu, Y. Tang, L. Zhai, Q. Chen, and D. Jiang, "Pyrolysis of covalent organic frameworks: a general strategy for template converting conventional skeletons into conducting microporous carbons for high-performance energy storage," *Chem Commun (Camb)*, vol. 53, no. 85, pp. 11690-11693, Oct 24 2017.
- [29] X. Hu *et al.*, "Two-dimensional covalent organic frameworks as self-template derived nitrogen-doped carbon nanosheets for eco-friendly metal-free catalysis," *Applied Catalysis B: Environmental*, vol. 244, pp. 25-35, 2019.
- [30] Q. Xu, Y. Tang, X. Zhang, Y. Oshima, Q. Chen, and D. Jiang, "Template Conversion of Covalent Organic Frameworks into 2D Conducting Nanocarbons for Catalyzing Oxygen Reduction Reaction," *Adv Mater*, vol. 30, no. 15, p. e1706330, Apr 2018.
- [31] S. Y. Ding and W. Wang, "Covalent organic frameworks (COFs): from design to applications," *Chem Soc Rev*, vol. 42, no. 2, pp. 548-68, Jan 21 2013.

- [32] P. J. Waller, F. Gandara, and O. M. Yaghi, "Chemistry of Covalent Organic Frameworks," *Acc Chem Res*, vol. 48, no. 12, pp. 3053-63, Dec 15 2015.
- [33] T. Gao, Z. Yan, V. Ordonsky, and S. Paul, "Design of Two-Dimensional Heteropolyacid-Covalent Organic Frameworks Composite Materials for Acid Catalysis," *ChemCatChem*, <https://doi.org/10.1002/cctc.202101450> vol. 14, no. 15, p. e202101450, 2022/08/05 2022.
- [34] Y.-R. Liu *et al.*, "Ternary CoS<sub>2</sub>/MoS<sub>2</sub>/RGO electrocatalyst with CoMoS phase for efficient hydrogen evolution," *Applied Surface Science*, vol. 412, pp. 138-145, 2017/08/01/ 2017.
- [35] S.-Y. Li, W.-H. Li, X.-L. Wu, Y. Tian, J. Yue, and G. Zhu, "Pore-size dominated electrochemical properties of covalent triazine frameworks as anode materials for K-ion batteries," *Chemical Science*, 10.1039/C9SC02340B vol. 10, no. 33, pp. 7695-7701, 2019.
- [36] M. G. Schwab, B. Fassbender, H. W. Spiess, A. Thomas, X. Feng, and K. Müllen, "Catalyst-free Preparation of Melamine-Based Microporous Polymer Networks through Schiff Base Chemistry," *Journal of the American Chemical Society*, vol. 131, no. 21, pp. 7216-7217, 2009/06/03 2009.
- [37] S. Roy, T. Chatterjee, B. Banerjee, N. Salam, A. Bhaumik, and S. M. Islam, "Cu(ii) anchored nitrogen-rich covalent imine network (CuII-CIN-1): an efficient and recyclable heterogeneous catalyst for the synthesis of organoselenides from aryl boronic acids in a green solvent," *RSC Adv.*, vol. 4, no. 86, pp. 46075-46083, 2014.
- [38] J. Liu, Y. Zhang, L. Zhang, F. Xie, A. Vasileff, and S.-Z. Qiao, "Graphitic Carbon Nitride (g-C<sub>3</sub>N<sub>4</sub>)-Derived N-Rich Graphene with Tuneable Interlayer Distance as a High-Rate Anode for Sodium-Ion Batteries," *Advanced Materials*, <https://doi.org/10.1002/adma.201901261> vol. 31, no. 24, p. 1901261, 2019/06/01 2019.

- [39] J. Xue, Y. Bai, and H. Liu, "Hybrid methods of surface plasmon resonance coupled to mass spectrometry for biomolecular interaction analysis.," *Anal. Bioanal. Chem.*, vol. 411, pp. 3721–3729, 2019.
- [40] J. G. Małecki and A. Maroń, "A ruthenium(II) hydride carbonyl complex with 4-phenylpyrimidine as co-ligand," *Transition Metal Chemistry*, vol. 37, no. 8, pp. 727-734, 2012/11/01 2012.
- [41] N. Bandara, Y. Esparza, and J. Wu, "Graphite Oxide Improves Adhesion and Water Resistance of Canola Protein-Graphite Oxide Hybrid Adhesive," *Sci Rep*, vol. 7, no. 1, p. 11538, Sep 14 2017.
- [42] M. P. Kumar, T. Kesavan, G. Kalita, P. Ragupathy, T. N. Narayanan, and D. K. Pattanayak, "On the large capacitance of nitrogen doped graphene derived by a facile route," *RSC Adv.*, vol. 4, no. 73, pp. 38689-38697, 2014.
- [43] Y. Zhang *et al.*, "Encased Copper Boosts the Electrocatalytic Activity of N-Doped Carbon Nanotubes for Hydrogen Evolution," *ACS Applied Materials & Interfaces*, vol. 9, no. 42, pp. 36857-36864, 2017/10/25 2017.
- [44] X. Cui *et al.*, "Pd-doped Ni nanoparticle-modified N-doped carbon nanocatalyst with high Pd atom utilization for the transfer hydrogenation of nitroarenes," *Green Chemistry*, 10.1039/C7GC03710D vol. 20, no. 5, pp. 1121-1130, 2018.
- [45] M. K. Bhunia, S. K. Das, P. Pachfule, R. Banerjee, and A. Bhaumik, "Nitrogen-rich porous covalent imine network (CIN) material as an efficient catalytic support for C-C coupling reactions," *Dalton Trans*, vol. 41, no. 4, pp. 1304-11, Jan 28 2012.
- [46] E. Alwin, M. Zieliński, A. Suchora, I. Gulaczyk, Z. Piskuła, and M. Pietrowski, "High surface area, spongy graphitic carbon nitride derived by selective etching by Pt and Ru

nanoparticles in hydrogen," *Journal of Materials Science*, vol. 57, no. 33, pp. 15705-15721, 2022/09/01 2022.

[47] H. Wang *et al.*, "Synthesis and applications of novel graphitic carbon nitride/metal-organic frameworks mesoporous photocatalyst for dyes removal," *Applied Catalysis B: Environmental*, vol. 174-175, pp. 445-454, 2015/09/01/ 2015.

[48] F. J. Escobar-Bedia *et al.*, "Active and Regioselective Ru Single-Site Heterogeneous Catalysts for Alpha-Olefin Hydroformylation," *ACS Catalysis*, vol. 12, no. 7, pp. 4182-4193.

[49] J. Ding, Q. Shao, Y. Feng, and X. Huang, "Ruthenium-nickel sandwiched nanoplates for efficient water splitting electrocatalysis," *Nano Energy*, vol. 47, pp. 1-7, 2018/05/01/ 2018.

[50] J. Mahmood *et al.*, "An efficient and pH-universal ruthenium-based catalyst for the hydrogen evolution reaction," *Nature Nanotechnology*, vol. 12, no. 5, pp. 441-446, 2017/05/01 2017.

[51] J.-Q. Chi *et al.*, "Hydrogen Evolution Activity of Ruthenium Phosphides Encapsulated in Nitrogen- and Phosphorous-Codoped Hollow Carbon Nanospheres," *ChemSusChem*, <https://doi.org/10.1002/cssc.201702010> vol. 11, no. 4, pp. 743-752, 2018/02/22 2018.

[52] T. Liu, B. Feng, X. Wu, Y. Niu, W. Hu, and C. M. Li, "Ru<sub>2</sub>P Nanoparticle Decorated P/N-Doped Carbon Nanofibers on Carbon Cloth as a Robust Hierarchical Electrocatalyst with Platinum-Comparable Activity toward Hydrogen Evolution," *ACS Applied Energy Materials*, vol. 1, no. 7, pp. 3143-3150, 2018/07/23 2018.

[53] Z. Pu, I. S. Amiin, Z. Kou, W. Li, and S. Mu, "RuP<sub>2</sub>-Based Catalysts with Platinum-like Activity and Higher Durability for the Hydrogen Evolution Reaction at All pH Values," *Angewandte Chemie International Edition*, <https://doi.org/10.1002/anie.201704911> vol. 56, no. 38, pp. 11559-11564, 2017/09/11 2017.

- [54] S. Liu *et al.*, "Ru decorated with NiCoP: an efficient and durable hydrogen evolution reaction electrocatalyst in both acidic and alkaline conditions," *Chemical Communications*, 10.1039/C7CC08340H vol. 53, no. 98, pp. 13153-13156, 2017.
- [55] Q. Wang, M. Ming, S. Niu, Y. Zhang, G. Fan, and J.-S. Hu, "Scalable Solid-State Synthesis of Highly Dispersed Uncapped Metal (Rh, Ru, Ir) Nanoparticles for Efficient Hydrogen Evolution," *Advanced Energy Materials*, <https://doi.org/10.1002/aenm.201801698> vol. 8, no. 31, p. 1801698, 2018/11/01 2018.
- [56] H.-S. Park *et al.*, "RuO<sub>2</sub> nanocluster as a 4-in-1 electrocatalyst for hydrogen and oxygen electrochemistry," *Nano Energy*, vol. 55, pp. 49-58, 2019/01/01/ 2019.
- [57] J. Li *et al.*, "Mechanistic Insights on Ternary Ni<sub>2-x</sub>CoxP for Hydrogen Evolution and Their Hybrids with Graphene as Highly Efficient and Robust Catalysts for Overall Water Splitting," *Advanced Functional Materials*, <https://doi.org/10.1002/adfm.201601420> vol. 26, no. 37, pp. 6785-6796, 2016/10/01 2016.
- [58] J. Su, Y. Yang, G. Xia, J. Chen, P. Jiang, and Q. Chen, "Ruthenium-cobalt nanoalloys encapsulated in nitrogen-doped graphene as active electrocatalysts for producing hydrogen in alkaline media," *Nature Communications*, vol. 8, no. 1, p. 14969, 2017/04/25 2017.
- [59] A. Maiti and S. K. Srivastava, "Ru-Doped CuO/MoS<sub>2</sub> Nanostructures as Bifunctional Water-Splitting Electrocatalysts in Alkaline Media," *ACS Applied Nano Materials*, vol. 4, no. 8, pp. 7675-7685, 2021/08/27 2021.
- [60] Q. Lu *et al.*, "Synthesis of Hierarchical 4H/fcc Ru Nanotubes for Highly Efficient Hydrogen Evolution in Alkaline Media," *Small*, <https://doi.org/10.1002/sml.201801090> vol. 14, no. 30, p. 1801090, 2018/07/01 2018.

- [61] K. Gao *et al.*, "Ru nanodendrites composed of ultrathin fcc/hcp nanoblades for the hydrogen evolution reaction in alkaline solutions," *Chemical Communications*, 10.1039/C8CC01343H vol. 54, no. 36, pp. 4613-4616, 2018.
- [62] Y. Luo *et al.*, "Mesoporous Pd@Ru Core-Shell Nanorods for Hydrogen Evolution Reaction in Alkaline Solution," *ACS Applied Materials & Interfaces*, vol. 10, no. 40, pp. 34147-34152, 2018/10/10 2018.
- [63] D. Yoon *et al.*, "Cactus-Like Hollow Cu<sub>2</sub>-xS@Ru Nanoplates as Excellent and Robust Electrocatalysts for the Alkaline Hydrogen Evolution Reaction," *Small*, <https://doi.org/10.1002/sml.201700052> vol. 13, no. 29, p. 1700052, 2017/08/01 2017.
- [64] J. Ding, Q. Shao, Y. Feng, and X. Huang, "Ruthenium-nickel sandwiched nanoplates for efficient water splitting electrocatalysis," *Nano Energy*, vol. 47, pp. 1-7, 2018/05/01/ 2018.
- [65] C.-Z. Yuan *et al.*, "Molecule-Assisted Synthesis of Highly Dispersed Ultrasmall RuO<sub>2</sub> Nanoparticles on Nitrogen-Doped Carbon Matrix as Ultraefficient Bifunctional Electrocatalysts for Overall Water Splitting," *ACS Sustainable Chemistry & Engineering*, vol. 6, no. 9, pp. 11529-11535, 2018/09/04 2018.
- [66] C.-Z. Yuan *et al.*, "Molecule-Assisted Synthesis of Highly Dispersed Ultrasmall RuO<sub>2</sub> Nanoparticles on Nitrogen-Doped Carbon Matrix as Ultraefficient Bifunctional Electrocatalysts for Overall Water Splitting," *ACS Sustainable Chemistry & Engineering*, vol. 6, no. 9, pp. 11529-11535, 2018/09/04 2018.

- [67] G. Chen *et al.*, "Accelerated Hydrogen Evolution Kinetics on NiFe-Layered Double Hydroxide Electrocatalysts by Tailoring Water Dissociation Active Sites," *Advanced Materials*, <https://doi.org/10.1002/adma.201706279> vol. 30, no. 10, p. 1706279, 2018/03/01 2018.
- [68] D. R. Liyanage, D. Li, Q. B. Cheek, H. Baydoun, and S. L. Brock, "Synthesis and oxygen evolution reaction (OER) catalytic performance of Ni<sub>2-x</sub>Ru<sub>x</sub>P nanocrystals: enhancing activity by dilution of the noble metal," *Journal of Materials Chemistry A*, 10.1039/C7TA05353C vol. 5, no. 33, pp. 17609-17618, 2017.
- [69] Z. Zhuang *et al.*, "Three-dimensional open nano-netcage electrocatalysts for efficient pH-universal overall water splitting," *Nature Communications*, vol. 10, no. 1, p. 4875, 2019/10/25 2019.
- [70] Y. Wang, J. Ma, J. Wang, S. Chen, H. Wang, and J. Zhang, "Interfacial Scaffolding Preparation of Hierarchical PBA-Based Derivative Electrocatalysts for Efficient Water Splitting," *Advanced Energy Materials*, vol. 9, no. 5, p. 1802939, 2019.
- [71] Y. Wang, S. Chen, and J. Zhang, "Hierarchical Assembly of Prussian Blue Derivatives for Superior Oxygen Evolution Reaction," *Advanced Functional Materials*, vol. 29, no. 45, p. 1904955, 2019.
- [72] Q. Yao, B. Huang, N. Zhang, M. Sun, Q. Shao, and X. Huang, "Channel-Rich RuCu Nanosheets for pH-Universal Overall Water Splitting Electrocatalysis," *Angewandte Chemie International Edition*, <https://doi.org/10.1002/anie.201908092> vol. 58, no. 39, pp. 13983-13988, 2019/09/23 2019.
- [73] C. Guan *et al.*, "Metal-organic framework-derived integrated nanoarrays for overall water splitting," *Journal of Materials Chemistry A*, 10.1039/C8TA02528B vol. 6, no. 19, pp. 9009-9018, 2018.

- [74] L. Wang *et al.*, "Atomically Dispersed Mo Supported on Metallic Co<sub>9</sub>S<sub>8</sub> Nanoflakes as an Advanced Noble-Metal-Free Bifunctional Water Splitting Catalyst Working in Universal pH Conditions," *Advanced Energy Materials*, <https://doi.org/10.1002/aenm.201903137> vol. 10, no. 4, p. 1903137, 2020/01/01 2020.
- [75] M. Qu *et al.*, "Regulating electron density of NiFe-P nanosheets electrocatalysts by a trifle of Ru for high-efficient overall water splitting," *Applied Catalysis B: Environmental*, vol. 263, p. 118324, 2020/04/01/ 2020.
- [76] X. Luo *et al.*, "Porous Co<sub>9</sub>S<sub>8</sub>/Nitrogen, Sulfur-Doped Carbon@Mo<sub>2</sub>C Dual Catalyst for Efficient Water Splitting," *ACS Applied Materials & Interfaces*, vol. 10, no. 26, pp. 22291-22302, 2018/07/05 2018.
- [77] X. Han *et al.*, "Ultrafine Pt Nanoparticle-Decorated Pyrite-Type CoS<sub>2</sub> Nanosheet Arrays Coated on Carbon Cloth as a Bifunctional Electrode for Overall Water Splitting," *Advanced Energy Materials*, <https://doi.org/10.1002/aenm.201800935> vol. 8, no. 24, p. 1800935, 2018/08/01 2018.
- [78] B. Tang, X. Yang, Z. Kang, and L. Feng, "Crystallized RuTe<sub>2</sub> as unexpected bifunctional catalyst for overall water splitting," *Applied Catalysis B: Environmental*, vol. 278, p. 119281, 2020/12/05/ 2020.
- [79] D. Chen *et al.*, "Ru-doped 3D flower-like bimetallic phosphide with a climbing effect on overall water splitting," *Applied Catalysis B: Environmental*, vol. 279, p. 119396, 2020/12/15/ 2020.

# Chapter 3

## **Simultaneous Upcycling of PET Plastic Waste and CO<sub>2</sub> Reduction through Co-electrolysis: A Novel Approach for Integrating CO<sub>2</sub> Reduction and PET Hydrolysate Oxidation**

Kilaparathi Sravan Kumar<sup>1</sup>, Ahmed Addad<sup>2</sup>, Alexandre Barras<sup>1</sup>, Sabine Szunerits<sup>1</sup>, and Rabah

Boukherroub<sup>1\*</sup>

This chapter has been published RSC Journal of Materials Chemistry A

**Reference:** *J. Mater. Chem. A*, 2023,11, 26075-26085

**DOI:** <https://doi.org/10.1039/D3TA05726G>

## Abstract

Improper handling of PET plastic waste contributes to CO<sub>2</sub> emissions during incineration. This study proposes an innovative strategy for tackling PET waste and CO<sub>2</sub> emissions simultaneously. Integrating CO<sub>2</sub> electrochemical reduction reaction (CO<sub>2</sub>RR) with PET hydrolysate oxidation offers a promising avenue. Bismuth oxide carbonate (BOC) loaded on reduced graphene oxide (rGO) and CuCoO on rGO were employed for cathodic CO<sub>2</sub>RR and anodic PET hydrolysate oxidation, respectively, for concurrent production of formate. The anodic CuCoO@rGO catalyst exhibited high electro-activity and a remarkable Faradaic efficiency (FE) of 85.7% at 1.5V *vs.* RHE. The cathodic BOC@rGO catalyst achieved a FE of 97.4% at -0.8 V *vs.* RHE, facilitating formate production from CO<sub>2</sub>RR. Employing this approach in an electrolyzer allowed formic acid production with a low 1.9 V cell voltage at 10 mA cm<sup>-2</sup> and a formate FE of 151.8%. This innovation offers a novel route for PET waste upcycling, CO<sub>2</sub> reduction, and environmental sustainability.

### 3.1 Introduction

The excessive CO<sub>2</sub> emissions, brought on by the ever-increasing usage of fossil fuels, have exacerbated the greenhouse gas effect and caused environmental issues [1]–[4]. A viable method for recycling carbon resources involves the electrochemical CO<sub>2</sub> reduction reaction (CO<sub>2</sub>RR), which can utilize renewable energy and allows the selective production of high-value products, such as formic acid that can be used as a fuel and common chemical [5], [6]. Based on a techno-economic study, formic acid (HCO<sub>2</sub>H) shows tremendous promise as a typical reduction product for energy-dense fuels. It may also be used as feedstock for fuel cells and as a chemical intermediary in a variety of industrial processes [6], [7]. However, the significant overpotential for activating stable molecular CO<sub>2</sub> and complex multi-electron transfer kinetics, along with the inevitable competition of the hydrogen evolution reaction (HER) in aqueous solutions, has significantly limited the successful utilization of CO<sub>2</sub> on a large scale. Additionally, the poor activity and low selectivity of target products further contribute to the challenges faced in effectively utilizing CO<sub>2</sub> on a larger scale.

Significant efforts have been made to improve the catalytic performance of CO<sub>2</sub> reduction using metals, such as Bi, Sn, In, Pb, Cd, Hg and others, demonstrating enhanced product selectivity and a lower overpotential for CO<sub>2</sub>RR [8]–[13]. Among them, bismuth (Bi) has considerable potential for CO<sub>2</sub> electroreduction to formate (HCO<sub>2</sub><sup>-</sup>), because of its natural inertness toward the competitive HER and its poor affinity for CO<sub>2</sub> intermediates. In order to achieve the high catalytic performance of CO<sub>2</sub>RR toward formate, a variety of approaches have been devoted to improving the morphology, structure, and composition of Bi-based materials, such as BiPO<sub>4</sub>, BiOX (Cl, Br, I), Bi<sub>2</sub>O<sub>2</sub>CO<sub>3</sub>, and so on [14]–[17]. Bi-based catalysts for the CO<sub>2</sub>RR were first produced and published by Komatsu et al. in 1995 [18]. CO<sub>2</sub>RR activity depends on the shape and morphology

of Bi, similar to other electrocatalysts. To date, a variety of morphological characteristics (single-atom catalysts, nanoparticles, one-dimensional nanowires and nanotubes, two-dimensional nanosheets, nanoflakes, nanofilms, and dendrites) have been explored, and they have been synthesized using various techniques, including hydrothermal, chemical- or electro-reduction, and electrodeposition methods [3], [19]–[22]. However, most published research demonstrated that the pre-catalyst-derived metal Bi is the actual catalytic component in the CO<sub>2</sub>RR process. For instance, Li et al. reported the synthesis of BiPO<sub>4</sub>-based catalysts through hydrothermal reaction followed by *in situ* electrochemical reduction for CO<sub>2</sub> electroreduction. In an H-type cell, they were able to achieve an optimal formate faradaic efficiency (FE) of 91.4 % at an applied voltage of -0.9 V vs. RHE [16]. Zhang et al. demonstrated, in their study, that high surface area Bi catalysts could be obtained by easy electrochemical reduction of BiOCl nanosheets with excellent FE for formate synthesis [23].

Despite major advances in the study of cathode reactions for CO<sub>2</sub> reduction, research into anodic reactions, notably the oxygen evolution process (OER), has been rather restricted. Due to the high-energy barrier and overpotential necessary for the OER process, large energy expenditures are involved with oxygen evolution at the anode. In fact, it is anticipated that the anode in a CO<sub>2</sub> reduction/OER electrolyzer consumes around 90% of the entire current input [24]. Hence, integrating CO<sub>2</sub> reduction with alternate oxidations may result in increased economic output, while lowering energy input. Moreover, it is desirable to couple suitable anodic half-reactions to concurrently produce the desired target products [25]–[27]. In this regard, we believe that environmental pollution and global warming are two interrelated scientific issues that demand considerable attention. A promising strategy to mitigate these problems could be the upcycling of plastic waste into value-added products, which could have positive economic and environmental

benefits. Recently, research has been conducted on alkaline hydrolysis, which provides viable approach for converting polyethylene terephthalate (PET) into terephthalic acid (TPA) and ethylene glycol (EG) monomers with high yields [28], [29]. While separation of TPA can be achieved very easily just by adjusting the pH to lower values, EG separation is problematic due to its high boiling point. Hence, researchers have tried to transform EG into other value-added products like formate *via* electrochemical oxidation under alkaline conditions [30]–[34].

In this work, we combined the anodic oxidation process of EG, derived from hydrolyzing PET plastic waste using CuCo@rGO electrocatalyst, with the cathodic CO<sub>2</sub> reduction reaction (CO<sub>2</sub>RR) using a bismuth phosphate (BiPO<sub>4</sub>)-functionalized reduced graphene oxide (BiPO<sub>4</sub>@rGO) catalyst synthesized using a straightforward one-step hydrothermal method followed by electrochemical activation to Bi<sub>2</sub>O<sub>2</sub>CO<sub>3</sub>@rGO (BOC@rGO). The catalyst displayed improved selectivity and activity with a faradaic efficiency of 97.4% for formate at -0.8 V (*vs.* RHE), and long-term durability for at least 22 h with almost no activity loss in 0.1M KHCO<sub>3</sub> electrolyte solution. The higher CO<sub>2</sub> adsorption capacity of the rGO hybrid and its quick interfacial charge transfer capabilities may be responsible for the increased CO<sub>2</sub>RR activity. Besides, we have employed CuCo@rGO electrocatalyst, synthesized by simple chemical reduction technique using NaBH<sub>4</sub>, for anodic PET electrocatalytic oxidation. The electrocatalyst recorded a high formate faradaic efficiency of 85.49% in PET hydrolysate solution at an overpotential of 1.5 V *vs.* RHE.

## **3.2 Experimental section**

### **3.2.1 Reagents and materials**

Graphene oxide (GO) was purchased from Graphitene Ltd. and was used without any further modifications. Bismuth nitrate pentahydrate (Bi(NO<sub>3</sub>)<sub>3</sub>·5H<sub>2</sub>O, 98%), monosodium phosphate

( $\text{NaH}_2\text{PO}_4 \cdot 2\text{H}_2\text{O}$ ,  $\geq 98\%$ ), potassium hydroxide (KOH), potassium bicarbonate ( $\text{KHCO}_3$ ,  $\geq 99.5\%$ ), ethylene glycol (EG, 99.5%), copper chloride ( $\text{CuCl}_2$ , 99%), cobalt chloride ( $\text{CoCl}_2$ , 99%), sodium borohydride ( $\text{NaBH}_4$ ) ( $\geq 99\%$ ), Nafion (5wt%) and Toray carbon paper were procured from Sigma-Aldrich (France). The Sustainion®X37-50-grade membrane was purchased from the fuel cell store. Proton-exchange membrane (Nafion 117) was obtained from Sigma-Aldrich (France). All the reagents were of analytical grade and utilized without any further purification. Ultrapure water (DI) ( $18 \text{ M}\Omega \cdot \text{cm}$ ) was used for preparation of all electrolyte solutions.

### **3.2.2 Synthesis of bismuth phosphate on reduced graphene oxide ( $\text{BiPO}_4@r\text{GO}$ )**

The synthesis of the pre-catalyst  $\text{BiPO}_4@r\text{GO}$  involves a multi-step procedure. In a typical experiment, 20 mg of  $\text{Bi}(\text{NO}_3)_3 \cdot 5\text{H}_2\text{O}$  were dissolved in a mixed solvent of 30 mL of ethylene glycol (EG) and water (volume ratio of 2:1) and stirred for 30 min at room temperature. 20 mg of graphene oxide (GO) were then added to the solution, and the mixture was ultrasonically processed for 1 h to produce a homogeneous suspension. To ensure the electrostatically driven assembly of positively charged  $\text{Bi}^{3+}$  ions on the surface of negatively charged GO sheets, the mixture was stirred for an additional hour. 20 mg of  $\text{NaH}_2\text{PO}_4 \cdot 2\text{H}_2\text{O}$  were later added to the mixture and stirred for 1 h. The resulting suspension was placed in an autoclave made of Teflon-coated stainless steel and heated at  $160^\circ\text{C}$  for 16 h. The autoclave was then allowed to cool naturally to room temperature. The precipitate was separated by centrifugation, and repeatedly rinsed with ultrapure water and ethanol. It was then dialyzed in ultrapure water for 24 h to remove unreacted moieties and impurities. The dialyzed solution was lyophilized to obtain the final  $\text{BiPO}_4@r\text{GO}$  product. Under same experimental conditions, pure  $\text{BiPO}_4$  nanorods were prepared as a control catalyst in the absence of GO precursor.

### **3.2.3 Synthesis of bimetallic Copper-Cobalt oxide on rGO (CuCoO@rGO)**

First, 0.75 mM of copper chloride ( $\text{CuCl}_2$ ) and cobalt chloride ( $\text{CoCl}_2$ ) were placed in 10 mL of ultrapure water and kept under stirring for 15 min. 20 mg of GO were uniformly dispersed in 10 mL of the above solution and ultrasonicated for 1 h until a dark brown solution was formed. Then, 6 mL of an aqueous solution of 0.9 M  $\text{NaBH}_4$  was added dropwise into the mixture under stirring. After 20 min reaction, the resulting product was separated by centrifugation, washed with water several times, and finally freeze-dried to produce CuCoO@rGO powder. The Co@rGO and Cu@rGO were prepared using the same method without adding  $\text{CuCl}_2$  and  $\text{CoCl}_2$  salts, respectively.

### **3.2.4. Hydrolysis of PET plastic**

In order to depolymerize PET, a clean PET water bottle was finely cut into small threads and washed with ethanol and water. Then, 0.5 g of the dried plastic threads was added into 30 mL of 2 M KOH solution and transferred into a 45 mL Teflon-lined autoclave, which was sealed and maintained at  $180^\circ\text{C}$  for 2 h. After cooling to room temperature, the resulting solution containing ethylene glycol (EG) and terephthalate (TPA) was filtered and used as the electrolyte for electrochemical tests and analyses.

### **3.2.5 Electrochemical transformation of $\text{BiPO}_4$ @rGO to BOC@rGO**

The electrochemical tests were performed on a ModuLab-MTS electrochemical test station (Solartron, France) using a standard H-type cell and a 0.1 M  $\text{KHCO}_3$  solution at room temperature. To create a homogeneous catalyst ink, the as-prepared sample (1 mg) was uniformly dispersed in 300  $\mu\text{L}$  of ethanol/water (1:1) and 10  $\mu\text{L}$  of 5% Nafion, and subsequently ultrasonicated for 0.5 h. For long-term controlled potential analysis, 150  $\mu\text{L}$  of ink was drop-casted onto carbon paper ( $1\times 1$

cm<sup>2</sup>) and allowed to dry at room temperature (RT). In other electrochemical tests, however, we employed a 3 mm diameter glassy carbon (GC) electrode. 5 μL of catalyst ink was dropped on the GC and dried at RT. The cathodic and anodic chambers were separated using a proton-exchange membrane (Nafion 117). A platinum coil and Ag/AgCl (3 M KCl) were used as counter and reference electrodes, respectively. The working and reference electrodes were placed in the cathode compartment for electrochemical testing, and the Pt counter electrode was placed in another anode compartment. For conducting control experiments, we undertook the electrochemical conversion of BiPO<sub>4</sub> nanorods into Bi<sub>2</sub>O<sub>2</sub>CO<sub>3</sub> (BOC) nanosheets, mirroring the methodology employed for the fabrication of BOC@rGO composite. Before the measurements, the electrolyte was saturated with CO<sub>2</sub> (pH 6.8) or N<sub>2</sub> (pH 8.3). The Nernst equation was used to convert the recorded potential (V<sub>Ag/AgCl</sub>) into reversible hydrogen electrode (V<sub>RHE</sub>) using the following equation: V<sub>RHE</sub> = V<sub>Ag/AgCl</sub> + 0.197 + 0.059\*pH. Electrochemical impedance spectra (EIS) with an amplitude of 10 mV were recorded at 0.65 V vs. RHE in the frequency range of 1 MHz to 1 Hz.

Different constant working potentials were applied throughout a 2 h CO<sub>2</sub> electroreduction experiment, and the catholyte was stirred at a rate of 300 rpm, while the flow rate of CO<sub>2</sub> gas was kept constant at 20 mL min<sup>-1</sup>. Bruker 300 MHz <sup>1</sup>H liquid NMR spectrometer was utilized for quantification of liquid products after the experiments using a water suppression approach. An internal standard approach was used to calculate the amount of produced formate. The following equation was applied to compute the Faradaic efficiency of formate:

$$FE(\%) = \frac{(\text{mole of produced product} \times n \times 96500)}{\text{total charge passed}}$$

where  $n$  is the number of electron transfer for each product,  $n=2$  for formate in  $\text{CO}_2$  reduction,  $n=3$  for formate in PET degradation.

### 3.3 Results and discussion

#### 3.3.1 Synthesis and characterization

In this study,  $\text{BiPO}_4@\text{rGO}$  nanocomposite was synthesized using a simple hydrothermal technique. The process was conducted over a 16-h period at  $160^\circ\text{C}$ , as illustrated in **Figure 1a**. The synthesis of the nanocomposites was achieved through the electrostatic interactions between positively charged  $\text{Bi}^{3+}$  cations and negatively charged functional groups, such as hydroxyl, carboxyl, and epoxy groups borne by the GO surface in aqueous solution [35], [36]. The addition of phosphate anions caused an ion-exchange reaction between  $\text{H}_2\text{PO}_4^-$  and  $\text{Bi}^{3+}$  cations adsorbed on GO sheets, which led to the growth of  $\text{BiPO}_4$  nuclei to nanorods at the interaction sites. These nuclei slowly expanded throughout the reaction and underwent structural transformation into  $\text{BiPO}_4$  nanorods.

**Figure 1c** depicts the X-ray diffraction (XRD) pattern of the as-prepared  $\text{BiPO}_4@\text{rGO}$  product. All of the diffraction peaks can be attributed to the hexagonal crystal system of  $\text{BiPO}_4$  (ICDD card no. 15-0766). Compared to the XRD pattern of control  $\text{BiPO}_4$  nanorods, the diffractogram of  $\text{BiPO}_4@\text{rGO}$  did not feature any significant variations. Additionally, neither the XRD patterns of pure  $\text{BiPO}_4$  nanorods nor that of  $\text{BiPO}_4@\text{rGO}$  nanocomposite contained impurity peaks, indicating the high crystalline quality of the final  $\text{BiPO}_4$  nanorods in both samples. The  $\text{BiPO}_4@\text{rGO}$  is stable at room temperature, although it undergoes a reductive change at cathodic potentials. We attempted to electrochemically reduce  $\text{BiPO}_4@\text{rGO}$ , which was loaded on a clean Toray carbon paper by applying a potential bias of  $-0.9$  V vs. RHE for 1h in  $\text{CO}_2$ -saturated  $0.5$  M  $\text{KHCO}_3$

electrolyte solution. After electrochemical conversion, we observed morphological and structural alterations in  $\text{BiPO}_4@\text{rGO}$  that were attributed to  $\text{Bi}_2\text{O}_2\text{CO}_3$  (BOC)-type nanosheets, as supported by XRD analysis. The XRD pattern of BOC@rGO in **Figure 1b** shows that, except for the signals related to the carbon paper substrate, all diffraction peaks match well with the typical tetragonal BOC phase (ICDD card no. 41-1488), which is the same as that of commercial BOC. This indicates that the electrochemical reduction of  $\text{BiPO}_4@\text{rGO}$  results in the formation of BOC-type nanosheets. Various control experiments were conducted to investigate the phase evolution (**Figure 1**). Initially, a freshly prepared electrode was immersed in  $\text{CO}_2$ -saturated 0.5 M  $\text{KHCO}_3$  electrolyte for a duration of 12 h, followed by XRD analysis. However, no discernible structural changes were observed during this experiment. Subsequently, a series of increasing voltages ranging from -0.5 to -0.8 V *vs.* SCE was applied, and the XRD analysis demonstrated that the formation of BOC commenced at a potential of -0.6 V *vs.* SCE. These findings collectively indicate that the formation of BOC is not a straightforward spontaneous reaction, but rather a complex process intricately influenced by dynamic conditions.

We have then performed field effect scanning electron microscopy (FESEM) analysis of both  $\text{BiPO}_4@\text{rGO}$  and BOC@rGO to understand the structural morphology of the nanomaterials. **Figure 2** depicts the SEM image of  $\text{BiPO}_4@\text{rGO}$  in its as-prepared state, which evidences nanorod-type morphology with an average diameter of approximately 215 nm. As seen, graphene sheets act as a supporting structure to prevent the aggregation and control of the size of  $\text{BiPO}_4$  nanorods, which is not the case in  $\text{BiPO}_4$  control material. The chemical composition of  $\text{BiPO}_4@\text{rGO}$  was further investigated by elemental mapping and revealed the existence of Bi, P, O, and C elements, as shown in **Figure 2**.

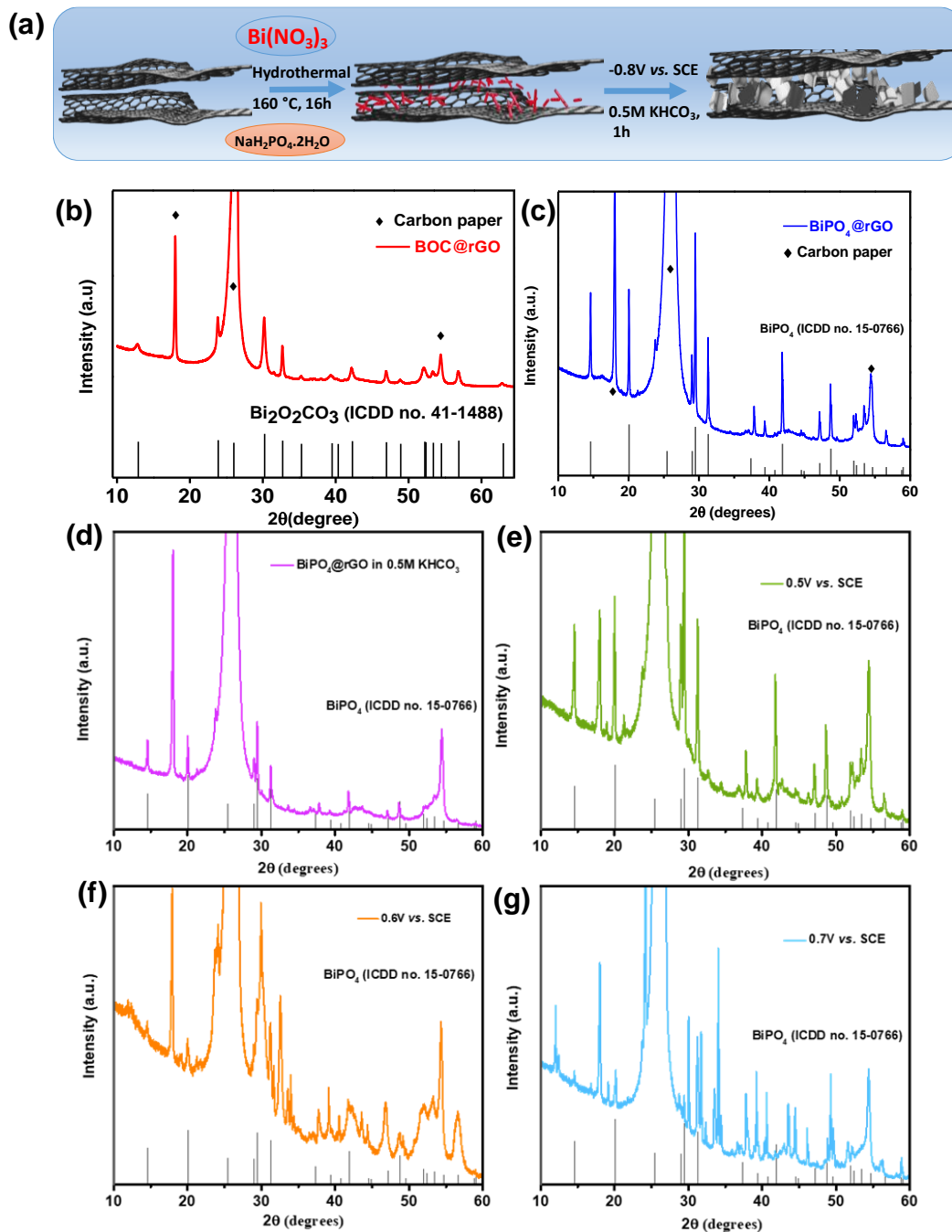


**Figure 1.** (a) Schematic illustration of the synthesis of  $\text{BiPO}_4@\text{rGO}$  nanorods and  $\text{BOC}@\text{rGO}$ . (b) XRD pattern of  $\text{BOC}@\text{rGO}$  nanosheets. (c) X-ray diffraction (XRD) pattern of the as-prepared  $\text{BiPO}_4@\text{rGO}$  product. (d,e,f,g) XRD patterns of electrochemical activation of  $\text{BiPO}_4@\text{rGO}$  at different potentials.

However, after the *in-situ* electrochemical reduction of  $\text{BiPO}_4@\text{rGO}$ , the electrocatalyst's surface morphology changed from nanorods to petal-shaped BOC nanosheet structure vertically aligned on rGO sheets (**Figure 3**). Also, we have assessed the chemical composition of  $\text{BOC}@\text{rGO}$  by elemental mapping, which evidenced the presence of Bi, O, and C elements and absence of P (**Figure 3**). Petal-shaped nanosheet structures often display many edges or unsaturated sites, which are beneficial to increase the contact area between the electrolyte and the electrocatalyst and circumvent mass transport limitations.

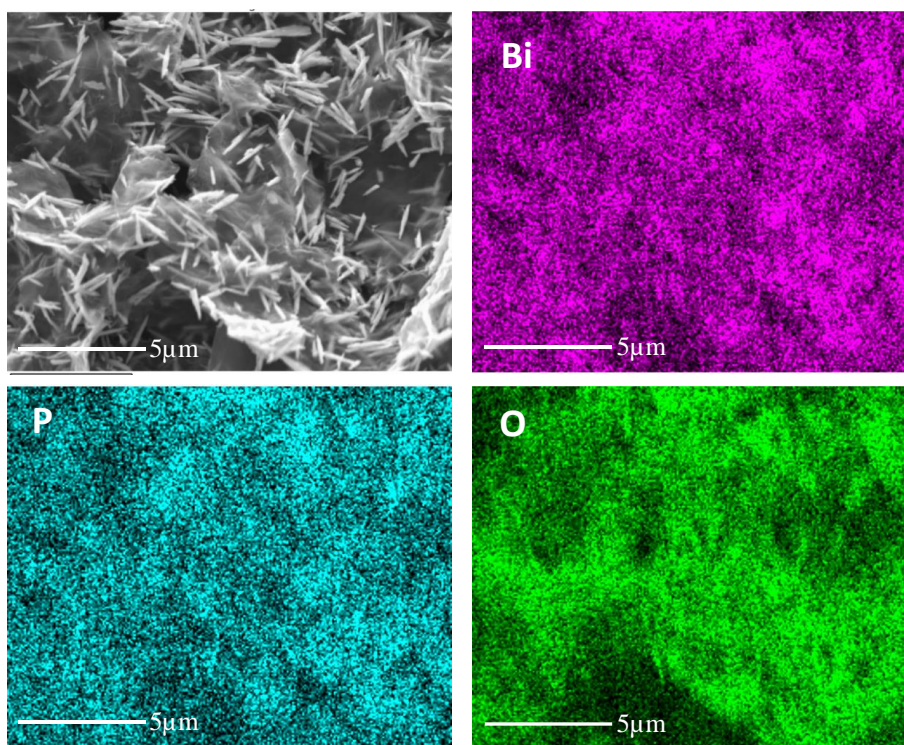


**Figure 2.** SEM images of  $\text{BiPO}_4@\text{rGO}$  and corresponding EDX mapping of Bi, P and O of  $\text{BiPO}_4@\text{rGO}$ .

In order to corroborate the XRD findings, we conducted a detailed examination of the  $\text{BOC}@\text{rGO}$  sample using high-resolution transmission electron microscopy (HRTEM). Through HRTEM imaging, along with the corresponding fast-Fourier transform (FFT) and inverse fast-Fourier

transform (IFFT) patterns, we were able to distinctly observe the presence of the (004) plane of  $\text{Bi}_2\text{O}_2\text{CO}_3$ , with an interplanar distance of 0.34 nm (**Figure 3b,c**).

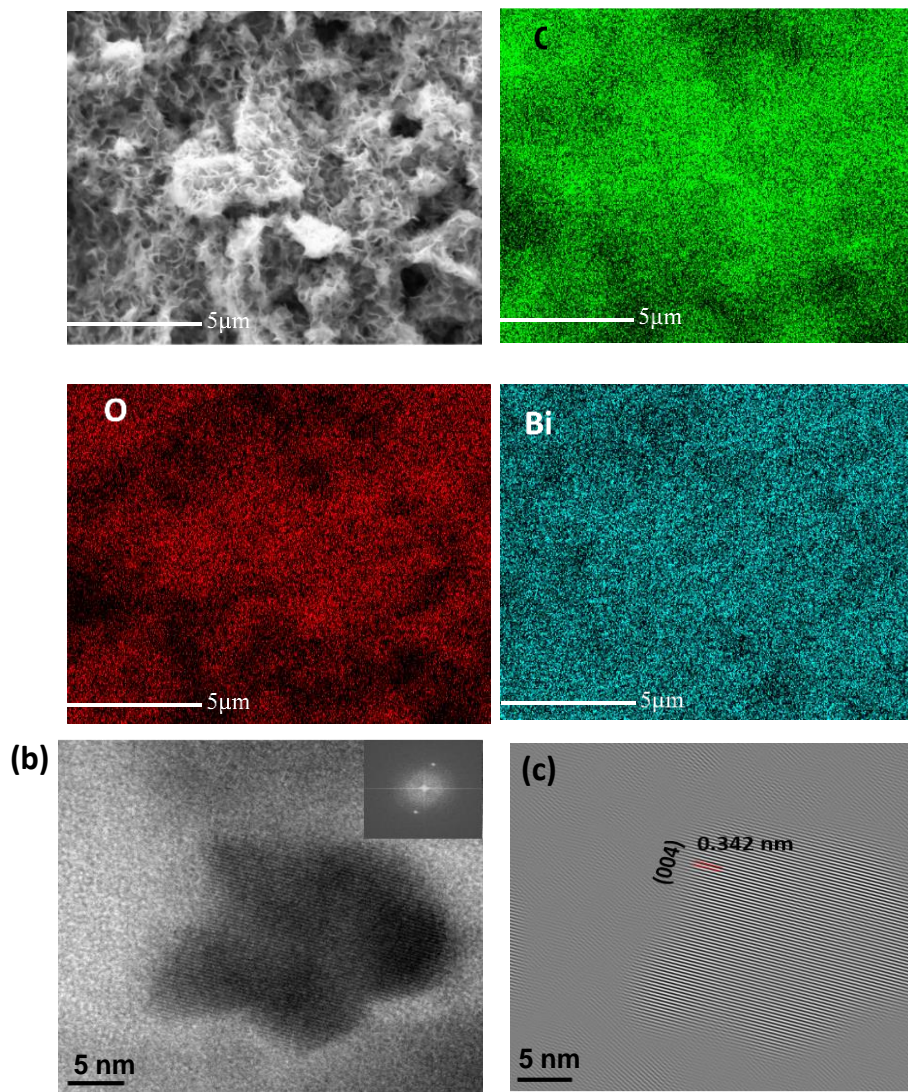


**Figure 3.** SEM images of BOC@rGO and corresponding EDX mapping of C, O and Bi of BOC@rGO electrode. (b) HRTEM image of the BOC@rGO sample (inset: corresponding fast-Fourier transform (FFT) image). (c) Inverse fast-Fourier transform (IFFT) pattern obtained from the HRTEM image.

Raman spectroscopy is a useful and non-destructive method for detecting material structural changes. In pristine  $\text{BiPO}_4$  nanorods, two bands due to the symmetric and asymmetric stretching

modes of the PO<sub>4</sub> units, respectively, could be seen at 964 and 1042 cm<sup>-1</sup> [37]. However, when comparing both BOC@rGO and BiPO<sub>4</sub>@rGO, the peaks associated with PO<sub>4</sub> symmetric and antisymmetric modes that were in the shaded region have vanished, revealing that BiPO<sub>4</sub> has been completely transformed (**Figure 4a**).

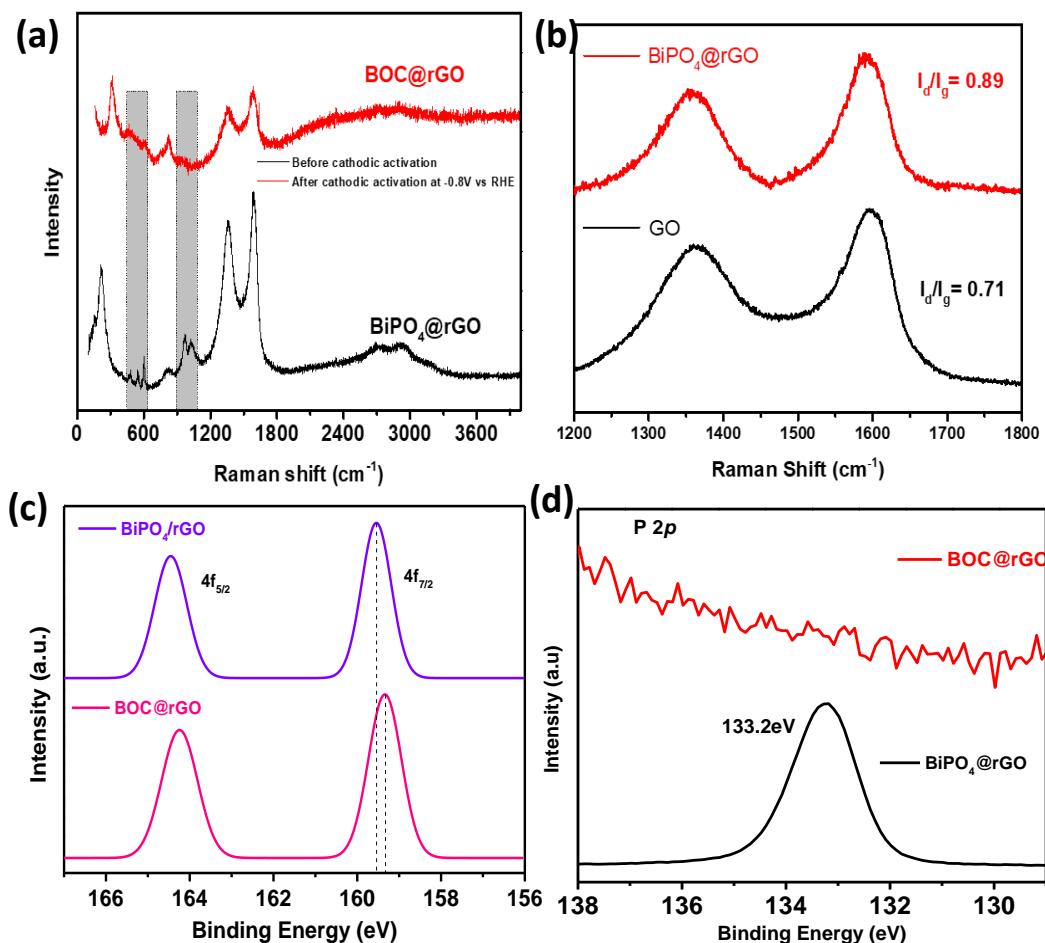


**Figure 4.** (a) Raman spectra of BOC@rGO and BiPO<sub>4</sub>@rGO. (b) I<sub>d</sub>/I<sub>g</sub> band ratio determined from the Raman spectra of BiPO<sub>4</sub>@rGO and GO. (c) High-resolution XPS spectra of Bi 4f of BiPO<sub>4</sub>@rGO and BOC@rGO. (d) High resolution XPS spectra of the P 2p of BOC@rGO and BiPO<sub>4</sub>@rGO.

Both D and G bands could be found in the Raman spectrum of GO at 1351 and 1594  $\text{cm}^{-1}$ , which correspond to structural flaws and first-order scattering of the  $E_{2g}$  mode of the  $\text{sp}^2$  carbon domains, respectively [38]. The structure disorder of rGO may be somewhat altered by the incorporation of Bi metal, according to the Raman and UV-visible spectroscopy analysis, indicating a possible interaction between Bi and rGO.

The electronic coupling between Bi and rGO was further confirmed using X-ray photoelectron spectroscopy (XPS) analysis. From **Figure 4c**, the signals at around 159.3 and 164.1 eV for BOC@rGO and  $\text{BiPO}_4$ @rGO are attributed to Bi  $4f_{7/2}$  and Bi  $4f_{5/2}$  of  $\text{Bi}^{3+}$ , respectively. Additionally, compared to  $\text{BiPO}_4$ @rGO, the binding energy of Bi 4f in BOC@rGO was shifted to lower energy values by approximately 0.5 eV, indicating high electron density transfer of Bi nanosheets, which are chemically bonded to the rGO surface *via* electrostatic interactions [39], [40]. The higher shift suggests that BOC@rGO has rather strong electron-donating capabilities. We did not observe any  $\text{Bi}^0$  on the surface due to the favorable oxide formation under ambient atmosphere. Additionally, BOC@rGO surface was found to be free of P, according to an XPS examination of its surface chemical composition, revealing that the  $\text{BiPO}_4$  nanorods have undergone full electrochemical transformation (**Figure 4d**).

### 3.2.2 Electrochemical $\text{CO}_2$ RR studies

The  $\text{CO}_2$  reduction reaction ( $\text{CO}_2$ RR) activities of BOC@rGO and BOC were evaluated using a two-compartment H-type cell with a three-electrode setup. To assess the impact of the competing hydrogen evolution reaction (HER) as a potential side reaction, linear sweep voltammetry (LSV) curves were acquired in  $\text{CO}_2$ - and  $\text{N}_2$ -purged 0.1 M  $\text{KHCO}_3$  aqueous solutions at a scan rate of 10  $\text{mV s}^{-1}$  (**Figure 5a**). BOC@rGO exhibited a substantially higher current density in a  $\text{CO}_2$ -saturated electrolyte with an onset potential of -0.64 V (*vs.* RHE), which continues to increase to -16 mA

cm<sup>-2</sup> at -1.2 V (vs. RHE). Control experiments revealed that, in the absence of CO<sub>2</sub>, the HER was the dominant cathodic process, with a much lower current density. However, BOC displayed lower current densities than BOC@rGO in a CO<sub>2</sub>-saturated electrolyte, indicating a lower activity.

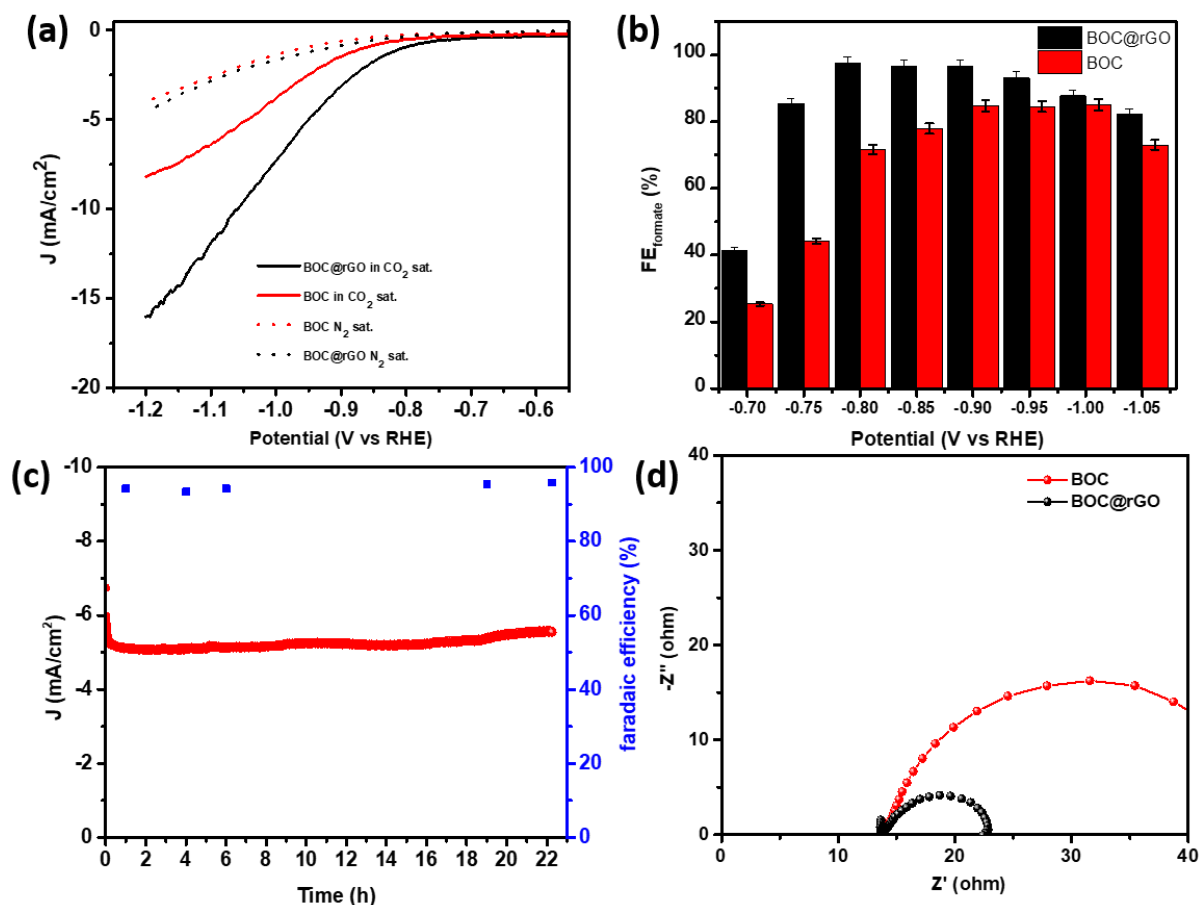


**Figure 5.** (a) CO<sub>2</sub>RR polarization curves of BOC@rGO and BOC electrodes at a scan rate of 10 mV s<sup>-1</sup> in N<sub>2</sub>- or CO<sub>2</sub>-saturated 0.1 M KHCO<sub>3</sub> solution. (b) Faradaic efficiencies (FE) of formate produced by BOC@rGO and BOC for 2 h of CO<sub>2</sub> reduction at different applied potentials. (c) Chronoamperometry analysis and the corresponding FE for HCOOH (blue squares) of BOC@rGO at -0.9 V in a CO<sub>2</sub>-saturated 0.1 M KHCO<sub>3</sub> solution. (d) Nyquist plots of the BOC@rGO and BOC at -0.65 V in CO<sub>2</sub>-saturated 0.1 M KHCO<sub>3</sub>.

To further analyze the catalytic performances for electrocatalytic CO<sub>2</sub> reduction, controlled potential electrolysis (CPE) was carried out at various potentials between -0.7 and -1.05 V (*vs.* RHE) for 2 h in order to identify and measure the reduction products since selectivity is a crucial factor in determining the activity for CO<sub>2</sub>RR.

In addition, in the current time transient plots (**Figure 6a,b**), both BOC@rGO and BOC are stable across a large potential range since the current densities did not fluctuate substantially throughout the electrolysis process. The liquid products were analyzed by <sup>1</sup>H nuclear magnetic resonance (NMR) at the end of each 2 h electrolysis, and the faradaic efficiency (FE) was calculated accordingly using the standard curve determined by <sup>1</sup>H NMR (**Figure 6c**).

The Faradaic efficiency of formate (FE<sub>formate</sub>) inferred a significant potential dependency for both catalysts. With BOC@rGO catalyst, formate was detected at low potential of -0.65 V with a maximum FE<sub>formate</sub> of 15.8%. The FE<sub>formate</sub> initially enhanced when the overpotential was gradually increased, peaking at -0.8 V with a value of 97.4%, and then decreased, most likely due to increased HER competition and mass transport restrictions in H cells, as shown in **Figure 5b**. The FE<sub>formate</sub> exhibited a similar tendency to that of BOC@rGO catalyst in the case of BOC catalyst, with an increasing overpotential. However, at -0.65 V, the formate product could not be identified using BOC, which is consistent with the BOC catalyst need for a higher negative onset potential for the CO<sub>2</sub>RR, in agreement with the LSV studies. In addition, at each potential investigated, FE<sub>formate</sub> of BOC@rGO was always relatively higher than that of BOC, demonstrating greater selectivity towards CO<sub>2</sub>RR to produce formate. Additionally, as shown in **Figure S6d**, the formate partial current densities (J<sub>HCOOH</sub>) of BOC@rGO and BOC were determined and plotted against the working potential in which BOC@rGO exhibited a higher J<sub>HCOOH</sub> all across the potential window

from -0.7 to -1.05 V (*vs.* RHE), leading to its superior formate selectivity. The maximum  $J_{\text{HCOOH}}$  achieved at -1.05 V (*vs.* RHE) for BOC@rGO was 10.56  $\text{mAcm}^{-2}$  which is twice the value of BOC (4.96  $\text{mAcm}^{-2}$ ) at the same potential.

Owing to its high catalytic activity for  $\text{CO}_2$  reduction, we have conducted cyclic voltammetry (CV) tests in the non-faradaic regions to obtain the  $C_{\text{dl}}$  values and the corresponding curves of charging current density differences *vs.* scan speeds were used to compare the electrocatalytic activities of BOC@rGO and BOC (**Figure 7a,b**). When compared to the BOC control electrode, the  $C_{\text{dl}}$  value increased by a factor of 8, indicating that BOC@rGO nanosheet morphology owns significantly increased number of catalytically active sites available for the enhancement of  $\text{CO}_2\text{RR}$  activity (**Figure 7c**).

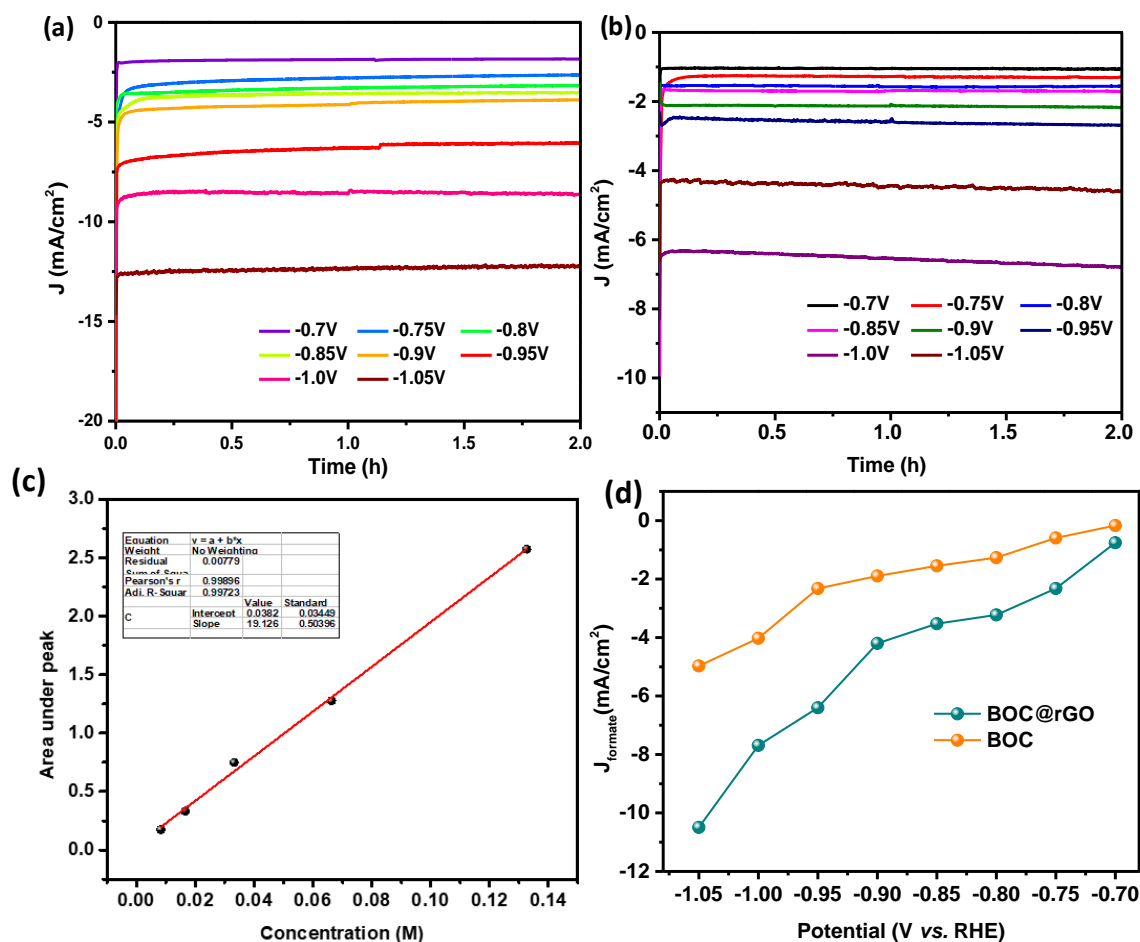


**Figure 6.** Chronoamperometry analysis at different potentials in  $\text{CO}_2$ -saturated 0.1M  $\text{KHCO}_3$  solution of (a) BOC@rGO and (b) BOC (c) Calibration curve for formate concentration determined by  $^1\text{H}$  NMR for  $\text{CO}_2\text{RR}$ . (d) Partial current densities for  $\text{HCOOH}$  production of BOC@rGO and BOC.

In order to gain insights into the mechanism of  $\text{CO}_2\text{RR}$ , we have analyzed the kinetics of formic acid ( $\text{HCOOH}$ ) formation based on Tafel plots presented in **Figure 7d**. The Tafel slopes for both catalysts (BOC@rGO and BOC) were found to be close to  $118 \text{ mV dec}^{-1}$ , suggesting that the rate-determining step (RDS) was  $\text{CO}_2^{\bullet-}$  intermediate formation. Additionally, a smaller Tafel slope

indicates more favorable catalytic properties. The BOC@rGO catalyst exhibited the lowest Tafel slope of  $126.4 \text{ mV dec}^{-1}$  than BOC ( $181.9 \text{ mV dec}^{-1}$ ), highlighting its superior catalytic [39].

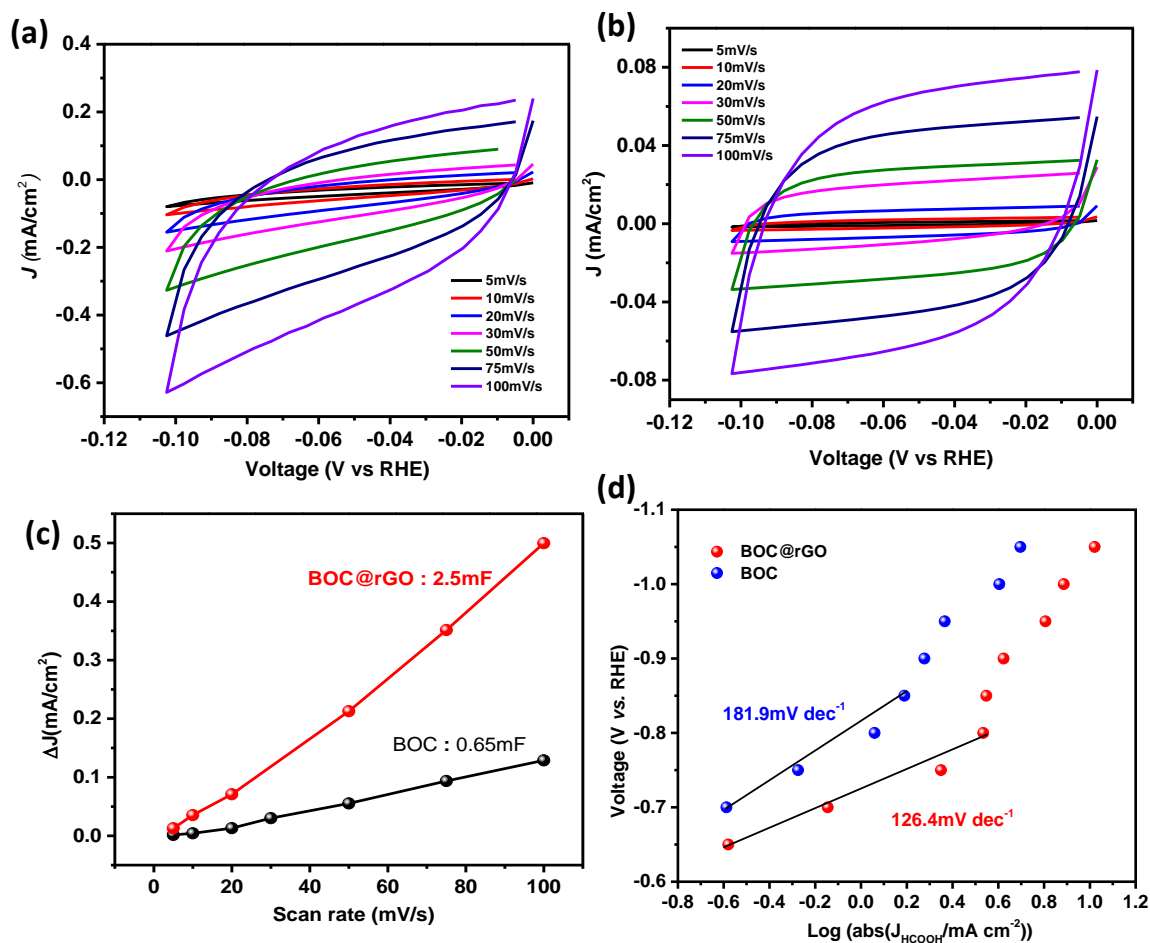


**Figure 7.** (a) CV curves of BOC@rGO and (b) BOC performed at different scan rates in Ar-saturated  $0.1 \text{ M KHCO}_3$  aqueous solution in non-faradaic region; (c)  $C_{dl}$  curves of BOC@rGO and BOC. (d) Tafel plots of BOC@rGO and BOC.

The stability of electrodes is a crucial factor in the steady and low-cost manufacturing for electrochemical processes, and is thus of paramount importance in real-world applications. In this study, the stability of BOC@rGO electrode was assessed, owing to its capacity for the reduction of  $\text{CO}_2$  to formate with a high FE. An extended electrochemical reduction experiment was

performed in a CO<sub>2</sub>-purged 0.1 M KHCO<sub>3</sub> electrolyte at a constant potential of -0.9 V vs. RHE. The results revealed that the current density remained essentially constant over the course of 22h, indicating the consistent catalytic capacity of the BOC@rGO electrode for CO<sub>2</sub> reduction (**Figure 2c**). Additionally, over the 22 h operational period, the BOC@rGO electrode displayed an outstanding FE<sub>formate</sub> (above 92%) without any significant catalytic degradation. Additionally, Bi 4f XPS and XRD analyses were carried out following the stability and showed that all peaks matched perfectly with the electrode used before electrolysis, indicating its good stability (**Figure 8**). Bi 4f<sub>7/2</sub> peak has undergone slight lower energy shift, indicating improvement in electrostatic interactions between Bi and rGO sheets.

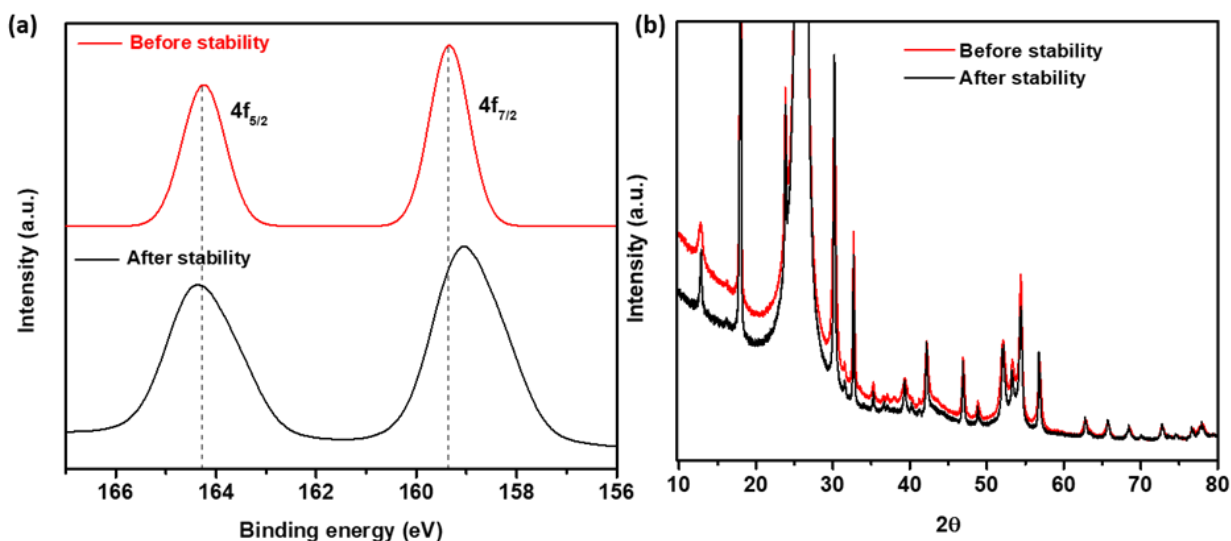


**Figure 8.** Bi 4f XPS spectra and XRD patterns of BOC@rGO after stability test. The spectra of as-prepared samples were shown for comparison.

Electron transport kinetics in CO<sub>2</sub> reduction were studied using electrochemical impedance spectroscopy (EIS). The Nyquist plots of BOC@rGO and BOC electrodes in a CO<sub>2</sub>-saturated 0.1M KHCO<sub>3</sub> solution were acquired and compared (**Figure 2d**). The results revealed that BOC@rGO had a smaller semicircle radius (22.4 Ω) compared to BOC (46.7 Ω), indicating lower interfacial

charge transfer resistance. This suggests faster electron transfer at the catalyst/electrolyte interface due to the favorable network conductivity of rGO. All EIS measurements were performed at a bias potential of -0.65 V vs. RHE.

### 3.3.3 Structural characterization of CuCoO@rGO

A facile one-step method was utilized to synthesize CuCoO@rGO electrocatalyst using chemical reducing agent NaBH<sub>4</sub>, as shown in **Figure 9a**. The crystal structure of the CuCoO@rGO sample was investigated using X-ray diffraction (XRD) analysis. The results indicated the presence of a bimetallic system with a cubic crystal structure for Cu (JCPDS no. 04-0836) and CoO (JCPDS no. 48-1719), as depicted in **Figure 9b**. Furthermore, the XRD patterns of the precursor catalysts exhibited similar patterns for copper reduction. However, for cobalt, only XRD patterns of Co(OH)<sub>2</sub> were observed. As a result of the coexistence of cobalt and copper ions, a synergistic phenomenon occurred, promoting the creation of a bimetallic crystal structure predominantly comprising metallic copper (Cu) and cobalt oxide (CoO). This crystal structure may feature a strong propensity for exceptional catalytic activity [41]. The morphology and microstructures of the produced samples were examined using field-emission scanning electron microscope (FE-SEM). **Figure 9c,d** presents the low and high magnification SEM images of the resulting CuCoO@rGO nanocomposite and showed aggregated and folded sheets composed of multiple graphene layers, alongside adjacent Cu and CoO nanoparticles. Energy-dispersive X-ray (EDX) analysis of the high magnification image exhibited a uniform distribution of both Cu and Co throughout the graphene sheets, confirming the coexistence of adjacent Cu and CoO particles (**Figure 9e**).

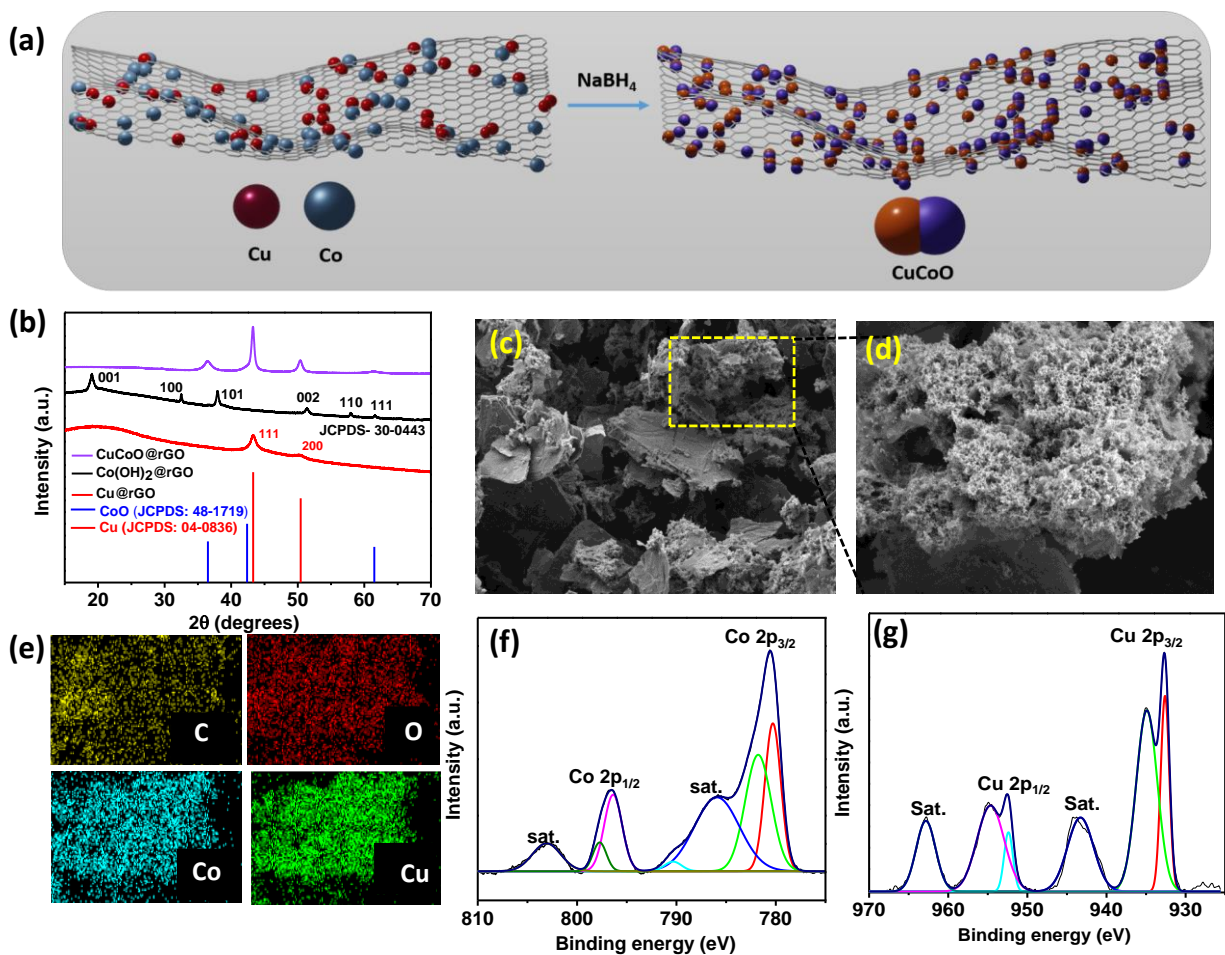


**Figure 9.** (a) Schematic illustration of CuCoO@rGO synthesis. (b) XRD patterns of Cu@rGO, Co@rGO and CuCoO@rGO. Low (c) and high (d) magnification SEM images of CuCoO@rGO. (e) EDS mapping of CuCoO@rGO electrode. High-resolution XPS spectra of (f) Co 2p and (g) Cu 2p of CuCoO@rGO.

Transmission electron microscopy (TEM) imaging of the CuCoO@rGO nanocomposite revealed the presence of CoO and Cu nanoparticles which are distributed on the rGO sheets (**Figure 10**). Moreover, the high-resolution TEM (HR-TEM) image in **Figure S10** revealed the existence of both Cu and CoO nanoparticles and also highlighted the interplanar distances between adjacent planes of 0.24 nm corresponding to the interplanar spacing of the (111) plane of CoO,

and 0.208 nm ascribed to the interplanar spacing of the (111) plane of Cu. This indicates that the Cu and CoO nanoparticles coexist adjacent to each other, forming bimetallic nanoparticles.

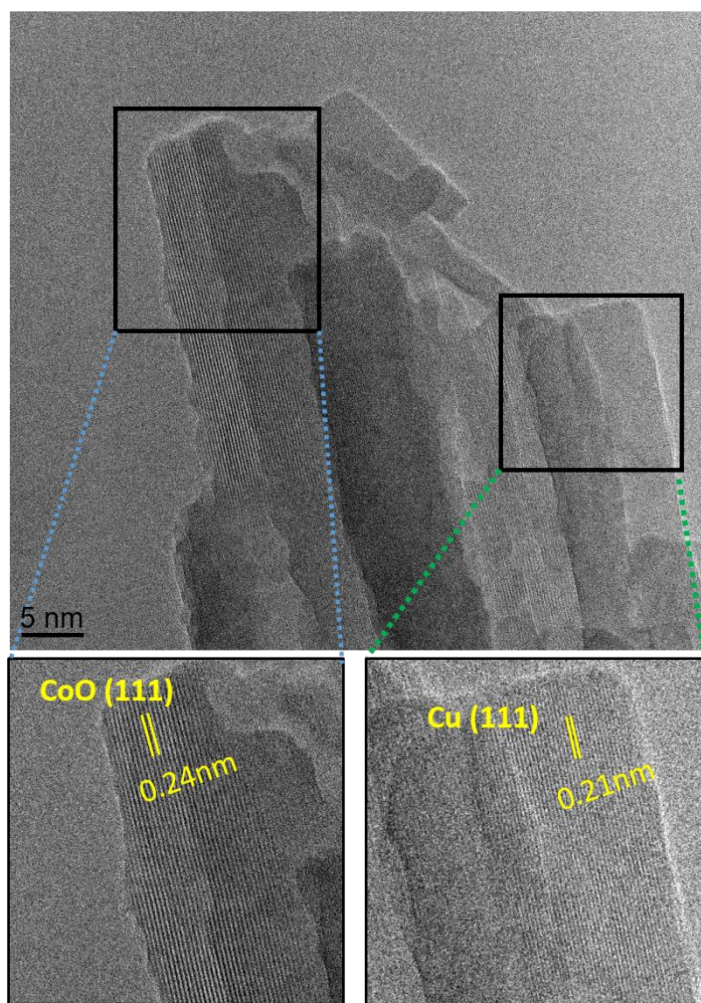


**Figure 10.** HR-TEM image of CuCoO@rGO nanocomposite.

The surface composition and chemical states of CuCoO@rGO were analyzed using X-ray photoelectron spectroscopy (XPS). The core level Co 2p high resolution XPS spectrum displayed three pairs of peaks, indicating the presence of multiple cobalt species with distinct chemical states (**Figure 9f**). The peaks observed at 779.8 and 795.0 eV correspond to the Co 2p<sub>3/2</sub> and Co 2p<sub>1/2</sub> of octahedral Co<sup>3+</sup>, respectively, while the peaks at 781.4 and 797.0 eV are ascribed to tetrahedral Co<sup>2+</sup> (784.2 and 801.8 eV). Furthermore, two satellite peaks were detected at 787.0 and 803.3 eV

(784.2 and 801.8 eV) were observed [42]. Furthermore, we have detected an another subtle and discernible satellite peak at 791.1 eV. This suggests the presence of  $\text{Co}^{3+}$  thereby unveiling the occurrence of cobalt oxide ( $\text{Co}_3\text{O}_4$ ) [43]. Meanwhile, the Cu 2p high-resolution XPS spectrum (**Figure 9g**) can be deconvoluted into Cu  $2p_{1/2}$  and Cu  $2p_{3/2}$  components corresponding due to metallic  $\text{Cu}^0$  (932.58 and 952.9 eV) and  $\text{Cu}^{2+}$  (935.1 and 955.0 eV) of  $\text{Cu}(\text{OH})_2$ . Also, we have observed two additional satellite peaks at 943.4 and 962.4 eV due to presence of oxides. These extra peaks are typically generated by the "shake up" phenomenon, where extra electrons are excited to higher energy levels [44]. These results match well the XRD data, which states the presence of Cu in metallic state. However, we have also observed some amount of  $\text{Cu}^{2+}$ , associated with  $\text{Cu}(\text{OH})_2$ , which could be possibly due to the use of KOH in synthesis process [45].

The electrocatalytic properties of  $\text{CuCoO@rGO}$  were examined using a three-electrode system. Prior to electro-reforming, the electrode was pretreated/activated by cyclic voltammetry at a scan rate of  $30 \text{ mV s}^{-1}$  in a 1 M KOH aqueous solution in the potential ranging from 0 to 0.8 V vs. Ag/AgCl electrode. The waste plastic was subjected to alkaline condition to partially hydrolyze it into TPA-K and EG, with the latter being selectively electrooxidized into valuable and separable chemicals. The concentration of EG obtained from PET hydrolysis was calculated using the calibration curve in **Figure 11 (a,b)** and found to be 42 mM. The LSV curves of  $\text{CuCoO@rGO}$  in 1 M KOH + PET hydrolysate solution displayed a lower onset potential of 1.15V and a high current density of  $20 \text{ mA cm}^{-2}$  was achieved at 1.45 V, as depicted in **Figure 12a**. In the absence of PET, the onset potential of the electrode was 1.4 V vs. RHE, and needed at least additional 0.2 V with respect to PET hydrolysate solution to achieve a current density of  $20 \text{ mA cm}^{-2}$ . Also, the LSV curves for individual  $\text{Cu@rGO}$  and  $\text{Co@rGO}$  were catalysts measured in 1M KOH which exhibited limited electrocatalytic performance when compared to the bimetallic

system. This phenomenon underscores the presence of a synergistic effect within the bimetallic catalyst, enhancing its catalytic activity (**Figure 11c**).

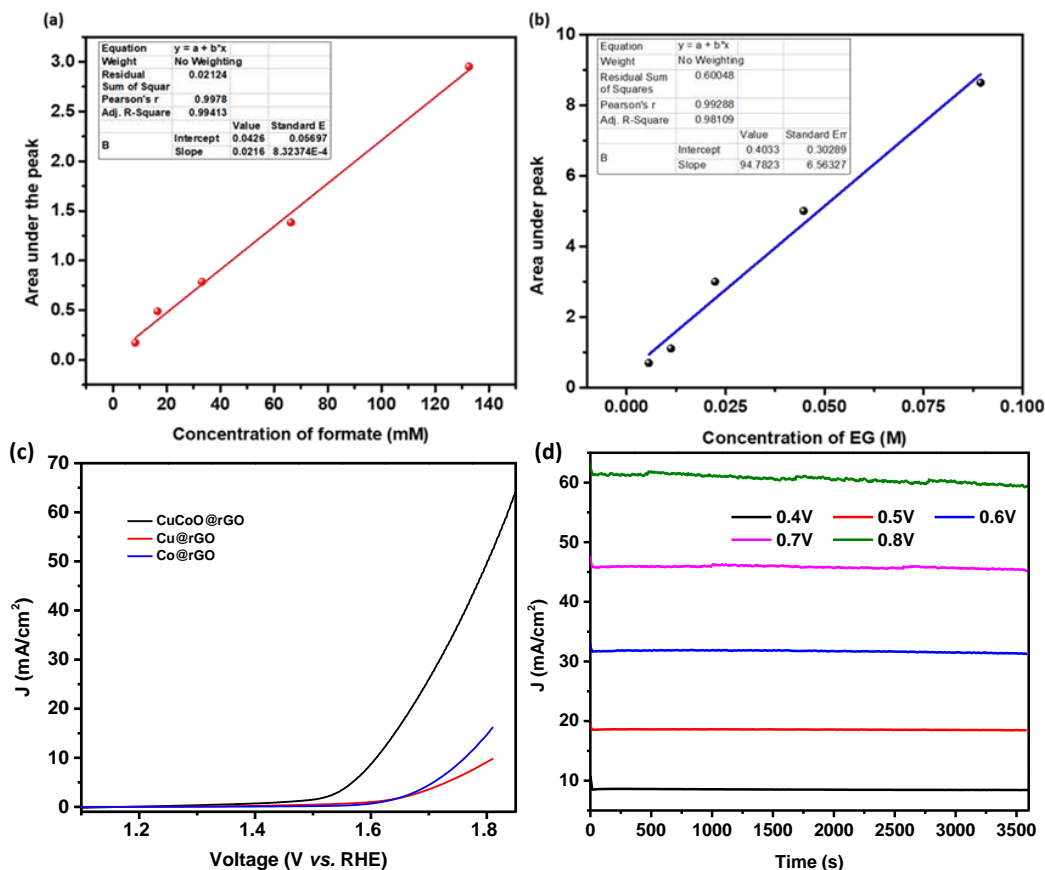


**Figure 11.** (a) Calibration curves for formate and (b) ethylene glycol concentrations determined by <sup>1</sup>H NMR for PET hydrolysate. (c) LSV curves of CuCoO@rGO, Cu@rGO and Co@rGO in 1M KOH solution at 10mV/s (d) Controlled potential electrolysis of PET hydrolysate solution using CuCoO@rGO.

For better understanding of intrinsic catalytic properties, the Tafel slope for PET hydrolysate oxidation was calculated to be 144 mV dec<sup>-1</sup>, while the Tafel slope for OER was considerably higher at 277 mV dec<sup>-1</sup>, as shown in **Figure 12b**, which suggests that EGOR is more favorable kinetically than OER. In **Figure 12c**, the Nyquist plot measured at 1.4 V vs. RHE demonstrated a decrease in the  $R_{ct}$  value from 103.9 to 8.5  $\Omega$  upon changing the electrolyte to PET hydrolysate.

This observation suggests enhanced charge transfer kinetics, indicating faster electron transfer processes that is consistent with high catalytic activity derived from the Tafel slope. To evaluate the oxidation products of the PET hydrolysate, we performed a CPE experiment in a solution containing 42 mM of EG in PET hydrolysate solution (**Figure 11c**). The qualitative and quantitative analysis of the electrolytic products was carried out using  $^1\text{H}$  and  $^{13}\text{C}$  nuclear magnetic resonance (NMR) spectroscopies. The highest FE, reaching 85.7%, was achieved at a potential of 1.5 V *vs.* RHE, which is considered the optimal potential in this study (**Figure 12d**). The obtained results revealed formate as the primary product of EG oxidation, as indicated by the chemical shift of approximately 8.45 ppm in  $^1\text{H}$  NMR. Upon complete electrolysis, the peak of EG at 3.5 ppm diminished, while the formate peak increased, indicating an efficient conversion of EG to formate during the electrolytic process (**Figure 13a**). To verify the durability of the CuCoO@rGO electrode for PET hydrolysate oxidation, we performed a long-term controlled-potential electrolysis for 72 h. After subjecting the CuCoO@rGO electrode to long-term electrolysis, the catalytic current density for the EG oxidation experienced a decrease primarily attributed to the consumption of EG present in the solution (**Figure 12e**). However, during this process, we also observed a corresponding increase and decrease in the concentration of formate (**Figure 12f**) after 30 h due to possibility of formate over-oxidation. To gain further insight into this phenomenon, we conducted  $^{13}\text{C}$  NMR analysis before, during and after electrolysis, which revealed a minor peak at 168 ppm after electrolysis in the  $^{13}\text{C}$  NMR plot, indicating the formation of carbonate ( $\text{CO}_3^{2-}$ ), resulting from the over-oxidation of formate present in the solution (**Figure 13b**) [30]. Additionally, the current decline could also be ascribed to Bi and Cu leaching into the electrolyte solution during the electrolysis process, as confirmed through ICP-MS analysis (**Table 1**).

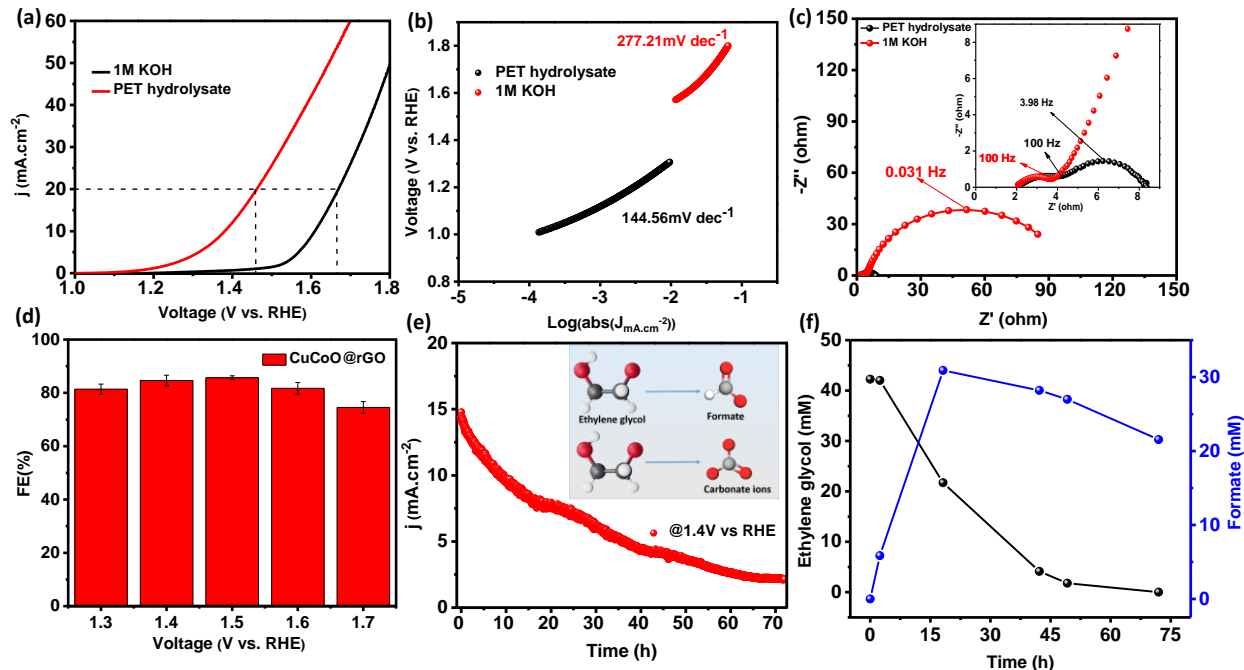


**Figure 12.** (a) LSV polarization curves of CuCoO@rGO in PET hydrolysate+1 M KOH solutions. (b) Tafel plots for OER and EG oxidation. (c) Nyquist plots for OER and 0.1 M EG oxidation at 1.4 V vs. RHE. (d) Faradaic efficiencies of EG oxidation at different potentials. (e) Long-term catalytic conversion of EG to formate. (f) Concentration profile of EG and formate during the long-term electrocatalytic process.

The conducted experiments collectively demonstrated the notable catalytic activity of CuCoO@rGO in the process of ethylene glycol (EG) oxidation, specifically derived from PET hydrolysate, leading to the production of formate and improving the profitability of PET recycling.

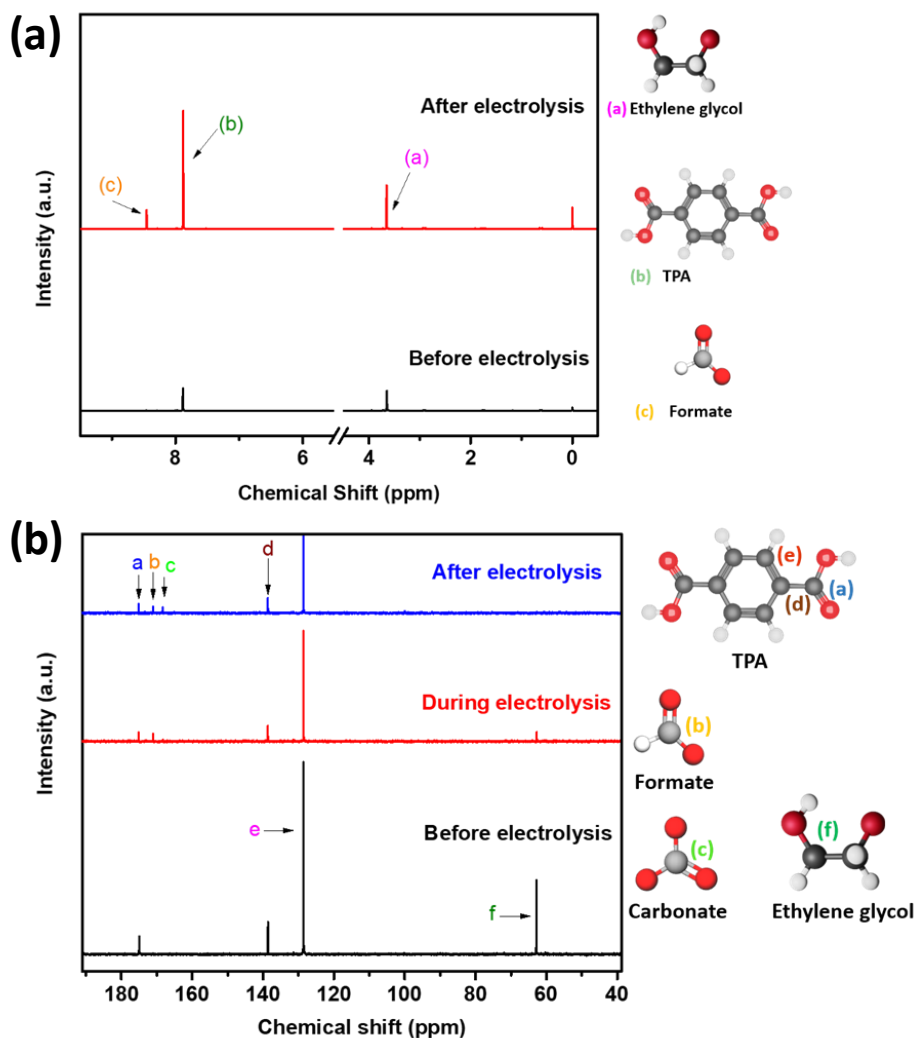


**Figure 13.** (a)  $^1\text{H}$  NMR before and after electrolysis of PET hydrolysate solution using CuCoO@rGO nanocomposite. (b)  $^{13}\text{C}$  NMR before, during and after electrolysis of PET hydrolysate solution using CuCoO@rGO.

### 3.3.4 Co-coupling of anode and cathode for concurrent production of formate

Based on the electrochemical studies, it was evidenced that CuCoO@rGO and BOC@rGO exhibited excellent activity for the anodic EG oxidation and cathodic  $\text{CO}_2\text{RR}$ , respectively. In the following experiment, a two-electrode electrolyzer (CuCoO@rGO||BOC@rGO) was constructed with CuCoO@rGO as the anode in 1 M KOH electrolyte+42 mM EG in PET hydrolysate solution,

and BOC@rGO as the cathode in 1 M KHCO<sub>3</sub> electrolyte for concurrent production of formic acid at the anode and cathode. Compared with the conventional OER-CO<sub>2</sub>RR system, the EG-CO<sub>2</sub>RR performance was significantly enhanced in terms of onset potential and current density due to the thermodynamically favorable EG oxidation over OER. The electrolyzer required a low potential of 1.9 V to achieve a current density of 10 mA cm<sup>-2</sup>, demonstrating superior formic acid synthesis performance through simultaneous cathodic CO<sub>2</sub>RR and anodic EG oxidation (**Figure 14a**). The required cell voltage was over 230 mV lower than conventional overall CO<sub>2</sub>RR to acquire 10 mA cm<sup>-2</sup>, which not only reduced energy consumption, but also favored formate formation as major product on both anode and cathode.

To evaluate the stability of the integrated system for formic acid production, a CPE analysis was conducted at various cell voltages ranging from 1.7 to 2.1 V in the two-electrode electrolyzer (**Figure 14c**). The coupled two-electrode system exhibited outstanding FE for formic acid production with a slight current decline most likely due to EG consumption. As depicted in **Figure 14b**, both CO<sub>2</sub>RR and anodic EG oxidation produced formic acid as a major product with a FE of 151.8% FE at a cell voltage of 1.9 V and achieved more than 130% in the entire potential range. This integrated approach not only offers an effective solution for converting PET plastic waste into valuable products, but also represents an attractive method for simultaneously producing formic acid with high Faradaic efficiency and minimal energy consumption at both the anode and cathode. However, it is noteworthy that research pertaining to concurrent formate production, particularly involving PET hydrolysate reactions, remains relatively limited. This underscores an opportune domain for advancement, ideally involving the development of a bifunctional electrocatalyst, thereby opening avenues for further enhancements in this burgeoning field [46]–[48].

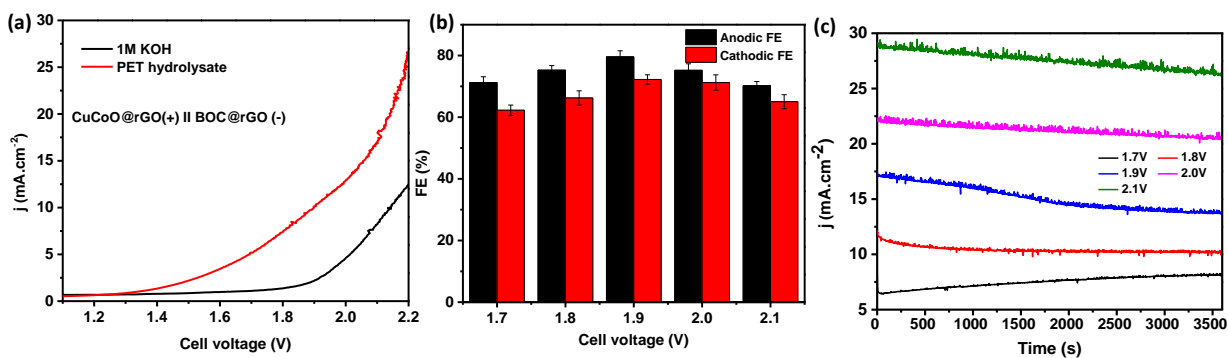


**Figure 14.** (a) LSV polarization curves of CuCoO@rGO in 1 M KOH+PET hydrolysate solution in a 2-electrode integrated electrolyzer. (b) Faradaic efficiencies at both cathode and anode at each potential using the 2-electrode integrated electrolyzer. (c) CPE analysis at various potentials in a 2-electrode system.

### 3.4 Conclusion

In this work, we report a co-electrolysis approach for concurrent generation of valuable formic acid from EG oxidation, derived from PET hydrolysis, and CO<sub>2</sub> reduction reaction at anode and cathode, respectively. Specifically, the anode and cathode attained formic acid production with Faradaic efficiencies of 85.7% and 97.4%, respectively, for their respective half-reactions. Furthermore, using a 2-electrode system, the electrolyzer achieved a remarkable Faradaic efficiency of 151.8% for formic acid synthesis at a cell voltage of 1.9 V. As a result, this integrated approach not only provides an effective solution for the valorization of PET plastic waste, but might pave the way for the economical and long-term production of value-added commodity chemicals from plastic waste and CO<sub>2</sub> reduction.

## References

- [1] P. De Luna, C. Hahn, D. Higgins, S. A. Jaffer, T. F. Jaramillo, and E. H. Sargent, “What would it take for renewably powered electrosynthesis to displace petrochemical processes?,” *Science* (80-. ), vol. 364, no. 6438, p. eaav3506, 2019, doi: 10.1126/science.aav3506.
- [2] Z. Li *et al.*, “Doping-modulated strain control of bifunctional electrocatalysis for rechargeable zinc–air batteries,” *Energy Environ. Sci.*, vol. 14, no. 9, pp. 5035–5043, 2021, doi: 10.1039/D1EE01271A.
- [3] S. Kim *et al.*, “Shape-controlled bismuth nanoflakes as highly selective catalysts for electrochemical carbon dioxide reduction to formate,” *Nano Energy*, vol. 39, pp. 44–52, 2017, doi: <https://doi.org/10.1016/j.nanoen.2017.05.065>.
- [4] J. Qiao, Y. Liu, F. Hong, and J. Zhang, “A review of catalysts for the electroreduction of carbon dioxide to produce low-carbon fuels,” *Chem. Soc. Rev.*, vol. 43, no. 2, pp. 631–675, 2014, doi: 10.1039/C3CS60323G.
- [5] D. Kim, J. Resasco, Y. Yu, A. M. Asiri, and P. Yang, “Synergistic geometric and electronic effects for electrochemical reduction of carbon dioxide using gold–copper bimetallic nanoparticles,” *Nat. Commun.*, vol. 5, no. 1, p. 4948, 2014, doi: 10.1038/ncomms5948.
- [6] Q. Gong *et al.*, “Structural defects on converted bismuth oxide nanotubes enable highly active electrocatalysis of carbon dioxide reduction,” *Nat. Commun.*, vol. 10, no. 1, p. 2807, 2019, doi: 10.1038/s41467-019-10819-4.
- [7] M. Fan *et al.*, “Uncovering the nature of electroactive sites in nano architected dendritic Bi for highly efficient CO<sub>2</sub> electroreduction to formate,” *Appl. Catal. B Environ.*, vol. 274, p. 119031, 2020, doi: <https://doi.org/10.1016/j.apcatb.2020.119031>.
- [8] J. Y. Kim *et al.*, “Electrodeposited CuAgHg Multimetallic Thin Films for Improved CO<sub>2</sub> Conversion: the Dramatic Impact of Hg Incorporation on Product Selectivity,” *ACS Appl. Energy Mater.*, vol. 3, no. 7, pp. 6670–6677, Jul. 2020, doi: 10.1021/acsaem.0c00784.
- [9] P. Ding *et al.*, “Metal-based electrocatalytic conversion of CO<sub>2</sub> to formic acid/formate,” *J. Mater. Chem. A*, vol. 8, no. 42, pp. 21947–21960, 2020, doi: 10.1039/D0TA08393C.
- [10] F. Cheng *et al.*, “Recent Progress of Sn-Based Derivative Catalysts for Electrochemical Reduction of CO<sub>2</sub>,” *Energy Technol.*, vol. 9, no. 1, p. 2000799, 2021, doi: <https://doi.org/10.1002/ente.202000799>.
- [11] A. Mustafa *et al.*, “Progress and perspective of electrochemical CO<sub>2</sub> reduction on Pd-based nanomaterials,” *Chem. Eng. Sci.*, vol. 245, p. 116869, 2021, doi: <https://doi.org/10.1016/j.ces.2021.116869>.
- [12] X. Huang *et al.*, “Ordered-Mesoporous-Carbon-Confined Pb/PbO Composites: Superior Electrocatalysts for CO<sub>2</sub> Reduction,” *ChemSusChem*, vol. 13, no. 23, pp. 6346–6352, 2020, doi: <https://doi.org/10.1002/cssc.202000329>.

- [13] V. S. S. Mosali *et al.*, “CdS-Enhanced Ethanol Selectivity in Electrocatalytic CO<sub>2</sub> Reduction at Sulfide-Derived Cu–Cd,” *ChemSusChem*, vol. 14, no. 14, pp. 2924–2934, 2021, doi: <https://doi.org/10.1002/cssc.202100903>.
- [14] Y. Wang *et al.*, “Sub-2 nm ultra-thin Bi<sub>2</sub>O<sub>2</sub>CO<sub>3</sub> nanosheets with abundant Bi-O structures toward formic acid electrosynthesis over a wide potential window,” *Nano Res.*, vol. 15, no. 4, pp. 2919–2927, 2022, doi: [10.1007/s12274-021-3903-0](https://doi.org/10.1007/s12274-021-3903-0).
- [15] L. Li, D.-K. Ma, F. Qi, W. Chen, and S. Huang, “Bi nanoparticles/Bi<sub>2</sub>O<sub>3</sub> nanosheets with abundant grain boundaries for efficient electrocatalytic CO<sub>2</sub> reduction,” *Electrochim. Acta*, vol. 298, pp. 580–586, 2019, doi: <https://doi.org/10.1016/j.electacta.2018.12.116>.
- [16] Y. Wang *et al.*, “BiPO<sub>4</sub>-Derived 2D Nanosheets for Efficient Electrocatalytic Reduction of CO<sub>2</sub> to Liquid Fuel,” *Angew. Chemie Int. Ed.*, vol. 60, no. 14, pp. 7681–7685, 2021, doi: <https://doi.org/10.1002/anie.202014341>.
- [17] T. Fan *et al.*, “Achieving high current density for electrocatalytic reduction of CO<sub>2</sub> to formate on bismuth-based catalysts,” *Cell Reports Phys. Sci.*, vol. 2, no. 3, p. 100353, 2021, doi: <https://doi.org/10.1016/j.xcrp.2021.100353>.
- [18] S. KOMATSU, T. YANAGIHARA, Y. HIRAGA, M. TANAKA, and A. KUNUGI, “Electrochemical Reduction of CO<sub>2</sub> at Sb and Bi Electrodes in KHCO<sub>3</sub> Solution,” *電気化学および工業物理化学*, vol. 63, no. 3, pp. 217–224, 1995, doi: [10.5796/kogyobutsurikagaku.63.217](https://doi.org/10.5796/kogyobutsurikagaku.63.217).
- [19] C. W. Lee *et al.*, “Selective Electrochemical Production of Formate from Carbon Dioxide with Bismuth-Based Catalysts in an Aqueous Electrolyte,” *ACS Catal.*, vol. 8, no. 2, pp. 931–937, Feb. 2018, doi: [10.1021/acscatal.7b03242](https://doi.org/10.1021/acscatal.7b03242).
- [20] X. Zhang, X. Sun, S.-X. Guo, A. M. Bond, and J. Zhang, “Formation of lattice-dislocated bismuth nanowires on copper foam for enhanced electrocatalytic CO<sub>2</sub> reduction at low overpotential,” *Energy Environ. Sci.*, vol. 12, no. 4, pp. 1334–1340, 2019, doi: [10.1039/C9EE00018F](https://doi.org/10.1039/C9EE00018F).
- [21] J. H. Koh *et al.*, “Facile CO<sub>2</sub> Electro-Reduction to Formate via Oxygen Bidentate Intermediate Stabilized by High-Index Planes of Bi Dendrite Catalyst,” *ACS Catal.*, vol. 7, no. 8, pp. 5071–5077, Aug. 2017, doi: [10.1021/acscatal.7b00707](https://doi.org/10.1021/acscatal.7b00707).
- [22] E. Zhang *et al.*, “Bismuth Single Atoms Resulting from Transformation of Metal–Organic Frameworks and Their Use as Electrocatalysts for CO<sub>2</sub> Reduction,” *J. Am. Chem. Soc.*, vol. 141, no. 42, pp. 16569–16573, Oct. 2019, doi: [10.1021/jacs.9b08259](https://doi.org/10.1021/jacs.9b08259).
- [23] H. Zhang, Y. Ma, F. Quan, J. Huang, F. Jia, and L. Zhang, “Selective electro-reduction of CO<sub>2</sub> to formate on nanostructured Bi from reduction of BiOCl nanosheets,” *Electrochem. commun.*, vol. 46, pp. 63–66, 2014, doi: <https://doi.org/10.1016/j.elecom.2014.06.013>.
- [24] S. Verma, S. Lu, and P. J. A. Kenis, “Co-electrolysis of CO<sub>2</sub> and glycerol as a pathway to carbon chemicals with improved techno-economics due to low electricity consumption,” *Nat. Energy*, vol. 4, no. 6, pp. 466–474, 2019, doi: [10.1038/s41560-019-0374-6](https://doi.org/10.1038/s41560-019-0374-6).
- [25] X. V Medvedeva, J. J. Medvedev, S. W. Tatarchuk, R. M. Choueiri, and A. Klinkova,

- “Sustainable at both ends: electrochemical CO<sub>2</sub> utilization paired with electrochemical treatment of nitrogenous waste,” *Green Chem.*, vol. 22, no. 14, pp. 4456–4462, 2020, doi: 10.1039/D0GC01754J.
- [26] J.-H. Guo and W.-Y. Sun, “Integrating Nickel-Nitrogen Doped Carbon Catalyzed CO<sub>2</sub> Electroreduction with Chlor-Alkali Process for CO, Cl<sub>2</sub> and KHCO<sub>3</sub> Production with Enhanced Techno-Economics,” *Appl. Catal. B Environ.*, vol. 275, p. 119154, 2020, doi: <https://doi.org/10.1016/j.apcatb.2020.119154>.
- [27] J. Na *et al.*, “General technoeconomic analysis for electrochemical coproduction coupling carbon dioxide reduction with organic oxidation,” *Nat. Commun.*, vol. 10, no. 1, p. 5193, 2019, doi: 10.1038/s41467-019-12744-y.
- [28] S. Ügdüler *et al.*, “Towards closed-loop recycling of multilayer and coloured PET plastic waste by alkaline hydrolysis,” *Green Chem.*, vol. 22, no. 16, pp. 5376–5394, 2020, doi: 10.1039/D0GC00894J.
- [29] C.-Y. Kao, W.-H. Cheng, and B.-Z. Wan, “Investigation of alkaline hydrolysis of polyethylene terephthalate by differential scanning calorimetry and thermogravimetric analysis,” *J. Appl. Polym. Sci.*, vol. 70, no. 10, pp. 1939–1945, 1998, doi: [https://doi.org/10.1002/\(SICI\)1097-4628\(19981205\)70:10<1939::AID-APP8>3.0.CO;2-G](https://doi.org/10.1002/(SICI)1097-4628(19981205)70:10<1939::AID-APP8>3.0.CO;2-G).
- [30] S. Behera, S. Dinda, R. Saha, and B. Mondal, “Quantitative Electrocatalytic Upcycling of Polyethylene Terephthalate Plastic and Its Oligomer with a Cobalt-Based One-Dimensional Coordination Polymer Having Open Metal Sites along with Coproduction of Hydrogen,” *ACS Catal.*, vol. 13, no. 1, pp. 469–474, Jan. 2023, doi: 10.1021/ACSCATAL.2C05270/ASSET/IMAGES/LARGE/CS2C05270\_0005.JPEG.
- [31] F. Liu, X. Gao, R. Shi, E. C. M. Tse, and Y. Chen, “A general electrochemical strategy for upcycling polyester plastics into added-value chemicals by a CuCo<sub>2</sub>O<sub>4</sub> catalyst,” *Green Chem.*, vol. 24, no. 17, pp. 6571–6577, 2022, doi: 10.1039/D2GC02049A.
- [32] Y. Li *et al.*, “Coupling of PET waste electroreforming with green hydrogen generation using bifunctional catalyst,” *Sustain. Energy Fuels*, vol. 6, no. 21, pp. 4916–4924, 2022, doi: 10.1039/D2SE01007K.
- [33] X. Li, J. Wang, M. Sun, X. Qian, and Y. Zhao, “Ti–Fe<sub>2</sub>O<sub>3</sub>/Ni(OH)<sub>x</sub> as an efficient and durable photoanode for the photoelectrochemical catalysis of PET plastic to formic acid,” *J. Energy Chem.*, vol. 78, pp. 487–496, 2023, doi: <https://doi.org/10.1016/j.jechem.2022.12.031>.
- [34] B. Zhang *et al.*, “Photoelectrochemical conversion of plastic waste into high-value chemicals coupling hydrogen production,” *Chem. Eng. J.*, vol. 462, p. 142247, 2023, doi: <https://doi.org/10.1016/j.cej.2023.142247>.
- [35] K. Chang and W. Chen, “In situ synthesis of MoS<sub>2</sub>/graphene nanosheet composites with extraordinarily high electrochemical performance for lithium ion batteries,” *Chem. Commun.*, vol. 47, no. 14, pp. 4252–4254, 2011, doi: 10.1039/C1CC10631G.
- [36] X. Bian, X. Lu, Y. Xue, C. Zhang, L. Kong, and C. Wang, “A facile one-pot hydrothermal

- method to produce SnS<sub>2</sub>/reduced graphene oxide with flake-on-sheet structures and their application in the removal of dyes from aqueous solution,” *J. Colloid Interface Sci.*, vol. 406, pp. 37–43, 2013, doi: <https://doi.org/10.1016/j.jcis.2013.05.075>.
- [37] E. Gao and W. Wang, “Role of graphene on the surface chemical reactions of BiPO<sub>4</sub>-rGO with low OH-related defects,” *Nanoscale*, vol. 5, no. 22, pp. 11248–11256, 2013, doi: [10.1039/C3NR03370H](https://doi.org/10.1039/C3NR03370H).
- [38] M. M. Lucchese *et al.*, “Quantifying ion-induced defects and Raman relaxation length in graphene,” *Carbon N. Y.*, vol. 48, no. 5, pp. 1592–1597, 2010, doi: <https://doi.org/10.1016/j.carbon.2009.12.057>.
- [39] D. D. Zhu, J. L. Liu, and S. Z. Qiao, “Recent Advances in Inorganic Heterogeneous Electrocatalysts for Reduction of Carbon Dioxide,” *Adv. Mater.*, vol. 28, no. 18, pp. 3423–3452, 2016, doi: <https://doi.org/10.1002/adma.201504766>.
- [40] S. Zhang, P. Kang, and T. J. Meyer, “Nanostructured Tin Catalysts for Selective Electrochemical Reduction of Carbon Dioxide to Formate,” *J. Am. Chem. Soc.*, vol. 136, no. 5, pp. 1734–1737, Feb. 2014, doi: [10.1021/ja4113885](https://doi.org/10.1021/ja4113885).
- [41] J. Zhao *et al.*, “Insights into Electrocatalytic Nitrate Reduction to Ammonia via Cu-Based Bimetallic Catalysts,” *ACS Sustain. Chem. Eng.*, vol. 11, no. 6, pp. 2468–2475, Feb. 2023, doi: [10.1021/acssuschemeng.2c06498](https://doi.org/10.1021/acssuschemeng.2c06498).
- [42] C. Guan, X. Liu, W. Ren, X. Li, C. Cheng, and J. Wang, “Rational Design of Metal-Organic Framework Derived Hollow NiCo<sub>2</sub>O<sub>4</sub> Arrays for Flexible Supercapacitor and Electrocatalysis,” *Adv. Energy Mater.*, vol. 7, no. 12, p. 1602391, Jun. 2017, doi: <https://doi.org/10.1002/aenm.201602391>.
- [43] N. Fontañá-Troitiño *et al.*, “Room-Temperature Ferromagnetism in Antiferromagnetic Cobalt Oxide Nanooctahedra,” *Nano Lett.*, vol. 14, no. 2, pp. 640–647, Feb. 2014, doi: [10.1021/nl4038533](https://doi.org/10.1021/nl4038533).
- [44] A. Roy, H. S. Jadhav, and J. Gil Seo, “Cu<sub>2</sub>O/CuO Electrocatalyst for Electrochemical Reduction of Carbon Dioxide to Methanol,” *Electroanalysis*, vol. 33, no. 3, pp. 705–712, Mar. 2021, doi: <https://doi.org/10.1002/elan.202060265>.
- [45] N. Cheng *et al.*, “Cu/(Cu(OH)<sub>2</sub>-CuO) core/shell nanorods array: in-situ growth and application as an efficient 3D oxygen evolution anode,” *Electrochim. Acta*, vol. 163, pp. 102–106, 2015, doi: <https://doi.org/10.1016/j.electacta.2015.02.099>.
- [46] Y. Pan *et al.*, “Renewable formate from sunlight, biomass and carbon dioxide in a photoelectrochemical cell,” *Nat. Commun. 2023 141*, vol. 14, no. 1, pp. 1–10, Feb. 2023, doi: [10.1038/s41467-023-36726-3](https://doi.org/10.1038/s41467-023-36726-3).
- [47] X. Wei, Y. Li, L. Chen, and J. Shi, “Formic Acid Electro-Synthesis by Concurrent Cathodic CO<sub>2</sub> Reduction and Anodic CH<sub>3</sub>OH Oxidation,” *Angew. Chemie Int. Ed.*, vol. 60, no. 6, pp. 3148–3155, Feb. 2021, doi: [10.1002/anie.202012066](https://doi.org/10.1002/anie.202012066).
- [48] J. Wang *et al.*, “Electrocatalytic Valorization of Poly(ethylene terephthalate) Plastic and CO<sub>2</sub> for Simultaneous Production of Formic Acid,” *ACS Catal.*, vol. 12, no. 11, pp. 6722–6728, Jun. 2022, doi: [10.1021/acscatal.2c01128](https://doi.org/10.1021/acscatal.2c01128).

# Chapter 4

## **Pulse Electrodeposition of Bismuth on Activated Carbon Felt for Efficient Electrocatalytic CO<sub>2</sub> Reduction and NiCoPO<sub>x</sub> for Effective Anodic PET Degradation to Formate**

Kilaparathi Sravan Kumar<sup>1</sup>, Ahmed addad, Sabine Szunerits<sup>1</sup>, and Rabah Boukherroub<sup>1\*</sup>

<sup>1</sup>Univ. Lille, CNRS, Univ. Polytechnique Hauts-de-France, UMR 8520 - IEMN, F-59000 Lille, France

## **Abstract**

Polyethylene terephthalate (PET), a common single-use plastic, significantly contributes to CO<sub>2</sub> emissions when discarded. In this study, we have employed an innovative approach by combining electrochemical PET hydrolysate oxidation and the CO<sub>2</sub> reduction reaction (CO<sub>2</sub>RR) to simultaneously produce formate. Utilizing simple electrochemical methods, a porous 3D carbon felt (CF) electrode was anodically oxidized to produce activated surface. The latter was used as a support for electrochemical deposition of bismuth oxide carbonate (BOC) and nickel cobalt phosphate (NiCoPO<sub>x</sub>) for CO<sub>2</sub>RR and anodic PET hydrolysate oxidation, respectively. Both electrodes exhibited faradaic efficiencies (FE) exceeding 90% in their respective half-cell reactions. When implemented in a two-electrolyzer setup, an outstanding combined FE of up to 157% for both reactions was recorded at a remarkably low cell voltage of 1.8V. This research highlights the use of non-noble metals to transform PET plastic waste and CO<sub>2</sub> into valuable products.

**Key words:** Carbon felt, PET hydrolysate, CO<sub>2</sub> reduction, formate, electrolyzer

## 4.1 Introduction

As worries about the depletion of fossil resources and the growth in greenhouse gas emissions grow, it is becoming increasingly vital to find sustainable methods for producing chemicals and fuels from renewable carbon sources rather than fossil fuels ([1], [2]). Electrochemical CO<sub>2</sub> reduction (CO<sub>2</sub>RR) represents an attractive approach for generating sustainable chemicals and fuels, while mitigating CO<sub>2</sub> emissions. Extensive efforts have been dedicated to enhancing CO<sub>2</sub> reduction catalysis using metal electrocatalysts like Sn, Bi, In, Cd, Hg, Pb, among others. These studies have shown improved product selectivity and reduced overpotential for CO<sub>2</sub>RR ([3]–[8]). However, most of these investigations employ traditional CO<sub>2</sub>RR cells, requiring a substantial overpotential and yielding low-value oxygen byproduct through the anodic oxygen evolution reaction (OER). The oxygen byproduct tends to generate reactive oxygen species, potentially leading to cell membrane degradation ([9], [10]). According to recent studies, the OER accounts for more than 90% of the energy required for CO<sub>2</sub> electrolysis to formic acid ([11]). To solve this issue, researchers have devoted substantial efforts for replacing OER with alternative thermodynamically favorable and economically feasible oxidation processes. By adopting this approach, the anodic process could be replaced by oxidation of small reductive organic molecules such as aldehydes [12], alcohols [13], [14], urea [15], glucose [16] and 5-hydroxymethylfurfural [17]. Recently, researchers revealed a method for producing formic acid that combines CO<sub>2</sub> reduction using SnO<sub>2</sub> grown on carbon cloth with anodic partial methanol oxidation using CuO nanosheets on copper foam [13]. Despite the fact that combining organic oxidation reactions with CO<sub>2</sub>RR has significant promise, the high cost and restricted manufacturing scale of pure organic molecules make it economically unfeasible and difficult to scale up for usage with CO<sub>2</sub>RR.

Another significant issue we face today is the massive accumulation of polyethylene terephthalate (PET) plastic debris in the ocean and landfills as a result of its extremely sluggish natural breakdown kinetics ([18], [19]). Several methods have been developed to recycle PET waste using mechanical, biological, and chemical processes, with the chemical method having the most potential for upcycling PET waste, due to its higher depolymerization rate and minimal reduction in material properties ([20], [21]). Alkaline hydrolysis can breakdown the polyester nature of PET into its monomers with excellent yields of terephthalate (TPA) and ethylene glycol (EG) ([18], [22], [23]). Recently, Zhou et al. have utilized EG, derived from PET alkaline hydrolysis, to produce potassium diformate, terephthalic acid and hydrogen fuel ([22]). They have synthesized nickel cobalt phosphide ( $\text{CoNi}_{0.25}\text{P}$ ) on nickel foam and achieved a formate faradaic efficiency (FE) of more than 80% at 1.8V cell voltage in an electrolyzer assembly. Wang et al. utilized copper nanowires based electrocatalyst for EG oxidation to formic acid. They achieved 88% FE after delivering 62C of charge in 0.1 M KOH/10 mM EG electrolyte. Using density functional theory (DFT) calculations, they found that CuO surface tends to selectively break the C-C bond into formate ([24]). These electro-reforming studies provided a promising way to convert PET plastic waste into valuable commodities. Taking into-account the many benefits stated before, it is viable to use electrocatalysis to couple  $\text{CO}_2\text{RR}$  and EG oxidation, produced from PET waste, to generate formate at both cathode and anode by replacing sluggish OER, which needs a high potential of 1.23V. However, there has been very limited reports on coupling  $\text{CO}_2\text{RR}$  with PET hydrolysate reaction ([25]). On the other hand, it is crucial for industrial applications to employ large, cost-effective and stable electrode materials. In this context, utilizing a 3D-based carbon felt (CF) electrode, which is economical, easily producible, and possessing superior conductivity, appears

promising ([26]). Nevertheless, CF electrodes are inherently hydrophobic, necessitating effective hydrophilization methods to enable the deposition of catalytic materials ([27]).

Our recent work introduced a novel approach involving cathodic polarization of CF at various potentials (-2, -2.5, -3, and -4 V *vs.* RHE) and pre-polarization periods (0.5, 2, 4, and 12 h) in 1M KOH solution to enhance its performance in metal-free hydrogen evolution reaction. X-ray photoelectron spectroscopy (XPS) analysis confirmed the formation of oxygen-containing groups on the CF surface after cathodic activation. These groups are believed to enhance water adsorption and serve as active sites for hydrogen generation ([26]). Importantly, this technique is simple and can be readily applied to a wide range of electrode materials. However, to generate more prominent oxygen content groups on CF, which act as binder free template for metal catalyst deposition, anodic polarization is better suited.

In this study, activated carbon felt (aCF) substrate was produced by anodic polarization in 1M KOH to introduce oxygen species into its surface, resulting in an enhanced number of active sites accessible for metal adsorption for electrocatalytic processes. Then, a simple pulse electrodeposition approach was employed to deposit bismuth oxide carbonate nanosheets on the activated carbon felt (BOC@aCF) for CO<sub>2</sub> reduction reactions (CO<sub>2</sub>RR). BOC@aCF electrode showed a significant increase in activity and selectivity, with a high faradaic efficiency (FE) of 95% for formate at an overpotential of 0.71V and long-term durability for at least 22 h in a 0.5 M KHCO<sub>3</sub> electrolyte solution. Furthermore, the same electrodeposition method was applied to deposit NiCoPO<sub>x</sub> on activated CF for ethylene glycol (EG) oxidation to produce formate, with the highest FE of 96% at 1.5 V *vs.* RHE. To simulate real-world applications, we built a two-electrode electrolyzer that demonstrated that both BOC@CF and NiCoPO<sub>x</sub>@CF electrodes achieved a

current density of 20 mA/cm<sup>2</sup> at a cell voltage of 1.8V, producing formate at the cathode and anode with an overall FE of 157%.

## **4.2 Materials and methods**

### **4.2.1. Reagents and materials**

Bismuth nitrate pentahydrate (Bi(NO<sub>3</sub>)<sub>3</sub>·5H<sub>2</sub>O, 98%), monosodium phosphate (NaH<sub>2</sub>PO<sub>4</sub>·2H<sub>2</sub>O, ≥98%), Citric acid (99%), Nitric acid (90%), potassium hydroxide (KOH), potassium bicarbonate (KHCO<sub>3</sub>, ≥99.5%), ethylene glycol (EG, 99.5%), Nickel nitrate hexahydrate (Ni(NO<sub>3</sub>)<sub>2</sub>·6H<sub>2</sub>O, 99%), and Cobalt nitrate hexahydrate (Co(NO<sub>3</sub>)<sub>2</sub>·6H<sub>2</sub>O, 99%), were procured from Sigma-Aldrich (France). The Sustainion®X37-50-grade membrane was purchased from the fuel cell store. Proton-exchange membrane (Nafion 117) was obtained from Sigma-Aldrich (France). All the reagents were of analytical grade and utilized without any further purification. Ultrapure water (DI) (18 MΩ·cm) was used for preparation of all electrolyte solutions.

### **4.2.2. Anodic activation of carbon felt**

A freshly cleaned untreated carbon felt (CF) was utilized as the working electrode, with Ag/AgCl (3M KCl) as the reference electrode and a Platinum coil as the counter electrode. Chronoamperometry was performed at 2.5 V (vs. RHE) for 1h in a 1M KOH solution. Subsequently, the activated CF (aCF) was cleaned three times with deionized water to remove excess electrolyte trapped within the 3D electrode structure. The CF had a geometric area of 2.8 cm<sup>2</sup> and dimensions of 1×1×0.2 cm, and this same area was considered throughout the entire study.

### **4.2.3. Pulse-electrodeposition of bismuth**

Bismuth dendrites were deposited on a freshly activated carbon felt (Bi@aCF, 1×1×0.2 cm) via a pulse electrodeposition method in a three-electrode system with a saturated calomel electrode (SCE) and a platinum coil as the reference electrode and the counter electrode, respectively. The electrolyte used for deposition consists of 15 mM Bi(NO<sub>3</sub>)<sub>3</sub>·5H<sub>2</sub>O, 5 mM citric acid and 0.1 M HNO<sub>3</sub>. The electrochemical deposition experiment was carried by 5s OFF and 2s ON pulses for 100 cycles. To ensure better metal ions transport to the active sites on aCF, we have adopted pulse electrodeposition technique. Later, the as-prepared Bi@aCF was subjected to thermal annealing at 200°C for 3h to ensure the formation of bismuth oxide (Bi<sub>2</sub>O<sub>3</sub>@aCF) and the temperature is set below the melting point of bismuth (270°C). The oxidized electrode was later transformed *in situ* into bismuth oxide carbonate (BOC@aCF) electrochemically by keeping at a constant potential of -0.8V (*vs.* SCE) for 1h in 0.5M CO<sub>2</sub> saturated KHCO<sub>3</sub> and the resulting electrode was cleaned thoroughly in DI water and kept for overnight drying at 60°C.

#### **4.2.4. Electrodeposition of NiCoPO<sub>x</sub>**

The synthesis method used in this study was adapted from our prior research ([28]). NiCoPO<sub>x</sub> on activated carbon felt (NiCoPO<sub>x</sub>@aCF) was prepared using a one-step electrochemical deposition technique. The electrolyte solution consisted of 58.6 mg of Ni(NO<sub>3</sub>)<sub>2</sub>·6H<sub>2</sub>O, 58.4 mg of Co(NO<sub>3</sub>)<sub>3</sub>·6H<sub>2</sub>O, and 22 mg of sodium hypophosphite monohydrate, which were sequentially added to a phosphate buffer mixture (40 mL) with a pH of 5.5. The electrodeposition process was carried out under a constant potential of -0.8 V *vs.* Ag/AgCl for 15 min. The setup included a three-electrode system with activated carbon felt as the working electrode (WE), Ag/AgCl as the reference electrode (RE), and platinum foil as the counter electrode (CE).

#### **4.2.5. Hydrolysis of PET plastic**

In order to depolymerize PET, a clean PET water bottle was finely cut into small threads and washed with ethanol and water. Then, 1 g of the dried plastic threads was added into 30 mL of 2 M KOH solution and transferred into a 45 mL Teflon-lined autoclave, which was sealed and maintained at 180°C for 2 h. After cooling to room temperature, the resulting solution containing ethylene glycol (EG) and terephthalate acid (TPA) was filtered and used as the electrolyte for electrochemical tests and analyses ([22]).

#### 4.2.6. Electrochemical CO<sub>2</sub> reduction

The electrochemical CO<sub>2</sub> reduction (CO<sub>2</sub>RR) was performed in a conventional H-cell with the cathodic and anodic chambers separated by a proton-exchange membrane (Nafion 117). A platinum coil and Ag/AgCl (3 M KCl) were used as counter and reference electrodes, respectively. The working and reference electrodes were placed in the cathode compartment for electrochemical testing, and the Pt counter electrode was placed in another anode compartment. Before the measurements, the electrolyte was saturated with CO<sub>2</sub> or N<sub>2</sub>. The Nernst equation was used to convert the recorded potential ( $V_{\text{Ag/AgCl}}$ ) into reversible hydrogen electrode ( $V_{\text{RHE}}$ ) using the following equation:  $V_{\text{RHE}} = V_{\text{Ag/AgCl}} + 0.197 + 0.059 \cdot \text{pH}$ . Electrochemical impedance spectra (EIS) with an amplitude of 10 mV were recorded at various potentials in the frequency range of 1 MHz to 1 Hz.

Different constant working potentials were applied throughout a 1 h-CO<sub>2</sub> electroreduction experiment, and the catholyte was stirred at a rate of 300 rpm, while the flow rate of CO<sub>2</sub> gas was kept constant at 20 mL min<sup>-1</sup>. Bruker 300 MHz <sup>1</sup>H liquid NMR spectrometer was utilized for quantification of liquid products after the experiments using a water suppression approach. An internal standard approach was used to calculate the amount of produced formate. The following equation was applied to compute the Faradaic efficiency of formate:

$$FE(\%) = \frac{(\text{mole of produced product} \times n \times 96500)}{\text{total charge passed}}$$

where n is the number of electrons transferred for each product, n=2 for formate in CO<sub>2</sub> reduction, n=3 for formate in PET degradation.

### 4.3. Results and discussion

Before deposition, the CF was electrochemically treated due to its hydrophobic nature and lack of oxygen containing groups on its surface. The treatment was performed by applying an oxidation potential of 2.5V (vs. RHE) for 30 min, and the activated sample was used as a substrate for the electrodeposition of metal ions. To assess the effects of the anodic activation, the morphology of the CF samples pre- and post-polarization was examined using field-effect scanning electron microscopy (FESEM). The high-magnification SEM image revealed smooth fiber walls with an average diameter of 2 μm, featuring a few protrusions (**Figure 1a**). After anodic activation, noticeable changes in the surface morphology were observed, characterized by patches visible even at low magnification (**Figure 1b**). These alterations are attributed to the release of carbon atoms, replaced by oxygen content, thus enhancing the electrocatalytic active surface area ([29]).

X-ray photoelectron spectroscopy (XPS) was employed to characterize the chemical composition of the surface of the CF before and after electrochemical treatment. The analysis revealed that the untreated CF surface predominantly consisted of carbon and oxygen elements which could be confirmed by the XPS survey spectrum (**Figure 1c,d**). However, we see some extra peaks in the XPS survey spectrum of the electrochemically-treated which may arise from the 1M KOH electrolyte during activation step. After treatment, the O/C ratio of CF increased from 5.29% to 20.78%. High-resolution XPS was utilized to examine the C<sub>1s</sub> region and determine the elemental states of the surface for comparison between the untreated CF and the treated samples.

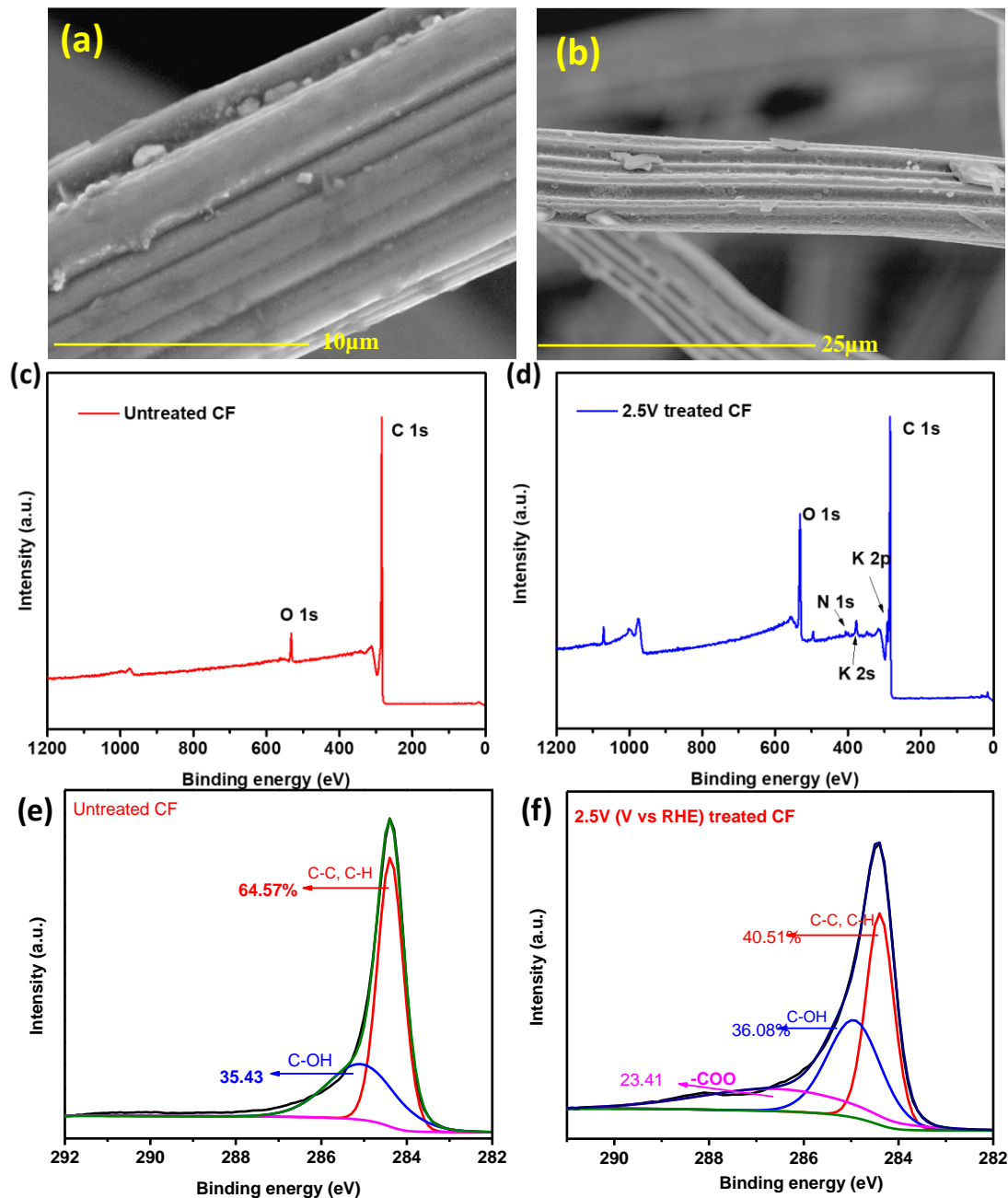


**Figure 1.** (a) SEM micrographs of untreated CF at high magnification. (b) Low magnification image of electrochemically treated CF at 2.5V vs. RHE in 1M KOH. XPS survey spectra of (c) untreated and (d) electrochemically treated CF. High resolution spectra of the C 1s of (e) untreated CF and (f) electrochemically-treated CF and quantity of specific functional groups measured by area under the peak in percentages.

The core level C<sub>1s</sub> XPS spectrum of the untreated CF could be deconvoluted by two distinct peaks, corresponding to graphitic carbon (284.6 eV) and carbon associated with alcohol, ether, or phenolic groups (286.2–286.5 eV) ([30]).

The relative composition of these peaks, expressed as the ratio of each peak area to the total peak area, is presented in **Figure 1e**. The untreated CF is curve-fitted with two peaks related to C-O (35.43%) and C-C (64.57%) (**Figure 1e**). Following the electrochemical oxidation treatment, three peaks were detected in the C<sub>1s</sub> region, corresponding to C-C, C-O and -COO bonds, with peak ratios of 40.51%, 36.08% and 23.41%, respectively (**Figure 1f**). These results indicate an increase in oxygen-containing groups on the oxidized CF surface, as evidenced by the greater -CO and -COO peak areas ([31]).

Subsequently, a simple pulse electrodeposition (pED) technique was employed to deposit bismuth (Bi) on the activated carbon fiber (aCF) surface (**Figure 2a**). This technique facilitates the access of Bi<sup>3+</sup> ions to all active sites on the aCF surface, effectively preventing mass transport limitations and ensuring uniform growth of the Bi coating over the aCF surface ([32]). To further enhance the catalytic surface area and maximize oxidation-based defects, the as-prepared Bi@aCF was subjected to thermal treatment at 220 °C for 4 h, resulting in the formation of bismuth oxide (Bi<sub>2</sub>O<sub>3</sub>) ([33]). XRD analysis confirmed the formation Bi dendrites to Bi<sub>2</sub>O<sub>3</sub> on the aCF, matching well with the ICDD no. 04-015-6851. However, when the as prepared Bi<sub>2</sub>O<sub>3</sub>@aCF was subjected to constant potential electrolysis at -0.8V vs. SCE for 1 h in a 0.5 M KHCO<sub>3</sub> solution, an *in-situ* transformation of the morphology to Bi<sub>2</sub>O<sub>2</sub>CO<sub>3</sub> (BOC) was observed. This transformation was confirmed by XRD measurements, which exhibited diffraction patterns matching the tetragonal Bi<sub>2</sub>O<sub>2</sub>CO<sub>3</sub> phase (ICDD card no. 41-1488) (**Figure 2b**).

FESEM imaging was conducted to investigate the morphology evolution. The initial pED process resulted in large dendritic structures covering the entire surface of the aCF, indicating efficient utilization of the surface area (**Figure 2c**). The high resolution image of Bi dendrites confirms the uniform deposition of Bi all over the aCF (**Figure 2d**). After thermal treatment, these dendrites were transformed into large particles of  $\text{Bi}_2\text{O}_3$ , as confirmed by energy dispersive X-ray (EDX) analysis, which revealed uniform deposition of Bi and O across the aCF (**Figure 2e,f**).

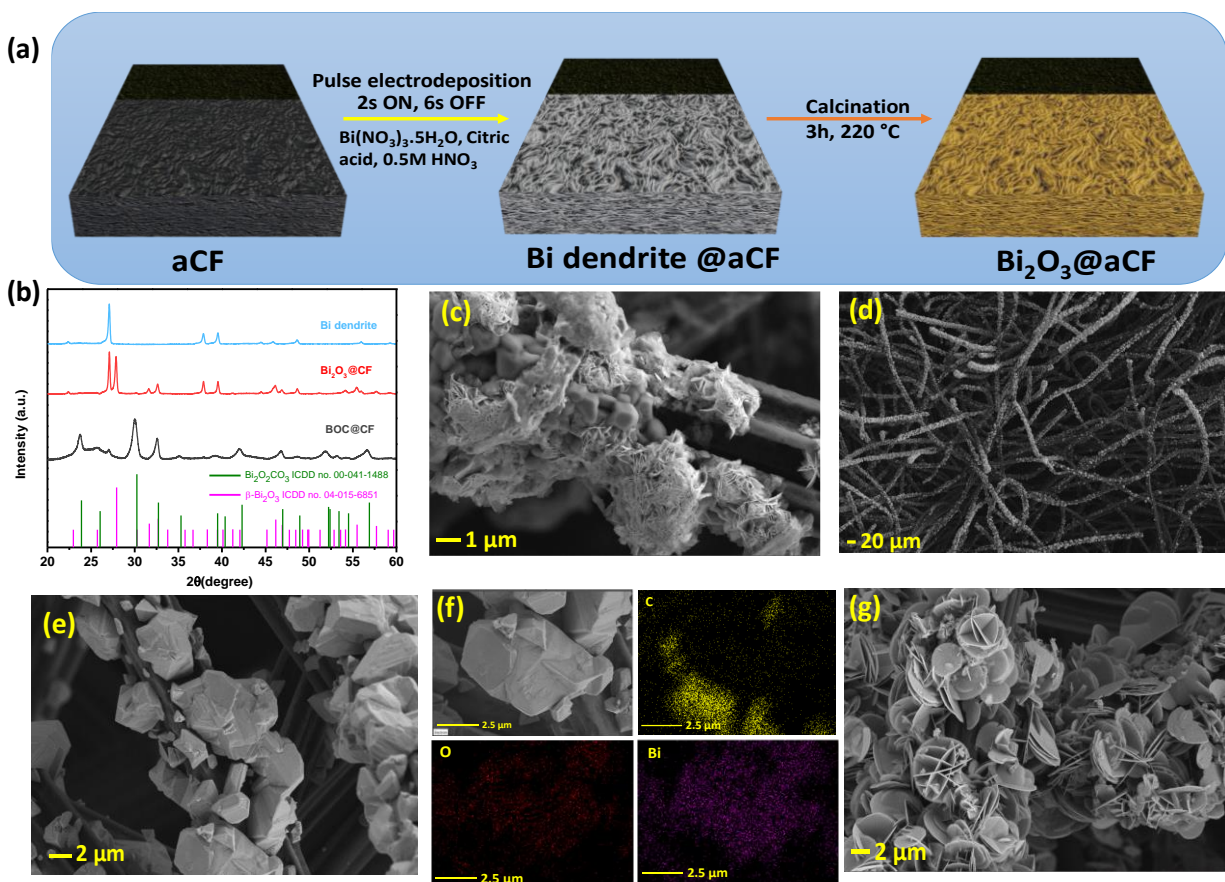


**Figure 2.** (a) Schematic of the synthesis of bismuth oxide deposited on activated carbon felt. (b) XRD patterns of Bi dendrites,  $\text{Bi}_2\text{O}_3$  and  $\text{Bi}_2\text{O}_2\text{CO}_3$  on aCF. SEM micrographs of (c) Bi dendrites@aCF. (d)  $\text{Bi}_2\text{O}_3$ @aCF at low magnification. (e)  $\text{Bi}_2\text{O}_3$ @aCF at high magnification. (f) EDX analysis of  $\text{Bi}_2\text{O}_3$ @aCF (g)  $\text{Bi}_2\text{O}_2\text{CO}_3$ @aCF at high magnification.

*In situ* Electrochemical activation led to the formation of petal-shaped BOC nanosheets with large surface area along the CF fibers as confirmed by SEM analysis (**Figure 2g**). This nanosheet type of morphology provides numerous edges and unsaturated sites, which could enhance the surface contact between the electrolyte and the electrocatalyst, thereby overcoming mass transport limitations ([34]).

The surface chemical properties of BOC@aCF were further explored by XPS analysis. In **Figure 3**, we present the high-resolution spectra for carbon ( $C_{1s}$ ), oxygen ( $O_{1s}$ ), and bismuth ( $Bi_{4f}$ ), which conclusively validate the presence of  $Bi_2O_3CO_3$  on the surface of aCF. In the  $C_{1s}$  spectrum (**Figure 3a**), three distinct peaks at 284.6, 285.23, and 288.09 eV could be observed. These peaks are attributed to the chemical groups C–C, C–O, and O–C=O, respectively, providing clear evidence of the existence of  $CO_3^{2-}$  species ([31]). Furthermore, the  $O_{1s}$  XPS plot (**Figure 3b**) of BOC@aCF was analyzed and deconvoluted into three peaks at binding energies of 530.4, 531.5, and 532.7 eV, corresponding to distinct oxygen environments: the lattice oxygen atoms within  $[Bi_2O_2]^{2+}$  layers, the oxygen atoms within  $CO_3^{2-}$  layers, and the presence of adsorbed water molecules, respectively ([34]).

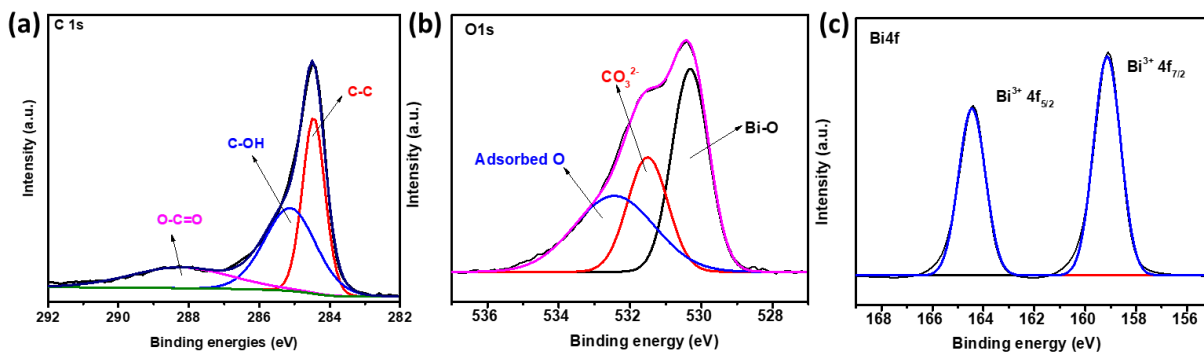


**Figure 3.** Core level X-ray photoelectron spectroscopy (XPS) spectra of BOC@aCF: (a)  $C_{1s}$ , (b)  $O_{1s}$  and (c)  $Bi_{4f}$ .

**Figure 3c** displays the core level plot of Bi<sub>4f</sub>, which comprises two prominent and symmetric peaks, situated at 159.21 and 164.49 eV. These observations signify the characteristic spin-orbit splitting of the Bi<sup>3+</sup> peaks and are representative of Bi 4f<sub>7/2</sub> and Bi 4f<sub>5/2</sub>, respectively ([35]). However, we did not observe metallic bismuth on the surface, which may be due to the favorable oxide formation under ambient atmosphere.

#### 4.3.1. Electrochemical CO<sub>2</sub> reduction using BOC@aCF

A series of electrochemical experiments were conducted using a three-electrode H-cell configuration separated with a Nafion cation exchange membrane. **Figure 4a** depicts the linear sweep voltammetry (LSV) profiles of BOC@aCF in two different electrolytes: one saturated with CO<sub>2</sub> in 0.5 KHCO<sub>3</sub> (pH = 7.3) and the other saturated with N<sub>2</sub> in 0.5 M KHCO<sub>3</sub> (pH= 9.1). The BOC@aCF catalyst exhibited good catalytic activity in CO<sub>2</sub> sat. electrolyte, achieving a cathodic current density of -20 mA.cm<sup>-2</sup> at a potential of -0.86 V vs. RHE. Interestingly, in the CO<sub>2</sub>-saturated electrolyte, the current density increased dramatically, accompanied by a decrease in the cathodic overpotential potential achieving a current density of -50 mA.cm<sup>-2</sup> at -1.15 V vs. RHE.

However, in N<sub>2</sub>-saturated 0.5 M KHCO<sub>3</sub> solution, the electrocatalytic performance of the BOC@aCF electrode was mainly attributed to the hydrogen evolution reaction (HER), requiring a higher potential of -1.1V vs. RHE to achieve a current density of -20 mA.cm<sup>-2</sup>. And the onset potential of CO<sub>2</sub>RR is at -0.54 V vs. RHE which is lower 100mV than the N<sub>2</sub> saturated electrolyte. In order to investigate the catalytic performance of the electrocatalyst towards CO<sub>2</sub>RR, a bulk electrolysis experiment was conducted for 1 h using the chronoamperometry technique (**Figure 4b**). The experiment involved application of a range of potentials from -0.65 to -0.95V (vs. RHE) to a BOC@aCF catalyst in a CO<sub>2</sub> sat. 0.5 M KHCO<sub>3</sub>. The resulting current-time behavior of CO<sub>2</sub>RR on the BOC@aCF catalyst indicated that the current densities remained relatively constant

throughout the electrolysis process, suggesting that the BOC@aCF catalyst exhibits excellent stability across a wide potential range for CO<sub>2</sub>RR. The electrolyte after the electrolysis was further analyzed using <sup>1</sup>H nuclear magnetic resonance (NMR), and the faradaic efficiency (FE) of the products was calculated accordingly using the standard formate curve determined by <sup>1</sup>H NMR.

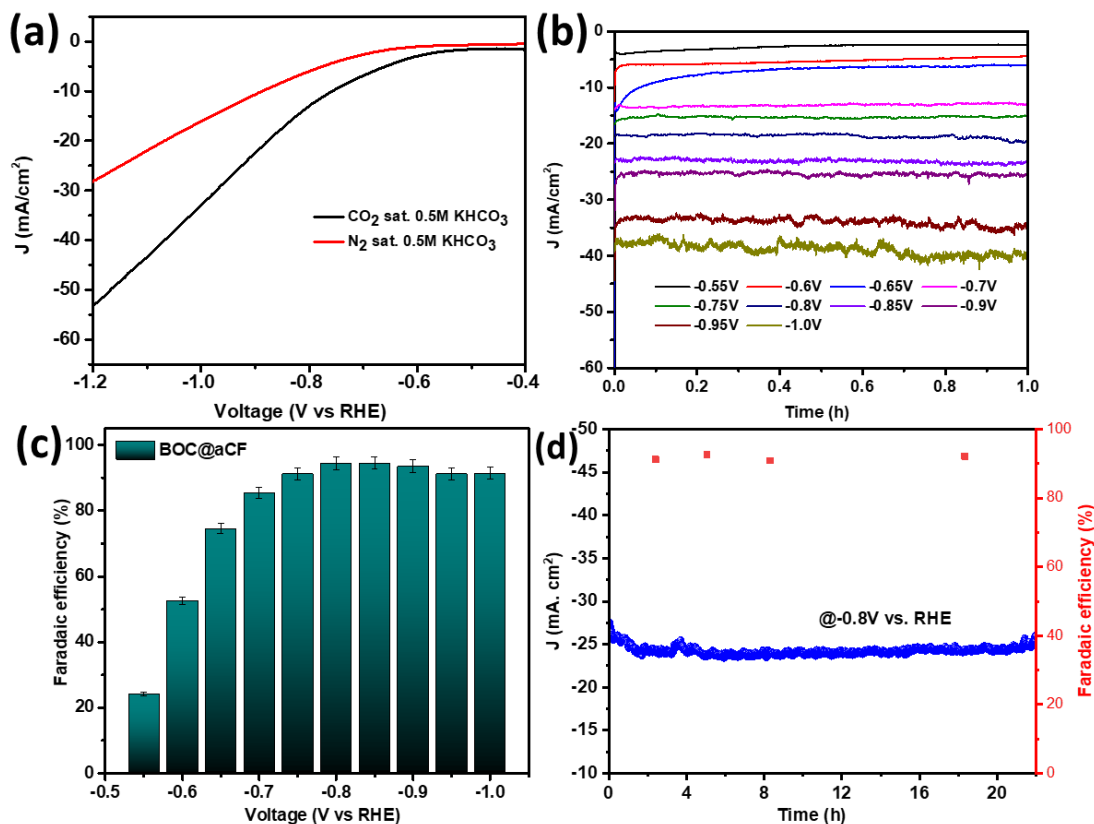


**Figure 4.** (a) CO<sub>2</sub>RR polarization curves of BOC@aCF electrode at a scan rate of 10 mV s<sup>-1</sup> in N<sub>2</sub>- or CO<sub>2</sub>-saturated 0.5 M KHCO<sub>3</sub> solution. (b) Chronoamperometry analysis at different potentials in CO<sub>2</sub>-saturated 0.5 M KHCO<sub>3</sub> solution of BOC@aCF. (c) Faradaic efficiencies (FE) of formate produced by BOC@aCF electrode for 1 h of CO<sub>2</sub> reduction at different applied potentials. (d) Long-term stability analysis and the corresponding FE for HCOOH (blue squares) of BOC@aCF at -0.8 V vs. RHE in a CO<sub>2</sub>-saturated 0.5 M KHCO<sub>3</sub> solution.

The FE of formate ( $FE_{\text{formate}}$ ) displayed a significant potential dependency, as shown in **Figure 4c**, in which formate was detectable at an onset potential of -0.55 V, and achieved a FE of up to 24.12%. As the overpotential increased,  $FE_{\text{formate}}$  initially increased and reached its maximum at 0.71 V with a value of 95%, after which it gradually declined, most likely due to limited mass transport of low  $\text{CO}_2$  concentration and competing HER in the aqueous electrolyte. Moreover,  $FE_{\text{formate}}$  exceeded 80% across a wide range of potentials, highlighting the promising applicability of BOC@aCF for  $\text{CO}_2$  reduction.

To assess the long-term stability of the BOC@aCF electrode, which is an essential factor for its potential application, we have conducted a 22 h test at a potential of -0.8V, as illustrated in **Figure 4d**. The results demonstrated that the current density remained stable over the stability test period, and the average FE for producing formate was maintained at a high level of above 90%. These findings highlighted the remarkable stability and selectivity of the BOC@aCF catalyst for the conversion of  $\text{CO}_2$  to formate. To further delve into the reaction kinetics of  $\text{CO}_2$  reduction to formate, Tafel plot analysis was carried out (**Figure 5a**). The Tafel slope of  $125 \text{ mV dec}^{-1}$  recorded for BOC@aCF is nearly identical to the theoretical value of  $118 \text{ mV dec}^{-1}$ , suggesting that the rate-determining step (RDS) was  $\text{CO}_2^{\bullet-}$  intermediate formation during  $\text{CO}_2\text{RR}$  ([36]). Additionally, as the potential increased, the sudden rise of Tafel slope often signifies the onset of  $\text{CO}_2$  transport limitation in the 0.5 M  $\text{KHCO}_3$  electrolyte. Additionally, FESEM analysis confirmed the stability of the catalyst, which showed that the morphology remained intact. and the EDX analysis showed an uniform distribution of metal species all along the BOC@aCF (**Figure 5b,c**).

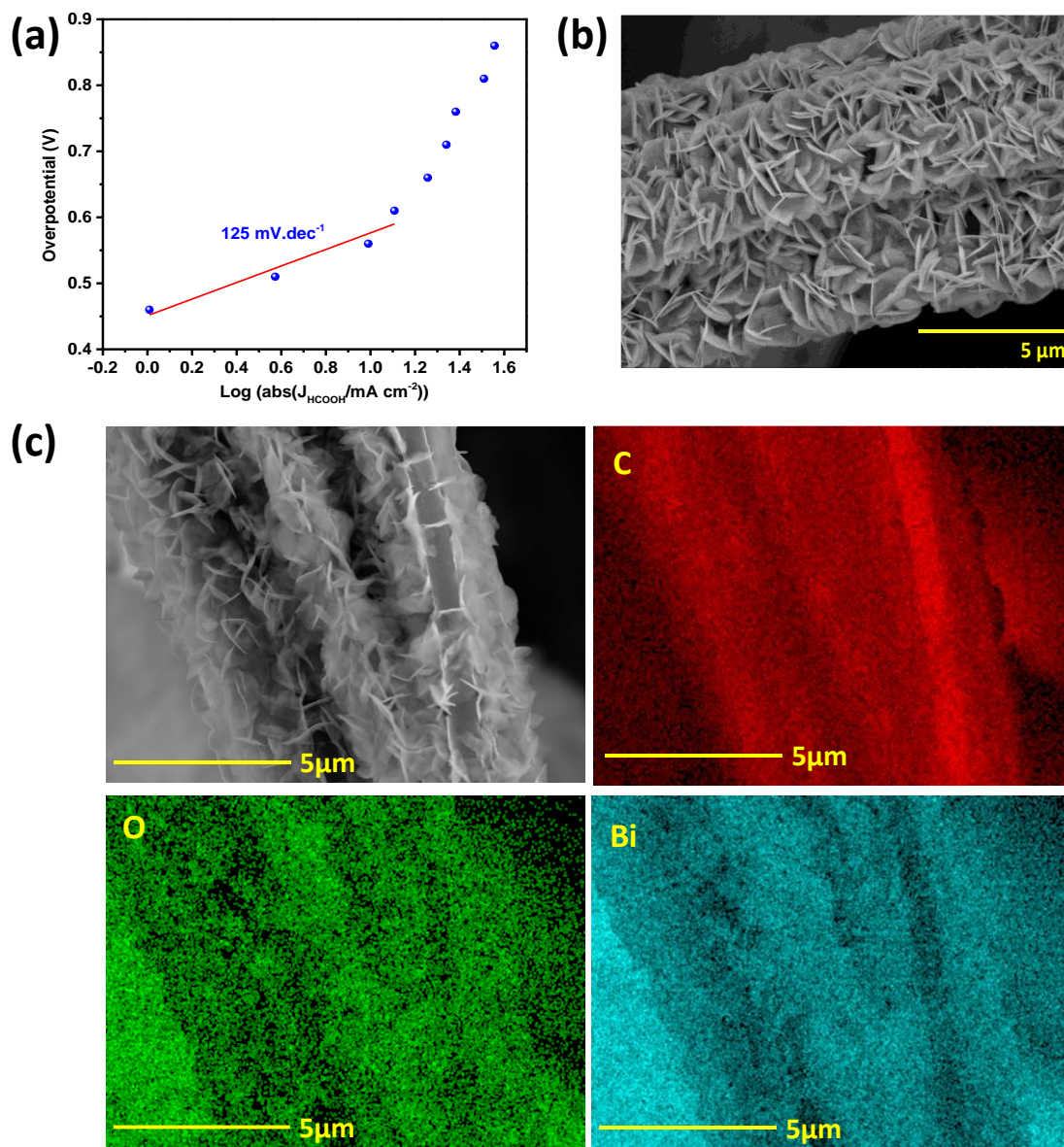


**Figure 5.** (a) Tafel analysis of BOC@aCF. (b) High magnification image and (c) FESEM image and the corresponding EDX mapping of Bi, C and O of BOC@aCF after the 22h stability test.

#### 4.3.2. Structural characterization of NiCoPO<sub>x</sub>

We employed a simple one-step electrodeposition (ED) technique to prepare the NiCoPO<sub>x</sub>@aCF electrode (**Figure 6a**), drawing inspiration from a previous publication from our research group

([28]). However, in this particular study, we employed electrochemically oxidized carbon felt as the substrate for ED.

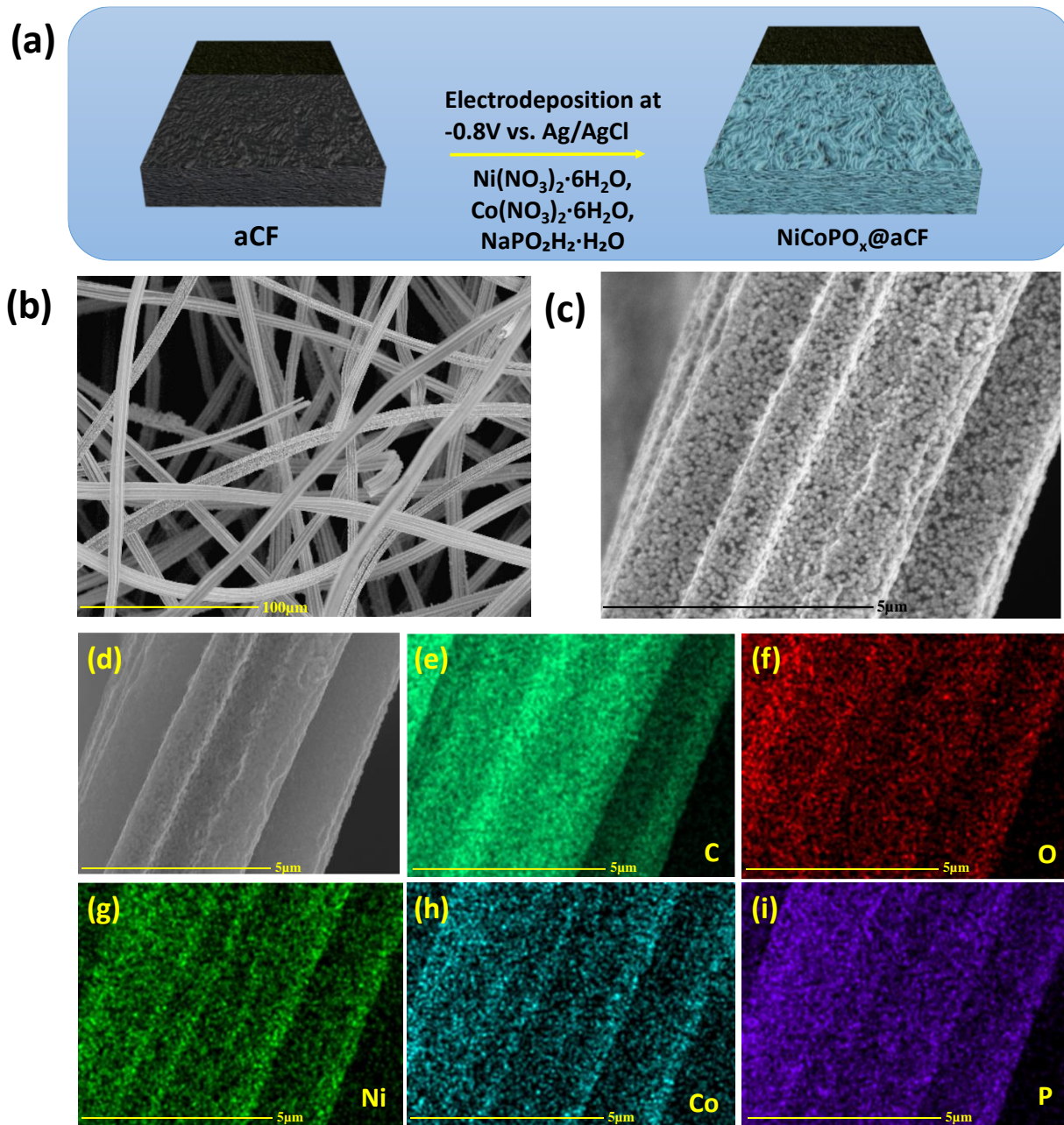


**Figure 6.** (a) Schematic illustration of the synthesis of  $\text{NiCoPO}_x$  on aCF. (b) Low magnification and (c) high magnification FESEM images of  $\text{NiCoPO}_x$ @aCF. (d) FESEM image and EDX analysis of (e) C, (f) O, (g) Ni, (h) Co, and (i) P of  $\text{NiCoPO}_x$ @aCF.

This process was conducted within a conventional three-electrode configuration cell, using an aqueous solution containing 5mM  $\text{Co}(\text{NO}_3)_3 \cdot 6\text{H}_2\text{O}$ , 5mM  $\text{Ni}(\text{NO}_3)_2 \cdot 6\text{H}_2\text{O}$ , and 5.1mM  $\text{NaH}_2\text{PO}_2 \cdot \text{H}_2\text{O}$ . FESEM imaging was utilized to investigate the structure and morphology of the resulting electrode. The high-magnification image revealed a uniform deposition of  $\text{NiCoPO}_x$ , a crucial aspect for achieving high electrocatalytic performance (**Figure 6b**). In contrast, the low-magnification image displayed small, sphere-like nanoparticles with an average size of 50 nm (**Figure 6c**). Energy-dispersive X-ray (EDX) analysis of the low-magnification image confirmed the presence of C, O, Ni, Co and P elements homogeneously distributed on the aCF surface, confirming the deposition of the  $\text{NiCoPO}_x$  composite (**Figure 6d-i**).

XPS was employed to investigate the surface composition and chemical states of  $\text{NiCoPO}_x$ @aCF. In the high-resolution XPS spectrum of  $\text{Co}_{2p}$  peak (**Figure 7a**), two primary peaks was deconvoluted into:  $\text{Co}_{2p_{3/2}}$  at 781.3 eV and  $\text{Co}_{2p_{1/2}}$  at 797.3 eV and two satellite peaks, indicating the presence of Co in its +2 oxidation state. Similarly, with the  $\text{Ni}_{2p}$ , two distinct peaks located at 855.8 and 873.5 eV were observed and subsequently deconvoluted into  $\text{Ni}_{2p_{3/2}}$  and  $\text{Ni}_{2p_{1/2}}$ , respectively (**Figure 7b**). Additionally, we detected two satellite peaks, providing evidence of the presence of  $\text{Ni}^{2+}$  ([37]). ([37]). Furthermore, the  $\text{P}_{2p}$  could be fitted with single peak at 132.6 eV, which is assigned to the PO bond, confirming the successful preparation of the  $\text{NiCoPO}_x$  composite on the activated carbon felt (**Figure 7c**) ([38]).

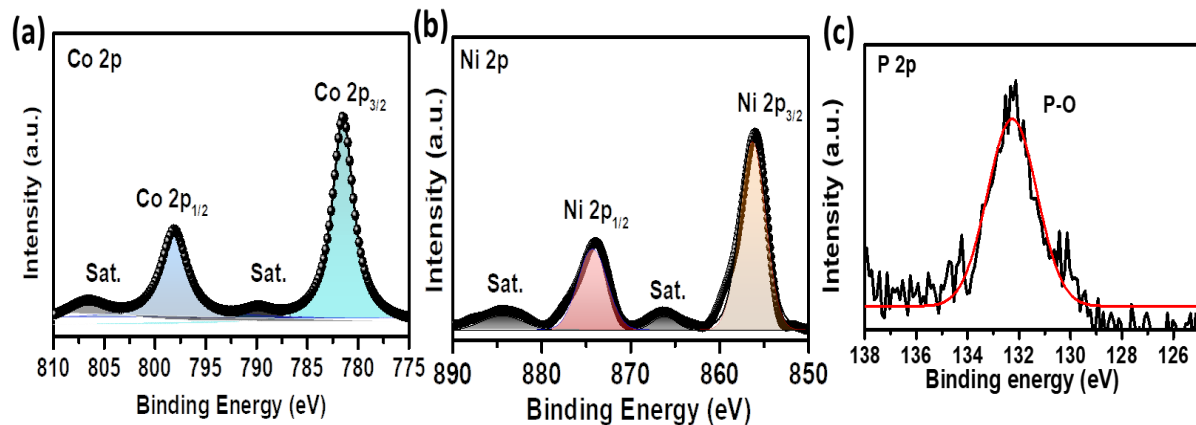


**Figure 7.** High resolution XPS spectra of (a)  $\text{Co}_{2p}$ , (b)  $\text{Ni}_{2p}$ , (c)  $\text{P}_{2p}$  of  $\text{NiCoPO}_x@\text{aCF}$ .

#### 4.3.3. Electrochemical oxidation of ethylene glycol (EG)

The literature extensively discusses the formation of ethylene glycol (EG) and terephthalic acid (TPA) as the primary products during alkaline PET hydrolysis. While TPA can be easily extracted by adjusting the pH of the solution, separating EG is more challenging ([39]). Thus, our aim was to utilize the PET hydrolysate solution directly as an electrolyte for EG oxidation, providing a cost-effective and time-saving approach. The concentration of EG obtained from PET hydrolysis was calculated using the calibration curve in **Figure 9b** and found to be 0.35 mM.

In this study, we conducted linear sweep voltammetry (LSV) of  $\text{NiCoPO}_x@\text{aCF}$  in both 1 M KOH and PET hydrolysate solution. The electrode revealed a lower onset potential of 1.24V (*vs.* RHE) and achieved a high current density of 20  $\text{mA cm}^{-2}$  at 1.48 V in the PET hydrolysate electrolyte (**Figure 8a**). In comparison, the  $\text{NiCoPO}_x@\text{aCF}$  electrode exhibited an onset potential of 1.54 V *vs.* RHE in 1 M KOH solution and required an overpotential of 1.72 V *vs.* RHE potential to reach a current density of 20  $\text{mA cm}^{-2}$ . To understand the kinetics of the reaction, we measured the Tafel slope from PET hydrolysate oxidation. A value of 98.6  $\text{mV dec}^{-1}$  was determined, which is lower than that recorded for the oxygen evolution reaction, OER, (225.9  $\text{mV dec}^{-1}$ ), indicating that the

EG oxidation reaction (EGOR) is kinetically favored over the OER (Figure 8b).

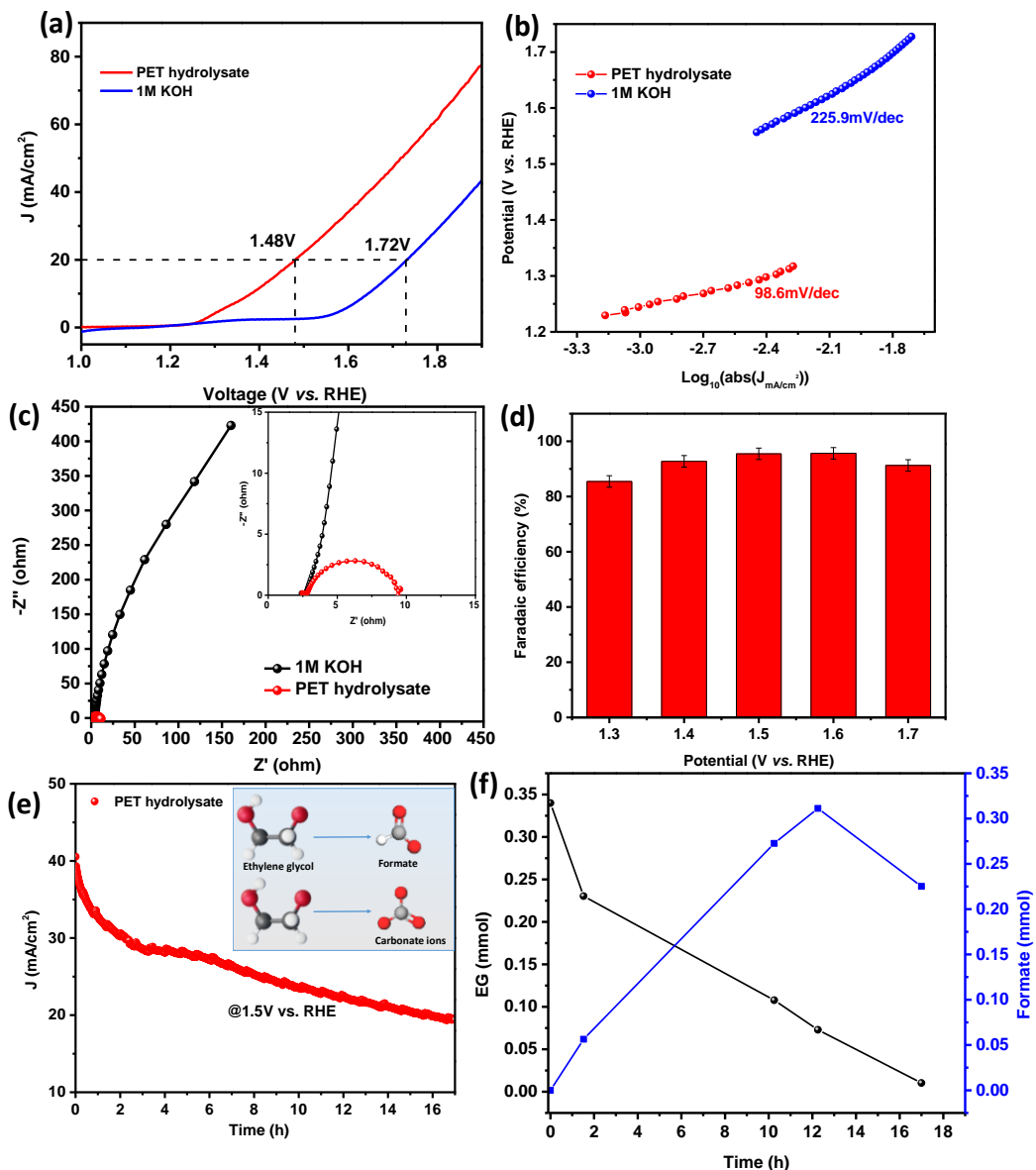


**Figure 8.** (a) LSV polarization curves of NiCoPO<sub>x</sub>@aCF in PET hydrolysate+1 M KOH solution. (b) Tafel plots for OER and EG oxidation. (c) Nyquist plots for 1M KOH and PET hydrolysate at 1.4 V vs. RHE. (d) Faradaic efficiencies of EG oxidation at different potentials. (e) Long-term catalytic conversion of EG to formate (inset: products formed during the electrolysis). (f) Concentration profile of EG and formate during a long-term electrocatalytic process.

The Nyquist plot measured at 1.4 V *vs.* RHE demonstrated a very low charge transfer resistance ( $R_{ct}$ ) value of approximately 9.75  $\Omega$  when the electrolyte was changed to PET hydrolysate, indicating enhanced charge transfer kinetics and high catalytic activity (**Figure 8c**). We have also performed quantitative and qualitative analysis of the electrolytic products generated by the oxidation of PET hydrolysate using  $^1\text{H}$  and  $^{13}\text{C}$  nuclear magnetic resonance (NMR) spectroscopy through a 1h CPE experiment. Only formate was encountered as the primary product during the anodic reaction, with a highest faradaic efficiency of 96% achieved at a potential of 1.5 V *vs.* RHE, which is one of the highest as compared to the reported catalysts ([39],[25],[24]) (**Figure 8d**). The formate FE calculations were performed using the calibration curve in **Figure 9a**.  $^1\text{H}$  and  $^{13}\text{C}$  NMR analysis, after the complete electrolysis, showed an increase in formate and a decrease in the peak corresponding to EG, indicating efficient conversion of EG to formate during the electrolytic process (**Figure 9c,d**). Long-term controlled-potential electrolysis for 17 h was performed at 1.5 V *vs.* RHE and demonstrated the durability of the NiCoPO<sub>x</sub>@aCF electrode for PET hydrolysate oxidation (**Figure 8e**).

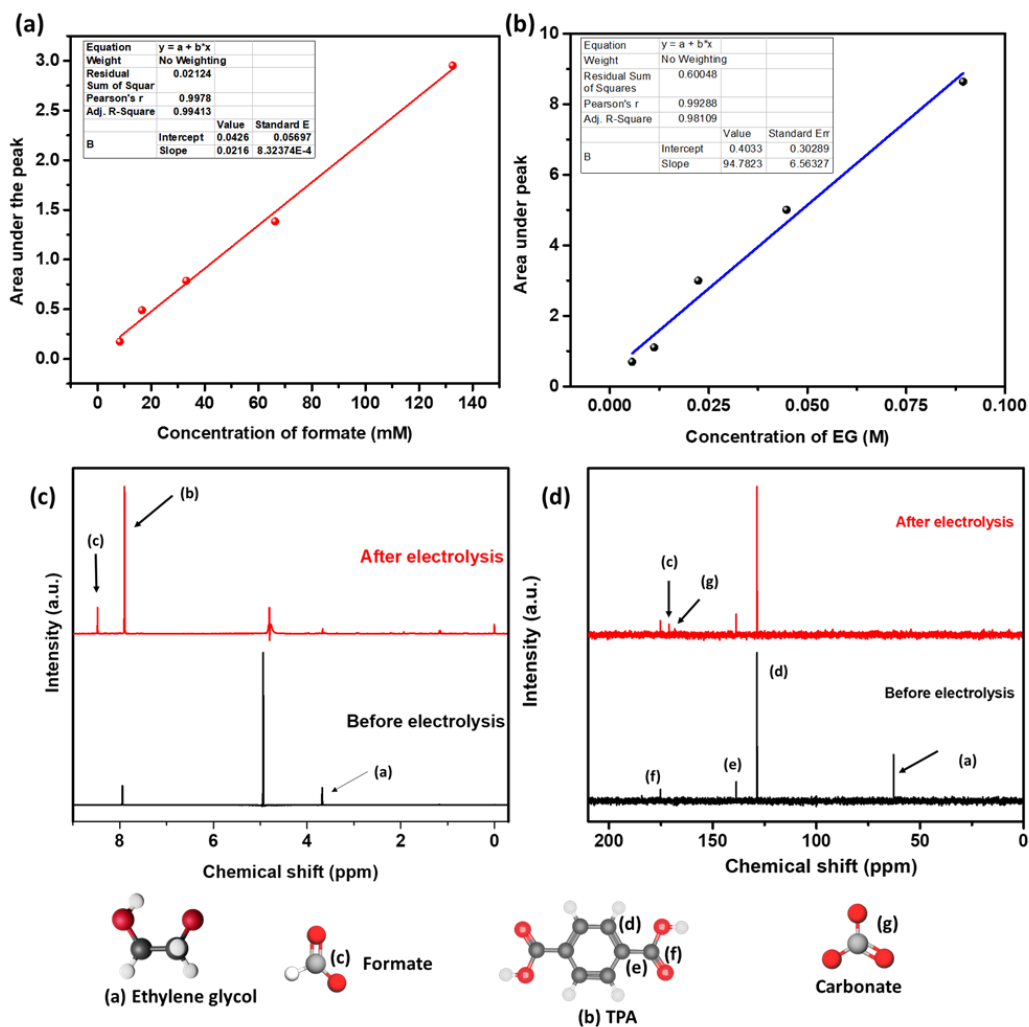


**Figure 9.** Calibration curves for (a) formate and (b) ethylene glycol determined by  $^1\text{H}$  NMR for PET hydrolysate. (c)  $^1\text{H}$  NMR and (d)  $^{13}\text{C}$  NMR before and after electrolysis of PET hydrolysate solution using  $\text{NiCoPO}_x@ \text{aCF}$ .

The catalytic current density for EG oxidation decreased primarily due to the consumption of EG in the solution. However, there was also a corresponding increase and subsequent decrease in the concentration of formate, indicating a possibility of formate over-oxidation (**Figure 8f**). In order to understand the phenomenon,  $^{13}\text{C}$  NMR analysis was performed and revealed the appearance of a small peak at 168 ppm attributed to the formation of carbonate species, resulting from the over-

oxidation of formate ([39]) (**Figure 9d**). Overall, the experiments demonstrated the effective catalytic activity of NiCoPO<sub>x</sub>@aCF for the oxidation of EG, derived from PET hydrolysate, leading to the production of formate and enhancing the profitability of PET recycling.

Additionally, a two electrolyzer setup (NiCoPO<sub>x</sub>@aCF || BOC@aCF) was assembled to simultaneously generate formate by coupling the anode and cathode. In this configuration, NiCoPO<sub>x</sub>@aCF acted as the anode in 1 M KOH electrolyte containing 0.35 mM EG from PET hydrolysate solution, while BOC@aCF served as the cathode in CO<sub>2</sub> sat. 1 M KHCO<sub>3</sub> electrolyte. The performance of EG-CO<sub>2</sub>RR was markedly improved compared to the conventional OER-CO<sub>2</sub>RR system, featuring a low cell voltage of 1.8 V to reach a current density of 20 mA cm<sup>-2</sup> and superior formate synthesis efficiency (**Figure 10a**). This integrated strategy resulted in reduced energy consumption and promoted formate production as the predominant product.

The stability of this integrated system was assessed through chronopotentiometry (CPE) analysis at different cell voltages. The coupled 2-electrode system demonstrated exceptional faradaic efficiency for formate production, with a minor decrease in current density most likely due to EG consumption (**Figure 10b**). Formate was generated as the primary product through both CO<sub>2</sub>RR and anodic EG oxidation, achieving a faradaic efficiency of 158% at a cell voltage of 1.8 V and maintaining over 130% efficiency across the entire potential range. This integrated method not only transforms PET plastic waste into valuable products, but also allows simultaneous high-efficiency formic acid production with minimal energy consumption at both the anode and

cathode.

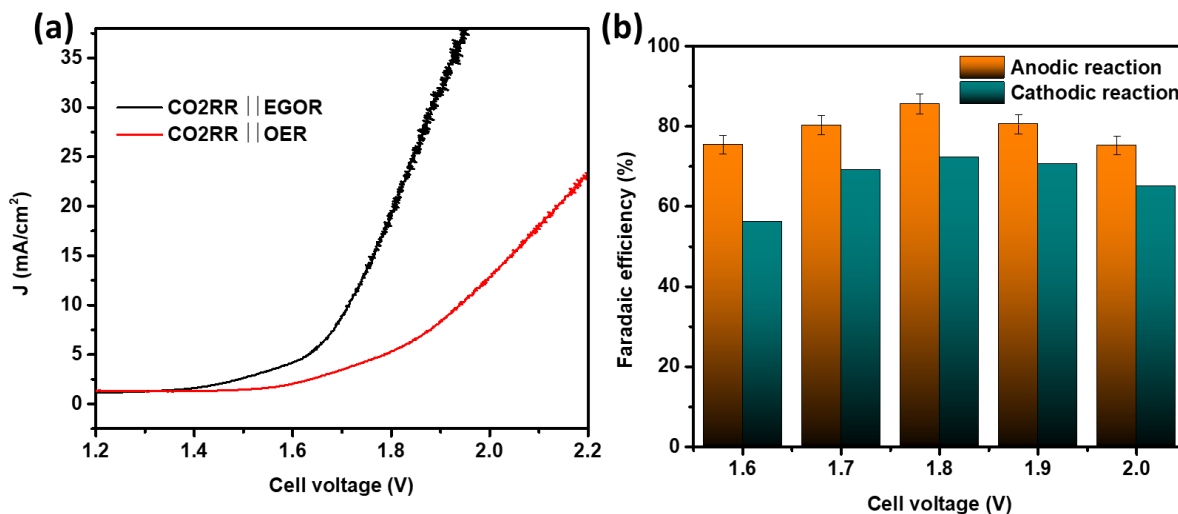


**Figure 10.** (a) LSV polarization curves of NiCoPO<sub>x</sub>@aCF in 1 M KOH+PET hydrolysate solution and BOC@aCF in CO<sub>2</sub> sat. 1M KHCO<sub>3</sub> solution in a 2-electrode integrated electrolyzer. (b) Faradaic efficiencies at both cathode and anode at each potential using the 2-electrode integrated electrolyzer.

#### 4.4. Conclusion

The findings of this study illustrate that the electrocatalytic properties of carbon felt (CF) could be enhanced through a straightforward anodic activation process in a 1 M KOH aqueous solution. By generating oxygen-containing species, we successfully utilized pulse electrodeposition and simple electrodeposition techniques to create BOC@aCF and NiCoPO<sub>x</sub>@aCF for CO<sub>2</sub> reduction and PET hydrolysate oxidation reactions, respectively. Specifically, the anode and cathode demonstrated formate production with impressive faradaic efficiencies of 96% and 95% for their respective reactions. Additionally, in a 2-electrode system, the electrolyzer achieved a remarkable Faradaic efficiency of 158% for formate synthesis at a cell voltage of 1.8 V. Consequently, this integrated

method not only offers an efficient solution for converting PET plastic waste, but also holds the potential for economically viable, long-term production of valuable chemicals from plastic waste and CO<sub>2</sub> reduction.

## References

- [1] P. De Luna, C. Hahn, D. Higgins, S. A. Jaffer, T. F. Jaramillo, and E. H. Sargent, “What would it take for renewably powered electrosynthesis to displace petrochemical processes?,” *Science* (80-. ), vol. 364, no. 6438, p. eaav3506, 2019, doi: 10.1126/science.aav3506.
- [2] F. Pan and Y. Yang, “Designing CO<sub>2</sub> reduction electrode materials by morphology and interface engineering,” *Energy Environ. Sci.*, vol. 13, no. 8, pp. 2275–2309, 2020, doi: 10.1039/D0EE00900H.
- [3] V. S. S. Mosali *et al.*, “CdS-Enhanced Ethanol Selectivity in Electrocatalytic CO<sub>2</sub> Reduction at Sulfide-Derived Cu–Cd,” *ChemSusChem*, vol. 14, no. 14, pp. 2924–2934, 2021, doi: <https://doi.org/10.1002/cssc.202100903>.
- [4] P. Ding *et al.*, “Metal-based electrocatalytic conversion of CO<sub>2</sub> to formic acid/formate,” *J. Mater. Chem. A*, vol. 8, no. 42, pp. 21947–21960, 2020, doi: 10.1039/D0TA08393C.
- [5] F. Cheng *et al.*, “Recent Progress of Sn-Based Derivative Catalysts for Electrochemical Reduction of CO<sub>2</sub>,” *Energy Technol.*, vol. 9, no. 1, p. 2000799, 2021, doi: <https://doi.org/10.1002/ente.202000799>.
- [6] A. Mustafa *et al.*, “Progress and perspective of electrochemical CO<sub>2</sub> reduction on Pd-based nanomaterials,” *Chem. Eng. Sci.*, vol. 245, p. 116869, 2021, doi:

<https://doi.org/10.1016/j.ces.2021.116869>.

- [7] J. Y. Kim *et al.*, “Electrodeposited CuAgHg Multimetallic Thin Films for Improved CO<sub>2</sub> Conversion: the Dramatic Impact of Hg Incorporation on Product Selectivity,” *ACS Appl. Energy Mater.*, vol. 3, no. 7, pp. 6670–6677, Jul. 2020, doi: 10.1021/acsaem.0c00784.
- [8] X. Huang *et al.*, “Ordered-Mesoporous-Carbon-Confined Pb/PbO Composites: Superior Electrocatalysts for CO<sub>2</sub> Reduction,” *ChemSusChem*, vol. 13, no. 23, pp. 6346–6352, 2020, doi: <https://doi.org/10.1002/cssc.202000329>.
- [9] B. Rausch, M. D. Symes, G. Chisholm, and L. Cronin, “Decoupled catalytic hydrogen evolution from a molecular metal oxide redox mediator in water splitting,” *Science (80-. )*, vol. 345, no. 6202, pp. 1326–1330, Sep. 2014, doi: 10.1126/science.1257443.
- [10] Z. W. Seh, J. Kibsgaard, C. F. Dickens, I. Chorkendorff, J. K. Nørskov, and T. F. Jaramillo, “Combining theory and experiment in electrocatalysis: Insights into materials design,” *Science (80-. )*, vol. 355, no. 6321, Jan. 2017, doi: 10.1126/SCIENCE.AAD4998.
- [11] S. Verma, S. Lu, and P. J. A. Kenis, “Co-electrolysis of CO<sub>2</sub> and glycerol as a pathway to carbon chemicals with improved technoeconomics due to low electricity consumption,” *Nat. Energy*, vol. 4, no. 6, pp. 466–474, 2019, doi: 10.1038/s41560-019-0374-6.
- [12] T. Wang *et al.*, “Combined anodic and cathodic hydrogen production from aldehyde oxidation and hydrogen evolution reaction,” *Nat. Catal.*, vol. 5, no. 1, pp. 66–73, 2022, doi: 10.1038/s41929-021-00721-y.
- [13] X. Wei, Y. Li, L. Chen, and J. Shi, “Formic Acid Electro-Synthesis by Concurrent

- Cathodic CO<sub>2</sub> Reduction and Anodic CH<sub>3</sub>OH Oxidation,” *Angew. Chemie Int. Ed.*, vol. 60, no. 6, pp. 3148–3155, 2021, doi: <https://doi.org/10.1002/anie.202012066>.
- [14] M. T. Bender, X. Yuan, and K.-S. Choi, “Alcohol oxidation as alternative anode reactions paired with (photo)electrochemical fuel production reactions,” *Nat. Commun.*, vol. 11, no. 1, p. 4594, 2020, doi: [10.1038/s41467-020-18461-1](https://doi.org/10.1038/s41467-020-18461-1).
- [15] X. V Medvedeva, J. J. Medvedev, S. W. Tatarchuk, R. M. Choueiri, and A. Klinkova, “Sustainable at both ends: electrochemical CO<sub>2</sub> utilization paired with electrochemical treatment of nitrogenous waste,” *Green Chem.*, vol. 22, no. 14, pp. 4456–4462, 2020, doi: [10.1039/D0GC01754J](https://doi.org/10.1039/D0GC01754J).
- [16] K. Xie, A. Ozden, R. K. Miao, Y. Li, D. Sinton, and E. H. Sargent, “Eliminating the need for anodic gas separation in CO<sub>2</sub> electroreduction systems via liquid-to-liquid anodic upgrading,” *Nat. Commun.*, vol. 13, no. 1, p. 3070, 2022, doi: [10.1038/s41467-022-30677-x](https://doi.org/10.1038/s41467-022-30677-x).
- [17] H. G. Cha and K.-S. Choi, “Combined biomass valorization and hydrogen production in a photoelectrochemical cell,” *Nat. Chem.*, vol. 7, no. 4, pp. 328–333, 2015, doi: [10.1038/nchem.2194](https://doi.org/10.1038/nchem.2194).
- [18] T. Uekert, H. Kasap, and E. Reisner, “Photoreforming of Nonrecyclable Plastic Waste over a Carbon Nitride/Nickel Phosphide Catalyst,” *J. Am. Chem. Soc.*, vol. 141, no. 38, pp. 15201–15210, Sep. 2019, doi: [10.1021/jacs.9b06872](https://doi.org/10.1021/jacs.9b06872).
- [19] R. Geyer, J. R. Jambeck, and K. L. Law, “Production, use, and fate of all plastics ever made,” *Sci. Adv.*, vol. 3, no. 7, p. e1700782, Oct. 2023, doi: [10.1126/sciadv.1700782](https://doi.org/10.1126/sciadv.1700782).

- [20] O. Guselnikova *et al.*, “‘Functional upcycling’ of polymer waste towards the design of new materials,” *Chem. Soc. Rev.*, vol. 52, no. 14, pp. 4755–4832, 2023, doi: 10.1039/D2CS00689H.
- [21] M. Okan, H. M. Aydin, and M. Barsbay, “Current approaches to waste polymer utilization and minimization: a review,” *J. Chem. Technol. & Biotechnol.*, vol. 94, no. 1, pp. 8–21, 2019, doi: <https://doi.org/10.1002/jctb.5778>.
- [22] H. Zhou *et al.*, “Electrocatalytic upcycling of polyethylene terephthalate to commodity chemicals and H<sub>2</sub> fuel,” *Nat. Commun.* 2021 121, vol. 12, no. 1, pp. 1–9, Aug. 2021, doi: 10.1038/s41467-021-25048-x.
- [23] S. Ügdüler *et al.*, “Towards closed-loop recycling of multilayer and coloured PET plastic waste by alkaline hydrolysis,” *Green Chem.*, vol. 22, no. 16, pp. 5376–5394, 2020, doi: 10.1039/D0GC00894J.
- [24] J. Wang, X. Li, T. Zhang, Y. Chen, T. Wang, and Y. Zhao, “Electro-Reforming Polyethylene Terephthalate Plastic to Co-Produce Valued Chemicals and Green Hydrogen,” *J. Phys. Chem. Lett.*, vol. 13, no. 2, pp. 622–627, Jan. 2022, doi: 10.1021/acs.jpcllett.1c03658.
- [25] J. Wang *et al.*, “Electrocatalytic Valorization of Poly(ethylene terephthalate) Plastic and CO<sub>2</sub> for Simultaneous Production of Formic Acid,” *ACS Catal.*, vol. 12, no. 11, pp. 6722–6728, Jun. 2022, doi: 10.1021/acscatal.2c01128.
- [26] M. Ifires *et al.*, “Cathodic pre-polarization studies on the carbon felt/KOH interface: An efficient metal-free electrocatalyst for hydrogen generation,” *Electrochim. Acta*, vol. 375, p. 137981, 2021, doi: <https://doi.org/10.1016/j.electacta.2021.137981>.

- [27] A. Döner, İ. Karcı, and G. Kardaş, “Effect of C-felt supported Ni, Co and NiCo catalysts to produce hydrogen,” *Int. J. Hydrogen Energy*, vol. 37, no. 12, pp. 9470–9476, 2012, doi: <https://doi.org/10.1016/j.ijhydene.2012.03.101>.
- [28] M. Li *et al.*, “An efficient cobalt-nickel phosphate positive electrode for high-performance hybrid microsupercapacitors,” *J. Energy Storage*, vol. 64, p. 107144, 2023, doi: <https://doi.org/10.1016/j.est.2023.107144>.
- [29] S. S. Barton, M. J. B. Evans, E. Halliop, and J. A. F. MacDonald, “Anodic Oxidation of Porous Carbon,” *Langmuir*, vol. 13, no. 5, pp. 1332–1336, Mar. 1997, doi: [10.1021/la9509413](https://doi.org/10.1021/la9509413).
- [30] Z. R. Yue, W. Jiang, L. Wang, S. D. Gardner, and C. U. Pittman, “Surface characterization of electrochemically oxidized carbon fibers,” *Carbon N. Y.*, vol. 37, no. 11, pp. 1785–1796, 1999, doi: [https://doi.org/10.1016/S0008-6223\(99\)00047-0](https://doi.org/10.1016/S0008-6223(99)00047-0).
- [31] J. Jiang, X. Yao, C. Xu, Y. Su, L. Zhou, and C. Deng, “Influence of electrochemical oxidation of carbon fiber on the mechanical properties of carbon fiber/graphene oxide/epoxy composites,” *Compos. Part A Appl. Sci. Manuf.*, vol. 95, pp. 248–256, 2017, doi: <https://doi.org/10.1016/j.compositesa.2017.02.004>.
- [32] X. An *et al.*, “Electrodeposition of Tin-Based Electrocatalysts with Different Surface Tin Species Distributions for Electrochemical Reduction of CO<sub>2</sub> to HCOOH,” *ACS Sustain. Chem. Eng.*, vol. 7, no. 10, pp. 9360–9368, May 2019, doi: [10.1021/acssuschemeng.9b00515](https://doi.org/10.1021/acssuschemeng.9b00515).
- [33] Y. Hinuma *et al.*, “Density Functional Theory Calculations of Oxygen Vacancy Formation and Subsequent Molecular Adsorption on Oxide Surfaces,” *J. Phys. Chem. C*, vol. 122,

- no. 51, pp. 29435–29444, Dec. 2018, doi: 10.1021/acs.jpcc.8b11279.
- [34] Z. Liu *et al.*, “In-situ construction of 2D/1D Bi<sub>2</sub>O<sub>2</sub>CO<sub>3</sub> nanoflake/S-doped g-C<sub>3</sub>N<sub>4</sub> hollow tube hierarchical heterostructure with enhanced visible-light photocatalytic activity,” *Chem. Eng. J.*, vol. 426, p. 130767, 2021, doi: <https://doi.org/10.1016/j.cej.2021.130767>.
- [35] J. Ma, J. Yan, J. Xu, J. Ni, H. Zhang, and L. Lu, “Dynamic ion exchange engineering BiOI-derived Bi<sub>2</sub>O<sub>2</sub>CO<sub>3</sub> to promote CO<sub>2</sub> electroreduction for efficient formate production,” *Chem. Eng. J.*, vol. 455, p. 140926, 2023, doi: <https://doi.org/10.1016/j.cej.2022.140926>.
- [36] D. D. Zhu, J. L. Liu, and S. Z. Qiao, “Recent Advances in Inorganic Heterogeneous Electrocatalysts for Reduction of Carbon Dioxide,” *Adv. Mater.*, vol. 28, no. 18, pp. 3423–3452, 2016, doi: <https://doi.org/10.1002/adma.201504766>.
- [37] Y. Shu, B. Li, J. Chen, Q. Xu, H. Pang, and X. Hu, “Facile Synthesis of Ultrathin Nickel–Cobalt Phosphate 2D Nanosheets with Enhanced Electrocatalytic Activity for Glucose Oxidation,” *ACS Appl. Mater. Interfaces*, vol. 10, no. 3, pp. 2360–2367, Jan. 2018, doi: 10.1021/acsami.7b17005.
- [38] W. Mai *et al.*, “CoMoP/NiFe-Layered Double-Hydroxide Hierarchical Nanosheet Arrays Standing on Ni Foam for Efficient Overall Water Splitting,” *ACS Appl. Energy Mater.*, vol. 3, no. 8, pp. 8075–8085, Aug. 2020, doi: 10.1021/acsaem.0c01538.
- [39] S. Behera, S. Dinda, R. Saha, and B. Mondal, “Quantitative Electrocatalytic Upcycling of Polyethylene Terephthalate Plastic and Its Oligomer with a Cobalt-Based One-Dimensional Coordination Polymer Having Open Metal Sites along with Coproduction of Hydrogen,” *ACS Catal.*, vol. 13, no. 1, pp. 469–474, Jan. 2023, doi:

10.1021/acscatal.2c05270.

# Chapter 5

## Conclusions and future perspectives

In this thesis work, we have explored various carbon based materials and utilized them as an electrocatalysts for electrochemical applications such as water electrolysis, CO<sub>2</sub> reduction and PET hydrolysate oxidation reactions. We have also tried to utilize environmental friendly methods to synthesize the materials, however some amount of thermal annealing was inevitable for better activity.

Firstly, our collaboration with Dr. Vitaly Ordonsky's team led to the preparation of a unique electrocatalyst composed of Ru/RuO<sub>2</sub> nanowires within a carbon nitride framework. This material was developed using a two-dimensional imine-based covalent organic framework (COF) incorporating a RuII–2-diphenylphosphinobenzaldehyde complex. By subjecting this framework to pyrolysis at 500 °C under a N<sub>2</sub> atmosphere, we successfully generated highly dispersed RuO<sub>2</sub> nanoparticles with low-valence Ru sites embedded in the layers of carbon nitride. This electrocatalyst exhibited exceptional performance, displaying a remarkably low overpotential of 53 mV at -10 mA cm<sup>-2</sup> for the hydrogen evolution reaction (HER) and 280 mV at 10 mA cm<sup>-2</sup> for the oxygen evolution reaction (OER) in a 1M KOH electrolyte. The enhanced catalytic activity was attributed to the creation of numerous active sites, as evidenced by electrochemical active surface area and charge transfer resistance measurements from electrochemical impedance spectroscopy (EIS). Additionally, chronopotentiometry measurements confirmed the catalyst's high stability in a corrosion-free environment, producing both hydrogen and oxygen for at least 45 hours. Moreover, the robustness of the developed electrocatalyst was demonstrated in a complete

water splitting setup, exhibiting only a slight degradation of 1.35% over at least 26 hours while delivering a current density of  $10 \text{ mA cm}^{-2}$ .

Secondly, we have employed a novel technique that combines the reduction of  $\text{CO}_2$  (CO<sub>2</sub>RR) with the oxidation of PET hydrolysate, generating formate simultaneously on both the anode and cathode. Bismuth oxide carbonate (BOC) functionalized reduced graphene oxide (rGO) for cathodic CO<sub>2</sub>RR and CuCoO on rGO for anodic PET hydrolysate oxidation were developed as the electrocatalysts. Implementing this method in a two-electrode electrolyzer led to formate production at a low cell voltage of 1.9 V at  $10 \text{ mA cm}^{-2}$  with a formate FE of 151.8%. This innovative approach provides a distinctive pathway for recycling PET waste, decreasing  $\text{CO}_2$  emissions, and supporting environmental sustainability.

Finally, we delved into a unique 3D carbon felt (CF) substrate, often overlooked due to its hydrophobic nature and limited electrochemical activity. To address this, we activated the substrate anodically in a 1M KOH solution, significantly increasing its oxygen content and making it hydrophilic. After activating the substrate, we employed a electrodeposition techniques to deposit Bismuth and Nickel cobalt phosphate on the activated carbon felt (aCF) for CO<sub>2</sub>RR and PET hydrolysate oxidation reactions respectively. Both the electrocatalysts exhibited more than 90% FE and in a two-electrolyzer setup, a formate FE of 157% at a low cell voltage of 1.8V. This work represents a significant advancement in the utilization of the 3D carbon felt substrate and offers a promising solution for  $\text{CO}_2$  reduction and PET waste management.

### **Future prospects**

In this thesis, we introduced two electrochemical systems to simultaneously produce formate. However, the use of H cell type electrolyzers posed challenges due to their high solution resistance

and limitations in CO<sub>2</sub> mass transport, preventing us from reaching high current densities. Additionally, the risk of over-oxidation in the anode compartment reduced the product yield. To address these issues, we considered exploring an electro dialysis system to separate formate from the electrolyte mixture during the reaction. While this approach might mitigate over-oxidation, it does not fully resolve the problem.

An alternative avenue involves conducting theoretical studies using density functional theory (DFT) to investigate the reaction intermediates during CO<sub>2</sub>RR and PET hydrolysate oxidation reactions. This theoretical approach could provide valuable insights into the reaction mechanisms, aiding in the development of more efficient electrocatalysts in the future. By combining experimental insights with theoretical understanding, we can pave the way for more effective and sustainable formate production methods.

# Appendix

## Experimental methods and Characterization

### Characterizations

The analysis of Ru and P (chapter 3) was performed with the use of an energy dispersive micro X-ray fluorescence spectrometer M4 TORNADO (Bruker). CHNO analysis was performed using the FlashSmart automated analyzer. N, C and H were detected as N<sub>2</sub>, CO<sub>2</sub> and H<sub>2</sub>O, respectively. The resulting gases were separated on a packed column and detected by a TCD detector. Oxygen was analyzed separately by pyrolysis with CO analysis. Fourier transform infrared spectroscopy (FTIR) experiments were carried out with a Thermo Fisher Scientific Nicolet 6700 FTIR instrument (32 scans at a resolution of 4 cm<sup>-1</sup>) equipped with a mercury cadmium telluride (MCT) detector. The Raman spectra were recorded on a Xplora Raman confocal microscope from Horiba Jobin Yvon. A 532 nm and 437 nm diode laser was used to excite the samples of chapter 3 and 4 respectively. The scattered light was guided through a 150 μm pinhole, dispersed and collected using a Peltier-cooled CCD. The laser power was reduced using density filters in order to avoid sample alteration.

The X-ray diffraction patterns (XRD) for chapter was recorded on a PANalytical Empyrean X-ray diffractometer in Bragg–Brentano configuration with a 0.02° step size and 1 s step time. The Cu Kα radiation (40 kV and 30 mA) was used as the X-ray source. The interplanar distances were calculated using Bragg equation:  $d = \frac{\lambda}{2\sin\theta}$ , where  $\lambda$  is the wavelength of X-ray radiation ( $\lambda = 1.5406 \text{ \AA}$ ) and  $\theta$  is the diffraction angle of the peak. While, for chapter 4, we have used Rigaku Smartlab rotated anode, working with a copper Kα radiation (1.5418 Å) at an applied voltage of

45 kV and an anode current of 200 mA in the  $2\theta$  range of 5–90°. The Brunauer-Emmett-Teller (BET) surface area, pore volume, pore diameter and N<sub>2</sub> sorption-desorption isotherms were measured on a Micromeritics Tristar Model 3020 Surface Area and Porosimetry analyzer. The samples (100 mg) were degassed under vacuum at 250 °C for 2 h prior to N<sub>2</sub> physisorption. Thermogravimetric analysis (TGA) measurements were performed using a SDT 2960 analyzer from TA instrument under air flow (50 mL min<sup>-1</sup>) with a temperature ramping rate of 10 °C min<sup>-1</sup>. Scanning transmission electron microscopy (STEM) analysis was performed on a Titan Themis 300 S/TEM equipped with a probe aberration corrector and a monochromator, allowing a special resolution of 70 pm and an energy resolution of 150 meV. The microscope is equipped with a Super-X windowless 4 quadrant SDD (silicon drift detector) detection system for the STEM–energy-dispersive X-ray (EDX) mapping and several annular dark field detectors. The experiment was performed with a spot size of about 500 pm, a semi-convergence angle of 21 mrad, and a probe current of approximately 100 pA. For the high-angle annular dark-field (HAADF) images, the collection angles were between 50 and 200 mrad. The STEM–EDX mapping was acquired with a dwell time of 15  $\mu\text{m}/\text{px}$  with continuous scanning over several frames during a total time of 10–15 min per acquisition. The microscope is also equipped with a CETA camera with a 4kx4k CMOS sensor for the TEM images and diffraction acquisition.

Ru K-edge X-ray absorption spectra (XAS) of samples diluted in cellulose were acquired at room temperature in the form of pellets. XAS spectra were collected in transmission mode for references Ru Black, RuCl<sub>3</sub> and RuO<sub>2</sub> and fluorescence mode for Ru@CIN-1 and Ru@g-CN<sub>x</sub> and Ru@g-CN<sub>x</sub> employing a Si311 double crystal monochromator and a 6 channel multi-element SDD detector available at the CLAES beamline of the ALBA synchrotron (see chapter 3). Several XAS repeats were collected to ensure reproducibility and statistics. The averaged spectra were

treated by the Athena software package <sup>34</sup>. The energy scale was calibrated by setting the first inflection point of the Ru metal spectra taken as 22117 eV. EXAFS were extracted using the AUTOBK algorithm employing  $R_{\text{bkg}}$  of 1.1 in the 0 to 15.3  $\text{\AA}^{-1}$  region of k-space. The FEFF6 code <sup>35, 36</sup> was used for scattering path generation, and multi ( $k^1$ ,  $k^2$ ,  $k^3$ )-weighted fits of the data were carried out in r-space and a k-range of 3-14  $\text{\AA}^{-1}$ . The  $S_0^2$  value was set to 0.9, and a global  $E_0$  was employed with the initial  $E_0$  value set to the first inflection point of the rising edge. Scattering paths were fit in terms of a  $\Delta_{\text{reff}}$  and  $\sigma^2$ , which represent the deviation from the expected interatomic distances and the structural disorder, respectively. To assess the goodness of the fits, both the  $R_{\text{factor}}$  (%R) and the reduced  $\chi^2$  ( $\chi^2_{\text{v}}$ ) were minimized, ensuring that the data was not over-fit. An increase in the number of variables is generally expected to improve the  $R_{\text{factor}}$ , however  $\chi^2_{\text{v}}$  may go through a minimum then increase, which is an indication that the model is over-fitting the data <sup>37</sup>. Best fit models were determined using a grid search with fixed values for path coordination numbers by employing Larch, the Python implementation of Artemis <sup>38</sup>. Ultraviolet-visible (UV-vis) spectra were recorded by using Safas Bio-UVmc<sup>2</sup> spectrophotometer using a quartz cell (1 cm path length) and tungsten-halogen source. Absorption spectra were recorded from 200 to 800 nm at  $25 \pm 1$  °C. The  $^1\text{H}$  and  $^{13}\text{C}$  NMR spectra were collected on a Bruker 300 MHz. The NMR samples were prepared by mixing 550  $\mu\text{L}$  of electrolyte with 50  $\mu\text{L}$  of  $\text{D}_2\text{O}$ . Water suppression method was used in all  $^1\text{H}$  NMR experiments.

# Publications

1. Tianyu Gao<sup>#</sup>, **Kilaparthy Sravan Kumar**<sup>#</sup>, Zhen Yan, Maya Marinova, Martine Trentesaux, Mohammed A. Amin, Sabine Szunerits, Yong Zhou, Vlad Martin-Diaconescu, Sebastien Paul\*, Rabah Boukherroub\*, and Vitaly Ordonsky\*. Covalent organic framework derived synthesis of Ru embedded in carbon nitride for hydrogen and oxygen evolution reactions. J. Mater. Chem. A, 2023,11, 19338-19348 (**Equal first author**)
2. **Kilaparthy Sravan Kumar**, Ahmed Addad, Alexandre Barras, Sabine Szunerits, and Rabah Boukherroub\*. Simultaneous Upcycling of PET Plastic Waste and CO<sub>2</sub> Reduction through Co-electrolysis: A Novel Approach for Integrating CO<sub>2</sub> Reduction and PET Hydrolysate Oxidation. J. Mater. Chem. A, 2023, 11, 26075
3. **Kilaparthy Sravan Kumar**, Ahmed addad, Sabine Szunerits, and Rabah Boukherroub\*. Pulse electrodeposition of Bismuth on activated Carbon Felt for Efficient Electrocatalytic CO<sub>2</sub> Reduction and NiCoPO<sub>x</sub> for Effective Anodic PET Degradation to Formate. (Manuscript under preperation)
4. Nasrin Shokouhfar, **Sravan Kumar Kilaparthy** , Alexandre Barras, B. Moses Abraham, Ahmed Addad, Sakshi Bhatt, SumanLata Jain, Sabine Szunerits, Ali Morsali\*, Rabah Boukherroubb\*. Solar-driven ammonia production through engineering of the electronic structure of a Zr-based MOF. (Manuscript accepted in ACS Inorganic Chemistry)
5. Tamazouzt Nait Saada<sup>#</sup>, Liuqing Pang<sup>#</sup>, **Kilaparthy Sravan Kumar**, André HB Dourado, Lucas D Germano, Eduardo D Vicentini, Ana PL Batista, Antonio GS de Oliveira-Filho, Franck Dumeignil, Sébastien Paul, Robert Wojcieszak, Sorin Melinte, Georgiana Sandu, Guido Petretto, Gian-Marco Rignanese, Adriano Henrique Braga, Taissa F Rosado\*, Dalila

Meziane, Rabah Boukherroub, Susana I Córdoba de Torresi, Anderson GM da Silva\*, Sabine Szunerits\*. The importance of the shape of Cu<sub>2</sub>O nanocrystals on plasmon-enhanced oxygen evolution reaction in alkaline media. Electrochimica Acta Volume 390, 10 September 2021, 138810.